EXPERIMENTAL STUDY OF AEROACOUSTIC NOISE PRODUCTION THROUGH COMBINED FLOW MEASUREMENTS AND ARRAY SIGNAL PROCESSING

Miguel Garcia Pedroche

Department of Mechanical & Manufacturing Engineering

Parsons Building

Trinity College

Dublin 2

Ireland

September 2013

A thesis submitted to the University of Dublin in partial fulfillment of the requirements for the degree of Ph.D.

Declaration

I declare that this thesis has not been submitted as an exercise for a degree at this or any other university and it is entirely my own work.

I agree to deposit this thesis in the University's open access institutional repository or allow the library to do so on my behalf, subject to Irish Copyright Legislation and Trinity College Library conditions of use and acknowledgement.

Miguel Garcia Pedroche, September 2013

Abstract

The underlying processes behind sound generation in turbulent flows are still a source of debate. The investigation presented in this thesis focuses on the experimental approaches that aim to clarify this issue by estimating the direct correlation between simultaneous flow-acoustic observations. Under the assumption of a Lighthill type source distribution, these experimental approaches attempt to quantify the contribution that turbulence measured in a small section of turbulent flow has at an observer's location in the acoustic field. However, it has been argued that the contribution that a small section of the flow has on the overall sound measured at an observer's location could be insignificantly small due to the presence of the large number of separate source mechanisms within the flow.

Only recently, a number of experimental approaches have attempted to overcome this issue by replacing the use of single microphones in the acoustic field by that of a combined phased array of receivers. These "flow-beamformed acoustic" studies have availed of the spatial filtering characteristics of phased arrays in combination with a number of non-intrusive flow measurement techniques in an attempt to improve correlation coefficients between simultaneous flow and acoustic observations. The study presented here contributes to these "flow-beamformed acoustic" experimental approaches by the novel introduction and adaptation of a frequency domain "reference" based beamforming algorithm in combination with Laser Doppler Velocimetry (LDV) as the non-intrusive flow measurement technique. Similarly, the use of Time Resolved Particle Image Velocimetry (TR-PIV) as a global, non-intrusive flow measurement method in a "flow-beamformed acoustic" study is presented here for the first time.

A number of experimental arrangements were designed to validate the proposed techniques. These included the study of the source generated by sets of tandem rods in a cross flow configuration and the study of the broad angle radiation of a Mach 0.25 jet.

The first case scenario highlighted the source identification capabilities of two separate "reference" based array signal processing algorithms in combination with the output of an LDV probe. The outcome of this experimental investigation successfully demonstrated how the proposed "reference" based beamforming algorithms can be applied in conjunction with an in-flow, irregularly sampled signal acquired via LDV to identify the location/s of a source of interest. In the free flow (jet) case scenario, TR-PIV was used as the non-intrusive flow measurement technique. On this occasion, flow-acoustic interactions were found to be dominated by an extended, narrowband flow instability. Further analysis associated this interaction to the presence of a localized source mechanism at the nozzle exit. However, the spatial extent of the measured correlation raised a question about the suitability of the "reference" based array algorithms used. Whilst the proposed "reference" based algorithms assume the presence of uncorrelated, compact source mechanisms with homogeneous directivity across the array aperture, the measured flow-acoustic interactions suggested the presence of a more complex source mechanism. A simple simulation designed to exemplify this issue showed how, when the source characteristics differ from those assumed in the array algorithm, this can lead to erroneous source field interpretations. The use of two separate "reference" based beamforming algorithms in combination with flow measurements acquired via LDV and TR-PIV was validated experimentally. The novel algorithm introduced in this investigation was deemed superior for the study of compact narrowband sources. In the presence of more complex sound fields however (i.e. free flow scenario), the use of the standard delay-and-sum "reference" approach was found preferable due to its inherent broadband characteristics and the readily available spatial filtered time domain information. The present investigation also highlights how caution must be exerted when the characteristics of the source/s under study are unknown. It is proposed that future investigations avail of the spatial and temporal resolution capabilities of global flow measurement techniques such as TR-PIV to form a more educated guess of the characteristics of the possible source/s mechanisms present in the flow under study. This information could be used to build tailor made beamforming algorithms including a representative source ansatz.

Contents

List of Figures

Chapter 1

Introduction

The European Commission reports "A Vision for 2020" [1] and the more recent "Flightpath 2050" [2] have set ambitious goals in the role that the European Union (EU) should play in the future of the aviation industry for the coming decades. The EU aims to deliver the best products and services and retain a share of 40% of the global market by 2050. Technological leadership has been identified as the key element through which the EU must reach these goals. A number of challenges have been highlighted in this agenda. Among these, high priority has been given to the reduction of the environmental impact of the aviation industry. Of particular interest is the aimed 65% reduction in the perceived noise emission of flying aircraft with respect to the levels recorded at the turn of the 21st century. Despite the fact that existing noise reduction technologies have reduced significantly the noise emitted by modern aircraft, renewed strategies will need to be implemented to meet this goal.

The pressing need to reduced aircraft noise, and jet noise in particular, has been present since the mid fifties. In fact, aviation noise has been the main driving force behind the ongoing research in the field of "Aeroacoustics". More than 60 years have elapsed since Lighthill [3] introduced the mathematical basis for the understanding of sound production by turbulent flows. Since then, and thanks to technological advancements in measurement and analytical tools, progress in the field of Aeroacoustics has been achieved by a combination of theoretical, experimental and numerical techniques. However, despite the years of research, the underlaying processes behind sound generated aerodynamically are still a source of heated debate among researchers.

Of particular interest for this investigation are the experimental approaches designed to

identify the link between turbulent flow mechanisms and their role in the production of sound. Among these, two methods will receive special mention. The first of these, determines the direct relation between the source mechanisms in the form of measured flow perturbations and their effect in the acoustic pressure field. The second, aims to extract specific information from complex flows by using microphone arrays to sample the related acoustic field. Whilst both experimental strategies have coexisted since the 70's, the synergy between both approaches is relatively new. This, added to recent technological advances in measurement equipment and data acquisition systems has opened the possibility to develop on the work presented to date.

1.1 Thesis Overview

The purpose of this investigation is the development and application of measurement strategies to the study of sound generated aerodynamically. To this purpose, the use of array signal processing alongside a number of non intrusive flow measurement techniques is proposed.

The contents of this thesis are organized as follows:

Chapter 2 introduces the theoretical background behind the experimental techniques used in this investigation alongside a detailed overview of previous work carried out by different researchers.

Chapter 3 presents the two types of "reference" based beamforming algorithms used throughout this investigation. These two approaches are used for the novel introduction of LDV and TR-PIV as flow measurement techniques in a flow-acoustic study type where an array of receivers is used to sample the acoustic field. Particular attention is given to the signal preconditioning necessary to include the signal of an LDV probe into both of the aforementioned techniques.

Chapter 4 describes the experimental facilities and the evaluation and characteristics of the experimental equipment used.

Chapter 5 introduces a preliminary experimental validation of the array signal processing techniques used in this investigation

Chapters 6 - 8 show the experimental and simulated results attained with the proposed

array signal processing and flow measurement techniques.

Finally chapter 9 introduces a summary of results and the possibilities for further research.

Chapter 2

Literature Review

2.1 Propagating Waves

2.1.1 Coordinate Systems

Throughout this chapter reference will be made to sources located in a three dimensional space with time being the fourth dimension. In mostly all cases, a single point in space will be referred in vector notation denoted by **bold** characters representing the source location using the three spatial variables in cartesian coordinates. In other cases, the spherical coordinates system depicted in figure 2.1 will be used.

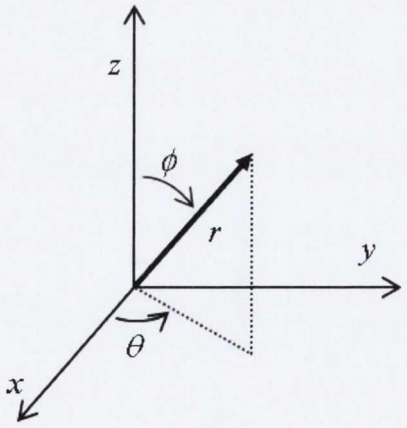

Figure 2.1: Spherical Coordinate System

Both systems, the cartesian and the spherical coordinate systems are related by the fol-

lowing trigonometric formulas:

$$\begin{aligned} x &= r\ sin\phi\ cos\theta \\ y &= r\ sin\phi\ sin\theta \\ z &= r\ cos\phi \end{aligned} \tag{2.1}$$

(2.2)

It should also be noted that the notation for euclidian norm $\|\cdot\|$ will be used to refer to the magnitude of a vector position from its origin, where:

$$\|\cdot\| = \sqrt{x^2 + y^2 + z^2} \tag{2.3}$$

In this way, we can refer to a spatiotemporal signal using the notation $f(\mathbf{r}, t)$ where $\mathbf{r}$ contains the spatial variables (x, y, z), or as in the case of isotropic spherical radiating waves using the notation $f(r, t)$ where r is the radial distance from the origin.

2.1.2 Plane Wave Equation

When a sound wave is transmitted through a fluid, it creates small fluctuations in pressure, density and volume along its path. The Plane Wave Equation (PWE) describing the physics of wave propagation through a medium as a function of space and time has been well documented in several texts on acoustic theory, as for example, Kinsler *et al* [4]. The three dimensional wave equation is described as

$$\nabla^2\varphi(\mathbf{r}, t) - \frac{1}{c_0^2}\frac{\partial^2}{\partial t^2}\varphi(\mathbf{r}, t) = 0 \tag{2.4}$$

where ∇ represents the Laplacian operator in a cartesian coordinate system, c_0 is the speed of sound in the medium and φ is a function of space and time $(\mathbf{r}, t)$ describing an scalar wave quantity such as acoustic pressure fluctuation or particle displacement at location $\mathbf{r} = (x, y, z)$ and time t.

The first assumption in order to solve equation 2.4 is that the wave propagation has time-harmonic dependency. This means that at any fixed point in space described by $\mathbf{r} = (x, y, z)$ the function $\varphi(\mathbf{r}, t)$ takes the form of a complex exponential of frequency

$\omega = 2\pi f$, that is

$$\varphi(\mathbf{r}, t) = \varphi_f(\mathbf{r}) e^{j\omega t} \tag{2.5}$$

substituting this value into equation 2.4 we obtain the time-independent *Helmholtz* equation as

$$\nabla^2 \varphi_f(\mathbf{r}) + k^2 \varphi_f(\mathbf{r}) = 0 \tag{2.6}$$

where now $\varphi_f(\mathbf{r})$ is only a function of space described by the three dimensional vector $\mathbf{r}$ and frequency f and

$$k = \frac{\omega}{c} = \frac{2\pi}{\lambda} \tag{2.7}$$

is the *wavenumber* which describes the wave frequency with units of radians per meter. In the case of free propagation equation 2.6 yields a time-independent solution of the form

$$\varphi_f(\mathbf{r}) = A\ e^{-j(\mathbf{k}\cdot\mathbf{r})} \tag{2.8}$$

where A is a complex constant, $\mathbf{r}$ describes the spatial point of interest with respect to the origin of the cartesian coordinate system and $\mathbf{k}$ is the "propagation vector" that defines the direction of wave propagation with a magnitude equal to the wavenumber k. Assuming that the dot product of $(\mathbf{k}\cdot\mathbf{r})$ is a constant, equation 2.8 describes a plane wave with constant phase traveling in the direction of the propagation vector $\mathbf{k}$.

2.1.3 Free Space Propagation Due To A Monopole Source

We shall now evaluate the contribution to the flow field at location $\mathbf{r}$ due to an idealized monopole source radiating at location $\mathbf{r}_0$ as shown in figure 2.2

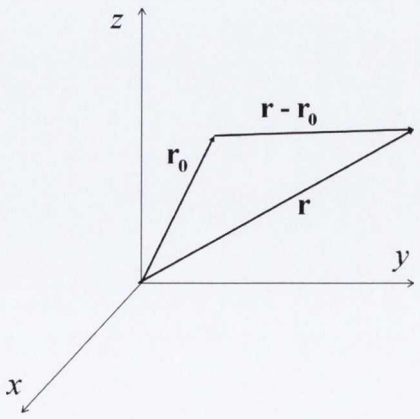

Figure 2.2: Source and observers locations, $\mathbf{r}_0$ and $\mathbf{r}$, described in a cartesian coordinate system.

The lossless, inhomogeneous Helmholtz equation is described by

$$\nabla^2 g(\mathbf{r}|\mathbf{r}_0) + k^2 g(\mathbf{r}|\mathbf{r}_0) = \delta(\mathbf{r} - \mathbf{r}_0) \tag{2.9}$$

where the impulse function $\delta(\mathbf{r} - \mathbf{r}_0)$ represents a unit-amplitude, omnidirectional point source at $\mathbf{r}_0$. The solution to this inhomogeneous Helmholtz equation is given by

$$g(\mathbf{r}|\mathbf{r}_0) = -\frac{e^{-jk\|\mathbf{r}-\mathbf{r}_0\|}}{4\pi\|\mathbf{r} - \mathbf{r}_0\|} \tag{2.10}$$

As described by Ziomek [5], the green's function $g(\mathbf{r}|\mathbf{r}_0)$ describes the response of a fluid medium at frequency f and spatial location $\mathbf{r}$ due to an impulse source of unit amplitude at $\mathbf{r}_0$.

2.2 Aeroacoustic Noise Source Identification

2.2.1 Lighthill's Acoustic Analogy

As described by Jordan and Gervais [6], sound generation by turbulence in fluid flows requires the conversion of the energy associated with the rotational hydrodynamic field into acoustic energy. The way in which this process takes place is still not well understood. The work presented by Lighthill [3] in 1952 represented an important step in the understanding of this process.

Lighthill compared the equations governing the density fluctuations in a real fluid to those applicable to describe acoustic wave propagation in a uniform medium. In this "Acoustic Analogy Theory" the difference between these two sets of equations was considered as the fluctuating force causing sound propagation in the acoustic medium at rest surrounding a small volume of fluid.

Lighthill's approach began with the exact equation of conservation of mass density, ρ and the equation of momentum density ρv_i for a medium under no external forces where v_i stands for the gas velocity three dimensional vector $[v_u, v_v, v_w]$. These equations are expressed as

$$\frac{\partial \rho}{\partial t} + \frac{\partial}{\partial x_i}(\rho v_i) = 0 \tag{2.11}$$

$$\frac{\partial}{\partial t}(\rho v_i) + \frac{\partial}{\partial x_j}(\rho v_i v_j + p_{ij}) = 0 \tag{2.12}$$

where equation 2.11 describes the principle of mass conservation in a fluid element and equation 2.12 states that the rate of change of momentum in a fixed volume changes at the same rate as if the gas were at rest under the combined action of: (1) the viscous stresses and hydrostatic pressure (real stresses) acting at the particle boundary described by the term p_{ij}, (2) the fluctuating Reynolds stresses $\rho v_i v_j$ representing the flow across the particle boundary.

In the case of a uniform acoustic medium at rest without external induced forces, the system would only be exposed to stresses in the form of a hydrostatic pressure field. The pressure fluctuations in this medium would be proportional to the variations in density $p \propto \rho$ by means of the constant of proportionality c_0^2 where the value c_0 is the speed of sound propagation in a uniform acoustic medium at rest. In this case, the momentum transfer assuming isotropic pressure would simply be described as

$$\frac{\partial}{\partial t}(\rho v_i) + c_0^2 \frac{\partial \rho}{\partial x_i} = 0 \tag{2.13}$$

Lighthill then stated that the density fluctuations in the real flow must be those given by the difference between the stresses in the real flow and those in the uniform acoustic medium at rest. This is what the Lighthill stress tensor T_{ij} describes as

$$T_{ij} = \rho v_i v_j + p_{ij} - c_0^2 \rho \delta_{ij} \tag{2.14}$$

where the term δ is the Dirac delta function where δ_{ij} is equal to 1 when $i = j$ and 0 elsewhere. This forcing term is then placed in the right hand side of the homogeneous momentum equation describing the transfer of momentum in an acoustic medium at rest. Under this conditions, equations 2.11 and 2.12 can now be reformulated as

$$\frac{\partial \rho}{\partial t} + \frac{\partial}{\partial x_i}(\rho v_i) = 0 \tag{2.15}$$

$$\frac{\partial}{\partial t}(\rho v_i) + c_0^2 \frac{\partial \rho}{\partial x_i} = -\frac{\partial T_{ij}}{\partial x_j} \tag{2.16}$$

The important significance of these equations is that, a fluctuating flow surrounded by a medium at rest would generate the same density fluctuations as an stationary acoustic medium under an externally applied stress T_{ij}. By eliminating the momentum density from equations 2.16 and 2.15 the well know Lighthill acoustic analogy is derived as:

$$\frac{\partial^2 \rho}{\partial t^2} - c_0^2 \frac{\partial^2 \rho}{\partial x_i^2} = \frac{\partial^2 T_{ij}}{\partial x_i \partial x_j} \tag{2.17}$$

which is no other than the homogeneous wave equation with the forcing Lighthill stress tensor on the right hand side. Also Lighthill argued that in the case of low Mach number flows and assuming isothermal conditions between the flow and the outside air, the viscous and conduction effects are negligible. The resulting approximate form of the stress tensor in equation 2.14 becomes

$$T_{ij} \approx \rho v_i v_j \tag{2.18}$$

which clearly states that under these conditions the main contributors to the sound production are the fluctuating Reynolds stresses $\rho v_i v_j$.

2.2.2 Free Turbulence

Turbulent mixing of fluids occurs not only when fluids flow over fixed boundaries but also when fluids stream pass each other at different velocities. For instance, in the case where a round jet discharges into a large expanse of quiescent fluid. The flow from a circular nozzle into stagnant air can be divided into regions as shown in figure 2.3. As the jet flow collides with the stagnant fluid it sets some of it into motion in a process defined as "entrainment" (see Masey [7]). The turbulence created as the jet and the stagnant fluid equalize their velocities forms an ill defined boundary layer. In the "transition region" this boundary layer remains small compared with the nozzle dimension and is followed by a quasi-plane mixing layer where the flow is "self-preserving" (see [8]) [1]. Departure from self-preservation occurs when the thickness of the "mixing region" becomes a appreciable fraction of the nozzle radius. This regions expands until it fully mixes with the inner core of jet flow that remains convecting at the original jet exit velocity. This unmixed, irrotational section of the jet flow is known as the jet's "potential core".

[1] As defined by George [9] "A flow is said to be self-preserving if there exist solutions to its dynamical equations and boundary conditions for which all terms have the same relative value at the same relative location". In other words self-preservation implies a kind of equilibrium in the flow where all of its dynamical influences evolve together.

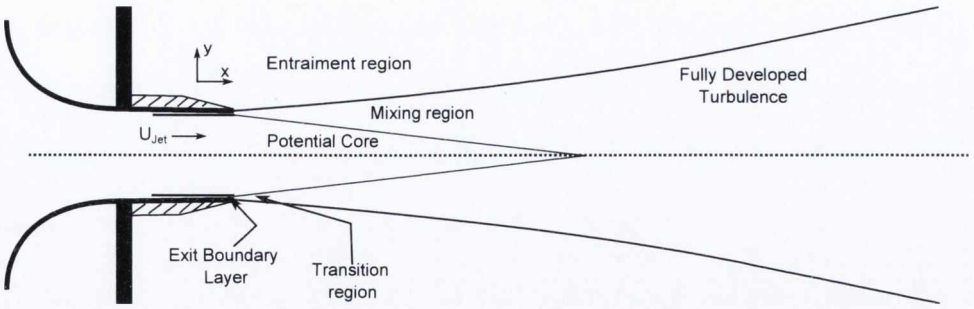

Figure 2.3: Schematic structure of a subsonic jet based on the schematic layout as presented by Bradshaw [8]

Originally, turbulence was regarded as a random assortment of small eddies. The same was assumed for the associated noise generation mechanisms. It wasn't until the 1960's that the existence of a more organized flow structure idea began to emerge. In 1967 Erik Mollo-Christensen [10] suggested that such organized structures could play a role in the noise generation process. In his investigation, he suggested that one should expect to see intermittently a rather regular spatial structure in the shear layer. He further found evidence of this by cross correlating near field microphone signals at different distances along the jet axis. While at small distances one frequency would seem to dominate the cross correlation, at larger distances a subharmonic oscillation was found to be dominant. It wasn't until the 70's when the aeroacoustic community began to focus into the study of these coherent structures. Independent studies carried out by Crow and Champagne [11] and Brown and Roshko [12], further corroborated experimentally the existence of these larger coherent structures or "wave-packets" using flow visualization techniques on unbounded flows.

It was in the 90's when a number of investigators (e.g. Tam *et al* [13, 14], Seiner and Krejsa [15]) suggested that two different source mechanisms were responsible for turbulent mixing noise in supersonic jets. The first, responsible for the characteristic radiation measured towards the aft-angle jet section $(20 - 40°)$ is attributed to the aforementioned large coherent structures. Its associated characteristic spectrum peaks at ≈ 0.2 Strouhal number and has a steep roll-off at either side. The second, related to the smaller turbulent structures referred to as "fine-scale", dominates the weaker radiation observed along the jet axis sideline. The associated spectral shape, measured at an angle of 90° from the jet axis, is characterized by a broader spectrum and a clear shift towards higher frequencies

peaking at ≈ 0.4 Strouhal number. The theory of dissimilar source components was again extended into the subsonic jet case by Tam *et al* [13]. He suggested that the two source theory should be true regardless of the jet's Mach number. Experimental evidence of this was supported by contrasting a large collection of far-field noise data [2]. This theory has driven many of the present jet noise investigations towards the characterization of these allegedly individual source mechanisms. However, this theory is not free from criticism. Among other critics, a recent review by Jordan and Colonius [17] argued that this dissimilarity in spectral shape at different radiation angles, does not constitute evidence of dissimilar source mechanisms. They suggested, based on the work reported by Papamoschou [18], that this dissimilarity in the radiated frequency content may also be explained by the directivity of a single "wave-packet" type source mechanism.
The link between a "wave-packet" type source and the noise radiated towards the aft-angle section of turbulent jets has been well documented, experimentally, numerically and analytically (see review by Jordan and Colonious [17]). However, the contribution of such source mechanism to the broad angle jet noise radiation (i.e. 90°) is still unclear.

2.3 Array Signal Processing

Whilst single acoustic pressure measurements quantify the sound field at a particular point in space, there are limitations to the possible information that can be extracted from them. In the presence of complex sound fields, these measurements become hindered by poor signal-to-noise ratio making the task of source identification even more demanding. These limiting factors have made Array Signal Processing an attractive solution when there is a need to extract specific information from signals carried by propagating waves. As described by Johnson & Dudgeon [19], combining the output of a number of receivers can

- Enhance the signal-to-noise ratio beyond that of a single receiver.
- Characterize the sound field by determining the number of sources, their location in space and the waveforms that these are emitting.

[2] A clear example of the far field spectral characteristics of jet noise as a function of polar angle is presented by Tam *et al.* [16]

- Track moving sources in space.

The term "Array Signal Processing" or "Beamforming", is given to the variety of techniques used to extract information from signals acquired by an array of sensors. As described by Dudgeon [20] beamforming can be thought of as the spatial analogy to a band pass filter in the frequency domain. In the same way as a temporal filter needs to acquire a signal over a temporal aperture, a spatial filter needs to acquire a signal over a spatial aperture. This is achieved by means of a continuous aperture, as in the case of acoustic mirrors, or by means of acquiring data at discretized locations, as in the case of an array of sensors [21]. In the case of acoustic mirrors, the spatial filtering effect is achieved by locating a receiver at the inner focal point of a concave mirror while the mirror's outer focal point is directed to the focal point of interest (see figure 2.4)

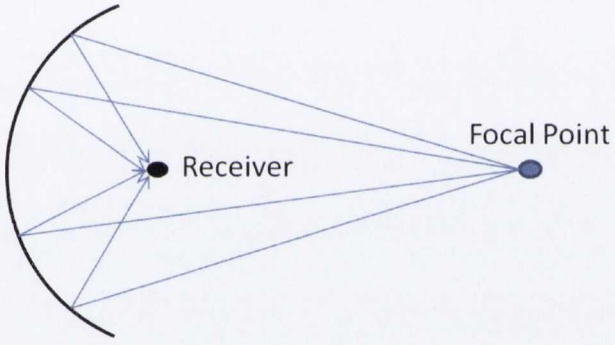

Figure 2.4: Schematic layout of an acoustic mirror.

Whilst ray paths arriving from the outer focal point location converge constructively at the inner focal point, rays from other locations are scattered causing destructive interference at the receiver location. In the case of microphone arrays, this spatial filtering effect is achieved by linearly combining the receivers signals using the signal processing methods that will be described later.

Early measurements attained by arrays of discrete sensors, could not outperform acoustic mirrors in spatial resolution, frequency range and signal-to-noise ratio. In recent times thanks to advances in computer capacity and data acquisition systems the disadvantages of array processing over acoustic mirrors are disappearing. These improvements, added to the much shorter times needed to obtain measurements when using arrays, have made array signal processing the preferred source location technique.

Some of the applications of spatial filters are, radar, sonar, geophysical exploration and as in our case, aeroacoustic source identification as in the early investigation carried out by Billingsley & Kinns [22] where the first example of a modern beamforming array was used to study the far field sound radiation of a full size jet-engine.
Prior to the introduction of a number of beamforming algorithms, the following section will introduce some of the basic concepts in array signal processing.

2.3.1 Background Beamforming Concepts

2.3.1.1 Continuous Apertures

The term *aperture* in array signal processing defines the spatial extent over which a transducer samples a propagating wave field. In the case of acoustic arrays, this is defined as the spatial extent of the electroacoustic transducer (i.e. microphone array) that is used to sample the acoustic field. An aperture is represented by its *aperture function*. The aperture function contains information about the size and shape of the transducer and the weighting given to the sampled field as a function of location within the aperture. When a propagating wave field described by $g(t, \mathbf{r})$ is observed through a continuous aperture of infinitesimal volume V at location $\mathbf{r}$ with impulse response $a(\mathbf{r})$ the output is given by the product of the convolution between both terms, as:

$$z(t, \mathbf{r}) = a(t, \mathbf{r}) * g(t, \mathbf{r}) \tag{2.19}$$

By taking the Fourier transform on both sides we obtain

$$Z(f, \mathbf{r}) = A(f, \mathbf{r})G(f, \mathbf{r}) \tag{2.20}$$

where the term $A(f, \mathbf{r})$ is known as the aperture function. In the literature, the response of the aperture function to a propagating wave as a function of frequency and direction of arrival is known as the *beampattern*, *directivity pattern*, or sometimes as the *aperture smoothing function*. In the simplified case of a propagating plane wave satisfied by the solution of equation 2.4 the directivity pattern and the aperture function form a spatial Fourier transform pair as:

$$D(f, \boldsymbol{\alpha}) = \mathfrak{F}_{\mathbf{r}}\{A(f, \mathbf{r})\} = \int_{-\infty}^{\infty} A(f, \mathbf{r}) e^{j2\pi\boldsymbol{\alpha}\cdot\mathbf{r}} d\mathbf{r} \tag{2.21}$$

where D represents the directivity pattern, $\mathfrak{F}_{\mathbf{r}}\{\cdot\}$ denotes the three dimensional Fourier transform and $\boldsymbol{\alpha} = (f_X, f_Y, f_Z)$ represent the spatial frequencies with units of cycles per meter in a spherical coordinate system, as:

$$\begin{aligned} f_X &= \frac{sin\phi cos\theta}{\lambda} \\ f_Y &= \frac{sin\phi sin\theta}{\lambda} \\ f_Z &= \frac{cos\phi}{\lambda} \end{aligned} \tag{2.22}$$

A typical example of an aperture function is described by a line segment of length L along the $x - axis$ with a weighting described as

$$A(f, \mathbf{r}) = \begin{cases} 1, & |\mathbf{r}| \leq L/2 \\ 0, & \text{otherwise} \end{cases} \tag{2.23}$$

where the spatial position vector describing the aperture location is $\mathbf{r} = (x, 0, 0)$ and so the aperture function becomes

$$A(f, x) = \boldsymbol{\alpha} \cdot \mathbf{r} = f_X x \tag{2.24}$$

therefore the directivity pattern for a one dimensional aperture is given by

$$D(f, f_X) = \int_{-L/2}^{L/2} A(f, x) e^{j2\pi f_X x} dx \tag{2.25}$$

which has a solution of the form

$$D(f, f_X) = Lsinc(f_X L) \tag{2.26}$$

where

$$sinc(x) = \frac{sin(x)}{x} \tag{2.27}$$

Figure 2.5(b) shows the directivity pattern for the rectangular aperture function described in equation 2.23 as a function of wavelength and angle of arrival with respect to a segment aperture of length L along the x axis. The width of the main lobe is defined by the ratio λ/L. It is easy to see that its width is directly proportional to the wavelength and inversely proportional to the length L of the aperture. The term *beamwidth* refers to a fraction of the total width of the lobe and its bounds are commonly defined by the half power points $(-3dB)$ as shown in figure 2.5(b).

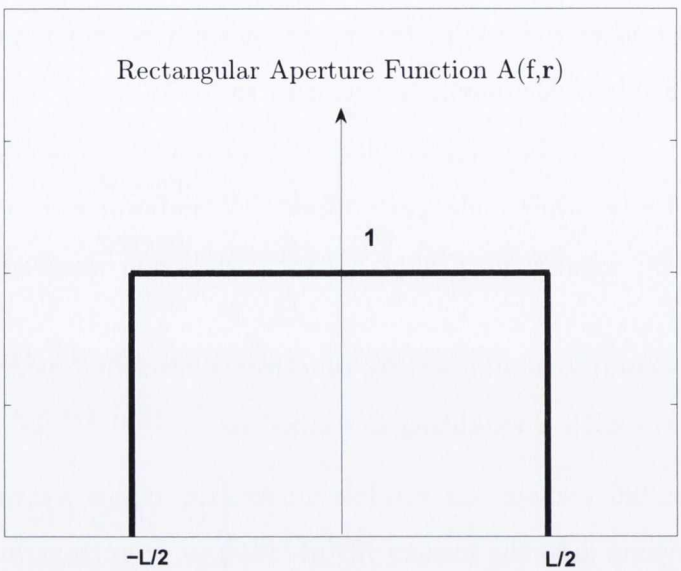

(a) Graphical representation of the aperture function A(f,**r**)

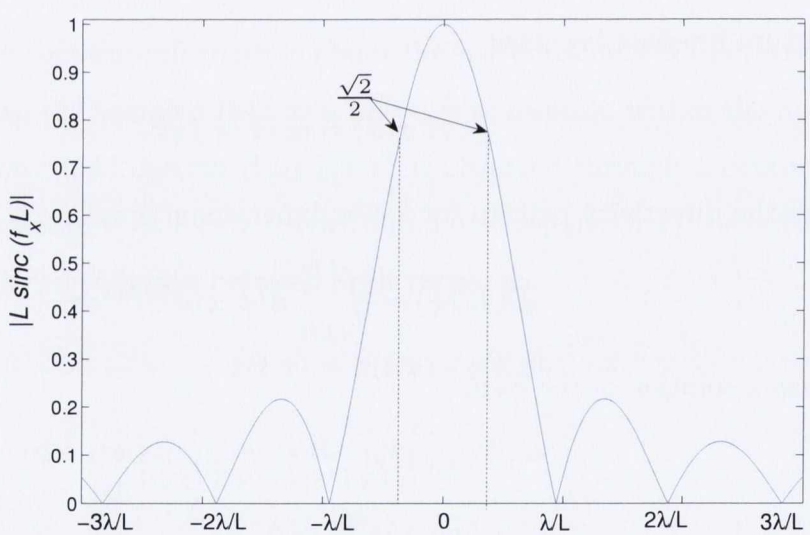

(b) Continuous aperture beampattern

Figure 2.5: Aperture function and beampattern for a continuous linear array

2.3.1.2 Arrays of discrete sensors

Whilst the previous section considered the continuous aperture case, this section describes the cases where a discretized aperture is used to sample the acoustic field. Consider the case of a one dimensional array with an M number of equi-spaced receivers with unit weighting ω_m along the x axis at locations x_m as shown in figure 2.6.

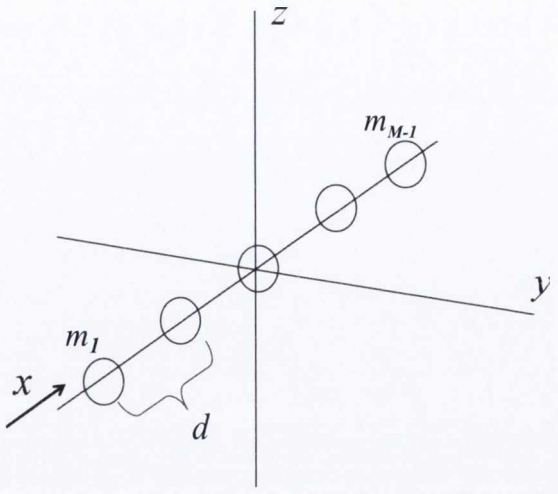

Figure 2.6: Representation of a discretized, equally spaced linear aperture with a distance d between receivers.

The aperture function of the discretized aperture can be described as the summation of a set of M impulse functions at each of the sensor positions as

$$A(f,x) = \sum_{m=1}^{M} \omega_m \delta(x - x_m) \tag{2.28}$$

where x_m is the position of each of the receiver along the x axis. In the case of far field wave propagation the corresponding directivity pattern, or as from now it will be refer to as beampattern becomes

$$D(f,f_X) = \sum_{m=1}^{M} \omega_m e^{j2\pi f_X x_m} \tag{2.29}$$

by setting the angle of arrival $\theta = 0$, f_X reduces to $sin\phi/\lambda$. The beampattern expression for a single frequency can then be expressed as

$$D(k,\theta) = \sum_{m=1}^{M} \omega_m e^{jksin\phi x_m} \tag{2.30}$$

were $k = 2\pi/\lambda$.

2.3.1.3 Variable Parameters in Discrete Apertures

The effects of varying the parameters of a discrete aperture are well described by Johnson and Dudgeon [19], these can be summarized as follows

- The aperture size determines the width of the beampattern mainlobe and by default the resolution of the array.
- The number of receivers in the array determines the beampattern sidelobe levels.
- The sensor weighting ω_m determines the detail shape of the beampattern.
- For a fixed array geometry the frequency of the wave field is inversely proportional to the width of the beampattern's mainlobe.

Examples of varying the array characteristics described above are shown in figures 2.7 & 2.8. Figure 2.7(a) clearly shows the effect that the aperture size has on the beampattern main lobe width. As the aperture size increases the mainlobe becomes narrower increasing the spatial resolution of the aperture. The limiting effect that increasing the aperture has while maintaining the number of receivers is determined by the *aliasing* effect that will be introduced later. In the case of a fixed aperture size, figure 2.7(b) shows the effect that increasing the number of receivers has on the beampattern. Whilst the mainlobe width in not affected, the sidelobe levels decrease with increasing number of receivers. The level difference between the main lobe and the side lobes determines the *dynamic range* of the beampattern, in other words, the maximum level difference between two sources that can be discriminated.

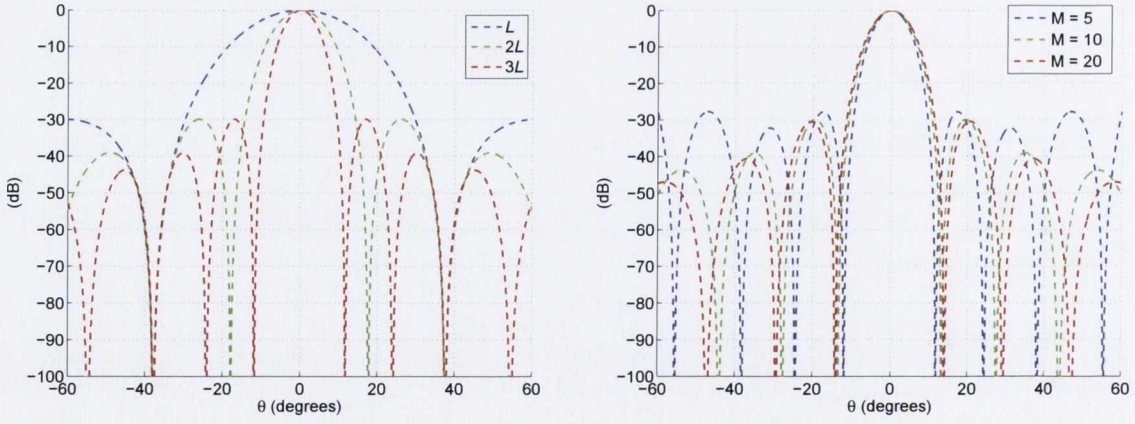

(a) Effect of increasing the array aperture with a fixed number of microphones

(b) Effect of increasing the number of microphones on a fixed size array aperture

Figure 2.7: Beampattern dependency on array length and number of receivers

The effects of varying the sensor weighting are shown in figure 2.8. Whilst the sidelobe levels are clearly reduced the main lobe width is increased [3].

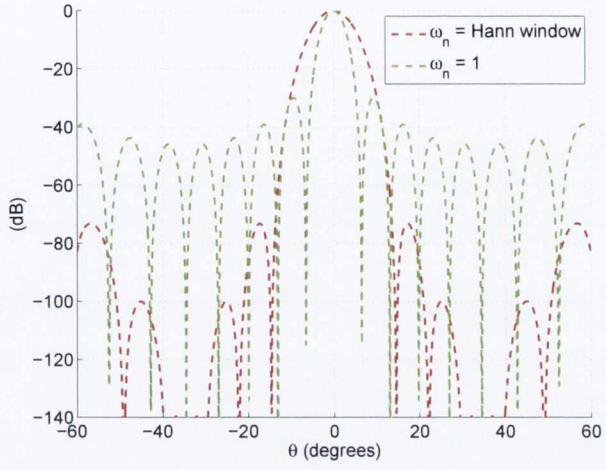

Figure 2.8: Effect of varying the sensor weighting

Figure 2.9 shows the beampattern's frequency dependency for a fixed array geometry. With increasing frequency the beampattern mainlobe width decreases. In most cases, this effect is desirable as it improves the spatial resolution of the array.
However, the spacing between receivers dictates the maximum frequency at which improved resolution can be achieved before the appearance of spurious main lobes. As it can be seen in figure 2.9, secondary main lobes termed *grating lobes* start to appear at approximately 5000Hz. In a similar way to audio sampling where the *Nyquist* frequency is given by half of the sample frequency, the equivalent *spatial Nyquist frequency* at which aliasing occurs is given by

$$f_c = \frac{c_0}{2d} \tag{2.31}$$

where c_0 is the speed of sound in air and d is the spacing between receivers.

[3]For a more detailed discussion on the effect of using different weighting coefficients and the type of weighting functions that are applied to linear arrays, the reader is referred to the work presented by Ziomek [23]

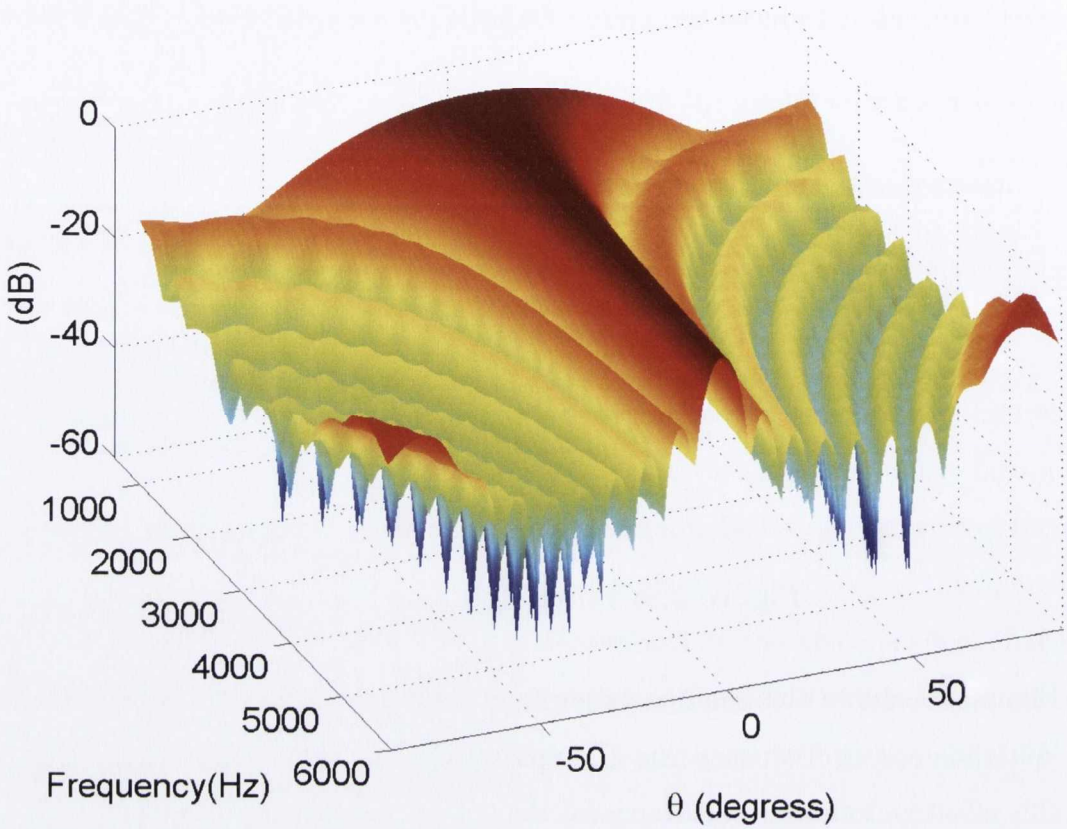

Figure 2.9: Linear array's beampattern as a function of frequency and angle of arrival.

2.3.1.4 Aperiodic Arrays and the Co-array

Whilst the resolution requirements at the lower frequency of interest determines the size of the aperture, the highest frequency determines the minimum distance between receivers. In most cases meeting these requirements would require the use of a high number of sensors. However, in most practical cases a compromise between the number of available sensors and audio channels and the type of source under study has to be met.

The previous section presented the half wavelength criteria that needs to be met by a regularly spaced array in order to avoid the effects of spatial aliasing. These secondary lobes in an array pattern are present when signal arriving from other than the steered angle are added coherently. The contribution of these can be mitigated by eliminating all the periodicities in the location of the array receivers. This is the principle behind the use of irregular or aperiodic arrays. The use of this type of arrays allows to reduce the number of sensors without the constrictions of the half wavelength criteria while maintaining a

fixed aperture size. Sparse arrays are designed to eliminate the periodicities in the spacing between receivers while maintaining a maximum number of unique intra-spaces. These type or arrays can be designed using a random process or by using an algorithm that guarantees non-redundancy in the sensor spacings.

As described by Underbrink [24] the co-array is the vector spacing view between the array receivers and is given by

$$\begin{aligned} \vec{X}_{co-array} &= \vec{x}_{i_{th}} - \vec{x}_{j_{th}}, \\ i_{th} &= 1 : N, \\ j_{th} &= 1 : N, \end{aligned} \tag{2.32}$$

where $\vec{x}_{i_{th}}$ is the vector location of the n_{th} receiver in the array. The maximum number of unique spacings in an array with an N number of receivers is given by

$$Sp_{co-array} = N^2 - (N - 1) \tag{2.33}$$

An optimized sparse array should have a number of unique vectors between receivers close to that of the value given by equation 2.33. An example of two different array distribution and their corresponding co-array are shown in figures 2.10 and 2.11.

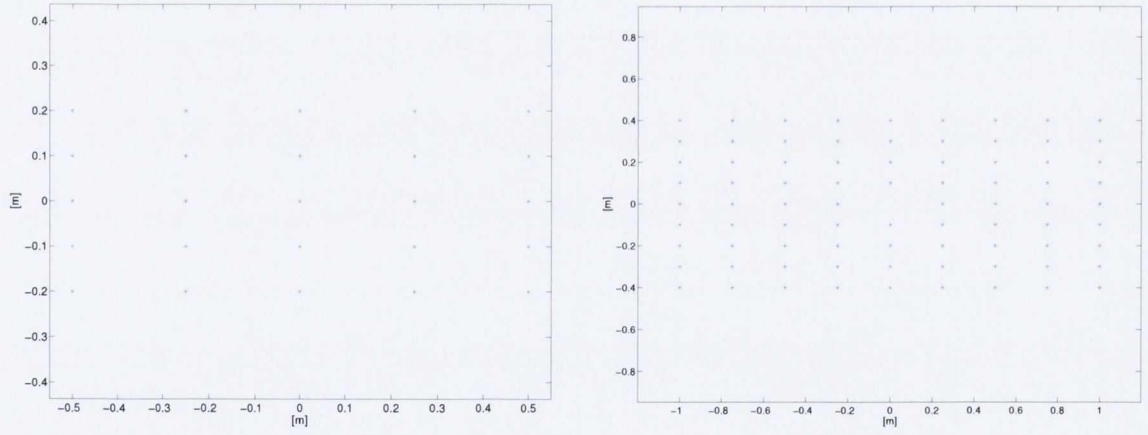

(a) 2-D Rectangular array microphone layout

(b) Co-array

Figure 2.10: 25 receivers rectangular planar array layout and corresponding co-array view

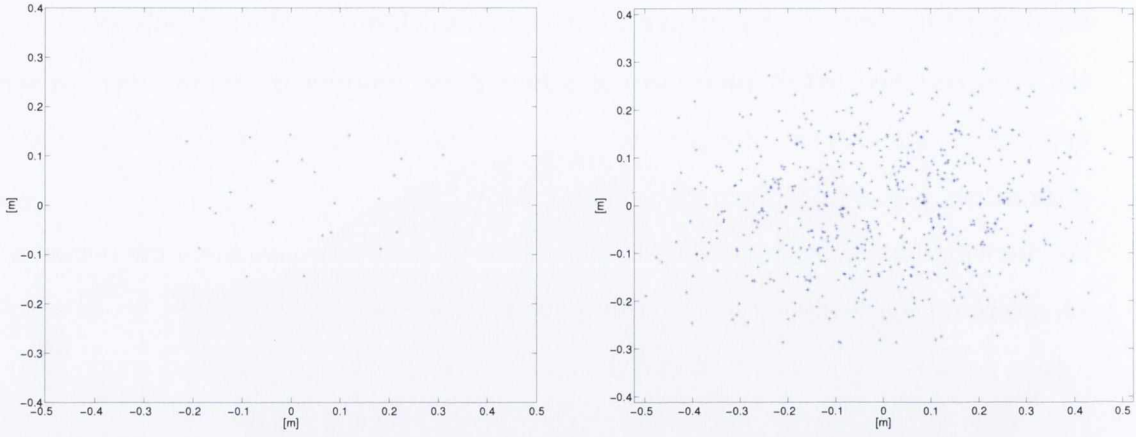

(a) 2-D Randomized array microphone layout (b) Co-array

Figure 2.11: 25 receivers randomized planar array layout and corresponding co-array view

Figures 2.10 shows a rectangular 25 receivers array and its corresponding co-array vector view. Out of the possible 601 unique spacings there's only 80 unique vector spacings. This co-array configuration can be contrasted to the vector spacing view in figure 2.11(b) obtained from the locations of the randomized array of receivers presented in figure 2.11(a). It is obvious how the unique intra-vector spacing between all receivers is kept at its maximum. These results show how sparse arrays can maximize the number of unique intra spacings between receivers. This in turn can reduce the appearance and level of spurious lobes when compared to those calculated with regularly spaced apertures with the same number of receivers.

2.3.1.5 Near field formulation

The aforementioned cases have considered far-field propagation. In other words, all these cases assumed the arrival of plane wavefronts at the array aperture. In the cases where sources are located in the near field with respect to the array aperture, the beampattern formulation needs to account for the curvature of the spherical waves impinging on the array. The rule of thumb to determine at which distance the near and far field assumptions hold is commonly know as the Rayleigh distance, which is described as

$$r = 2L^2/\lambda \tag{2.34}$$

where r is the distance to the source from the array center, L is the maximum dimension of the array and λ is the source wavelength. In order to compensate for the difference in time of arrival at the receivers due to the curvature of the wavefront, the path lengths between the receivers and the focal point of interest $\boldsymbol{\xi}$ are calculated using the center point of the array as the coordinate system origin. Assuming a number n of potential point source locations $\boldsymbol{\xi}_n$ and the presence of a unit point source in the near field at $\boldsymbol{\xi}_s$ the beampattern is calculated as

$$D(k,\xi) = \sum_{m=1}^{M} \omega_m \frac{r^s}{r_m^s} e^{-jk[(r^s - r^n) - (r_m^s - r_m^n)]} \tag{2.35}$$

where r^s and r_m^s are the radial distances from the source location $\boldsymbol{\xi}_s$ to the axis origin **O** (see figure 2.12) and to each of the receivers along the x-axis and r^n and r_m^n are the radial distances from the axis origin and each of the array receivers to a number of assumed focal locations represented by $\boldsymbol{\xi}_n$. By inspection, it is easy to see that the beampattern's maximum sensitivity is obtained when $r^s = r^n$ and $r_m^s = r_m^n$. The ratio between r^s and r_m^s accounts for the amplitude difference between receivers due to spherical wave propagation.

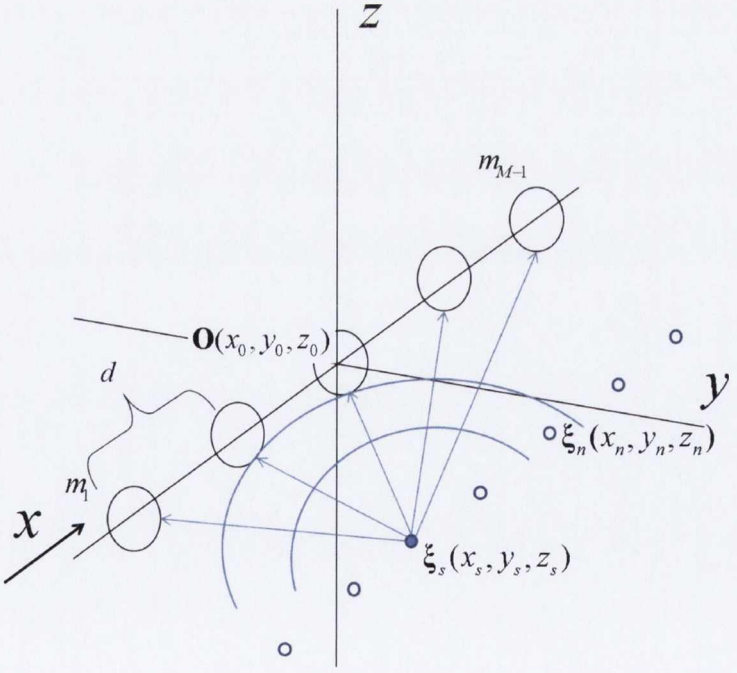

Figure 2.12: Spherical wave arriving at the array receivers from a near field point source at $\boldsymbol{\xi_s}$. **O** represents the coordinate system origin and $\boldsymbol{\xi_n}$ represents an n_{th} focal point.

In the work carried out in this investigation we will be mostly interested with the near-

field assumption as in all of our experiments, the array will be located at a distance well within Rayleigh distance near field criteria.

Up to now we have looked at the spatial filtering characteristics obtained from continuous and discretized apertures. We have also considered the effect that varying the aperture parameters, such as array length or sensor weighting has on the aperture's beampattern. The next step necessary to apply spatial filtering over an area of interest would be to "*steer*" the beampattern maximum sensitivity to a desired direction or location in space. The following section introduces the signal processing techniques used to this purpose.

2.3.2 Beamforming Algorithms

Consider a point source radiating in space at an arbitrary location $\boldsymbol{\xi_0}$ and a number of microphones located in a three dimensional coordinate system. The location of these receivers in space is described by $\mathbf{r}_m = (x, y, z)$, where the subscript $(\cdot)_m$ specifies the receiver number from 1 to M. The pressure fluctuation at each of the receiver locations is described by:

$$p_m(t) = p(\mathbf{r}_m, t) \tag{2.36}$$

Assuming that a point source exists at location $\boldsymbol{\xi_0}$, the acoustic pressure at each receiver is described by:

$$p(\mathbf{r}_m, t) = \frac{\sigma(t - \Delta t_{em})}{4\pi \|\mathbf{r}_m - \boldsymbol{\xi_0}\|} \tag{2.37}$$

where $\sigma(t)$ is the emitted source and Δt_{em} is the emission time delay between the source location and receiver m described as

$$\Delta t_{em} = \frac{\|\mathbf{r}_m - \boldsymbol{\xi_0}\|}{c_0} \tag{2.38}$$

where c_0 is the speed of sound propagation in the acoustic medium.

Beamforming algorithms cleverly combine the microphone signals in order to identify the location of the impinging source/s on the array. All these algorithms make use of the respective arrival time differences between array receivers to identify the source location. An extensive number of algorithms are available. However, two of these, *delay-and-sum* and *conventional beamforming*, still form the basis for most of the more advanced beamforming algorithms. These two basic beamforming algorithms are presented next.

2.3.2.1 Delay-and-sum

The delay-and-sum algorithm estimates the contribution from a number of potential source locations $\boldsymbol{\xi_n}$ by delaying the receiver's signals by an amount Δt_{foc}. This delay corresponds to the direct path propagation at the speed of sound in the acoustic medium c_0 between each of the array receivers and the focal location $\boldsymbol{\xi_n}$. The mean squared value of the delayed and summed signals is calculated at each of the focal locations as shown in equation 2.39.

$$Beam_{ds}(\boldsymbol{\xi_n}) = \frac{1}{T}\int_0^T \left[\frac{1}{M}\sum_{m=1}^{M} p_m(t - \Delta t_{foc})\right]^2 dt \tag{2.39}$$

It is when the applied delay Δt_{foc} to each of the receiver signals corresponds to that of the emission time delay Δt_{em} that the output of equation 2.39 is maximized. This is clearly observed by substituting equation 2.37 into 2.39. Assuming negligible amplitude loss due to spherical propagation this can be written as

$$Beam_{ds}(\boldsymbol{\xi_n}) = \frac{1}{T}\int_0^T \left[\frac{1}{M}\sum_{m=1}^{M} \sigma(t + \{\Delta t_{em} - \Delta t_{foc}\})\right]^2 dt \tag{2.40}$$

By inspection of equation 2.40, it is easy to see that when the estimated delay Δt_{foc} coincides with the emission delay Δt_{em} the output of equation 2.40 is maximized whilst when this is not the case the microphone signals are summed incoherently and the array output is in most cases minimized.

2.3.2.2 Conventional Beamforming

The first step in conventional beamforming is to Fourier transform the time pressure signals $p_m(t)$ recorded by each of the array microphones as

$$P(f) = \int_{-\infty}^{\infty} p_m(t) e^{-2\pi j f t} dt \tag{2.41}$$

This yields an M-number of vectors of complex pressures. A Hermitian Cross Spectrum Matrix (CSM) of size $M \times M$ is now formed with the microphone complex pressures as:

$$\Phi_{n,l} = \langle P_n(f) P_l^*(f) \rangle \tag{2.42}$$

where each element of Φ in row n and column l corresponds to the ensemble averaged cross spectrum of the complex pressures at microphones n_{th} and l_{th}. This CSM contains the

relative phase between the array microphone signals as a function of frequency, distance between the source and each microphone and the propagation time. Array "steering" to each of the predetermined focal locations $\boldsymbol{\xi}_n$ is achieved by a vector of length M containing the theoretical Green's function for spherical wave propagation from each of these focal points to each of the microphone locations of the form

$$\boldsymbol{\omega}(\boldsymbol{\xi_n}) = e^{-jk(\|\mathbf{r}_m - \boldsymbol{\xi}_n\|)} \tag{2.43}$$

The narrowband beamforming output for a given focal point $\boldsymbol{\xi}_n$ is then calculated as:

$$Beam_{freq}(\boldsymbol{\xi_n}, f) = \boldsymbol{\omega}^* \Phi \boldsymbol{\omega}^T \tag{2.44}$$

where the superscript * denotes complex conjugate and the superscript ^{T} denotes a non-conjugate transpose. When the "steering" vector $\boldsymbol{\omega}$ contains the relative phase information between each of the receivers and the actual source, the phase differences between receivers in the CSM is corrected. In this instance, the microphone signals are summed constructively and maximum output is achieved from the phased array.

2.3.3 Diagonal Removal (DR)

In some experimental set-up conditions, the microphone auto-powers that contain no usable source localization information have much higher levels than those obtained from cross-powers between receivers. This effect can limit the dynamic range of the beamforming output. Two cases in which this effect can affect the beamformer output were described by Sijtsma [25]. The first is when microphones are affected by hydrodynamic disturbances as is the case of measurements carried out at close wind tunnel sections. The second and less obvious is when there is a loss of coherence between receivers. This can be the case when sound travels through a turbulent medium (i.e. jet's shear layer) before arriving at the receivers. In this cases "cleaner" noise maps can be attained by removing the auto-powers terms before estimating the beamform output.

The process of subtracting the auto-powers from the cross spectral matrix in the conventional beamforming algorithm is normally referred to as "Diagonal Removal". This is achieved by modifying equation 2.44 as:

$$Beam_{freq}(\boldsymbol{\xi_n}, f) = \sum_{(n,l)\in S}^{N} \boldsymbol{\omega}_n^* \Phi_{(n,l)} \boldsymbol{\omega}_l^T \tag{2.45}$$

where S is a sub-set of all possible microphone (n, l) combinations that eliminates the auto-power components

$$S = \{(n, l) \in [1 \dots N] \times [1 \dots N]; n \neq l\} \tag{2.46}$$

This advanced technique is not solely applicable to the frequency domain algorithm. In 2004 Dougherty [26] introduced the time domain equivalent. As described by Dougherty [26], recalling expression 2.39 the delay-and-sum beamforming expression can be re-written as

$$Beam_{ds}(\boldsymbol{\xi_n}) = \frac{1}{T}\int_0^T \sum_{m=1}^{M} p_m^2(t - \Delta t_{foc}) + \sum_{m \neq l} p_m(t - \Delta t_{foc}) p_l(t - \Delta t_{foc}) dt \tag{2.47}$$

where the subscripts m and l denote a particular receiver in the array and Δt_{foc} represents the straight path propagation delay between a particular microphone and the focal location $\boldsymbol{\xi_n}$. The first sum on equation 2.47 would be the equivalent to the main diagonal terms on the conventional beamforming CSM ($n = l$). By subtracting this term from equation 2.39 the simplified expression for time domain with DR can be written as

$$Beam_{ds,DR}(\boldsymbol{\xi_n}) = \frac{1}{T}\int_0^T \left[\sum_{m=1}^{M} p_m(t - \Delta t_{foc})\right]^2 - \sum_{m=1}^{M} p_m^2(t - \Delta t_{foc}) dt \tag{2.48}$$

2.4 Flow Measurement Techniques

A number of measurement techniques are available in order to extract specific information from turbulent flows. This section introduces two of these techniques that are of particular interest for this investigation. The first part of this section will introduce the working principles and signal analysis techniques attached to Laser Doppler Velocimetry (LDV). The second will introduce the working principles behind Particle Image Velocimetry (PIV).

2.4.1 Laser Doppler Velocimetry (LDV)

In aeroacoustics applications where an inflow measurement is needed, it is always beneficial to have the ability to do so without physically interfering with the flow. LDV

accomplishes this task efficiently by quantifying the light diffracted by fine seeding particles added to the flow. Figure 2.13 shows an schematic representation of an LDV system in forward scatter mode.

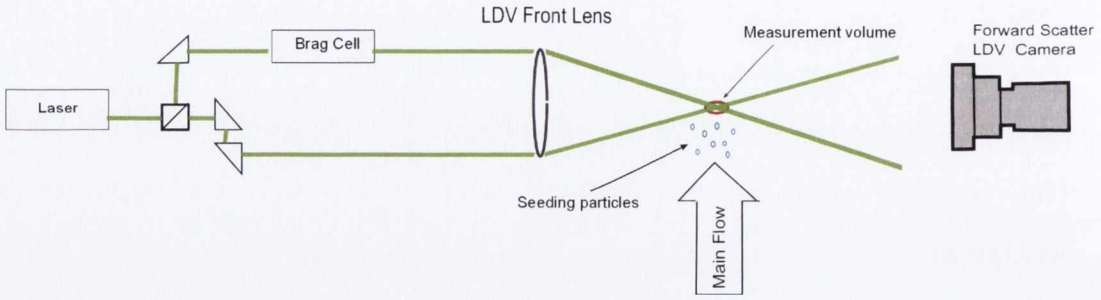

Figure 2.13: Schematic representation of an LDV system in forward scatter

A laser beam is separated into two beams of equal intensity. One of the split beams is passed through a brag cell. This device introduces a fixed frequency shift that in turn allows to determine the sign of the measured velocity. Both signals are then passed through a set of lenses and made to intersect at a set distance from the LDV's probe. At this point, a set of interference patterns is formed. This region is defined as the LDV's measurement volume. As the brag cell introduced a fixed frequency shift in one of the beams this causes the fringe pattern to roll along the preset orientation with a constant velocity. When this is the case, even a stationary particle would scatter light with a frequency (F_0) equal to the one introduced by the brag cell. Therefore a seeding particle moving in the opposite direction of the traveling fringes will produce a Doppler burst of higher frequency ($F > F_0$) while particles traveling in the direction of the fringes will produce a frequency ($F < F_0$) lower than the one introduced by the brag cell. The frequency F of the burst can then be directly related to the velocity of the particle crossing the measurement volume.

Two methods are used to capture the light diffracted by the flow particles. The "backscatter" mode uses the laser transmitting probe simultaneously as the receiving optics. The "forward scatter" mode uses a separate set of receiving optics located opposite the laser probe (see figure 2.13). As described by Raffel *et al.* [27], the light scattered by small particles is a function of the ratio between the refractive index of the particle and its surrounding medium. Furthermore, the scattered light also depends on the observation

angle. Figure 2.14 shows the polar distribution of light scattered by a $1\mu m$ oil particle in air for an incident source of $\lambda = 532nm$.

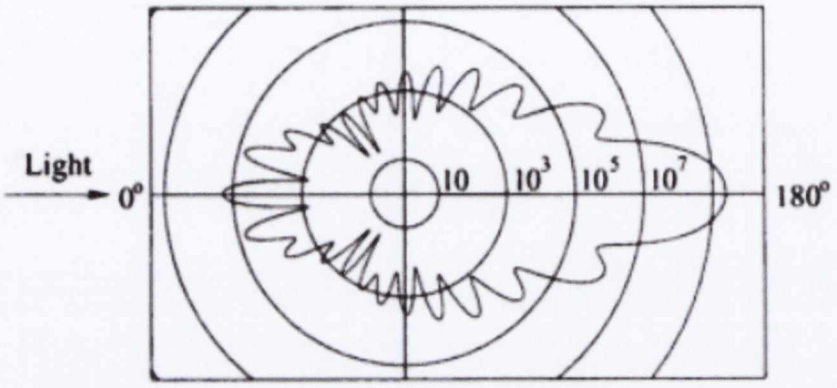

Figure 2.14: Light scattering by a $1\mu m$ oil particle in air, image obtained from Raffel *et al.* [27]

As it can be seen in figure 2.14, a much smaller amount of light is scattered in the direction of the impinging light when compared to the amount of light refracted in the forward direction. Observing this result, it is easy to understand how an LDV system in *forward scatter* would improve the data acquisition rate and the signal to noise ratio. Specially, when analysing fast flows, where small seeding particles stay for very short periods in the LDV's measurement volume, forward scatter is sometimes the only way to obtain measurements.

The strength of LDV as a measurement technique is its fine spatial and temporal resolution. Nevertheless, as the flow data is obtained at irregular time intervals dependent on random particles crossing the LDV's measurement volume the application of traditional signal processing techniques becomes more involved. The signal processing procedures required to analyze irregularly sampled signals are introduced next.

2.4.1.1 Sample-and-Hold Reconstruction

Sample-and-hold is probably the most intuitive of the techniques used to reconstruct irregularly sampled signals. Sample-and-hold reconstructs the data set by holding the value of each data point until a new data point is validated. As the time at which samples are acquired is irregular, the reconstructed data needs to be uniformly re-sampled so as to

allow for conventional signal processing techniques to be applied. This process is shown in figure 2.15

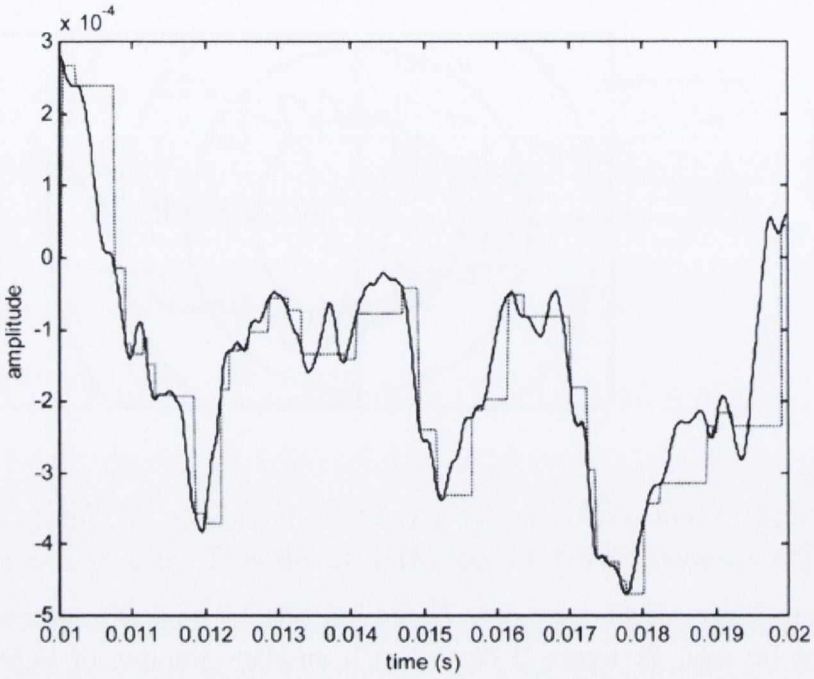

Figure 2.15: Sample-and-hold reconstruction, the solid line represents the time line of the original signal, the doted line represents the sample-and-hold equally re-sampled signal. Image obtained from Simon & Fitzpatrick [28]

2.4.1.2 Irregularly Sampled Data Analysis

The direct analysis of reconstructed sample-and-hold signals introduces uncertainty in the results. The errors associated with sample-and-hold have been documented by Adrian & Yao [29] and Boyer & Searby [30]. These consist of the addition of a constant bias due to step noise and a low pass filter effect on the spectrum of the estimated signal. The system is illustrated in figure 2.16. Here the step noise is represented by $s(t)$ and the low pass filter effect by $L(f)$, $r(t)$ is the sample-and-hold reconstructed signal while $u(t)$ represents the true value of the velocity time series.

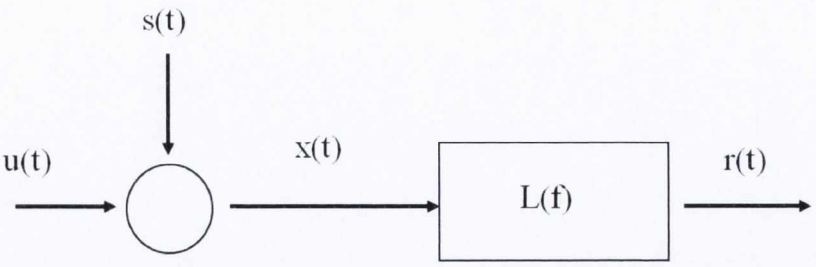

Figure 2.16: Schematic representation of sample-and-hold reconstruction as presented by Simon & Fitzpatrick [28]

Adrian and Yao showed that the errors introduced in the spectral content of the reconstructed signal were dependent on the irregular mean sample rate and the maximum frequency to be analysed. In their investigation they determined that the threshold frequency that could be resolved by the reconstructed signal using sample-and-hold was

$$f_{max} = f_m/(2\pi) \tag{2.49}$$

where f_{max} is the maximum frequency that can be resolved, and f_m is the mean sample frequency obtained from the irregularly sample data. This frequency threshold was improved by a correction technique proposed by Simon & Fitzpatrick [28]. They showed that reliable results could be obtained up to a frequency of $f_m/2$. This correction technique is introduced next.

2.4.1.3 Auto-Spectrum Estimation of an LDV Signal

As described by Simon & Fitzpatrick [28] and Fitzpatrick & Simon [31], if the characteristics of the low pass filter are known and the step noise can be approximated, the auto-spectrum $G_{rr}(f)$ can be corrected so as to obtain the estimate of the velocity signal auto-spectrum $G_{uu}(f)$ (see figure 2.16). The correction for the low pass filter proposed by Fitzpatrick & Simon [31] is shown in equation (2.50). Here the discrete filter is a function of the mean data rate f_m and the re-sample rate f_r.

$$|L_d(f)|^2 = \frac{f_m}{2f_r} \cdot \left(\frac{1 - e^{-2f_m/f_r}}{1 - 2\cos(2\pi f(1/f_r)) + e^{-f_m/f_r} + e^{-2f_m/f_r}} \right) \tag{2.50}$$

this is equivalent to the low pass recursive filter shown by Bendat and Piersol [32] as

$$L_d(f) = \frac{1 - e^{f_m/f_r}}{1 - e^{-f_m/f_r} e^{-j2\pi f_m/f_r}} \tag{2.51}$$

As the spectrum of the step noise introduced by sample-and-hold is white, this can be statistically estimated by calculating the variances of the signals. Even though is not possible to determine the variance of $u(t)$, Simon & Fitzpatrick [28] have shown that this is equivalent to the variance of the reconstructed signal σ_r^2. Therefore the variance of the step noise can now be found from:

$$\sigma_s^2 = \sigma_x^2 - \sigma_u^2 \tag{2.52}$$

The step noise correction constant over N points is now given by:

$$G_{ss} = \frac{1}{N}\left(\sum \frac{G_{rr}(f)}{|L(f)|^2} - \sum u(t)^2\right) \tag{2.53}$$

An estimate of the true spectrum G_{ee} can now be found by subtracting the step noise spectrum from the filter corrected spectrum.

$$G_{ee}(f) = \frac{G_{rr}(f)}{|L(f)|^2} - G_{ss} \tag{2.54}$$

An example of the use of this technique on simulated data is presented by Simon & Fitzpatrick [28]. In order to simulate LDV data an original signal was sampled using two irregular mean data rates (f_m) of 500Hz & 5kHz. The set of irregular data points was reconstructed by means of sample-and-hold interpolation and re-sampled at a frequency of 50kHz. Figure 2.17(a) presents the autospectrum of the original set of data G_{uu} against the autospectrum G_{rr} directly estimated from the sample-and-hold using a f_m of 500Hz. Figure 2.17(a) clearly shows the low pass filter effect and the high frequency bias introduced by the sample-and-hold. Figure 2.17(b) shows the effects of applying a higher f_m

value (5000Hz) and the correction proposed in equation 2.54. It is shown that the original signal can be correctly estimated from the irregularly sampled signal up to about a frequency corresponding to half of the mean data rate f_m.

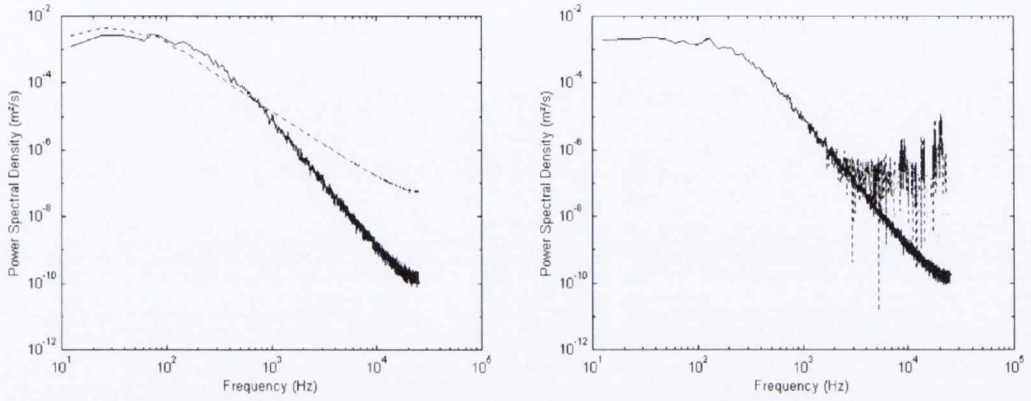

(a) $Guu_{(solid)}$ & $Grr_{(dots)}$ ($f_m = 500Hz$) (b) $Guu_{(solid)}$ & $Gee_{(dots)}$ ($f_m = 5000Hz$)

Figure 2.17: PSD of the original signal and the direct sample-and-hold reconstruction for mean sample rate of 500Hz (left) & low pass filtered and step noise corrected sampled-and-hold reconstructed signal with a mean sample rate of 5000Hz (right)

2.4.1.4 Cross-Spectrum Between an LDV and a Regularly Sampled Signal

In a number of the tests carried out in this investigation, the cross spectrum between an LDV measurement and a regularly sampled microphone signal was required. The schematic representation of this particular case is presented in figure 2.18,

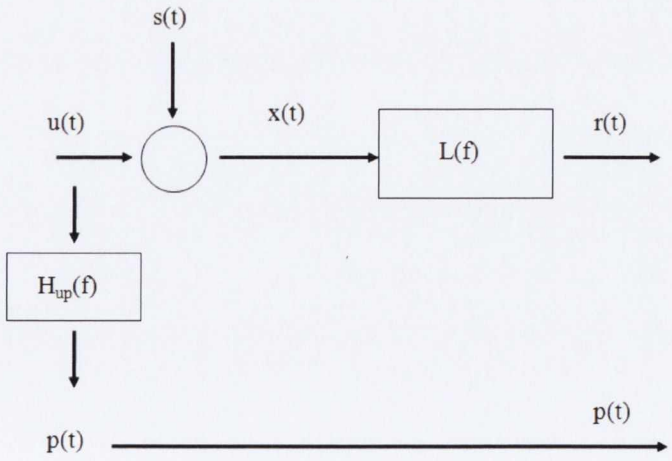

Figure 2.18: Schematic representation of a sample-and-hold LDV signal and a regularly sampled signal using a conventional device (e.g hot-wire or microphone)

where p(t) represents a single regularly sampled microphone signal and H_{up} represents

the frequency response function between the two measurements.
As shown by Fitzpatrick and Simon [31] the relation between the elements in figure 2.18 can be written in the frequency domain as:

$$\begin{aligned} P(f) &= H_{up}(f)U(f) \\ R(f) &= L(f)\{U(f) + S(f)\} \end{aligned} \tag{2.55}$$

The cross-spectrum between the LDV and the microphone signal becomes:

$$\begin{aligned} G_{rp}(f) &= \langle R^*(f)P(f)\rangle \\ &= L^*(f)\{\langle U^*(f)P(f)\rangle + \langle S^*(f)P(f)\rangle\} \end{aligned} \tag{2.56}$$

where the superscript * represents the complex conjugate. As the noise due to sample and hold $s(t)$ is uncorrelated with the microphone signal $p(t)$ the term $\langle S^*(f)P(f)\rangle$ in equation (2.56) reduces to zero, giving:

$$G_{rp}(f) = L^*(f)G_{up}(f) \tag{2.57}$$

If the estimate of $L(f)$ is given by equation (2.51) the estimate of the cross-spectrum between the true LDV and the pressure signal, $G_{eup}(f)$, can be found as

$$G_{eup}(f) = \frac{G_{rp}(f)}{L^*(f)} = G_{xp}(f) \tag{2.58}$$

2.4.2 Particle Image Velocimetry (PIV)

Particle Image Velocimetry (PIV) is an optical non-intrusive flow measurement technique. Similarly to LDV, PIV measures the velocity of a fluid element by measuring the displacement of seeding particles suspended within it. The strength of PIV over the rest of flow measurement techniques (e.g. Hot Wire Anemometry, LDV, Optical Deflectrometry or

Rayleigh Scattering) resides in its ability to resolve simultaneously, the velocity vector fields of large regions of the flow. Additionally, as PIV measures flow fluctuations in equi-spaced time steps, this allows for the application of standard signal processing techniques without the need for the added signal conditioning as for example shown earlier in the LDV case.

Figure 2.19 shows the schematic representation of a typical PIV test set up. In the PIV technique referred to as "double frame/double exposure", a double pulsed laser beam with known delay between pulses is passed through a set of light-sheet-forming optics. The double pulsed laser sheet illuminates a planar section of seeded fluid flow with fluid particles in suspension. An image of the light diffracted by the flow particles is generated for each of the laser pulses and digitized. The digitized frames are then subdivided into small regions referred to as "interrogation windows". The estimate of flow velocity corresponding to each of the interrogation windows is then calculated via spatial cross-correlation of both acquired frames as shown schematically in figure 2.20.

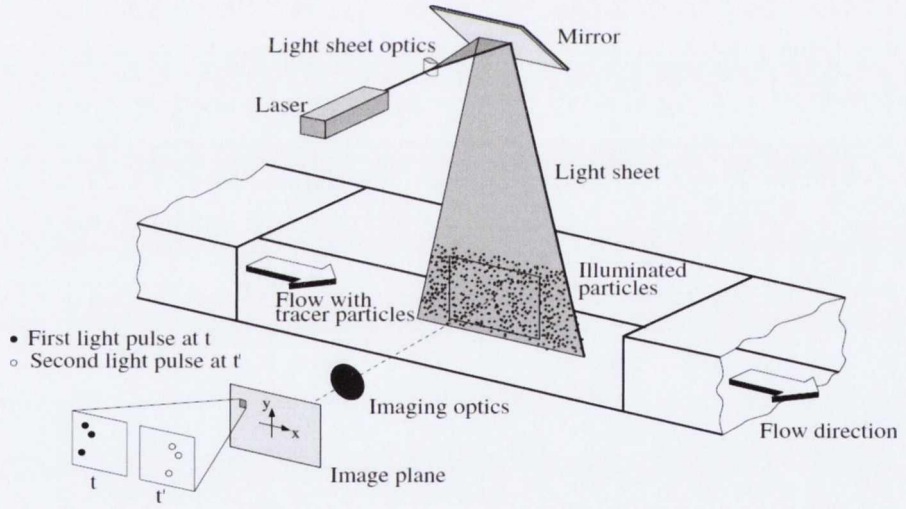

Figure 2.19: Example of a PIV experimental arrangement on a wind tunnel. Image obtained from Raffel *et al.* [27]

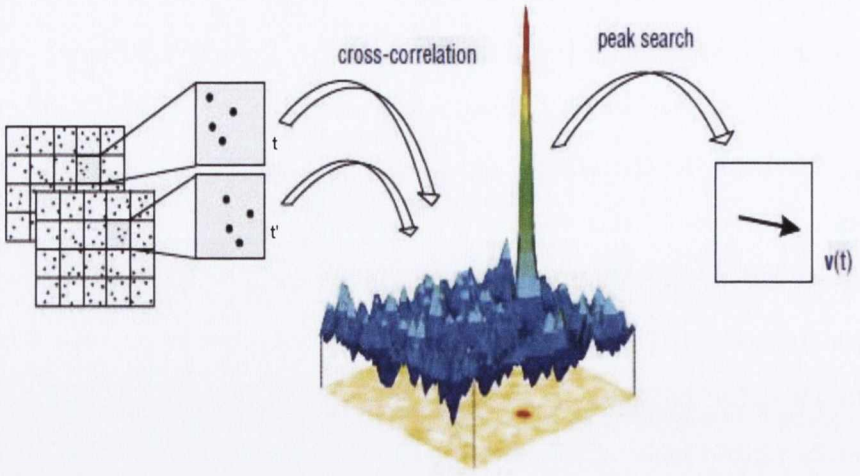

Figure 2.20: Velocity vectors calculation with the "double frame/double exposure" PIV method. Image obtained from LaVision product manual [33].

2.4.2.1 Interrogation Windows

The interrogation window size must be chosen so as to assume that a statistically significant number of homogeneously moving particles are contained within it. In addition, it should also be sufficiently small such that the second order effects (i.e. displacement gradients) can be neglected. As an example, an interrogation window of 64×64 pixels would subdivide an image of 1280×1024 pixels into 20×16 interrogation windows with a possible total of 320 velocity vectors. The number of vectors achievable can be increased by overlapping the interrogation windows. The same case as described above with an overlapping of 50% would produce 1209 vectors with the same window size of 64×64 pixels. Therefore, it is obvious that the interrogation window size and overlap are the factors determining the number of vectors attainable from a PIV frame.

An important feature when evaluating the spatial cross-correlation between interrogation windows is the "window shift". This can be done by applying repeated iterations in the calculation of each interrogation window pair. The first iteration is used to find an estimate of the corresponding velocity vector. Subsequent iterations use this information to shift the interrogation windows accordingly. In this way, a more precise cross-correlation is obtained as the number of related flow particles between interrogation windows is maximized. This "multi-pass" and window shifting process is detailed in figure 2.21.

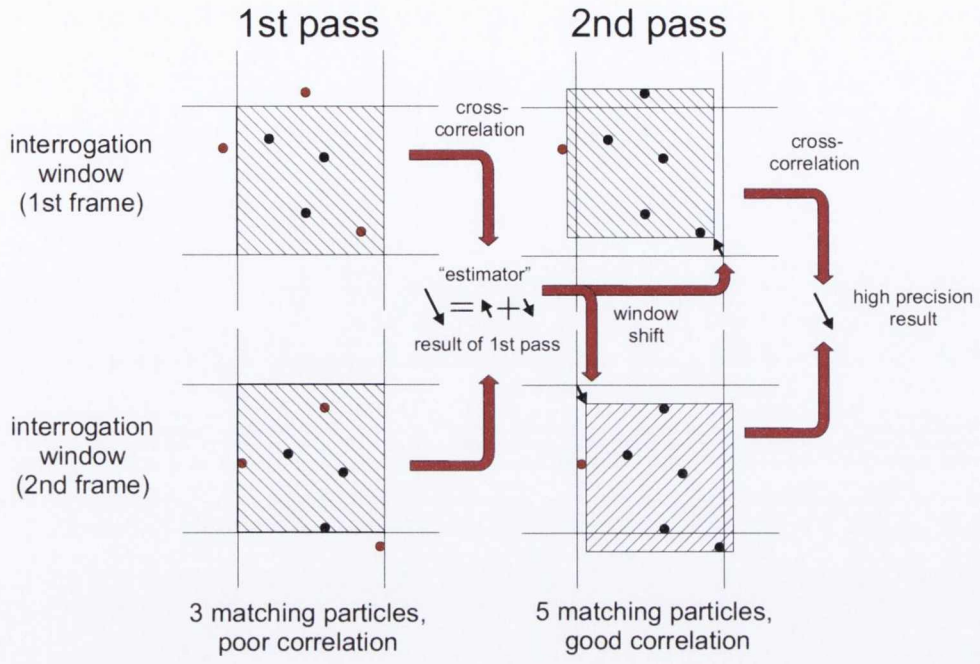

Figure 2.21: Interrogation window shift in the multi-pass. Image obtained from LaVision product manual [33]

The same principle can be used to improve correlation levels by applying a constant initial window shift to each interrogation window prior to the calculation of the cross-correlation coefficients. For this, a reference vector velocity field at each of the interrogation windows locations must be previously calculated. Each estimated velocity vector is then used to shift the interrogation windows accordingly so as to maximize the number of matching particles between interrogation windows.

2.4.2.2 PIV Data 2-D Cross-Correlation Calculation

The standard cross-correlation expression used to calculate the vector fields is shown in equation 2.59

$$C(dx, dy) = \sum_{x=0,y=0}^{x<n,y<n} I_1(x, y) I_2(x + dx, y + dy), -\frac{n}{2} < dx, dy < \frac{n}{2} \tag{2.59}$$

where I_1 and I_2 are the image intensities of the 1st and 2nd "interrogation windows", C gives the 2 dimensional correlation coefficients for all integer displacements dx and dy between the two interrogation windows and n is the size (number of pixels along one

dimension) of the "interrogation window". Mathematically this calculation is achieved in the frequency domain taking the advantage of the correlation theorem that states that the cross-correlation of two functions is equivalent to a complex conjugate multiplication of their Fourier transforms. This process is shown in figure 2.22

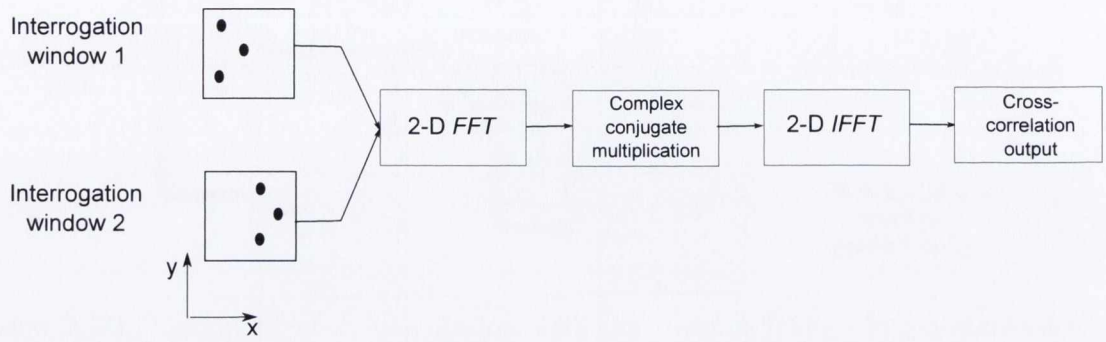

Figure 2.22: Implementation of cross-correlation on a interrogation window using Fast Fourier Transforms.

The calculation of the cross-correlation coefficients in the frequency domain reduces the computational work. Compared to a N^4 iterations needed with the direct cross-correlation expression shown in equation 2.59, processing in the frequency domain reduces the number of iterations to $N^2 log_2 N$ (see Raffel *et al.* [27]).

The calculation process described in figure 2.22 introduces a weighting of the correlation coefficients with emphasis towards small pixel displacements. To avoid erroneous interpretation, the average particle displacement between frames should be less than approximately 1/3 of the interrogation window size. Various parameters such as, interrogation window size, initial window shift or time between frames can be varied to accommodate for this.

A "Second-order" correlation function can be used in combination with the correlation function shown in equation 2.59. This second order method multiplies the correlation functions calculated from two slightly shifted interrogation windows (See figure 2.23).

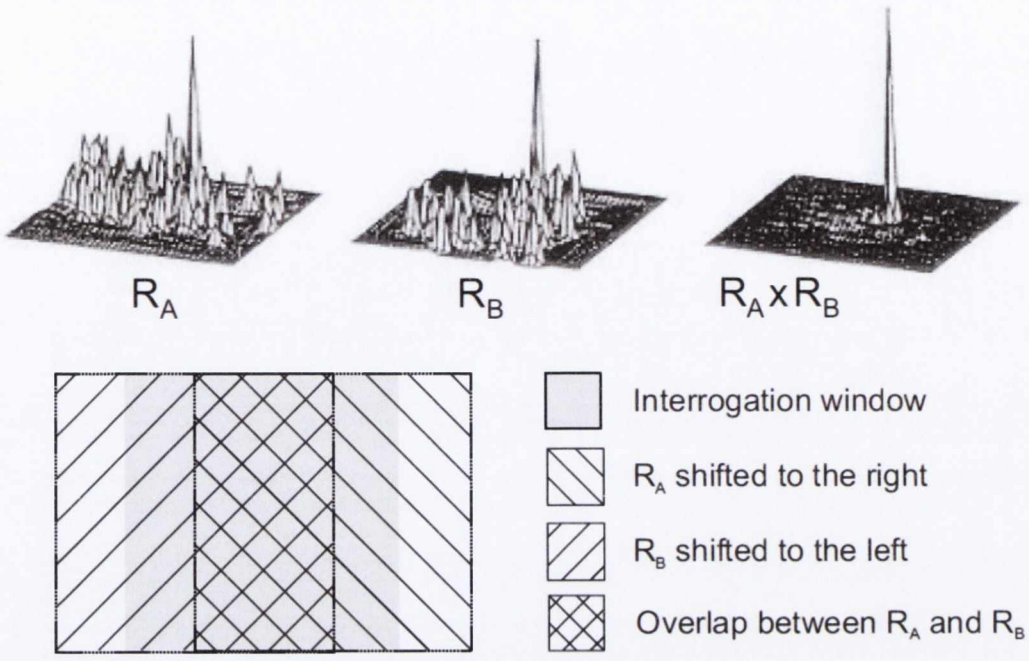

Figure 2.23: Schematic representation of the second order cross-correlation function. Picture obtained from LaVision product manual [33]

The first correlation R_A is calculated from shifting one of the interrogation windows 1/4 of its size to the right. The second calculated correlation R_B is calculated by shifting the interrogation window 1/4 of its size to the left. Assuming that the particle displacement is contained within the overlapping regions and that velocity is constant the correlation peak should be nearly the same in each calculated correlation. The two correlation outputs R_A and R_B are the cross multiplied. This increases the correlation peak and reduces the random noise background levels.

2.4.2.3 PIV Data Quality Evaluation

An important parameter in the calculation of flow vectors via PIV is the size of the seeding particles. As reported by Raffel *et al.* [27] in the evaluation of "double exposure" PIV data the ideal particle image diameter is $\approx$ 1.5 pixels. If the seeding particles are too small, estimated pixel displacements tend to be biased towards integral values. This biasing, which in turn can affect the accuracy of the calculated velocity vectors, is known as "peak locking". The presence of this biasing effect towards integer pixel displacements

can be detected by plotting a histogram of the particle displacement as shown in figure 2.24. If "peak locking" is present, the particle size must be adjusted.

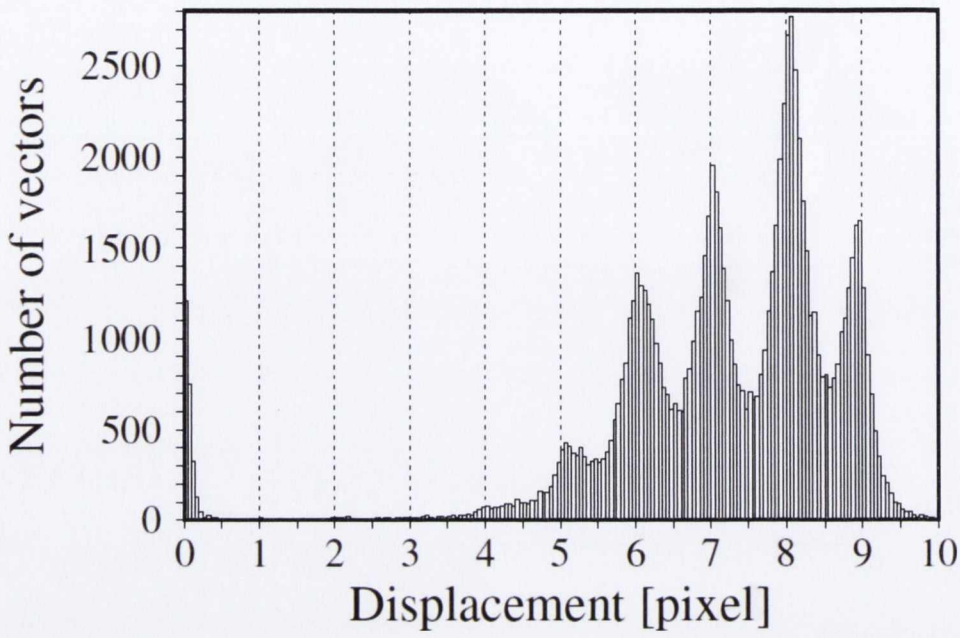

Figure 2.24: Histogram of calculated PIV particle displacement showing a clear tendency towards integer pixel values ("Peak locking"). Image obtained from Raffel *et al.* [27]

Several correlation peaks can be detected when calculating the cross-correlation between PIV frames. If there's a low ratio between first and secondary peak heights, the correctness of the measured velocity vector is questionable. The Q-factor can be used as a post processing tool to eliminate vectors below a pre-set threshold. The Q-factor defined as $Q = \frac{P_1 - min}{P_2 - min} > 1$ where min is the lowest value of the correlation and $P1$ and $P2$ are the first and second highest correlation peaks (see figure 2.25).

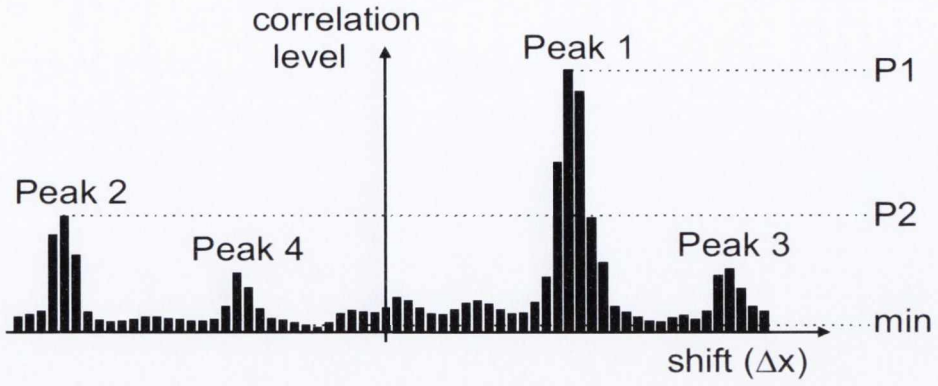

Figure 2.25: Schematic representation of the Q-Factor rejection factor. Image obtained from Lavision product manual [33]

This is a useful tool when calculating mean flow variables as the presence of "bad vectors" would affect the averaged values. However, even if a number of correct vectors are rejected by this process, accurate average values will still be calculated by the remaining high confidence vectors. If the calculated Q-factor in an interrogation window is close to 1 it is likely that the vector calculated based on the highest peak in false. In the cases where this factor exceeds 1.5 there's good probability that the calculated vector is correct.
Along with the Q-factor the "Median Filter" technique can be also used to ensure the quality of the PIV vector fields. This filter removes calculated vectors that exceed a preset condition. Each vector value is compared to the median and the allowed deviation (RMS) from the surrounding 8 neighboring vectors. The criteria used for keeping the evaluated vector is shown in equation 2.60

$$U_{median} - U_{rms} <= U <= U_{median} + U_{rms} \tag{2.60}$$

2.5 Causal Correlation

Efforts to experimentally define the causal effects of sound production due to unbounded turbulence lead, among other techniques, to the the development of simultaneous flow-acoustic observations. These measurements seek to define a direct relation between the

acoustic pressure (effect) outside the hydrodynamic flow to one or more of Lighthill's stress tensor source terms that can be physically measured in the flow (cause). As described in the review by Jordan & Gervais [34] the appeal of the technique introduced by Lee and Ribner [35], is that the farfield pressure autocorrelation can be formally related to the source-farfield correlation which in turn can be related to the source-source correlation. A two point flow-acoustic correlation is in fact a measure of the local contribution of a point in the flow to the sound intensity measured at the observers location. Figure 2.26 shows Lee's and Ribner's [35] schematic representation of the causality correlation technique. An in-flow measurement at position $\mathbf{y}$ was attained via a hot film whilst a simultaneous measurement was attained outside the flow at position $\mathbf{x}$ using a microphone.

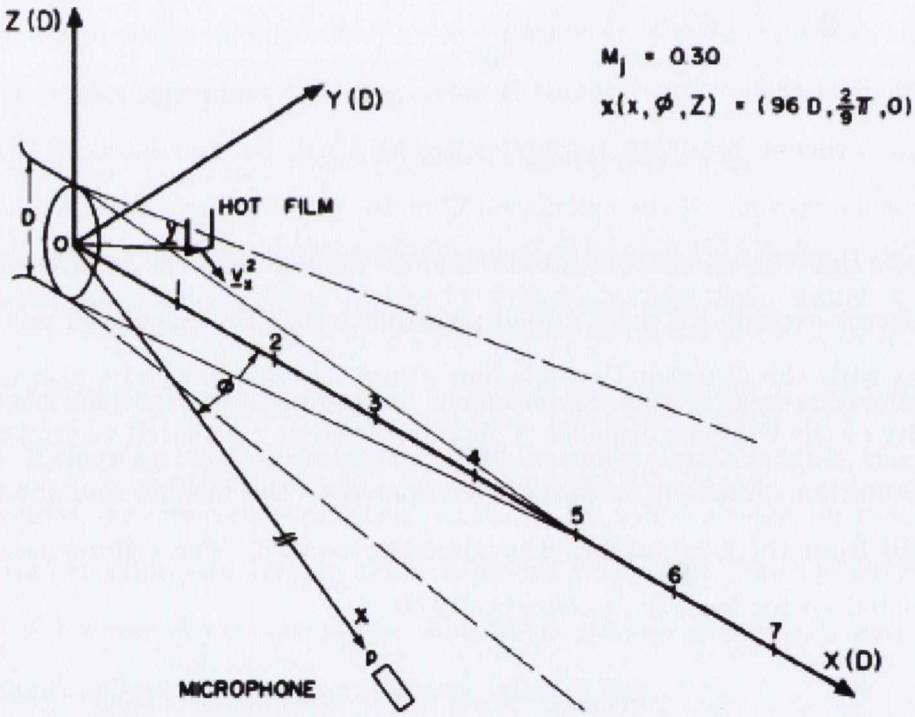

Figure 2.26: Lee's and Ribner's original schematic representation of the causal correlation technique. Figure extracted from Lee and Ribner [35]

2.5.1 Theoretical Approach

The causal correlation technique introduced by Lee and Ribner [35] and Siddon [36] is based on Proudman's [37] solution of Lighthill's acoustic analogy equation.

$$p(\mathbf{x},t) \approx \frac{\rho_0}{4\pi r c_0^2} \int_V \frac{\partial^2}{\partial t^2} [V_x^2(\mathbf{y},t)]_{t-r/c_0} dv \tag{2.61}$$

where $p(\mathbf{x}, t)$ is the pressure fluctuation at point $\mathbf{x}$ and time t, r is the path distance between the in-flow reference point $\mathbf{y}$ and the observers location $\mathbf{x}$, dv is the volume element and V_x is the velocity in the direction of observation. The derivation of equation 2.61 is possible under assumptions of isothermal conditions, negligible viscosity and an incompressible jet flow where $\rho_0 \approx \rho'$. Under these conditions the acoustic farfield pressure autocorrelation (i.e. microphone location in figure 2.26) can be deduced from equation 2.61 as:

$$R_{pp}(\mathbf{x}, \tau) = \frac{\rho_0}{4\pi r c_0^2} \int_V \left\langle \frac{\partial^2}{\partial t^2} R_{V_x^2 p}(\mathbf{x}, \mathbf{y}, \tau') \right\rangle_{\tau' = \tau + r/c_0^2} dv \tag{2.62}$$

where the term $R_{V_x^2 p}(\mathbf{x}, \mathbf{y}, \tau')$ is the time averaged cross-correlation $\langle V_x^2(\mathbf{y}, t) p(\mathbf{x}, t + \tau') \rangle$ between the source flow term and microphone pressure evaluated at the retarded time $(t + \tau')$. The velocity component V_x in the direction of observation can be further decomposed into the sum of its mean value and its fluctuating component as $V_x = \bar{v}_x + v'_x$. With this assumption, the cross-correlation can be written as:

$$R_{V_x^2,p}(\mathbf{x}, \mathbf{y}, \tau') = \underbrace{2\bar{v}_x R_{(v',p)}(\mathbf{x}, \mathbf{y}, \tau)}_{shearnoise} + \underbrace{R_{(v'^2,p)}(\mathbf{x}, \mathbf{y}, \tau')}_{selfnoise} \tag{2.63}$$

where the first term of equation 2.63 is related to the "shear noise" while the second is related to the "self noise" as described by Ribner's theory on flow induced sources of sound [38].

2.5.2 Causal Correlation 1970's Up To Date

The first examples in which fluctuating velocity components were measured and correlated to farfield pressure measurements are attributed to the work presented by Lee and Ribner [35]. Their flow measurements were obtained by means of a hot-film probe located in the flow of a Mach 0.3 jet while a single microphone recorded pressure values in the acoustic field at an angle of 40° from the jet axis. The experimental layout used in this investigation is shown in figure 2.26. They determined that the measured inflow turbulence contributed to a maximum of about $1 - 2\%$ of the rms pressure measured at the microphone location. With this information and under the assumption that the flow was composed of independent incoherent sources, Lee and Ribner estimated the total number of uncorrelated noise-producing sources within the jet.

Seiner and Reethof [39] applied the causal correlation technique using Hot-Wire-Anemometr (HWA) as their inflow measurement technique. The acoustic pressure recorded by a microphone at a 30° angle from the jet axis was correlated with the measured "shear" and "self-noise" components measured in the flow on a mach 0.32 jet. The contribution from the "shear" source term was found to exceed that of the "self-noise" by approximately 13dB, reaching its peak when flow measurements were acquired in the jet's transition region. Similar studies shown by Scharton and White [40] and Hurdle *et al.* [41] alternatively studied the cross-correlation between inflow and acoustic pressure fluctuations by using pressure probes as their in-flow measurement technique.

The main drawback with the type of techniques aforementioned was the intrusive nature of the flow measurement. As the probe altered the flow it was difficult to quantify the effects of such alteration. Siddon [42] termed this uncertainty issue as the "Probe Contamination Factor". To avoid this issue, a number of different researchers availed of the development of non-intrusive flow measurement techniques.

An early example where Laser Doppler Velocimetry (LDV) was used to measure velocity fluctuations within the flow was presented by Schaffar [43]. In his investigation Schaffar determined the dependency of correlation values on jet velocity when he reported correlation values of 0.05 on a Mach 0.98 jet. Maximum correlation values were obtained at shallow angles $(20 - 30°)$ using "shear" and "self-noise" source terms measured 5-10 jet diameters downstream. In the same investigation, Schaffar was able to reproduce the microphone autospectrum from the cross-correlation between the "shear-noise" term and a microphone located at a shallow angle from the jet's axis demonstrating the validity of equation 2.62 (see figure 2.27).

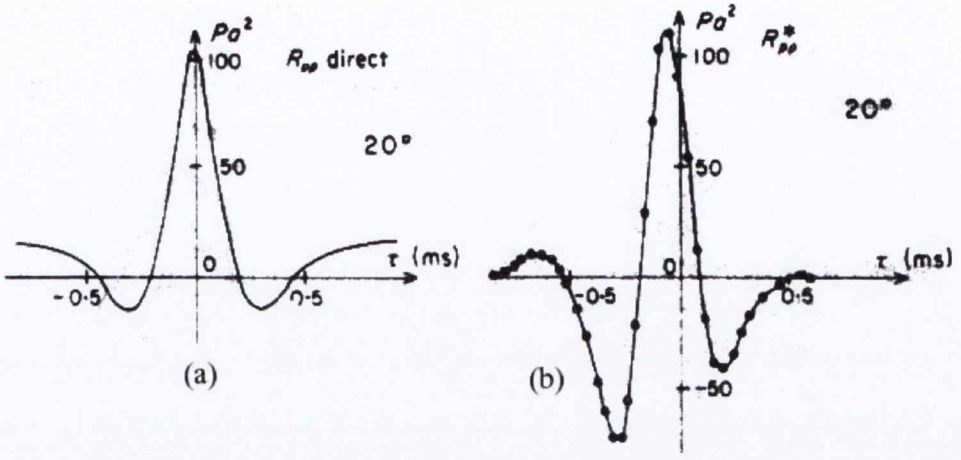

Figure 2.27: Microphone autocorrelation for a microphone located at a 20° angle from the jet axis of a Mach 0.98 jet a) measured by a microphone b) calculated using the causality principle using the shear noise term $< u'; p' >$ (Figure obtained from Schaffar [43])

Other researchers, as in the case of Juvé *et al.* [44], minimized the probe contamination effect by designing a special hot wire probe where the solid prongs of the holding device were kept outside of the flow. As in previous studies, flow fluctuating quantities were correlated to acoustic pressure fluctuations measured at a 30° angle from the jet exit. The jet axial region 4-10 jet diameters downstream of the jet nozzle was again reported as the most efficient noise emitting area. Of particular interest was the reported *intermittency* of the most significant noise events. It was determined that 50% of the emitted noise was produced during only $10 - 20\%$ of the time whereas previous correlation estimates had assumed a stationary process.

During the 80's, little is documented apart from the continued work by Shaffar and Hancy [45]. Using LDV as the flow measurement technique Shaffar and Hancy measured the correlation values with microphones located at different polar angles with respect to the jet's exit. Their investigation identified the polar angle dependency of the measured correlation levels. Maximum values were again obtained at the shallow angles with respect to the jet axis (i.e. 30°) whilst at 45° & 60° the values decreased significantly. At the 30° position the "shear-noise" was reported to contribute up to 75% of the total measured noise meanwhile 15% of the total noise measured at the same location was attributed to the "self-noise" term.

More recently, Panda and Seasholtz [46] and Panda *et al.* [47] recalled the causality

method using a non-intrusive Rayleigh scattering based flow measuring technique. By quantifying the laser light scattered by gas molecules present in air, Rayleigh scattering is able to obtain a direct measurement of density fluctuations along with one component of velocity without the need for added seeding in the flow. Rayleigh scattering allowed the evaluation of the Lighthill stress tensors $\rho(t), u(t), v(t), \rho uu(t)$ and $\rho vv(t)$ (see equation 2.18) without the previously used assumption of negligible density fluctuations. Flow measurements attained at different locations within the flow were correlated with acoustic pressure measurements attained by microphones in the far-field at polar angles ranging from $30 - 90°$. Measured flow quantities u' and ρ' were similar while noticeable difference was only found with the velocity term in radial direction v'. As in previous correlation studies, Panda *et al.* [47] reported maximum correlation values at shallow angles (30°) when flow observations were acquired at the end of the potential core.

Henning *et al.* [48–50] presented a causal correlation study were Particle Image Velocimetry (PIV) was used as the flow measurement technique. Whilst previous techniques were restricted to single point measurements, PIV allowed to obtain instantaneous flow velocity information over an extended flow region. Cross-correlation coefficients were achieved by coupling a large number of PIV measurements (5000 frames) measured at a sample rate of 2.5Hz with pressure measurements attained at a much higher sampling rate. As the time resolution of the PIV was much smaller than the characteristic time-scale of the flow, each PIV frame was considered as statistically independent. Hence, the measured velocity-pressure correlation coefficients were characterized by independent flow occurrences rather than the contribution of particular events on the flow. This technique was validated using a number of experimental configurations including the vortex created by a cylinder in cross flow and a free jet with Mach numbers ranging from 0.5 to 0.9. Despite the temporal resolution of the PIV used by Henning *et al.* [48–50] the experimental results presented, demonstrated the validity of PIV as a non-intrusive flow measurement technique when evaluating correlation levels between flow and acoustic perturbations.

Veltin *et al.* [51] applied Optical Deflectrometry (OD) to measure flow and near-field perturbations in an open jet. This non-intrusive flow measurement technique relies on light diffraction due to density gradients [4]. Veltin *et al.* [51] measured correlations between

[4]For more detailed information on OD the reader is referred to the work presented by Doty and

microphones in the farfield and an OD probe located at 4 jet diameters downstream from the nozzle in the shear layer of a Mach 1.5 jet. Maximum correlation values were found to be dependent on the polar location of the microphones. Correlation values sharply dropped with increasing polar angle, being at its maximum at an angle of 22° from the jet axis whilst disappearing at the 41° position. When the OD probe was moved axially along the jet's lipline, maximum correlation was reported at $5-6$ jet diameters from the jet axis. Similarly, a shift towards high frequencies was observed when correlations were attained with the OD probe near the nozzle exit. In the same investigation correlation values were obtained when the OD probe was located in the acoustic near field of the jet. Based on these results, it could be argued that OD measurements attained in the shear layer could be also affected by sound propagating waves that are generated elsewhere within the flow, (e.g. end of the potential core) which in turn can lead to an erroneous interpretation of the source location. Panda and Seasholtz [46] reported about this issue when applying Rayleigh scattering, "...density fluctuations from the acoustic waves are at least 4 orders of magnitude below that from the turbulent flow, and therefore fall below the measurement noise floor. Sound generated from sources along the centreline has to propagate through the turbulent flow before emanating into the outside quiescent region. Since density fluctuations from this propagating part are too weak to be detected, the present technique only identifies the sound sources and excludes the propagating sound waves". It is unclear from the results presented by Veltin *et al.* [51] if this is the case when using OD to measure density gradients in flows. In addition, Doty [52] raised concerns about the application of OD. As Doty explains "...the light beam integrates density gradient fluctuations over the entire length that it travels, rather than focusing at a point. Thus, strictly speaking, the correlations are not point correlations, but rather, are correlations integrated over a line". This was the reason why correlations along the centerline were deemed untrustworthy and finally discarded in the investigation carried out by Veltin *et al.* [51].

Recent developments in PIV hardware equipment have led to the introduction of Time Resolved Particle Image Velocimetry (TR-PIV). The frame rates achievable by current TR-PIV ($\approx 10kHz$) are now sufficiently high so as to temporally resolve flow fields regions

McLaughlin [52]

depending on the characteristic flow time-scales. A recent study by Breakey and Fitzpatrick [53] used Time Resolved PIV (TR-PIV) as the non-intrusive flow measurement technique. Normalized cross-correlation coefficients between the axial velocity component u' and pressure fluctuations p' were reported in a number of flow configurations including a tandem cylinder in cross flow and a cold jet at Mach 0.3. Their results demonstrated the validity of TR-PIV as the flow measurement technique in a two point flow-acoustic correlation study type. When comparing their TR-PIV data to that obtained via HWA, Breakey and Fitzpatrick [53] highlighted the effects of aliasing from higher frequencies in the PSD estimated via TR-PIV. However, its effects on the cross-correlation coefficients calculated between flow and acoustic perturbations were not estimated.

2.5.2.1 Inflow-Pressure Correlation Measurements using LES Data

Independently of the technique used, experimental methods are hindered by extraneous noise, this being introduced by the in-flow measuring device or by the nature of the data acquisition technique. Progress in Computer Fluid Dynamics (CFD) has allowed the use of numerical data in order to approximate the noise source mechanisms responsible for radiated noise in jets. These techniques have introduced a new approach to investigate sound production mechanisms in parallel with experimental techniques. Simulated data has the advantage of being free from external noise issues as those encountered by experimental techniques. However, at present, computational limitations do not allow to simulate complex flow fields at sufficiently high enough Reynolds numbers. For this reason, simplified methods such as Large Eddy Simulation (LES), have become a popular tool for the study and prediction of jet noise. By reproducing only large turbulent scales, this technique is able to generate high enough Reynolds number flows that can be directly compared to the results obtained from experimental methods.

An example of the application of LES data in a flow-acoustic study is reported by Bogey and Bailly [54, 55]. Shear and self-noise terms measured along the axis and lipline of a simulated jet flow at different Reynolds numbers were correlated with estimated fluctuating pressure in the far field. The results obtained from this investigation are in agreement to those obtained from experimental data by for example Panda *et al.* [56] and Hileman *et al.* [57]. Maximum correlation values were obtained between pressure measurements

acquired at shallow angles and flow variables measured at the end of the potential core. Similarly to the experimental cases reported by Henning *et al.* [48–50] or more recently Breakey and Fitzpatrick [53], Bogey and Bailly [54] highlighted the variation in the expected propagation time from the source to the microphone position. The calculated time domain correlation signatures presented by Bogey and Bailly between the flow data and the acoustic pressure, suggested the presence of a convected, coherence fluctuation along the jet axis with a localized radiation region at the end of the potential core. These results led them to the conclusion that strong correlations between the flow and acoustic perturbations do not constitute prove of noise emission being originated at the location of the in-flow measurement.

More recently, Arthurs and Fitzpatrick [58] applied causal correlation measurements to the same set of LES data used by Bogey and Bailly. Their study showed the contribution to the sound radiated at two different radiation angles ($40°, 90°$) from each of the "shear" and "self-noise" source mechanisms described in Ribner's theory [38]. To do this, a Spectral Estimation Method (SEM) based on partial coherence analysis was used. This frequency domain analysis, had the advantage of eliminating mutually correlated aspects of the modeled sources. In this way the relationship between the individual source mechanism and the pressure measurement was obtained. As in previous investigations, the "shear-noise" u' term, measured at the end of the potential core region, was found to dominate shallow angle radiation.

2.6 Beamforming Applied to Aeroacoustics

It was also during the 1970's, in parallel to the introduction of the causal correlation technique, when the first modern digital array signal processing device was introduced. Since then, improvements in data acquisition capabilities and array data post-processing techniques have made array signal processing the most popular tool for the localization of sound sources. In this section, we will review the development of array signal processing, or as otherwise know as *beamforming*, with particular emphasis on the instances where this technique has been applied in the field of aeroacoustics.

Billingsley & Kinns [22] presented the earliest example of a modern beamforming device.

In their investigation, a linear array composed of 14 condenser microphones was located in the far field of a Rolls-Royce/SNECMA Olympus engine in order to study its noise distribution at different power settings. The array microphones were connected to a mini computer via 100 meter long cables where the signals were digitized with a resolution of 8 bits at a sampling frequency of 20kHz. The processed beamforming output was displayed on a colour TV screen in a similar way to modern beamform array equipment. Their experimental results, showed how under a low power setting the apparent main sources in the engine were close to the nozzle exit whilst at high power settings these were found further downstream. In the latter case, the most significant region of sound generation was found downstream at a distance between 3 and 9 nozzle diameters. More noticeably, in the same study, Billingsley & Kinns [22] evaluated the beamformer source identification capabilities in the presence of complex non-compact sources. The effect that a closely radiating correlated source would have on the directivity pattern, was first proposed separately by Kinns [59]. Kinns showed using a simple dipole source example, how cancellation effects in closely correlated radiating sources have a pronounced effect on the overall directivity pattern. Based on this findings, Billingsley & Kinns [22] argued that the power spectral density for a particular beamforming array focal location can be approximated only when the array resolution is: 1 - insufficient to separate the line source correlated components and 2 - the directionality of the source region does not lead to large changes in signal intensity across the microphone array.

During the same period, Soderman & Noble [60] also reported the use of a four element directional linear array to study flow induced noise in large wind tunnels. Their experimental results reported a rejection of between 5 to 12 dB of reverberation and background noise levels within the $0.4 - 10$kHz frequency range.

The first measurements carried out using two dimensional arrays were shown, among others, by Brooks *et al* [61]. A planar array located out-of-flow was used to identify rotor noise on a scale model under anechoic conditions. In addition, in the same investigation the array resolution was kept constant independently of frequency by means of the addition of weighting coefficients to the microphone signals.

In 1998 Humphreys *et al.* [62] performed tests on a wing-flap model using two different array configurations. The first, a large aperture directional array (LADA), which consisted

of 35 receivers in a logarithmic spiral configuration, was used to produce high spatial resolution noise source localization along the test piece. The second, a small aperture directional array (SADA), formed by 33 microphones mounted on four concentric irregular circles, was designed to measure the directivity and spectral characteristics of particular test sections. In order to compensate for the loss of coherence due to the effects of sound diffraction in shear layers, an amplitude and phase correction as a function of frequency and microphone location was added to the steering vectors using the approach described by Schlinker & Amiet [63, 64].

In 1999 Brooks and Humphreys [65] introduced a method to retrieve absolute spectral values from array measurements. Assuming a source distribution of uncorrelated point sources and defining an integration area around the source region, they were able to determine that the total noise spectral output could be retrieved from array measurements. By comparing simulated and real data to a calibrator source, the integration method yielded reliable results. Only when the integration method was combined with Diagonal Removal (DR) the technique was less reliable. As described earlier, DR involves the removal of the main diagonal terms that contain the receivers' auto-powers from the cross-spectral matrix. The use of DR is often inevitable in situations with low signal-to-noise ratio as in the case of wind tunnel measurements. A good example of the beneficial effects of DR when the array receivers are subject to flow noise was presented by Oerlemans *et al.* [66].

A more recent example of the application of phased arrays to the study of jet acoustics was presented by Lee & Bridges [67]. Using a linear array in conjunction with the conventional beamforming algorithm (see section 2.3.2.2), they presented a study of jet noise distribution as a function of Strouhal number, jet temperature and Mach number. In their findings, the peak source locations were reported to vary from the nozzle end towards downstream positions as the frequencies decreased. Their results were found to be in agreement with similar experiments carried out by earlier researchers using acoustic mirrors. (see Chu *et al* [68] and Grosche [69]).

In 2003 Venkatesh *et al.* [70] introduced a novel beamforming algorithm that traded angular resolution for an increased sidelobe reduction. It is the first algorithm that tried

to adjust the resolution of the array so as to satisfy the first of the two conditions [5] stated earlier by Billingsley & Kinns [22]. Their objective was to recover the average source strength over a small region as opposed to find the exact source strength at each spatial location as in standard beamforming methods. Their algorithm was able to adjust resolution and sidelobe rejection so as to approximate the source power spectral density over the predetermined correlated length. Nevertheless, no consideration was given to the directivity of closely radiating correlated sources and the effect of source intensity variation across the array aperture.

Papamoschou and Dadvar [71] pointed out the effect of using large aperture arrays in the presence of sources with complex directivity. Whilst a large aperture is desirable to improve spatial resolution, the drawback is that one will integrate over dissimilar sources. Taking into consideration Tam's [13,16,72,73] dissimilar jet noise source theory, this would certainly be the case if an array aperture covering an extensive polar angular aperture was used to sample the acoustic field produced by a turbulent jet. These were the arguments behind the investigation carried out by Papamoschou and Dadvar [71]. Here, a reduced aperture array was used to characterize the acoustic field of a Mach 0.9 cold jet at broad (90°) and shallow (30°) angles from the jet axis. Whilst a narrow band spectrum peaking at 0.2 Strouhal number characterized the array measurements attained at a 30° angle from the jet axis, the measurements obtained at 90° showed a broader spectrum of lesser amplitude peaking at a ≈ 0.6 Strouhal number. These results were in agreement with the two source theory introduced by Tam *et al.*

As discussed earlier, array outputs present the noise field convolved with the array's aperture function, which depends on frequency, aperture size, microphone weighting and array geometry. A key development for phased array signal processing was introduced by Brooks and Humphreys [74]. Their deconvolution based technique, (DAMAS), was able to remove from the beamforming outputs the characteristics of the array aperture function. This approach was able to overcome the existing resolution and dynamic range limitations found in classical beamforming methods. Brooks and Humphreys method was soon

[5] Billingsley & Kinns [22] argued that the power spectral density for a particular beamforming array focal location can be approximated only when the array resolution is: 1 - insufficient to separate the line source correlated components and 2 - the directionality of the source region does not lead to large changes in signal intensity across the microphone array.

followed by new deconvolution methods as those presented by Dougherty, ("DAMAS2", "DAMAS3" & more recently "TIDY") [75, 76] and Sijtsma ("CLEAN-SC") [77].

The application of phased array techniques to the study of complex aeroacoustic sources and jet noise in particular has led to criticism as most algorithms are based on a monopole source assumption. As described by Dougherty [76], based on Michel's [78] description of correlated source directivity in jets, the use of phased arrays for this purpose is justified provided that its aperture subtends a reasonably small angle with respect to the jet's exit. Dougherty [76] further points out that for this to be the case a conservative constraint would be to reduce the array aperture so that its resolution is larger than the presumed source correlation length under study. However, no consideration was given to the existence of extended correlated structures extending far beyond integral correlation lengths as those attributed to "wave-packets". In the same investigation, Dougherty [76] showed interesting results on the application of array deconvolution techniques ("TIDY") to the study of jet noise. A small aperture array designed to suit the above mentioned angular aperture constraint was located at a broad (90°) and shallow angle (40°) from the axis of a cold subsonic jet. Whilst at the (90°) location high frequency noise is clearly identified along the shear layer, at the shallow angle high frequency noise is detected at the nozzle lip. These findings are in agreement with separate studies where the contribution from a source related to the presence of the nozzle exit has also been reported as for example in the numerical results by Viswanathan [79] or in the experimental results reported by Tinney *et al.* [80].

The results presented in this short review, showed how array signal processing has become a stand alone and well accepted technique in the field of aeroacoustics. Previous disadvantages over its predecessors, such as resolution and dynamic range have been overcomed by the recent advances in data acquisition systems and advanced post processing algorithms with the added benefit of a much shorter time required to acquire measurements.

2.7 "Flow-Beamformed Acoustic" Observations

In all the previously discussed experimental investigations based on the causal correlation approach, an unsteady flow quantity was correlated to the acoustic pressure measured by

a single microphone. A number of factors can limit the correlation levels attainable using this technique. These were considered by Dougherty *et al.* [81]. In the first instance, no fluid disturbance can be expected to be a perfect acoustic source or even in some occasions these may not contribute whatsoever to sound radiation. The second and more relevant to this investigation, is that the noise produced by a jet could well be considered to contain several independent sources. Therefore, a single pressure measurement will be composed of the sound from the source measured by the flow measurement device plus the addition of all the other sources contained within the jet that radiate towards the microphone location.

These realizations led to the introduction of array signal processing in the causality based correlation measurements. This was done by substituting the single pressure measurements by that of a beamforming array focused at the location of the flow measurement. Theoretically, the array's spatial filtering characteristics should improve correlation levels by reducing the contribution from sources arriving at the microphones from regions other than the one of interest. What follows here is a review of publications were this relatively novel experimental approach was used.

An early example found in the literature where a "reference" measurement was correlated to the pressure measurements acquired by an array of receivers was presented in 2001 by Siller *et al.* [82]. In their experimental set-up a dynamic pressure transducer (rumble probe) was located in the combustion chamber of a full sized aero-engine whilst a far field array using a simple delay-and-sum algorithm was focused on the exit plane of the jet. Their results identified a clear contribution from the combustion chamber to the far-field noise measured by the array under certain operating conditions.

In 2005, Dougherty *et al.* [81] presented an experimental set up where fluid disturbances in a Mach 0.98 jet were measured by a Rayleigh Scattering probe while an array of receivers using a delay-and-sum algorithm was focused at the flow measurement volume. Under the assumption of an idealized jet flow with an M number of equal strength independent sources, Dougherty estimated that the use of an array of receivers would improve the correlation coefficient output by a factor of $\sqrt{N}$ where N is the number of receivers in the array. A three-dimensional array capable of a resolution of approximately 1 jet diameter at a frequency of $\approx$18kHz was designed for this investigation. The cross-correlation be-

tween the array output and the signal obtained from the Rayleigh scattering probe was computed at different regions of the flow of a Mach 0.98 jet. In the best case scenario, the beamformed correlated output improved correlation levels by a factor of two when compared to that of a single receiver. At low frequencies, increased correlation coefficients were attained when the array was steered upstream of the location of the flow measurement volume. More noticeably, high frequency correlations obtained in the shear layer showed a negative delay between the in-flow and acoustic pressure measurements. Dougherty attributed this effect to a separate radiating source that radiated towards the array and the in-flow measurement volume locations. Discrepancies in the expected delay times between in-flow and acoustic pressure measurements in the form of negative delays, have also been reported in experimental and simulation studies where a single receiver was used to sample the acoustic field (see [48–50, 53, 55]).

In 2010, Henning *et al.* [83] applied a similar approach where PIV was used to measure flow instabilities in a configuration that included the flow perturbations generated by a rod and airfoil in cross flow. The response of an 87 microphone array was focused at the location of the PIV flow measurement via the delay-and-sum algorithm. Due to the low sampling frequency achievable by the PIV system, the same statistical approach used in their previously discussed experiments (see Henning *et al.* [48–50]) meant that the measured flow-acoustic correlation coefficients, were characterized by independent flow occurrences rather than the contribution of particular events on the flow. Similar to the findings of Dougherty *et al.* [81], Henning *et al.* also reported a discrepancy in the expected and calculated time domain cross-correlation peaks. This discrepancy, again in the form of negative delay between flow and acoustic measurements, was attributed to the influence of a localized dominant radiating mechanism at the nozzle exit and the presence downstream of convected, non-radiating disturbances generated by the source mechanism. During the same period, Papamouschou *et al.* [84] made use of an OD system to synchronously measure density gradients at 4 consecutive points aligned along the axis of a Mach 1.75 jet. Simultaneously, a small aperture array centered at 30° from the jet axis recorded pressure fluctuations in the farfield. Similarly to the work presented earlier by Siller *et al.* [82], Henning *et al.* [83] and Dougherty *et al.* [81], delay-and-sum was used to focus the response of the array at the location of the OD in-flow measurements. The

novelty introduced by Papamouschou *et al.* could be termed as the "in-flow beamformed signal". As contiguous flow points parallel to the jet's axis were synchronously sampled in time, the calculated convection velocity and the distance between OD measurement points was used to delay-and-sum the flow acquired signals using one of them as reference. Correlation coefficients were estimated between the OD signal and the array output while varying the array's focal location along the jet axis. In most cases, maximum correlation between the flow and steered array signal did not coincide with the location of the OD measurement volume. Only when the OD probe was located outside of the flow, maximum correlation was obtained at the corresponding location of the OD measurement volume. This bias was particularly accentuated when OD was used to measure density fluctuations along the jet's centerline. Papamouschou *et al.* attributed these results solely to the effects of the shear layer diffraction in the trajectory of sound waves towards the array location. However, no ray path correction was attempted to prove this. All the aforementioned "flow-beamformed acoustic" approaches made used of delay-and-sum algorithm to focus the array response at the location of the in-flow measurement. However, also in 2010 a separate approach to correlate the response of a focused array aperture with that of a "reference" signal was introduced by Guidati [85]. Whilst his approach was not applied to the study of "flow-acoustic" beamformed observations, it is worth noting that in his investigation the response of an array of receivers was combined with the output of a single "reference" signal in an attempt to identify the location of sources coherent to that of the "reference" chosen value.

2.8 Thesis Objectives

As documented in previous sections, extensive experimental work has attempted to identify the sound generating mechanisms in free flows by means of simultaneous flow-acoustic observations. In most of these cases, experiments have been restricted to correlations between flow fluctuations measured at a single point and pressure measurements acquired by a single microphone. As discussed in the previous section, correlations levels attained in this manner can be detrimentally affected by a number of factors. In an effort to improve measured correlation levels, a number of investigations substituted the single microphone

output by that of a combined array of microphones. These experimental approaches made use of a number of non-intrusive flow measurement techniques such as Rayleigh Scattering, PIV and OD. However, none of these "flow-beamformed acoustic" correlation studies have availed of the fine time resolution and 2 dimensional flow velocity measurement capabilities of LDV as the non-intrusive flow measurement technique. Similarly, in all the aforementioned cases "delay-and-sum" was the beamforming algorithm used to combine the flow and array signals. The application of a similar approach in the frequency domain as that introduced by Guidati [85] for the identification of coherent sources, has not been yet documented.

Additionally, most of the aforementioned flow measurement techniques, including LDV, are only able to sample a small volume of the flow at a time (4 simultaneous points at best in the case of OD). In the cases where PIV was used, the low time resolution achievable by the laser equipment was unable to temporally resolve the flow field. Due to this, statistical approaches had to be applied to calculate the correlation between flow occurrences and the acoustic pressure field. While standard PIV laser equipment is limited to a few frames per second (e.g. $\approx$ 4Hz), modern TR-PIV equipment is able to achieve sample rates up to 10kHz. This high repetition rate would potentially allow to study the acoustic signature of time resolved flow structures over extended regions of the flow. An investigation where TR-PIV is used to calculate correlation coefficients between in-flow perturbations and a beamformed acoustic pressure signal is missing from the literature.

Based on these findings, this study has a number of objectives:

- The application of LDV as a non-intrusive measurement technique in a "flow-beamformed acoustic" correlation study and the development a novel approach to combine flow and beamformed acoustic observations.
- The introduction of TR-PIV as the in-flow measurement technique in a "flow-beamformed acoustic" correlation study designed to characterize broad angle sound radiation in a subsonic jet.
- The evaluation of the aforementioned techniques, experimentally and by means of simplified source models.

Chapter 3

Experimental Techniques

This chapter introduces the signal processing techniques necessary to implement the experimental "flow-beamformed acoustic" correlation studies proposed in section 2.8. The first section of this chapter will introduce the existing beamforming techniques that allow to calculate the correlation between an steered array signal and that of a "reference" measurement (i.e. in-flow measurement in the present cases). The second section, will introduce the signal preconditioning necessary for the novel introduction of LDV as the flow measurement technique for the aforementioned "flow-beamformed acoustic" correlation investigations. The final section of this chapter will summarize the applications of the signal processing techniques introduced and their application in the experimental tests presented in later chapters.

3.1 "Reference" Beamforming

3.1.1 Delay-and-sum Based Reference Beamforming

The most intuitive of the two approaches presented here, makes use of the basic delay-and-sum beamforming algorithm introduced in section 2.3.2.1. Whilst prior investigations availed of the use of combined "reference" signals and phased array measurements (e.g. see *Siller et al.* [82]), Dougherty *et al.* [81] reported the first attempt where this type of signal processing technique was used to measure correlation levels between a phased array signal and a flow turbulence measurement. As described in section 2.7, the introduction of array signal processing in these type of experimental approaches, was done in an attempt to improve correlation levels between flow and acoustic observations.

The first step is to use the delay-and-sum algorithm to "steer" the maximum response of an array of microphones at the location of the measurement used as "reference" (i.e. in-flow measurement volume) as

$$b_{ds}(\boldsymbol{\xi}_{(ref)}, t) = \frac{1}{M} \sum_{m=1}^{M} p_{(Mic_m)}(t - \Delta t_{foc}) \tag{3.1}$$

where $p_{(Mic_m)}(t)$ is the signal at array microphone m and Δt_{foc} is the straight propagation time delay between the local measurement of interest $\boldsymbol{\xi}_{(ref)}$ and the corresponding microphone m.

Standard signal processing techniques can then be applied to the output of the steered array signal in equation 3.1 and the output of the "reference" signal measured at the location of interest represented by $g(\boldsymbol{\xi}_{(ref)}, t)$. The cross-spectrum between the local measurement (e.g. in-flow measurement) and the output of the delay-and-sum algorithm steered at the "reference" measurement location $g(\boldsymbol{\xi}_{(ref)}, t)$, or as it from now on will be referred to as *Cross-Spectral Reference Beamforming*, can be calculated as

$$S_{GB_{ds}}(\boldsymbol{\xi}_{(ref)}, f) = \langle G(\boldsymbol{\xi}_{(ref)}, f)^* \cdot B_{ds}(\boldsymbol{\xi}_{(ref)}, f) \rangle \tag{3.2}$$

where G and B_{ds} are the Fourier transforms of the truncated local measurement and beamformed time signals g and b_{ds} respectively, $\langle\rangle$ represents block ensemble averaging and * represents the conjugate transpose. The output of equation 3.2 can be normalized via the *ordinary coherence function* (see ref [86]) as

$$\gamma^2_{GB_{ds}}(\boldsymbol{\xi}_{(ref)}, f) = \frac{|S_{GB_{ds}}(\boldsymbol{\xi}_{(ref)}, f)|^2}{S_{(G,G)}(\boldsymbol{\xi}_{(ref)}, f) S_{(B_{ds},B_{ds})}(\boldsymbol{\xi}_{(ref)}, f)} \tag{3.3}$$

where $S_{(G,G)}(\boldsymbol{\xi}_{(ref)}, f)$ and $S_{(B_{ds},B_{ds})}(\boldsymbol{\xi}_{(ref)}, f)$ represent the auto-spectrums of the "reference" signal attained at $\boldsymbol{\xi}_{(ref)}$ and the steered array output focused at the same location. The output of the *Cross-Spectral Reference Beamforming* normalized via the ordinary coherence function, that ranges between the values of 0 and 1, is a measure of the linear association between both, the "reference" and steered array signals.

Additionally, *Cross-Spectral Reference Beamforming* can also be used to identify additional radiating regions that are coherent with the measured "reference" signal. To do this, the cross-spectrum between the "reference" signal and the array response focused at

a set of predetermined focal locations can be formulated as

$$S_{GB_{ds}}(\boldsymbol{\xi}_n, f) = |\langle G(\boldsymbol{\xi}_{(ref)}, f)^* \cdot B_{ds}(\boldsymbol{\xi}_n, f)\rangle| \tag{3.4}$$

where $\boldsymbol{\xi}_n$ represents the steered array additional focal locations and || represents the absolute value of the calculated cross-spectrum. The output of equation 3.4 can be used to generate a spatial "coherent map" as a function of frequency f and steered focal location $\boldsymbol{\xi}_n$. Maximized output is attained when the steered signal is focused to regions where sources coherent with the reference signal are present.

The output of the delay-and-sum shown in equation 3.1 also renders itself to the direct application of standard time domain signal processing techniques. The time domain cross-correlation between the "reference" signal of interest $g(\boldsymbol{\xi}_{(ref)}, t)$ and the output of the steered array focused at the location of the "reference" measurement, or as it from now on will be referred to as *Cross-Correlation Reference Beamforming*, can be formulated as

$$R_{gb_{ds}}(\boldsymbol{\xi}_{(ref)}, \tau) = \langle g(\boldsymbol{\xi}_{(ref)}, t) b_{ds}(\boldsymbol{\xi}_{(ref)}, t + \tau)\rangle \tag{3.5}$$

where $\langle\rangle$ represents the time ensemble average and τ is the time domain correlation related lag. Similarly to its frequency domain counterpart the *Cross-Correlation Reference Beamforming* output can be normalized as

$$\varrho_{gb_{ds}}(\boldsymbol{\xi}_{ref}, \tau) = \frac{R(\boldsymbol{\xi}_{ref}, \tau)}{\sigma_{ref}\sigma_{b_{ds}(\boldsymbol{\xi}_{ref})}} \tag{3.6}$$

where σ_{ref} and $\sigma_{b_{ds}}(\boldsymbol{\xi}_{ref})$ represent the square root of the variance of the "reference" and steered array signals respectively. The output of equation 3.6 is a measure of the association between both, the steered array and reference signals, at the retarded time τ. Similarly, the cross-correlation between a fixed "reference" signal and the output of a phased array steered to additional locations can be estimated as

$$R_{gb_{ds}}(\boldsymbol{\xi}_n, \tau) = \langle g(\boldsymbol{\xi}_{(ref)}, t) b_{ds}(\boldsymbol{\xi}_n, t + \tau)\rangle \tag{3.7}$$

where $\boldsymbol{\xi}_n$ represents the steered array additional focal locations. Increased correlation coefficients as a function of retarded time τ are attained when the phased array is steered at a location $\boldsymbol{\xi}_n$ where a source correlated to the "reference" signal is present. The

advantage of time domain methods over their frequency domain counterparts, particularly in the case of non-deterministic signals, is that the time lag τ of the correlation peaks can be related to the straight path propagation between cause and effect. In turn, this information can be related to the relative location of the source/s under consideration. In the case of strongly deterministic signals (i.e. tonal sources), where no clear single correlation peak is evident as a function of the retarded time τ, the maximum value or standard deviation of the cross-correlation result calculated in equation 3.7 can be used to identify the origin of sources correlated to that of the "reference" signal.

3.1.2 Guidati's Reference Beamforming

As reported by Guidati [85], a similar "reference" based beamforming approach, or as it from now on will be referred to as *Guidati's* method, can be applied by transforming all signals into the frequency domain prior to the "steering" of the array. The first step is to Fourier transform the "reference" (e.g. in-flow measurement) and each of the individual array microphone signals as shown in equations 3.8 and 3.9.

$$G(\boldsymbol{\xi}_{(ref)}, f) = \int_{-\infty}^{\infty} g(\boldsymbol{\xi}_{(ref)}, t) e^{-2\pi j f t} dt \tag{3.8}$$

$$P_{Mic_m}(f) = \int_{-\infty}^{\infty} p_{(Mic_m)}(t) e^{-2\pi j f t} dt \tag{3.9}$$

where $G(\boldsymbol{\xi}_{(ref)}, f)$ and $P_{Mic_m}(f)$ are the narrowband fourier coefficients of the "reference" signal and microphone m respectively. A Cross-Spectrum Matrix (CSM) of size M can now be formulated as

$$\Phi_{(Mic_m, ref)} = \langle G(\boldsymbol{\xi}_{(ref)}, f)^* \cdot P_{Mic_m}(f) \rangle \tag{3.10}$$

where each entry is formed by the cross-spectrum of the complex pressures at microphone m and that of the "reference" signal. *Guidati's* "reference" based beamforming output is then expressed as

$$B_G(\boldsymbol{\xi}_{(ref)}, f) = \boldsymbol{\omega}_{(\boldsymbol{\xi}_{(ref)}, f)} \cdot \Phi \tag{3.11}$$

where the m_{th} entry in the complex vector $\boldsymbol{\omega}$ of length M, contains the theoretical Green's function for spherical wave propagation from a point source at the array focal location

$\boldsymbol{\xi}_{(ref)}$ to the m_{th} microphone location $\mathbf{r}_m$ of the form

$$\boldsymbol{\omega}(\boldsymbol{\xi}_{(ref)}) = \frac{e^{-jk(\|\mathbf{r}_m - \boldsymbol{\xi}_{(ref)}\|)}}{4\pi\|\mathbf{r}_m - \boldsymbol{\xi}_{(ref)}\|} \tag{3.12}$$

where k corresponds to the wavenumber at which the beamforming algorithm is applied. As shown previously with the delay-and-sum reference based beamforming algorithms, the maximum response of the array can be steered at locations other than that of the "reference" signal. This allows to form a "map" of coherent radiating regions impinging on the array over a number predetermined locations of interest. In *Guidati's* "reference" based beamforming method, the "steering" of the array towards a number of predetermined locations is achieved by modifying the steering vector as

$$\boldsymbol{\omega}(\boldsymbol{\xi}_n) = \frac{e^{-jk(\|\mathbf{r}_m - \boldsymbol{\xi}_n\|)}}{4\pi\|\mathbf{r}_m - \boldsymbol{\xi}_n\|} \tag{3.13}$$

where $\boldsymbol{\xi}_n$ is the three dimensional vector containing the predetermined focal location. *Guidati's* "reference" based beamforming is then re-formulated as

$$B_G(\boldsymbol{\xi}_n, f) = |\boldsymbol{\omega}_{(\boldsymbol{\xi}_n, f)} \cdot \Phi| \tag{3.14}$$

where Φ is the CSM matrix previously calculated in equation 3.10 and $||$ represents the absolute value. As with the delay-and-sum reference based beamforming algorithms shown in equations 3.4 & 3.7, the output of equation 3.14 is maximized when the array is steered towards the location of a source that is coherent to that of the "reference" signal used to form the CSM defined in equation 3.11.

3.2 Irregularly sampled "Reference" Signal

As discussed in section 2.4.1 the data obtained by an LDV probe is dependent on the rate of seeding particles crossing the laser beams. As a consequence, the samples acquired are recorded at irregularly time steps. Due to this, the LDV signal must be preconditioned so as to attain a correct estimation of its spectral content. It is for this reason that this signal preconditioning applies to both of the aforementioned types of "reference" based beamforming algorithms in which cross-spectrum calculations are performed. This section introduces the signal preconditioning necessary to combine an LDV irregularly sampled signal as "reference" into both, *Guidati's* and the *Cross-Spectral Reference Beamforming* techniques introduced in the previous section.

3.2.1 LDV Signal Preconditioning Applied to *Guidati's* Beamforming Method

In the cases where the acquired signals, including the irregularly sampled LDV "reference" measurement, are transformed into the frequency domain prior to cross-spectrum calculations, the parameters conditioning the frequency resolution of the Fourier transforms of all the signals must be set first. These must be selected so as to obtain equal frequency resolution in both, the array microphones and LDV flow velocity signals. As an example, consider the case where the array data is acquired at a fixed rate of 12kHz while the mean sample rates obtained by the LDV system is $\approx$ 30kHz. The LDV signal is then resampled at 120kHz using the sample-and-hold technique described in section 2.4.1.1. Equal frequency resolution can now be set by choosing the block size of the Fourier transforms. For a frequency resolution of $\approx$ 12Hz the block lengths for the microphone and LDV signal are 1024 and 10240 respectively. All the signals can now be Fourier transform using a Fast Fourier algorithm. Prior to the cross-spectrum calculation the LDV signal is now filtered using the result shown in equation 2.51. The signal preconditioning process applied to the LDV signal and each of the array microphones prior to the application of *Guidati's* reference beamforming technique is detailed in the schematic layout presented in figure 3.1.

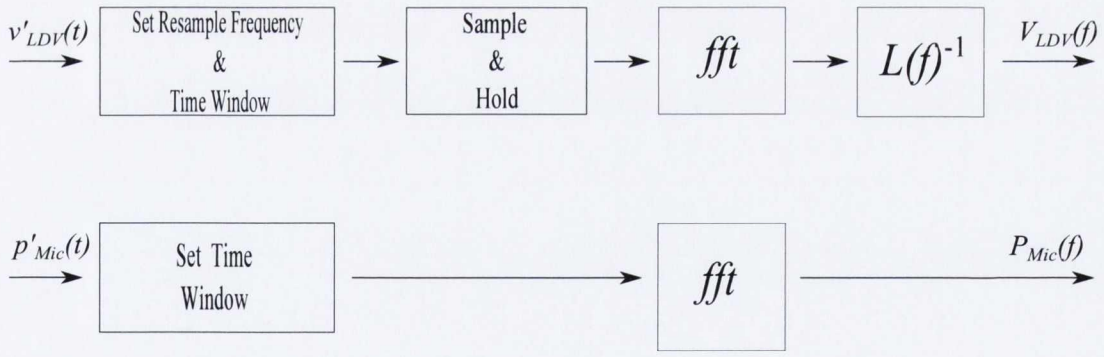

Figure 3.1: Schematic representation of the signal preconditioning applied to: 1) the LDV "reference" signal (Top), 2) one of the array channels (Bottom), prior to the application of *Guidati's* reference beamforming technique.

Each of the entries in the cross-spectrum matrix of size M shown in equation 3.10, can now be estimated using the preconditioned microphone and LDV signals as

$$\Phi_{(Mic_m,LDV)}(f) = \langle V_{LDV}(f)^* \cdot P_{Mic_m}(f) \rangle \tag{3.15}$$

where Mic_m represents the m^{th} array microphone.

Guidati's reference beamforming algorithm, where the maximum array response is steered to the location/s of interest can now be expressed as

$$B_G(\boldsymbol{\xi}_n, f) = |\boldsymbol{\omega} \cdot \Phi| \tag{3.16}$$

where the steering vector $\boldsymbol{\omega}$ of length M, contains the theoretical Greens function for spherical wave propagation between the array's focal location $\boldsymbol{\xi}_n$ and each of the microphones in the array and || represents the absolute value.

3.2.2 LDV Signal Preconditioning Applied to *Cross-Spectral Reference Beamforming*

In the case where the *Cross-Spectral Reference Beamforming* approach presented in equation 3.2 is applied, the preconditioning process for the LDV signal remains unchanged. The main difference lies in the array "steering" process. In this case, delay-and-sum is used to focus the maximum array response to a predetermined location (e.g. LDV measurement volume). The beamformed output can now be treated as a single channel pressure measurement. The resample frequency of the LDV signal and the length of the time segments used for the Fourier transforms must now be set using the same criteria as in the previous example. This process is detailed in figure 3.2

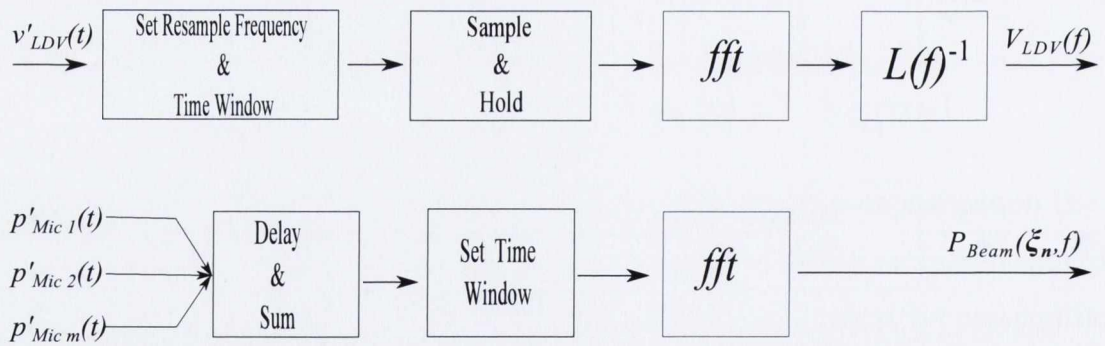

Figure 3.2: Schematic representation of the signal preconditioning applied to: 1) the LDV "reference" signal (Top), 2) the steered array signal focused at the location of the LDV measurement.

The output of the steered array and the preconditioned LDV signal can now be used to "map" the sources that are coherent with the signal used as "reference" (i.e LDV output)

over a predetermined number of focal points as

$$B_{CS}(\boldsymbol{\xi}_n, f) = |\langle V_{LDV}(f)^* \cdot P_{Beam}(\boldsymbol{\xi}_n, f)\rangle| \tag{3.17}$$

where $V_{LDV}(f)$ and $P_{Beam}(\boldsymbol{\xi}_n, f)$ are the fourier transform of the LDV and steered array signals, $\boldsymbol{\xi}_n$ represents the array focal location and $||$ is the absolute value.

3.3 Summary

This chapter has introduced the signal processing techniques that are used to enhance the correlation measurements between flow and acoustic observations via the addition of a beamforming array or receivers. The introduced techniques, namely *Guidati's reference beamforming*, *Cross-Spectral Reference Beamforming* and *Cross-Correlation Reference Beamforming* will be used in later chapters in combination with separate flow measurement techniques. Extra consideration was given to the techniques that will be used in conjunction with LDV. Section 3.2 introduced the signal preconditioning necessary for the novel introduction of LDV as the "reference" signal measurement technique in conjunction with *Guidati's reference beamforming* and the *Cross-Spectral Reference Beamforming* methods.

Chapter 4

Experimental Facilities and Instrumentation

This chapter describes the experimental facilities and the measurement equipment used in this investigation. The design process and characteristics of the microphone arrays used in a "rods in cross flow" and "free flow" experimental configurations will be introduced first followed by the description of the open jet facility used in both setups. The last section of this chapter will be dedicated to the data acquisition and flow measurement equipment used in the experimental tests.

4.1 Array Design

4.1.1 Array design for the "rods in cross flow" configuration

A purpose built array was designed for the first of the two experimental configurations. The array design process and array characteristics are described next. Even though the array configuration presented next was used in a number of different experimental setups (i.e. varying source parameters), the original array design criteria was based on the aeroacoustic source generated by a tandem of 5mm threaded rods spanning along the entire width of the jet flow of a Mach 0.25 jet as shown in figure 4.1.

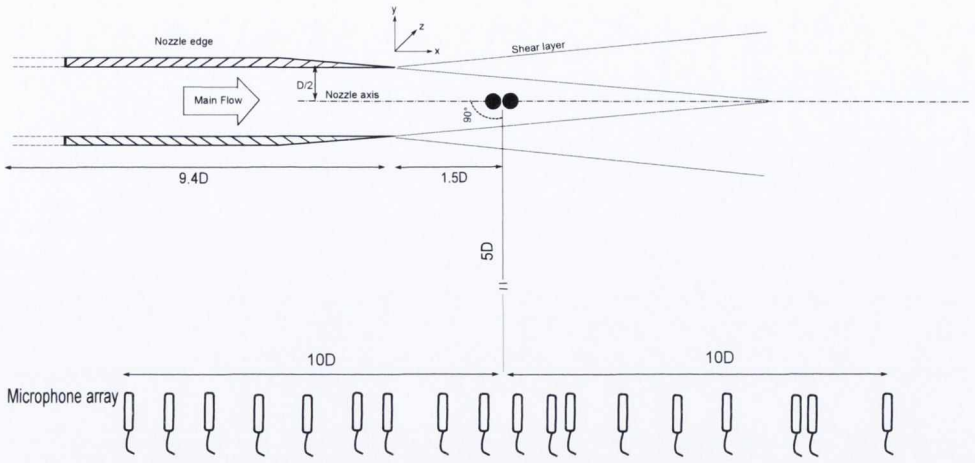

Figure 4.1: Side view of the proposed experimental layout showing the relative location between the nozzle exit, $5mm$ rods in cross flow (black dots) and the microphone array.

The orientation of the rods across the flow was chosen due to the directivity and tonal characteristics of the aeroacoustic source generated. Even though the way in which the source is generated by the interfering flow passing the rod's tandem is not discussed here, the characteristics of the source itself (i.e frequency and directivity) were important for the array design process. The tonal characteristics generated by a set of tandem rods of equal diameter and varying surface characteristics has been well documented experimentally by Hutcheson and Brooks [87]. The directivity of the source generated approaches that of a dipole with dominant radiation in a direction perpendicular to the flow and with origin at the center of the set of rods. It is for this reason that the center of the array aperture was located normal directly below of the set of tandem rods. This orientation was chosen so as to avoid focusing the array aperture over the varying dipole source directivity generated in the direction of the flow stream. In other words, the experimental setup was designed so that the array aperture was exposed to a "monopole like" omnidirectional source as that assumed by the beamforming algorithms used hereafter. Whilst, Hutcheson and Brooks [87] reported that the tone produced by a set of tandem rods in cross flow with separation in the region of 1 diameter is higher than that shed by a single rod of the same diameter, an approximation of the setup depicted in figure 4.1 was calculated using equation 4.1 (see ref. [7]) which estimates the vortex shedding from a singular cylinder in cross flow as

$$f = 0.198 \cdot \left(1 - \frac{19.7}{Re}\right) \cdot \left(\frac{V}{d}\right) \tag{4.1}$$

where f is the vortex shedding frequency, d is the rod diameter, V is the velocity of the flow and Re is the Reynolds number. Based on the test rig discharge velocity of ≈87m/s and a nozzle of diameter D_{Jet} = 50mm, the Reynolds number was estimated at $\approx 3 \times 10^5$. Using equation 4.1 the vortex shedding frequency found was to be approximately 3kHz. With this information, and considering constrains such as the number of receivers available (25), the two major design criteria for the final microphone array configuration were resolution and sidelobe level rejection. The response of a number of microphone configurations were evaluated by simulating a 3kHz sinusoidal point source at a distance of 5 D_{Jet} from the center of the array. Among the configurations analysed were spiral, rectangular, cross and randomized microphone arrays. Straight propagation paths were used to evaluate the phase difference between the source and the array microphones. This information was then used to generate a time series at each of the array receivers. Considering the narrowband characteristics of the source under study, conventional beamforming was the algorithm chosen to simulate the array's response. Whilst increasing the array aperture would improve resolution, large distances within receivers would restrict the array's working frequency range due to spatial aliasing effects. In order to increase the array's aperture whilst retaining the maximum number of unique intra spacings between receivers a randomized array configuration was favoured (see section 2.3.1.4). Similarly, the results from simulation showed how the randomized configurations consistently outperformed regularly spaced receivers configurations. For this reason, a randomized array configuration was preferred. The final randomized array configuration presented in figure 4.2 was chosen over a number of 30 randomized planar array configurations. This particular array configuration was selected as it yielded the best results in terms of array resolution and sidelobe level rejection.

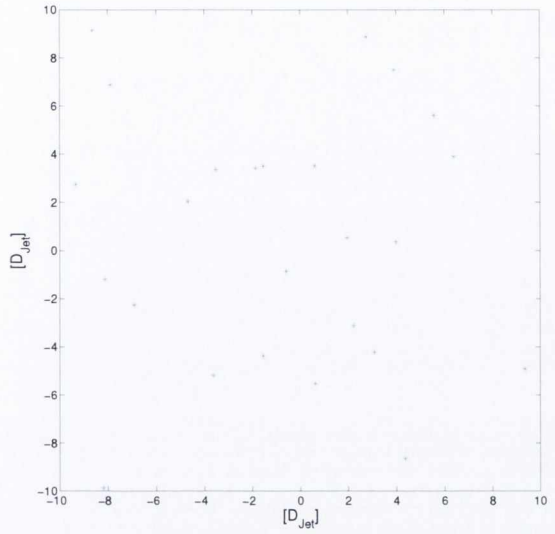

(a) Randomized array microphone layout

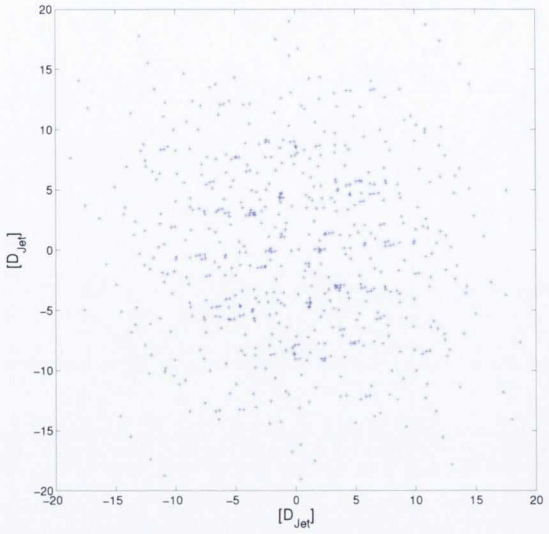

(b) Co-Array

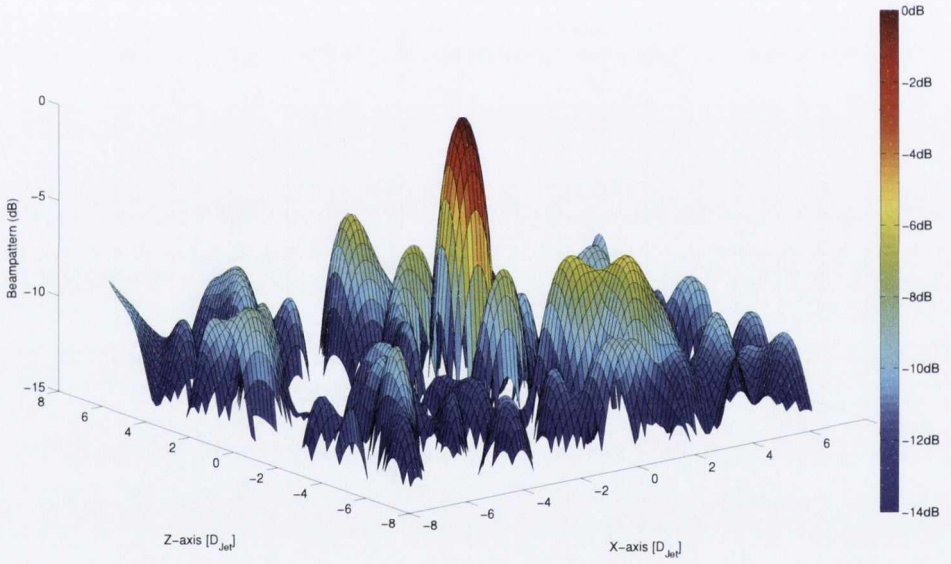

(c) Array simulated response (3D-view)

Figure 4.2: Array layout, Co-array and Array's beampattern at 3kHz

Figure 4.2(a) shows the planar array microphone layout whilst figure 4.2(b) shows its corresponding co-array. The co-array distribution shows how the randomized microphone array layout produces a desirable maximized number of unique intra spacings between receivers. This should help to reduce the appearance and level of spurious lobes. The array's beampattern for a 3kHz narrowband source at a distance of 5 D_{Jet} from the center of the array is shown in figure 4.2(c). The main lobe corresponding to the source location can be clearly appreciated at the center of the beampattern. The highest sidelobe level

(SLL) is found at approximately 7dB below that of the main lobe.

The response of the same array set up was then simulated as a function of source frequency. These results are summarized in figure 4.3.

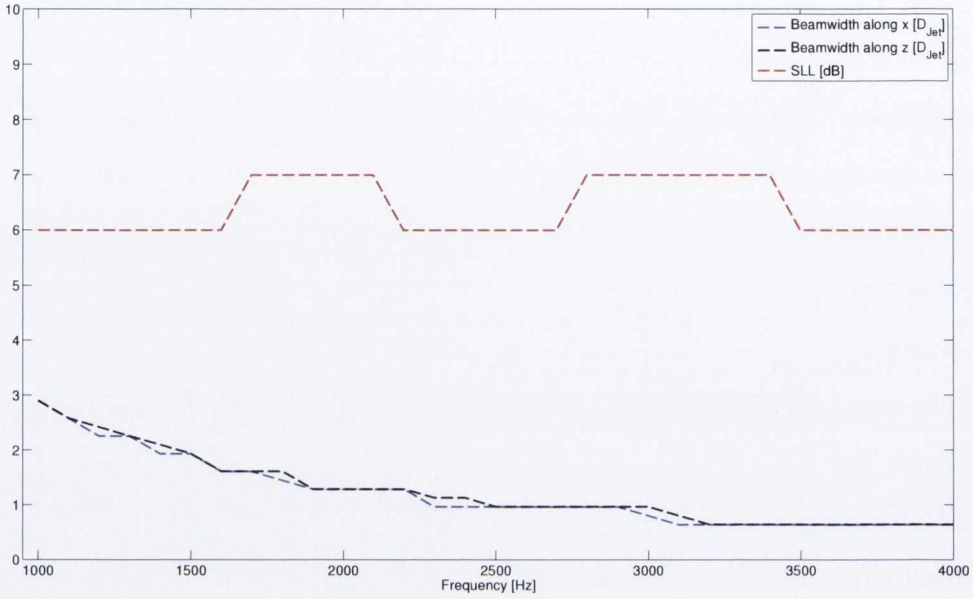

Figure 4.3: In this figure: array's SLL rejection in dB (– red) and width of the main lobe at the -3dB point ("beamwidth") in D_{Jet} along the x (– blue) and z (– black) axis as a function of beamformed frequency.

For the frequency range shown, the SLL was kept between 6 to 7dB below that of the main lobe. The array's beamwidth along the x and z axis ranged from $\approx 3D_{Jet}$ at the lower frequencies up to $\approx 0.7D_{Jet} - 1D_{Jet}$ at the desired frequency of 3kHz.

4.1.2 Simulated Response of the "Free Flow Configuration" Array

The randomized 25 microphone array layout used in the "free flow configuration" set up and its corresponding co-array are presented in figure 4.4.

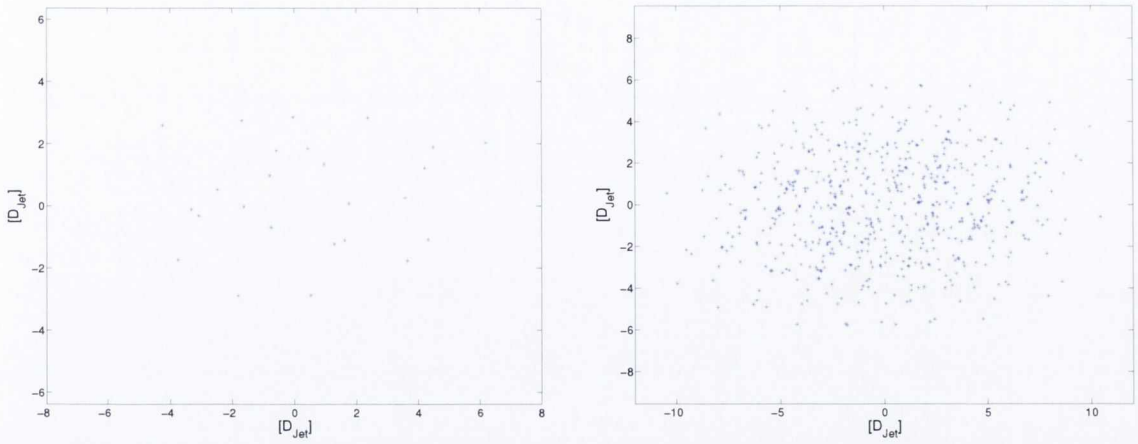

(a) Randomized 25 microphone array layout (b) Co-array

Figure 4.4: Microphone layout and corresponding co-array

This microphone layout was used in a flow-acoustic correlation investigation aimed at the broad angle radiation of a Mach 0.25 jet. The type of source under study determined some of the array constrains. Whilst a large aperture would have again been desirable to improve resolution, the directivity characteristics of turbulent flows discussed in section 2.2.2 restricted the polar angle extent covered by the array's aperture. Based on the two dissimilar source theory introduced by Tam *et al.* [13], an aperture covering a large polar angle with respect to the jet exit would integrate over dissimilar source types. With this in mind, the reduced array aperture shown above was favoured for this investigation. The location and orientation of the microphone array with respect to the jet axis is shown in figure 4.5. As detailed in figure 4.5(a), the array center was located at 90° and 12 D_{Jet} distance from the jet's centerline position $[5D_{Jet}, 0, 0]$ where the origin $[0, 0, 0]$ corresponds to the center of the jet exit. The array aperture covered the polar angle range between $90° - 50°$ with respect to the jet exit.

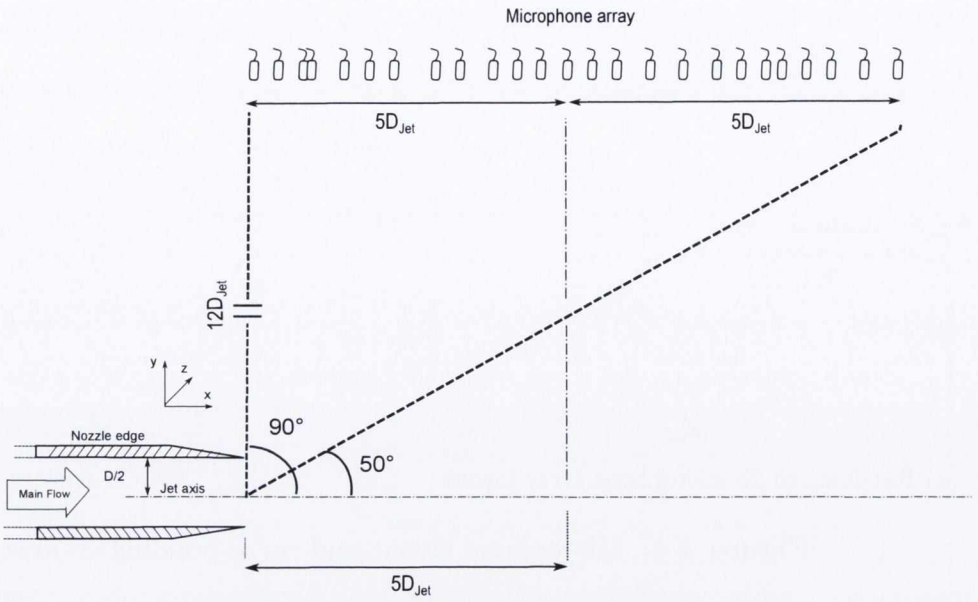

(a) Experimental layout side view and detail of the polar angle range covered by the array aperture.(Layout not drawn to scale)

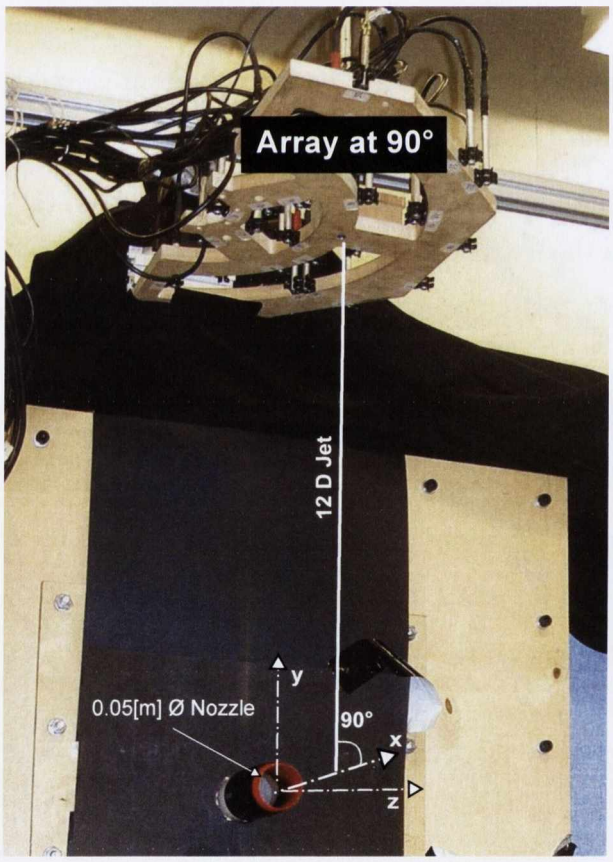

(b) Picture of the planar array location and nozzle exit.

Figure 4.5: Detail of the location and polar angle range covered by the array's aperture with respect to the jet exit.

The array's resolution as a function of focal location along the jet's longitudinal axis was evaluated. This was done so as to assure that the array resolution did not vary as a function of focal location along the jet axis. To do this, the array response was evaluated by generating individual sources along the jet's centerline as depicted by the red circles in figure 4.6. Separate array responses were simulated at each of the individual source locations along the jet axis. Each of the sources, separated by a distance $dx = D_{Jet}/6$ was generated using a 27000 points Gaussian random distribution. Each beampattern was simulated over a mesh of focal points on a plane along the jet's centerline as depicted in figure 4.6.

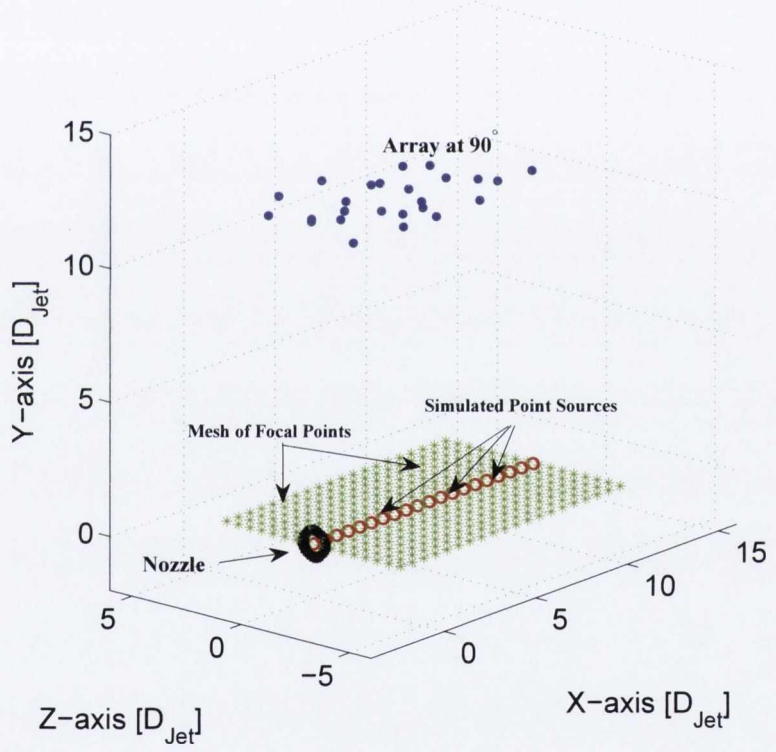

Figure 4.6: Simulation set up to evaluate the array resolution as a function of focal location along the jet axis. Blue (•) represent the location of the individual microphones in the array. Red (○) illustrate the location and orientation of a number of the individual simulated sources generated along the jet's centerline. Green (∗) illustrate the mesh of focal points used to simulate the array's response.

The estimated time of arrival from the location of each simulated source to the array microphones was calculated using straight propagation paths and a constant sound speed propagation of 344m/s. This calculated propagation time was used to delay the source

arrival at each of the array receivers. Each microphone signal was then band passed using a 2.5 - 3.5kHz phaseless 4^{th} order Butterworth filter prior to the application of the delay and sum beamforming algorithm. The simulated array resolution or beamwidth (-3dB) measured along the x and z axis as a function of array's focal location along the jet axis is presented in figure 4.7. The array's resolution remains fairly constant as function of focal location along the jet axis. However, a slight improvement of $\approx 0.5D_{Jet}$ is found directly below the array center at $5D_{Jet}$ along the x-axis. The effects of the array orientation are also clear. As the aperture extends further along the x-axis the resolution obtained along this direction is improved with respect to the resolution obtained along the z-axis.

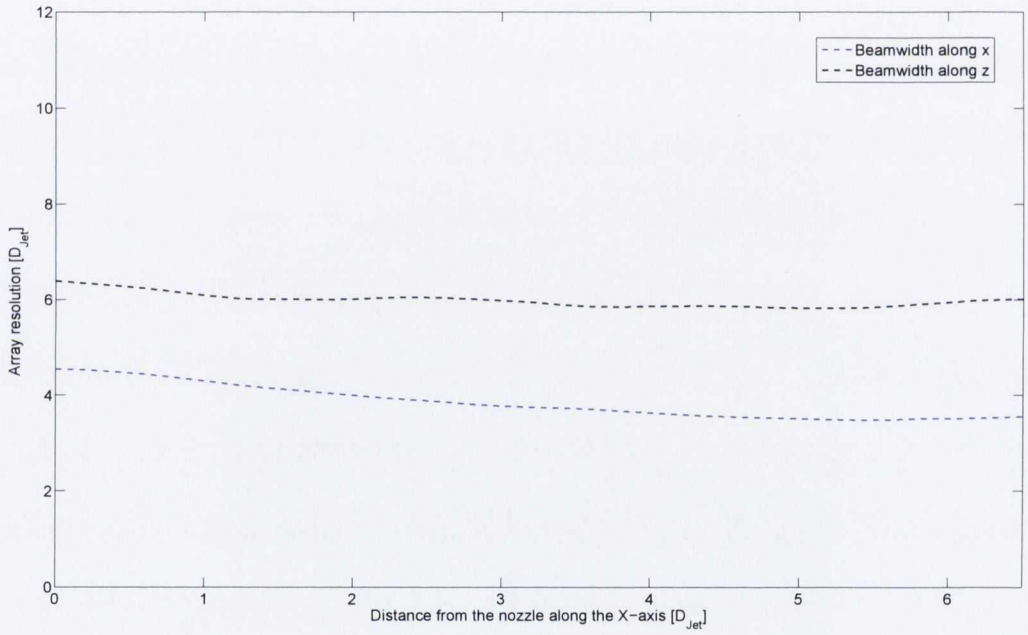

Figure 4.7: Array resolution along the x and z-axis as a function of focal point.

The response of the microphone array was then estimated as a function of frequency. To do this, a sinusoid point source was generated at the [$5D_{Jet}$,0,0] axis location. The calculated beamwidth and SLL rejection as a function of source frequency are presented in figure 4.8.

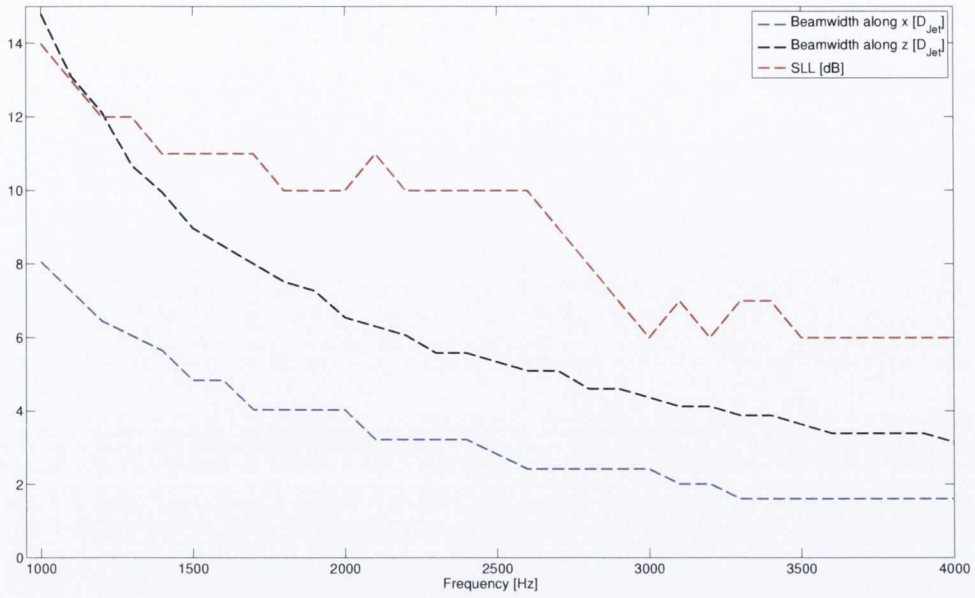

Figure 4.8: In this figure: 1- Array's beamwidth in D_{Jet} along the x (blue) and z (black) axis as a function of frequency for a simulated narrowband point source located at [$5D_{Jet}$,0,0] . 2- SLL rejection in dB (red) as a function of frequency.

Whilst resolution values ranged between 14 to $4D_{Jet}$ along the z-axis, improved resolution ranging from 8 down to $2D_{Jet}$ is achieved along the x-axis. SLL rejection ranges from 14dB in the lower frequencies ≈1kHz up to a minimum of ≈7dB at 4kHz.

4.2 Open Jet Facility

The experiments were performed in the subsonic open jet facility at Trinity College Dublin as described by Chatellier and Fitzpatrick [88]. A $5.5kW$ centrifugal blower with 8 blades operating at 2860 *rpm* powers a jet capable of velocities from ≈ 30 m/s to ≈ 87 m/s and associated Reynolds numbers based on the exit nozzle diameter between 1×10^5 and 3×10^5. The centrifugal blower exit is connected to a diffuser and a plenum where an arrangement of honeycombs and screens followed by the bell-mouth ensures that the flow in the nozzle has a low turbulence level and is aerodynamically uncoupled with the upstream fan. A schematic representation of the inlet, diffuser and plenum and a picture of the facility are shown in figures 4.9 and 4.10.

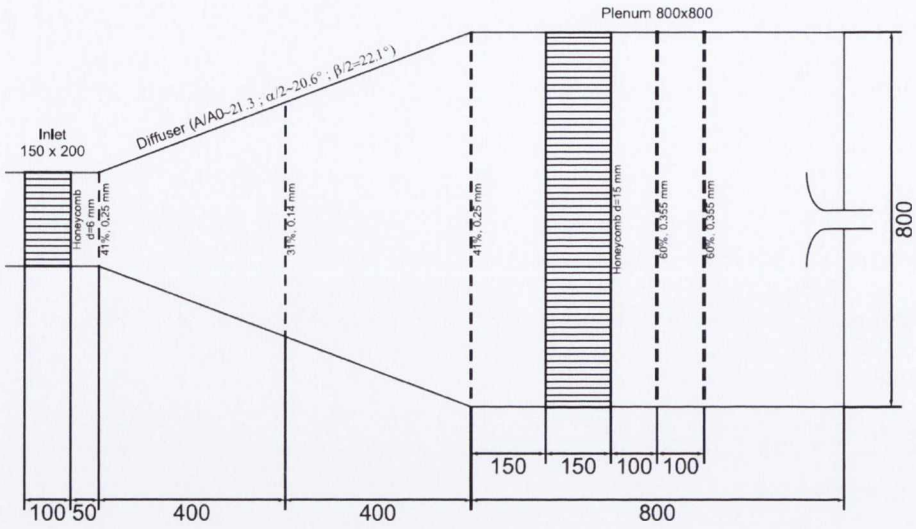

Figure 4.9: Schematic representation of the inlet, diffuser and plenum obtained from Chatellier and Fitzpatrick [88]

Figure 4.10: Picture of the centrifugal blower, plenum and nozzle.

4.3 Data Acquisition

4.3.1 Laser Doppler Velocimetry Equipment

The LDV system used in this investigation consists of a 500mW Argon-ion laser and a dual beam Dantec optical head with blue (488nm) and green (514nm) wavelengths for

vertical (w) and longitudinal (u) velocity components respectively. Dimensions of the measurement volumes are $0.12 \times 0.12 \times 1.6$mm where the largest dimension corresponds to the measurement volume length. The system was operated in the forward scatter mode. The receiving lens was located in front of the beam head at an off-axis angle (see figure 6.3). A pinhole of approximately 0.1mm diameter in the receiving optic is used to collect the scattered light. The LDV and audio data acquisition systems were synchronized by an external trigger. The LDV data collected was analysed using a Dantec burst spectrum analyser type BSA F50 and stored on the PC ready for post processing. Sample-and-hold was used to reconstruct the irregularly sampled LDV signals prior to the application of standard signal processing techniques. The effects, limitations and correction techniques used for the application of sample-and-hold as a signal reconstruction technique were introduced in section 2.4.1.

4.3.2 TR-PIV Equipment and Data Processing

The TR-PIV system employed in this investigation included a Quantronix Darwin Duo (15 mJ/pulse @ 1 kHz) dual-cavity laser capable of repetition rates of up to 10 kHz per oscillator. An LaVision HighSpeedStar 6 camera with 8 GB of onboard memory capable of 5400 fps at full frame ($1024px \times 1024px$) was used to capture flow images. In all experiments, the equipment was operated in the "double frame/double exposure" acquisition mode. In order to increase the TR-PIV sampling frequency, the camera field of view focused on a plane orientated longitudinally along the jet axis was reduced to a size of 1024×256 pixels. This allowed to record a total of 10915 double frame images per measurement location at a rate of 9kHz. TR-PIV image processing was carried out using LaVision DaVis 7.2 software using a three-pass correlation routine. The "second-order" correlation function along with a reference vector velocity field was used in the initial pass with an interrogation window size of with 64×64 pixel and 50% overlap. Subsequent iterations were carried out with a final window size of 32×32 pixels and 50% overlap. This yielded a final vector spacing of $1.1mm$ and a 64×16 velocity vector field per image.

4.3.3 TR-PIV Experimental Data Quality Evaluation

Evaluation of the data quality attained by the TR-PIV at two of the measured locations within the jet flow is presented next. The relative location of these two measurement regions with respect to the jet exit are detailed in figure 4.11

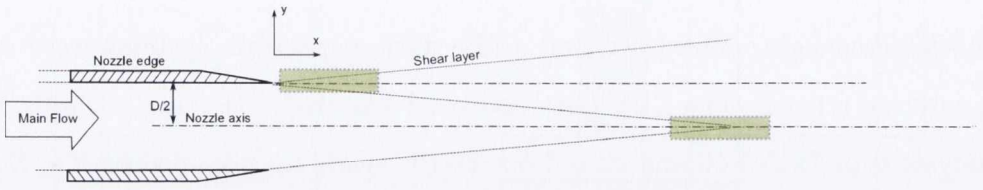

Figure 4.11: The green rectangles represent the location of the two measurement areas of size $1.2 \times 0.28 D_{Jet}$ used for data quality evaluation (drawn not to scale).

Both of these TR-PIV measurement locations were chosen as they experience the highest velocity gradients along the jet's lip and centerline respectively. This is particularly pronounced in the shear layer measurements. Here, parts of the flow within the TR-PIV frame are stagnant while contiguous sections of the flow accelerate rapidly within a very small region up to the jet exit velocity. This peculiarity makes the TR-PIV vector estimation more challenging.

Figure 4.12 shows the data evaluation for the TR-PIV measurements acquired at the end of the potential core. A Q-factor threshold was set to remove vectors where the highest correlation peak did not reach at least 1.3 times higher than that of the second peak. In addition, the median filter was set to remove vectors exceeding twice the RMS value of surrounding vector fields. Using this post-processing criteria the ratio of rejected vectors per frame and location within the TR-PIV frame are presented in figures 4.12(a) and 4.12(b). The average value of missing vectors per individual TR-PIV frame is approximately 0.5% of the total. Only in five individual TR-PIV frames this value reaches $\approx 5\%$ of the total. The ratio of missing vectors per location shows how the majority of these, up to 50% in some locations, are concentrated at the edges of the frames. For this reason, vectors calculated at the edges of the TR-PIV frames were discarded from the experimental results. The mean velocity vector profile calculated from the remaining vectors is shown in figure 4.12(c). The mean flow velocity values clearly captures the end of the potential core region where the exit velocity $U_{Jet} \approx 87 m/s$ reduces down to 0.95% of its

original value. However, a slight misalignment between the jet core and the centerline of the TR-PIV frame can be appreciated of the same figure.

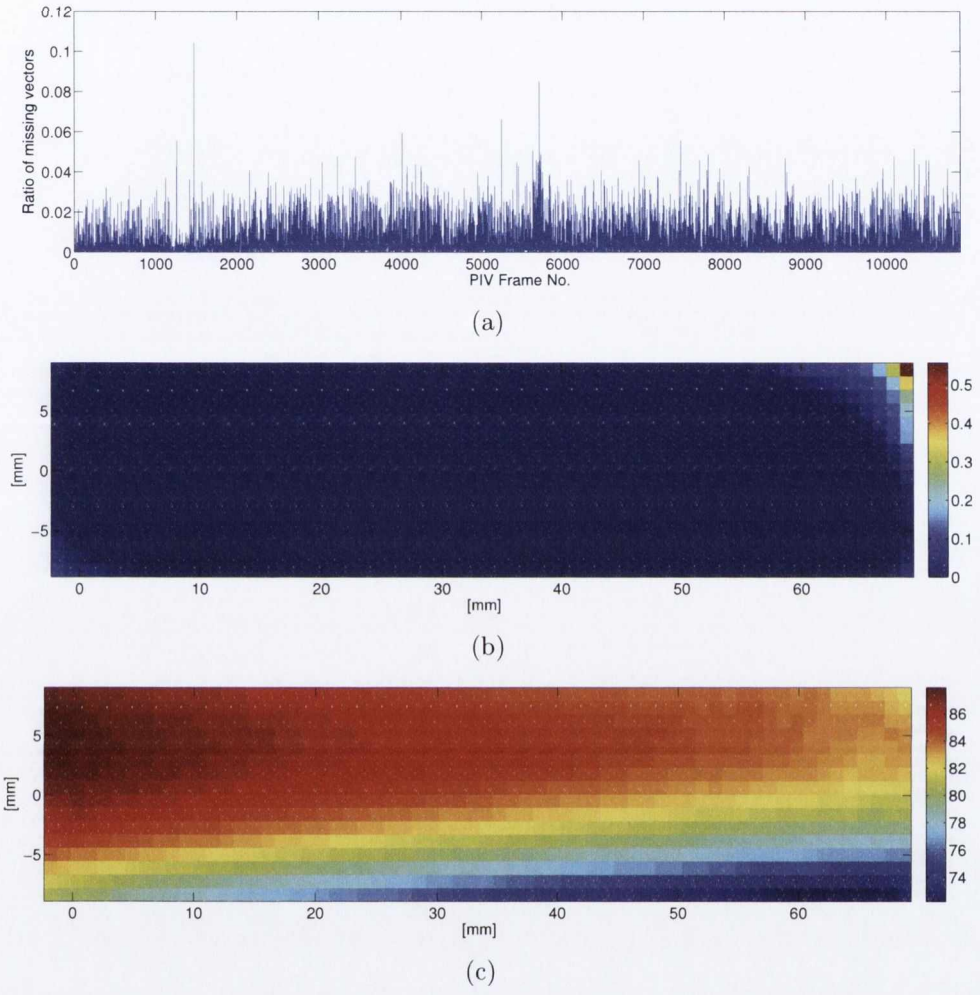

Figure 4.12: TR-PIV quality data example. (a) Ratio of missing velocity vectors per calculated PIV frame. (b) Ratio of missing vectors per location within the total number of PIV frames. (c) Mean velocity flow profile measured at the end of the potential core where $U_{Jet} = 87m/s$ reaches 0.95% of its original value.

A histogram of pixel displacement of one of the calculated vectors within the PIV frame is shown as an example in figure 4.13. It is clear from this result that the calculated pixel displacements are not biased towards integer values. In other words, the measured TR-PIV data is relatively free from the "peak locking" effect described in section 2.4.2.3.

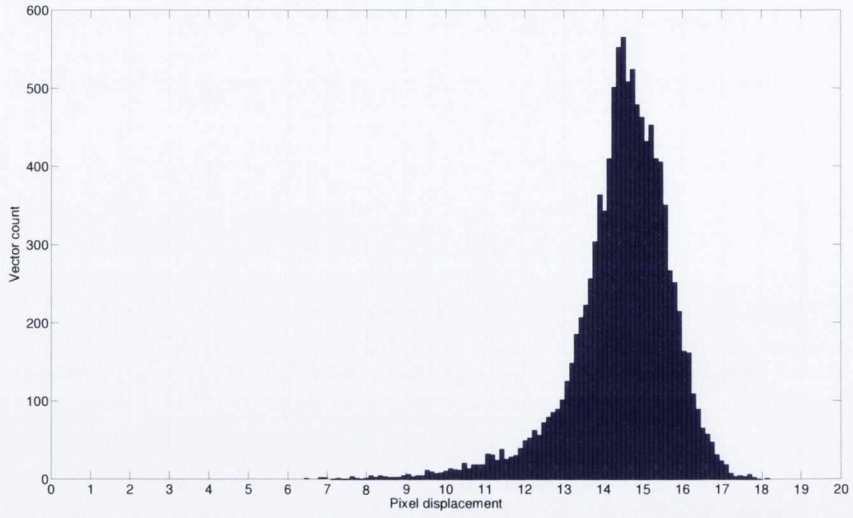

Figure 4.13: Pixel displacement histogram

The same postprocessing parameters were applied to the data acquired along the jet's shear layer. These results are shown in figure 4.14. In the shear layer case, the number of missing vectors per frame only reaches an average of approximately 0.3%. As before, most of the rejected vectors are concentrated at the edges of the TR-PIV frame. These regions within the TR-PIV frames were discarded from all measurements. Only an approximate 5% of vectors are missing from some regions at the center of TR-PIV frame. The mean velocities estimated from the validated vectors shown in figure 4.14(c) clearly show the transition between the jet's core and the stagnant flow in the vicinity and the shear layer growth along the downstream direction. As in the previous case, the histogram of pixel displacement shown in figure 4.15 clearly shows that "peak-locking" is not present in the calculated velocity vectors.

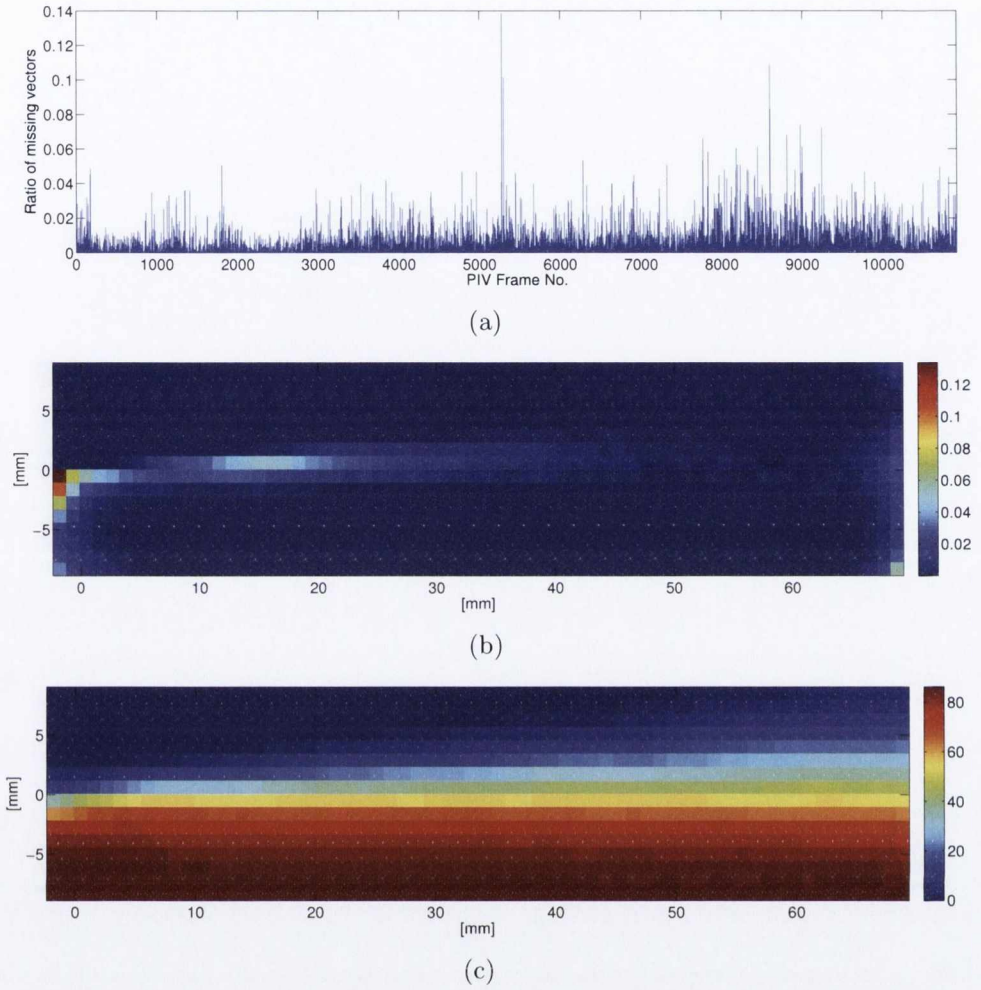

Figure 4.14: TR-PIV quality data example. (a) Ratio of missing velocity vectors per calculated PIV frame. (b) Ratio of missing vectors per location within the total number of PIV frames. (c) Mean velocity flow profile measured at the transitional region at the jet exit. In the same figure can be appreciated a section of the jet core at $U_{Jet} \approx 87m/s$, a section of the entrainment region where the flow is stagnant and the growth of the shear layer towards the downstream section of the PIV frame.

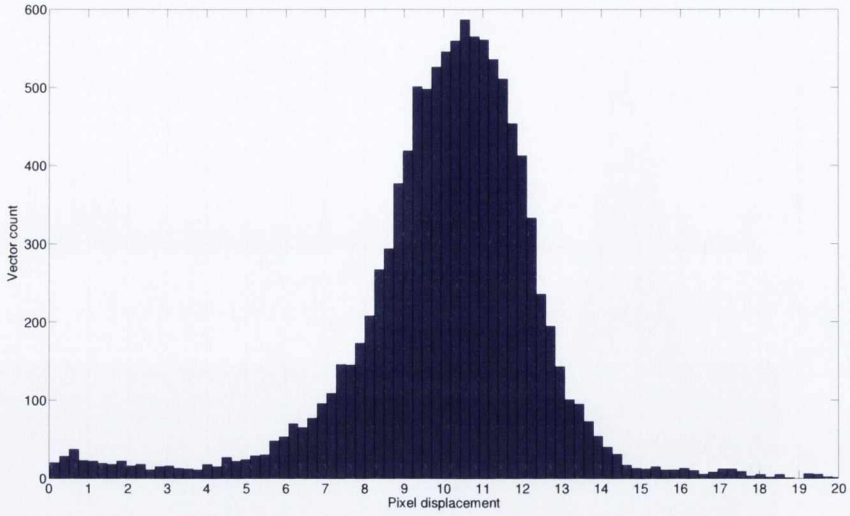

Figure 4.15: Pixel velocity Histogram

4.3.4 Array Microphones, DAQ System and Video Device

All the arrays used in this investigation were built using 25 KE4 Sensheiser electret microphones with a 20-20kHz range and integrated amplifiers. A pistonphone was used to determine the sensitivity of one of the electret microphones. This selected microphone was used as reference to match the overall gain factor of the remaining 24 microphones. To do this, each of the array microphones was flush mounted at the closed end of an impedance tube with a plane wave cut off frequency of 3.5kHz alongside the reference microphone. A speaker radiating white noise was located at the open entrance of the tube opening. The calculated magnitude of the transfer function between each of the receivers and the reference microphone at 1kHz was used to equalize the gain of all the receivers. Frequency dependent phase calibration between receivers was not performed.
In addition to the 25 electret microphones a 1.3 megapixel Hercules webcam was located at the center of the microphone array presented in section 4.1.1. The webcam captured pictures of the scanned area while audio measurements were obtained. This allowed to overlay real images of the area of interest over the beamformed contour plots. The image processing toolbox in Matlab was used to capture and overlay the webcam images over the beamformed plots.
The array microphone data was acquired simultaneously using a National instruments 32 channel, 24 bit data acquisition system. The National Instrument system consisted of

a NI PXI-1033 frame with 4 NI PXI-4472B cards with 8 input channels each. Labview software was used to set the measurement variables and the data was stored in a PC ready for postprocessing. All measurements between the array and flow measurements devices were synchronized via a 5V input trigger set in a dedicated channel of one of the NI PXI-4472B cards.

4.4 Flow Seeding

The seeding used for all the LDV and PIV was generated using a PeaSoup Ltd, Phantom PS31 smoke machine. An oil based fluid (Pea Soup Smoke oil 135) was used as the basis for the smoke generation. A supply of nitrogen is used to nebulize the oil based fluid before being vaporized at the heat exchanger in a process known as "flashing". As the vapor mixes with cooler air outside the machine's nozzle it forms an opaque aerosol of particles. The approximate size of oil based particles generated with the set up used for all experiments was in the range of $1.5\mu m$. The diffraction pattern for a similar particle size and an incident wavelength of $532nm$ is shown in figure 2.14.

Chapter 5

Array Preliminary Results

A number of experimental test setups were designed to test the characteristics of a number of different beamforming algorithms described in previous sections. The first section of this chapter presents an experimental arrangement designed to demonstrate the capabilities of the *delay-and-sum* and *conventional beamforming* algorithms introduced in section 2.3.2. The second section uses a similar experimental setup to demonstrate the source identification capabilities of the *Cross-Spectral Reference Beamforming* and *Guidati's* reference based beamforming techniques introduced in section 3.1. The randomized microphone array layout described in section 4.1.1 was chosen for all test carried out throughout this chapter. The microphones were flat mounted on a $1m^2$ flat wooden panel with an opening at its center that fitted a webcam. The use of a video device allowed to overlay images of the measurement area over the beamformed results. For all preliminary array test, a semi-anechoic environment effective down to approximately 500 Hz as that used in a previous investigation by Jordan *et al.* [89] was placed around the measurement area.

5.1 Time vs Frequency Domain

5.1.1 Single source case

In the first experimental setup, a small aperture loudspeaker was placed at 1m distance from the center of the array. Figure 5.1 shows the camera view from the array's center. A continuous 3150Hz sinusoid signal was driven through the speaker. Simultaneously, the 25 microphone array recorded 10 seconds of pressure data at a sampling frequency of 15kHz. Each of the microphone signals were automatically low pass filtered to avoid

aliasing.

Figure 5.1: Speaker located in front of the microphone array

The array response was analyzed using the *conventional* and the *delay-and-sum* algorithms presented in section 2.3.2. In both cases the data analysed was restricted to the first 2.18 seconds of data recorded which corresponded to the first 32768 data points. This was done to shorten the processing time. In the case of the conventional beamforming algorithm this data truncation was achieved using a block length of 1024 for the FFT averaged over 32 data sets. It should be pointed that, as measurements were relatively free from extraneous noise and the source was invariant, longer integration times did not yield improved results.

Figure 5.2 shows the conventional beamforming output at the narrowband frequency of 3150 Hz. The loudspeaker is clearly identified as the main source within the scanned area. The same data set was then analysed using the delay-and-sum time domain algorithm. Prior to the application of the time domain beamforming algorithm each of the microphone signals was filtered using the 1/12 octave phaseless band pass filter depicted in figure 5.3(b). This narrowband band pass filter was chosen to simulate the response of the conventional frequency domain narrowband algorithm. As shown in figure 5.3(a), the output of the delay-and-sum algorithm also identifies the loudspeaker as the main noise source. However, clear irregularities can be observed in the isocontours when compared to the results obtained via the conventional beamforming algorithm.

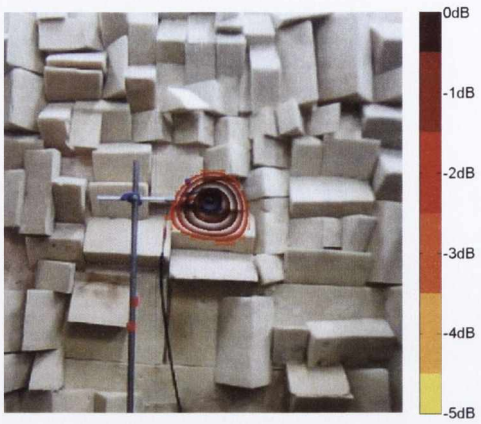

Figure 5.2: Conventional beamforming output at 3150Hz

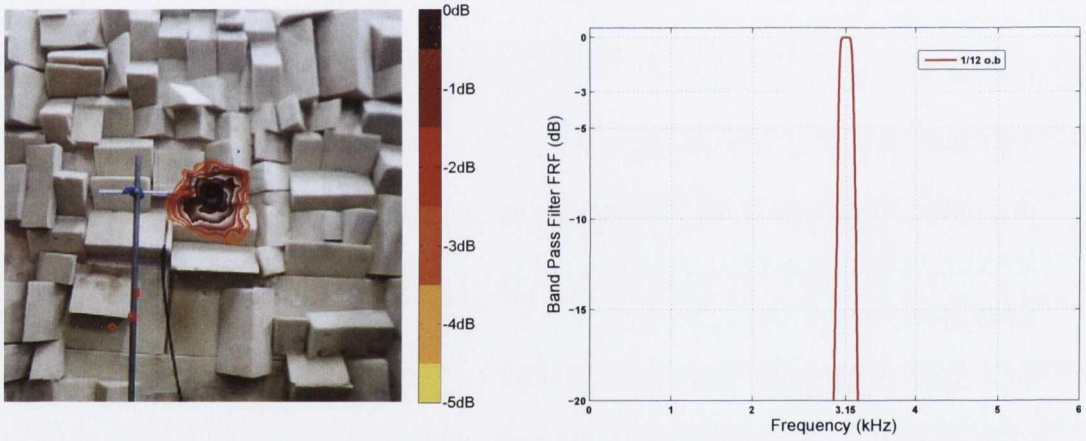

(a) 1/12 o.b. Band passed time domain beamforming output

(b) Phaseless Butterworth 1/12 octave band filter

Figure 5.3: Delay-and-sum beamforming output and FRF of the 1/12 band pass filter

These irregularities in the beamforming output are an effect of the relatively low sampling frequency used. Whilst the sampling rate used in the frequency domain based beamforming algorithms needs just to satisfy the the nyquist criteria, time domain algorithms yield best results when the sampling rate is increased. As reported by Jaeckel [90], optimal results when applying time domain beamforming algorithms are acquired when the sampling frequency is 10 times higher than that of the source of interest. To prove this point, the microphone data series used on the previous example was up-sampled at 5 times the original sampling frequency. As the acquired data was automatically low passed filtered limiting its frequency content, linear interpolation could be used to estimate the value

between samples. This allowed to up-sample the existing time series without adding new frequency information. The beamforming output obtained from the up-sampled time series is shown in figure 5.4. Direct comparison of figures 5.3(a) and 5.4 shows the improved results obtained from using a higher time resolution when applying the delay-and-sum algorithm.

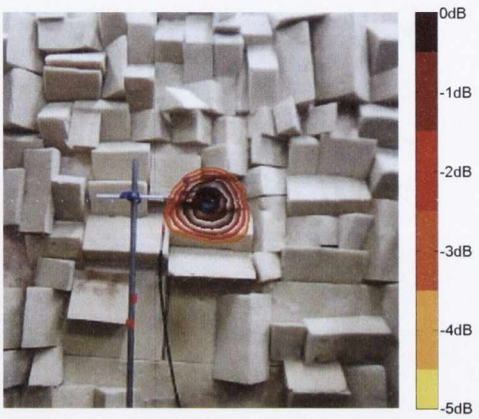

Figure 5.4: Delay-and-sum output of the up-sampled microphone signal.

Whilst the sampling frequency constraints make the frequency domain technique computationally less expensive, there are two important inherent benefits when analysing the data in time domain. The first is the readily available broadband beamforming method. As the microphone signal are not transferred into complex narrowband Fourier coefficients with a predetermined bandwidth, its output contains the frequency information over the desired frequency bandwidth of interest in one single calculation. The second, is the capability of identifying transient sources. As reported by Jaeckel [90], applying short enough block length of data for the analysis of transients in frequency domain affects 1- the achievable frequency resolution 2- the attainable time resolution. Frequency based beamforming algorithms limit the achievable time resolution as a large number of time blocks need to be analyze to acquire an accurate estimate of the Cross-Spectrum Matrix. On the other hand, maximum time resolution can be achieved by the time domain algorithms without the loss of achievable frequency resolution.

5.1.2 Multiple source case

In the second test, two speakers of equal specification were located at 1m distance from the array. The camera view from the center of the array is shown in figure 5.5

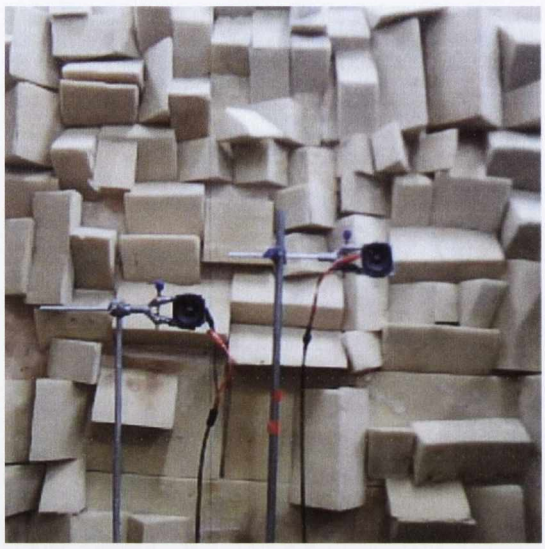

Figure 5.5: Speakers located in front of the array receiver

Two continuous sinusoids of equal amplitude and different frequency were driven through each of the speakers shown in figure 5.5. The left speaker was driven by a 2600Hz sinusoid while the sinusoid signal sent to the speaker on the right was fixed at 3670Hz.
As in the previous example, the microphone signals were analysed using the conventional and delay-and-sum algorithms. Figure 5.6(a) shows the conventional beamforming output centered at the narrow frequency band of 2600Hz. A clear contribution from the speaker on the left is identified while the speaker on the right is ignored. Figure 5.6(b) shows the conventional beamforming output at the narrow frequency band centered at 3670Hz. The speaker on the right is now identified as the main source while the speaker on the left is ignored. The effects of frequency dependent resolution can be easily observed when comparing the area covered by the contours around each of the sources in figures 5.6(a) & 5.6(b).

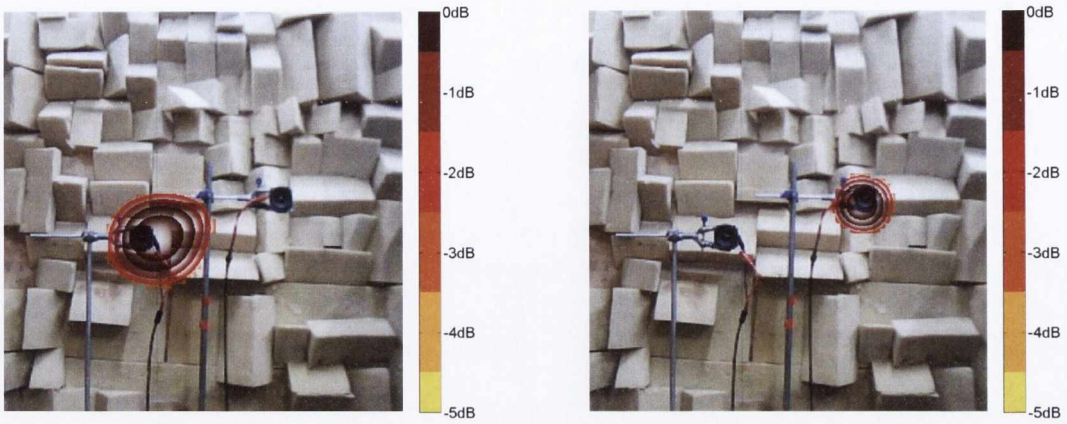

(a) Conventional beamforming output at 2600Hz (b) Conventional beamforming output at 3670Hz

Figure 5.6: Frequency domain beamforming output

The same data set was analysed using the delay-and-sum algorithm. As before, previous to the application of the beamforming algorithm, all the microphone signals were band pass filtered and up-sampled. In this case, phaseless band pass filters of different bandwidths were used. The Frequency Response Function (FRF) of the band pass filters used for this purpose are shown in figure 5.7. The half-power points (-3dB) of the filters are the limits of the frequency bands chosen for the band pass filters used in each case.

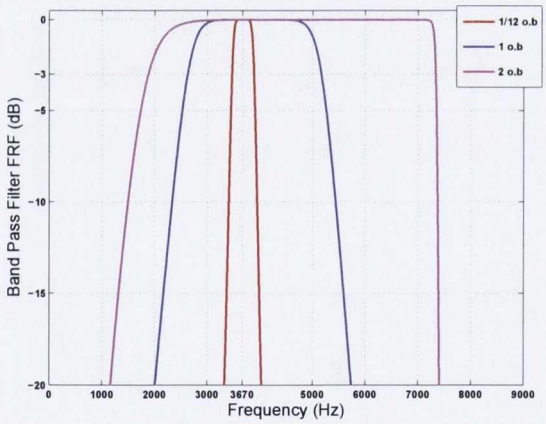

Figure 5.7: FRF of the phaseless Butterworth octave band filters used in the delay-and-sum beamforming calculations.

The filters central frequency was chosen at 3670Hz, corresponding to that of the source radiating through the speaker on the right. As in the previous example, the 1/12 octave band (o.b) filter was used to obtain a direct comparison between the delay-and-sum and

conventional beamforming algorithms. The 1 & 2 o.b filters were chosen to show the inherent broadband capabilities of the time domain algorithm.

Figure 5.8 shows the results from the time domain beamforming methods after application of the band pass filters.

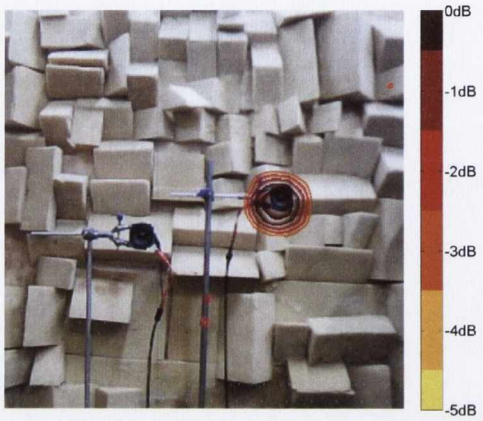

(a) Delay-and-sum 1/12 o.b. filtered array output

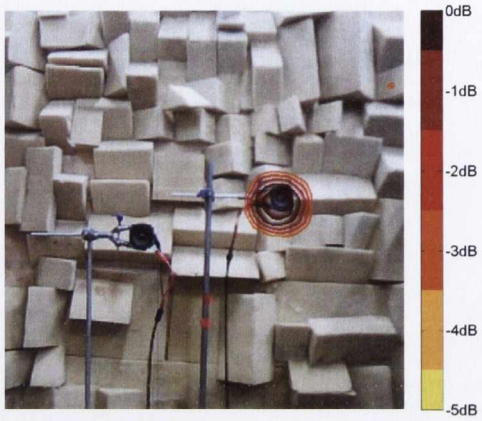

(b) Delay-and-sum 1 o.b. filtered array output

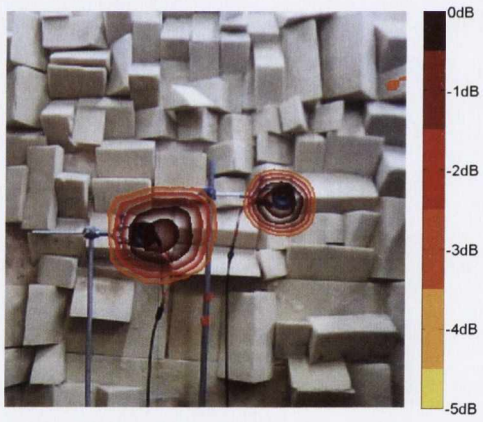

(c) Delay-and-sum 2 o.b. filtered array output

Figure 5.8: Band pass filtered beamformer response.

As expected, the beamformed output filtered by the 1/12 o.b shown in 5.8(a) only identifies the 3670Hz source on the right. This is also the case in the result attained by the 1 o.b filtered data shown in figure 5.8(b). The contribution of the sinusoid at $2600Hz$ is clearly dampened by the effect of the band pass filter. It is only when the 2 o.b filter (see figure 5.8(c)) is used that the contribution from the lower frequency source on the left can be seen along side the higher frequency source on the right. The inherent broadband

nature of the time domain algorithms allow the identification of sources radiating at well separated frequencies in a single calculation. Whilst this is still possible in the frequency domain, separate calculations would have to be carried out for each separate narrowband to achieve the same result.

The effects of applying the time domain beamforming algorithm without the use of any band pass filter are shown in figure 5.9. Even though main sources are still identified, there is a clear loss in resolution and dynamic range due to the contribution of low frequencies.

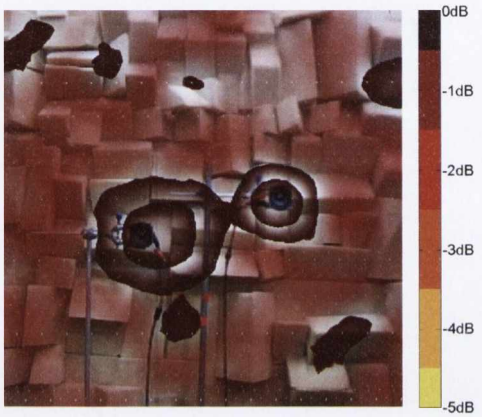

Figure 5.9: Non filtered delay-and-sum beamforming output.

5.2 "Reference" Based Beamforming

The results shown from both of the aforementioned beamforming techniques (i.e. conventional and delay-and-sum) identified the location of main sources within the predetermined scanned region. Nevertheless, a major drawback in both techniques is that weaker sources within the same frequency band can be masked by the limited dynamic range of the beamformer plot (i.e. sidelobe levels). To demonstrate this point, two loudspeakers radiating incoherent broadband noise were located at 1m from the array as shown in figure 5.10.

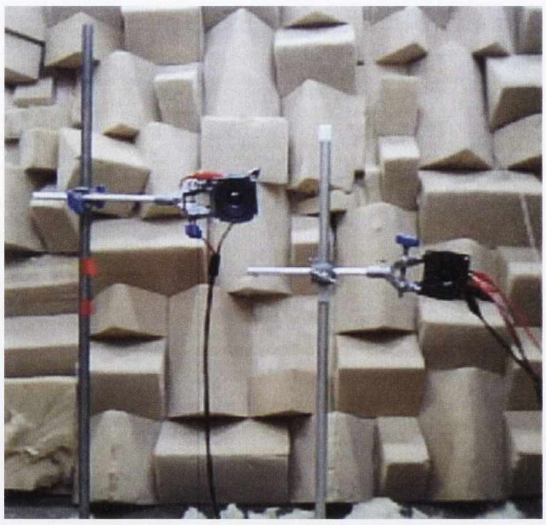

Figure 5.10: Speakers located in front of the array receiver

The SPL (Sound Pressure Level) generated by the source on the left was approximately 17dB lower than the source on the right. Figure 5.11(a) shows the delay-and-sum beamformer output for the 0.5-4.8kHz frequency band. It's clear that the input of the weaker source on the left is outside the dynamic range as sidelobes start to appear at third locations as secondary sources. As is obvious, these factors can become an issue when trying to identify weaker sources in complex sound fields.

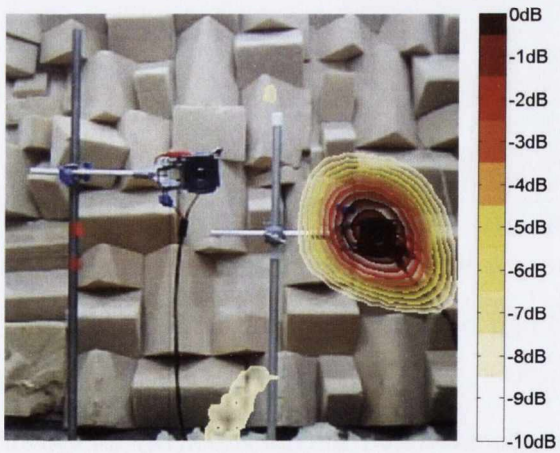

(a) 0.5-4.8kHz band passed delay-and-sum beamforming output

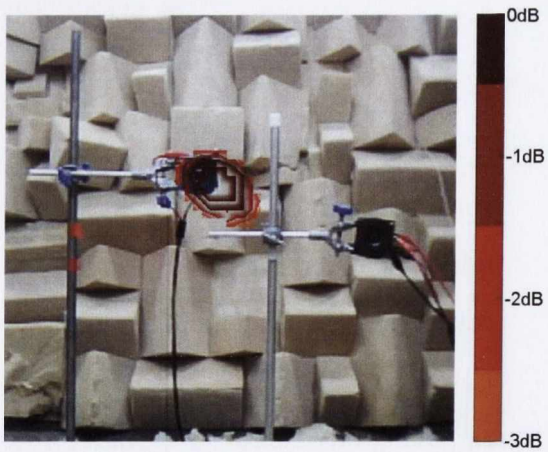

(b) Output of the Cross-Spectral Reference Beamforming algorithm centered at 4000kHz

Figure 5.11: Outputs of the band passed delay-and-sum and Cross-Spectral Reference beamforming algorithms.

The same set of data was analysed using the *Cross-Spectral Reference Beamforming* algorithm presented in equation 3.4. The signal fed to the left speaker was used as the

"reference" signal whilst the array maximum response was "steered" over a number of 10000 focal locations equally distributed across the 2 dimensional region shown in the picture. The output of the *Cross-Spectral Reference Beamforming*, centered at 4kHz, clearly identifies the contribution from the weaker source whilst the louder source (i.e. right speaker) radiating within the same frequency band is suppressed.

The same data set was also analyzed using the conventional and Guidati's reference based beamforming algorithms. The output of the conventional beamforming algorithm centered at the 4kHz narrowband frequency is shown in figure 5.12(a). As in the delay-and-sum result presented in figure 5.11(a), only the speaker on the right is identified before the appearance of secondary lobes at approximate 6 - 7dB below that of the main source. As before, the dynamic range of the beamforming output is insufficient to identify the contribution of the weaker source radiating within the same frequency band (i.e. left speaker).

The output of Guidati's reference based beamforming algorithm is presented in figure 5.12(a). As in the previous example, the array response was "steered" over a number of 10000 focal locations whilst the signal fed to the left speaker was used in this case as the "reference" value in equation 3.14. The output of Guidati's reference based beamforming algorithm also identifies the contribution of the weaker source generated by the left speaker whilst the louder source on the right, un-correlated with the reference signal, is ignored.

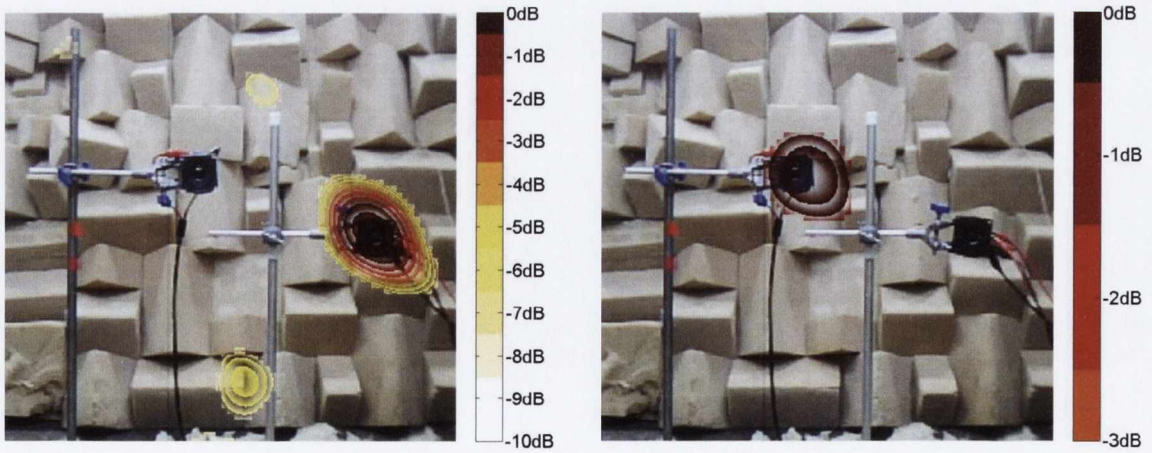

(a) Conventional beamforming output (4000Hz)

(b) Guidati's "reference" based beamforming output (4000Hz)

Figure 5.12: Outputs of the conventional and Guidati's reference based beamforming algorithms.

These results show how reference based beamforming algorithms are an attractive alternative to classical beamforming algorithms when a local measurement of the source or radiating region of interest is attainable.

Chapter 6

Case 1: Rods In Cross Flow

A key objective of this investigation is the application of Laser Doppler Velocimetry (LDV) in combination with the "reference" based beamforming techniques introduced in section 3.2. This chapter presents the experimental results attained from applying this non-intrusive in-flow measurement technique in combination with the aforementioned beamforming techniques in a number of different scenarii. The experimental setups presented here, were designed to highlight the source localization capabilities when these techniques are combined in an flow-acoustic correlation study type. The first section introduces an experimental setup where two uncorrelated sources, generated by two separate set of rods in cross flow, are isolated by the application of the aforementioned beamforming algorithms in combination with LDV (see ref [91]). The second aims to highlight the effects of extended correlation when applying the same methodology to the source generated by a single set of rods in a cross flow configuration.

6.1 Incoherent Sources

6.1.1 Test Setup

The experiments were performed in the subsonic open jet facility at Trinity College Dublin as described in section 4.2. A 0.05m diameter nozzle with a length of 470mm was used for the current tests. The randomized 25 microphone array described in section 4.1.1 along with a webcam located at its center was located below the measurement area as shown in figure 6.1.

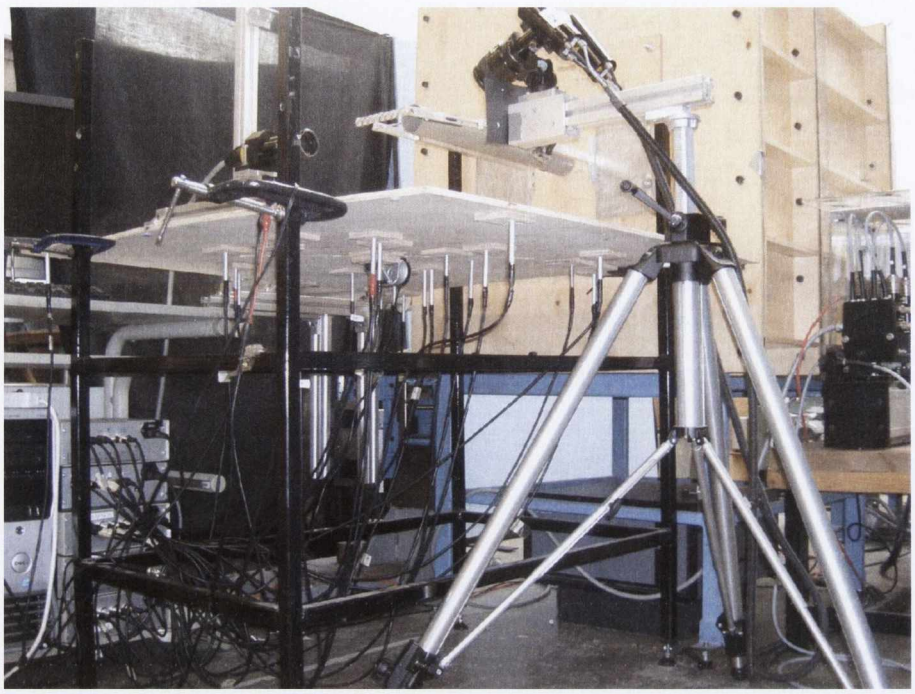

Figure 6.1: Detail of the nozzle, LDV system in forward scatter mode and the planar array with a webcam attached at its center

In the first test set up, two pairs of 4mm threaded rods were located in the wake of the jet stream as shown in figures 6.2 and 6.3. The aim was to generate two uncorrelated noise sources of approximately the same level and with overlapping frequencies. By means of trial and error, it was found that the source generated by the set of rods spanning only a partial section of the cross section of the jet flow had a broader frequency content than that generated by the same set of rods spanning across the full cross section of the jet flow. This characteristic was particularly helpful when trying to generate individual sources with overlapping frequency content. Additionally, in order to minimize possible flow interaction between the vortex street generated by the upstream and downstream set of rods, these were offset along the vertical and horizontal axis by approximately 1cm as detailed in figures 6.2 and 6.5.

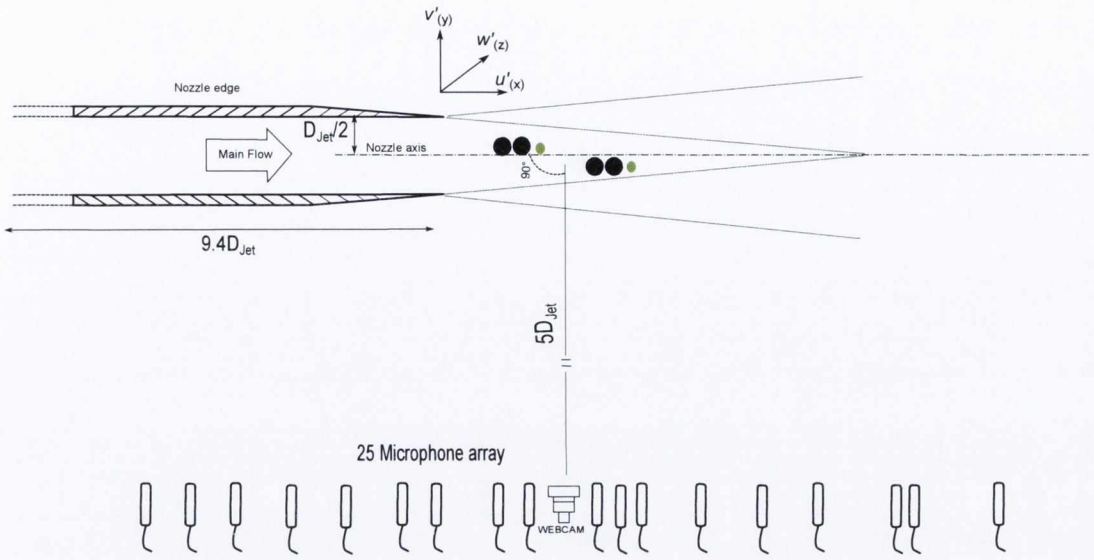

Figure 6.2: Experimental layout (Side view). The black dots represent the location of the 4mm diameter rods in cross flow. The green dots represent the location of the LDV measurements

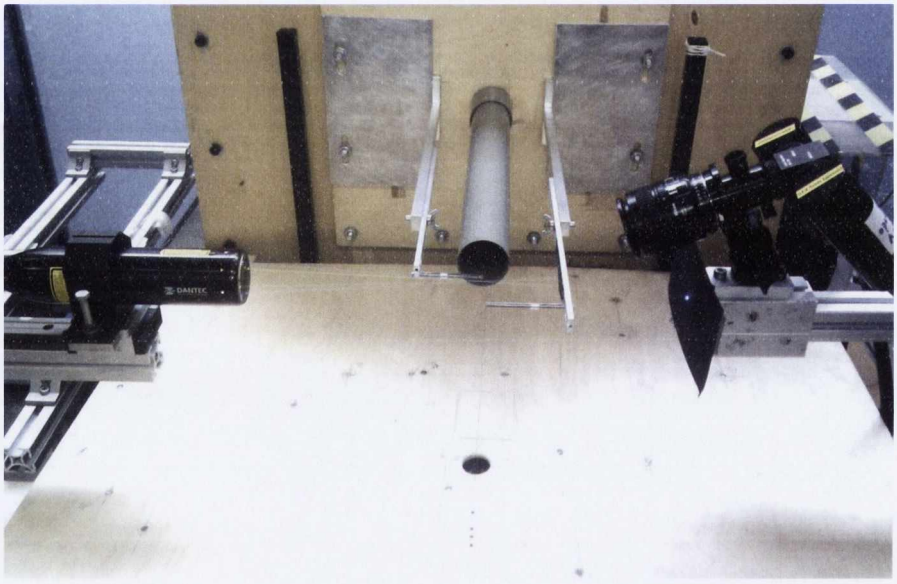

Figure 6.3: Detail of the jet's nozzle, array location and LDV equipment in forward scatter mode.

Each array measurement was acquired at a sampling frequency of 12kHz whilst the LDV mean sample rates varied from approximately 20kHz to 40kHz. In the cases where *Guidati's* reference based beamforming technique was applied, the audio sampling frequency was kept at 12kHz whilst the sample-and-hold resample frequency applied for the LDV data was fixed at 120kHz. However, this audio sampling frequency was found to be

insufficient to resolve the source location whilst applying the *Cross-Spectral Reference Beamforming* technique where the beamforming calculation is performed prior to the cross-spectrum calculation via the delay-and-sum algorithm. As discussed in the previous chapter, best results when applying time domain beamforming algorithms are attained when the sampling frequency is at least 10 times that of the source of interest. For this reason, and taking into account that the audio data was automatically low pass filtered, linear interpolation was used to up-sample the array data prior to the application of the *Cross-Spectral Reference Beamforming* technique. In these occasions, the array data was up-sampled at 48kHz whilst the LDV sample-and-hold re-sampling frequency was fixed at 480kHz. This increase in the LDV up-sampling frequency would introduce sharp discontinuities in the time series when compared to those up-sampled at a lower rate. This would translate in increased step noise in the spectrum of the LDV output. However as shown in equations 2.56 & 2.57 the effect of introducing uncorrelated step noise in the cross-spectrum calculation can be considered negligible. On the other hand, up-sampling allowed for the application of *Cross-Spectral Reference Beamforming* without the need for an extra set of experimental measurements carried out at a higher sampling frequency. The frequency resolution for both algorithms, was fixed at $\approx$ 23Hz by selecting the corresponding window lengths for the fourier transforms. These were of 512 (audio) and 5120 (LDV) data points for *Guidati's* reference based beamforming technique and 2048 (audio) and 20480 (LDV) data points for the *Cross-Spectral Reference Beamforming* method.

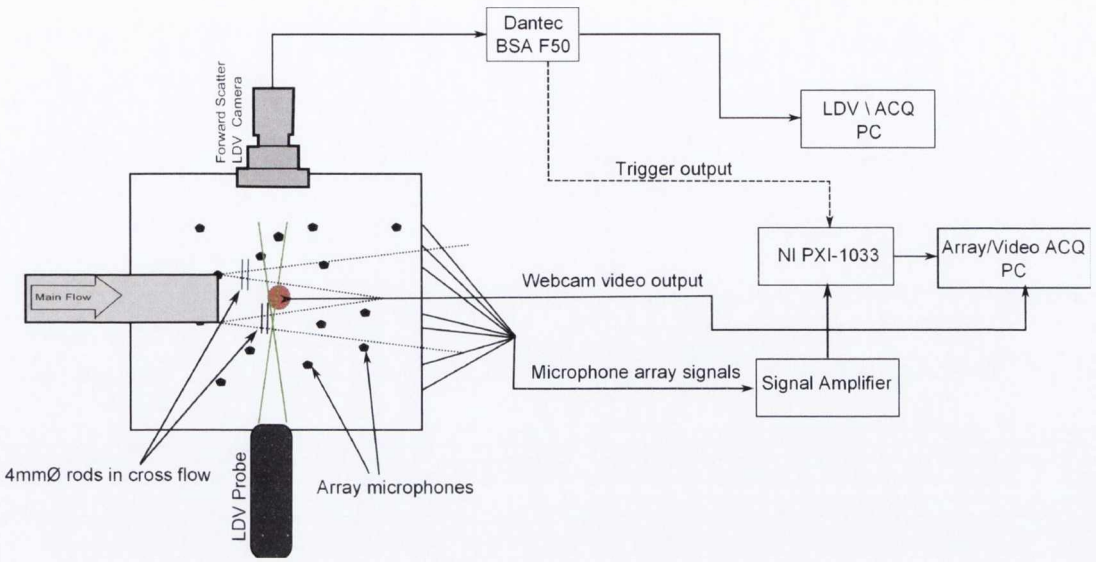

Figure 6.4: Schematic representation of the experimental set up (Plan view) and box representation of the measurement equipment.

The first experimental test comprised of two main parts, for which the velocity of the jet was kept constant at approximately 87m/s. The first section of the test focused the LDV volume on the vortex wake created by the set of rods in close proximity to the nozzle exit as shown in figure 6.5(a). Simultaneously, the microphone array located below the test piece, at a distance of 0.25m, measured the sound field. The second part of the test, was a repetition of the first set of tests, the only variation being that the LDV volume was located in the wake created by the second set of rods further downstream of the nozzle exit as shown in figure 6.5(b).

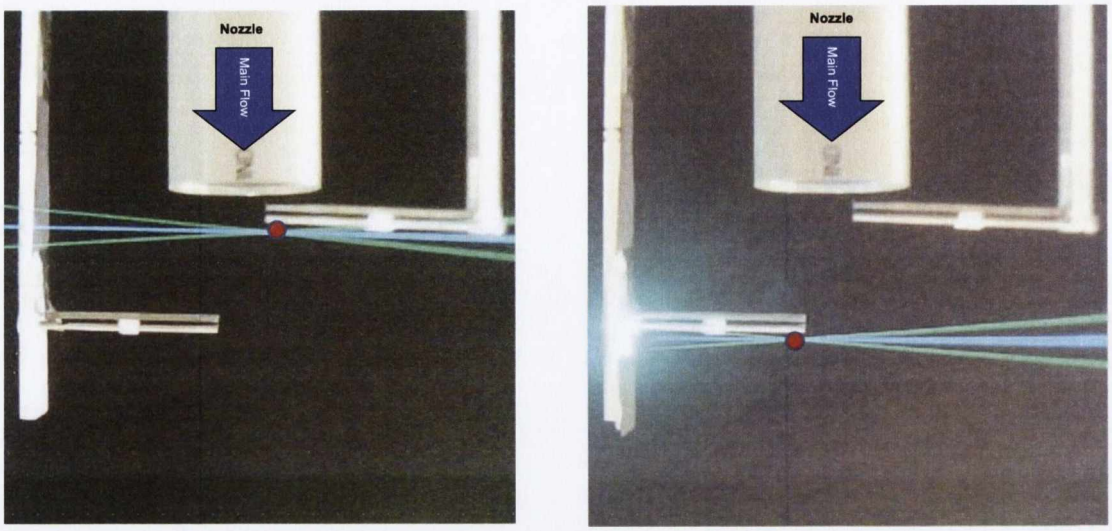

(a) Upstream (b) Downstream

Figure 6.5: Test setups. The red dot indicates the location of the LDV measurement volume for each test

6.1.2 Tonal Characteristics of the Experimental Rig

The frequency characteristics of the sound generated by placing both sets of rods within the jet's flow are shown in figure 6.6. Figure 6.6(a) shows the background noise characteristics of the jet, as measured by a single array microphone, in free flow conditions (no rods) whilst figure 6.6(b) presents the same result when the sets of rods depicted in figure 6.5 are in the flow. Whilst there are clear similarities in the region below 2kHz, the acoustic energy measured between 3 to 5.5kHz and peaking at around 3.8kHz can be attributed to the addition of the sets of rods within the flow.

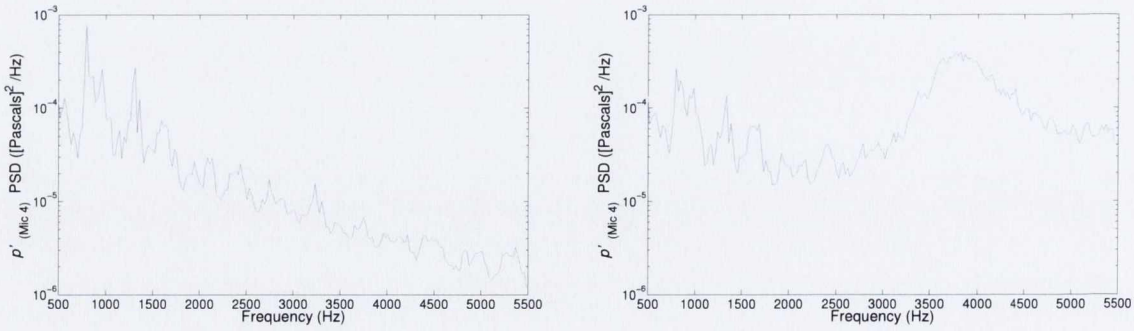

(a) No rods in the flow (b) With rods in place

Figure 6.6: Single microphone autospectrum with and without the set of rods

6.1.3 Test Result at the Upstream Location

Prior to the application of the "reference" based beamforming algorithms, the microphone array data was analyzed using standard beamforming techniques. The outputs from both, the conventional and delay-and-sum algorithms are presented in figure 6.7 [1].
The conventional beamforming output centered at the 3.8kHz narrowband, clearly identifies the rod locations as the dominant sources of sound. Similarly, the output from the delay-and-sum algorithm for the 2-5.5kHz frequency band [2] shown in figure 6.7(b) clearly identifies the rod locations as the main contributors to sound radiation.

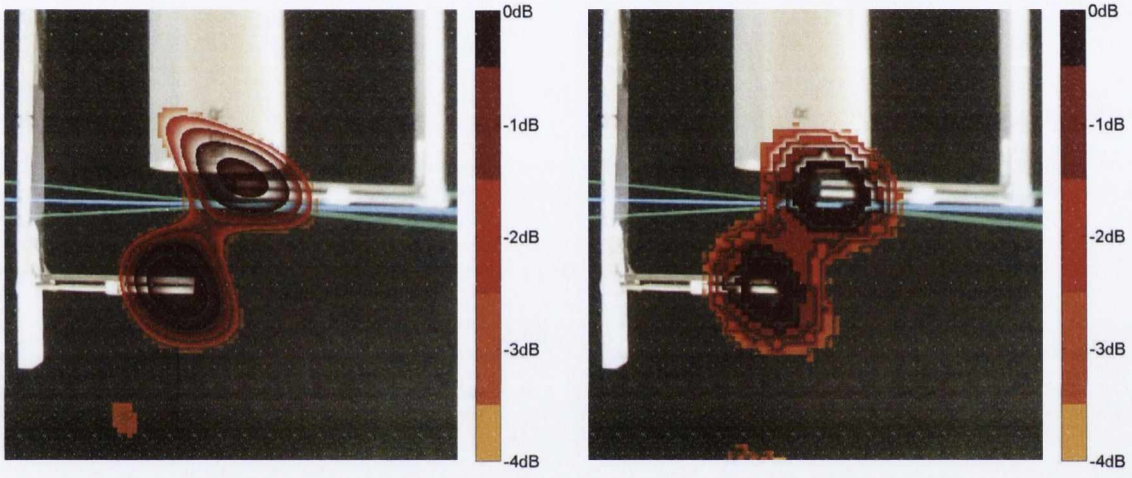

(a) Conventional beamforming output at 3.8kHz

(b) Delay-and-sum beamforming output for the 2.5-5.5kHz frequency band

Figure 6.7: Conventional and delay-and-sum beamforming outputs.

As discussed in section 2.4.1.3 the step noise and filter corrected LDV spectrum can estimate the true fluctuating velocity spectrum up to frequencies of $\approx f_m/2$, where f_m is the LDV's mean sample rate. Based on the minimum acquired f_m value of $\approx$ 20kHz the true spectrum of the LDV signal can be estimated up to a frequency of $\approx$ 10kHz. This cut off value is well above the frequency range of interest for the tests shown here. The step noise and filter corrected auto-spectrums of the fluctuating velocities in the axial (u') & vertical (v') directions (see figure 6.2) measured by the LDV at the upstream location

[1] It should be clarified that, even though the LDV measurement volume can be seen in both test images presented in figure 6.7, the beamforming outputs are the produce of the analysis of the microphone data only via the conventional and delay-and-sum algorithms.

[2] The bandpass filter used here, a phaseless 4^{th} order Butterworth between the 2.5-5.5kHz frequency band, was chosen for the delay-and-sum beamforming calculations as most of the acoustic energy generated by the sets of rods was concentrated within its bounds (see figure 6.6(b)).

are shown in figure 6.8. Whilst it is more obvious in the v' case, both auto-spectrums show a narrow peak of energy at around 3.8kHz.

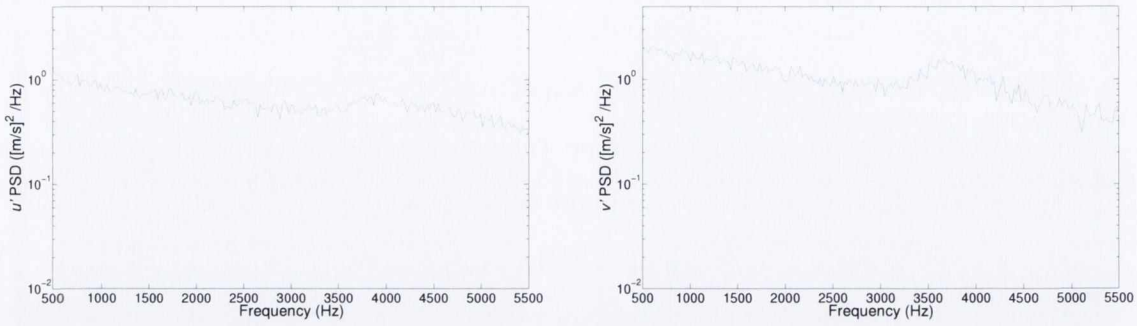

(a) Velocity autospectrum $G_{u'u'}$ (b) Velocity autospectrum $G_{v'v'}$

Figure 6.8: LDV's u' & v' auto-spectrums measured at the upstream location.

Figures 6.9(a) & 6.9(b) present the low pass filtered corrected cross-spectrum calculated using the procedure introduced in section 2.4.1.4 between the LDV fluctuating velocity components, u' & v', and the acoustic fluctuating pressure measured by a single microphone located at the center of the array. As in the previous two examples, the cross-spectrum results between the acoustic pressure and the LDV measured flow components u' & v' peaks at approximately 3.8kHz. It is obvious from these results that a clear relation exists between the acoustic pressure measured at the array location and the flow perturbations measured by the LDV probe.

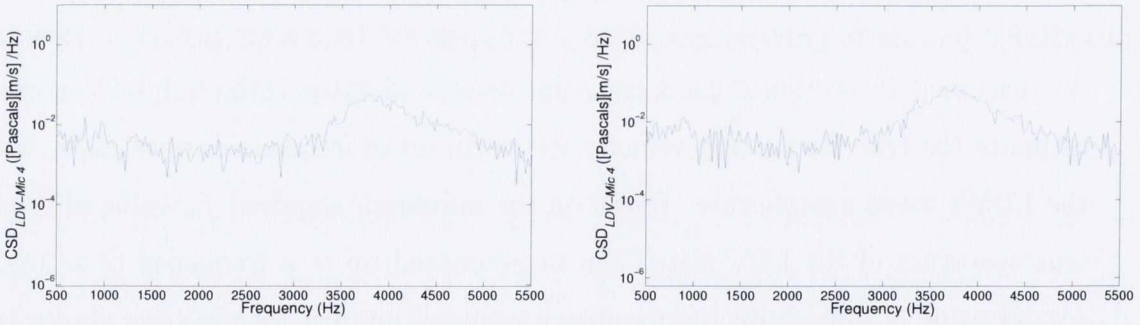

(a) Cross-spectrum between the LDV (u') signal and Mic No.4 (b) Cross-spectrum between the LDV (v') signal and Mic No.4

Figure 6.9: Cross-spectrum between a single microphone at the center of the array (Mic No.4) and u' & v' velocity fluctuating components measured at the upstream location.

Prior to the application of Guidati's reference based beamforming technique, the array and LDV signals were preconditioned as described in 3.2.1. The truncated, Fourier trans-

formed, preconditioned signals were then used to form the entries in the Cross Spectrum Matrix described in equation 3.15. *Guidati's* reference based beamforming technique was then used to evaluate the correlation between the in-flow measured signals and the array response focused over a number of 4900 focal locations equally distributed across the 2 dimensional region shown in figure 6.5. The output of *Guidati's* reference based algorithm is shown in figure 6.10. In both cases where the LDV measured u' & v' signals were used as "reference", the source generated by the upstream set of rods is identified whilst the source generated downstream is suppressed. These results clearly show how solely the source generated by the upstream set of rods is well correlated with both of the flow fluctuating quantities measured by the LDV. It is interesting to note that even though the LDV measurement location is located at a short distance downstream of the set of rods the main source is identified slightly further upstream at the rods location.

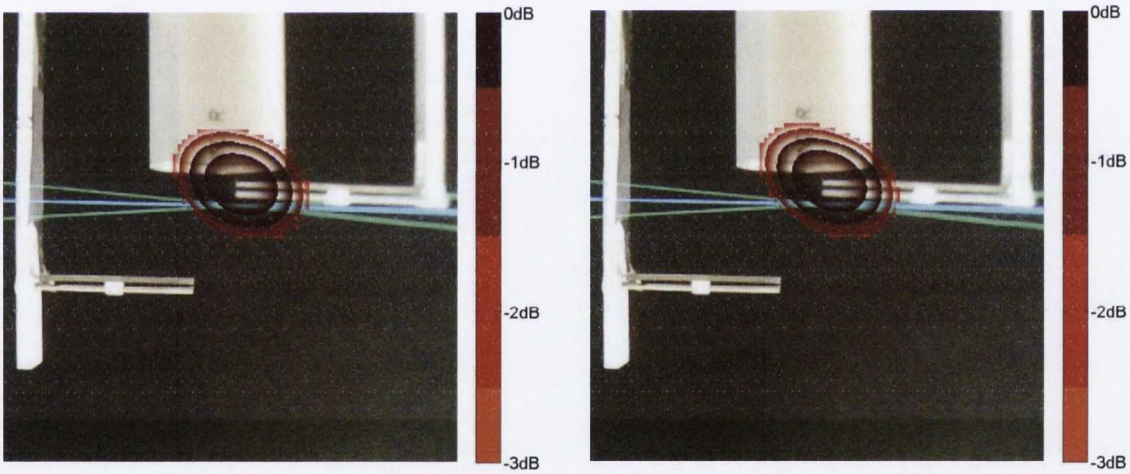

(a) u' velocity component used as "reference" (b) v' velocity component used as "reference"

Figure 6.10: Output of Guidati's reference based beamforming focused at the 3800Hz narrowband frequency.

Figure 6.11 shows the result attain whilst using the preconditioned LDV output as the "reference" value in the *Cross-spectral Reference Beamforming* algorithm (see section 3.2.2). The steered array output, centered at the 3800Hz narrowband frequency, identifies once again the contribution of the upstream source whilst the source downstream is suppressed. Similarly, the main radiation location is identified at the rods location upstream of the LDV measurement volume.

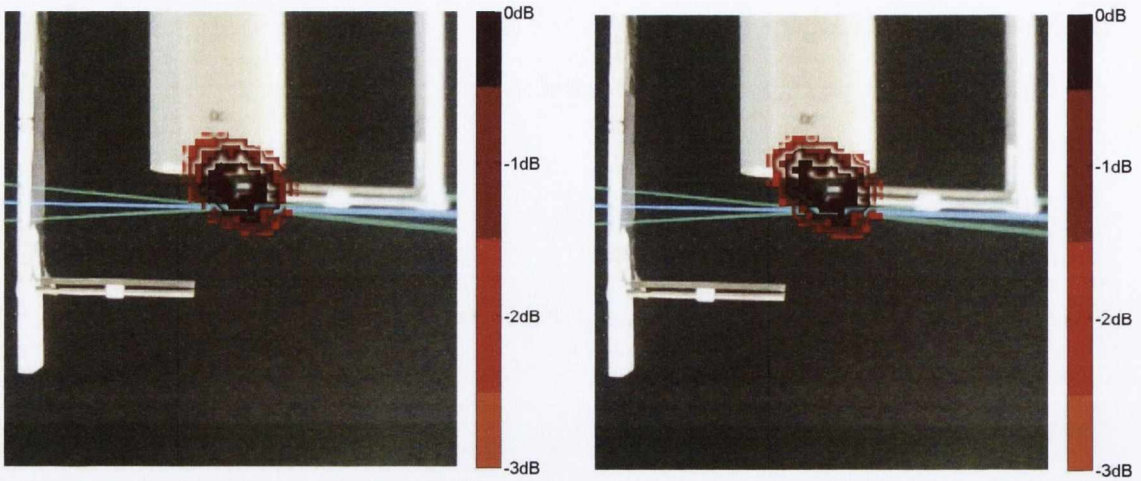

(a) u' velocity component used as "reference" (b) v' velocity component used as "reference"

Figure 6.11: Output of the *Cross-spectral Reference Beamforming* focused at the 3800Hz narrowband frequency.

6.1.4 Test Result at the Downstream Location

The synchronized LDV and array measurements were repeated this time with the LDV measurement volume located in the wake of the set of rods downstream as shown in figure 6.5(b). As in the upstream case, the output of standard beamforming algorithms shown in figure 6.12 [3] identify two dominant sources coinciding with the location of the upstream and downstream sets of rods. Similarly, the step noise and filter corrected auto-spectrums presented in figure 6.13 show a narrow band of energy centered at a frequency of $\approx$ 3.8kHz, confirming that both, up and downstream sets of rods, generate flow fluctuations within the same narrow frequency band.

[3] As in the previous example it should be clarified that, even though the LDV measurement volume can be seen in both test images presented in figure 6.12, the beamforming outputs are the produce of the analysis of the microphone data only via the conventional and delay-and-sum algorithms.

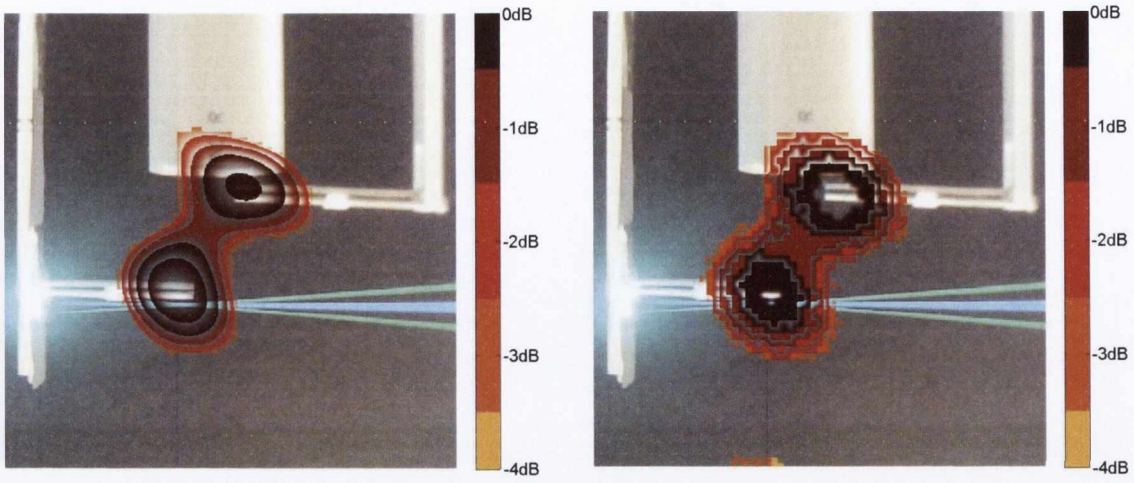

(a) Conventional beamforming output at 3.8kHz (b) Delay-and-sum beamforming output for the 2.5-5.5kHz frequency band

Figure 6.12: Conventional and delay-and-sum beamforming outputs.

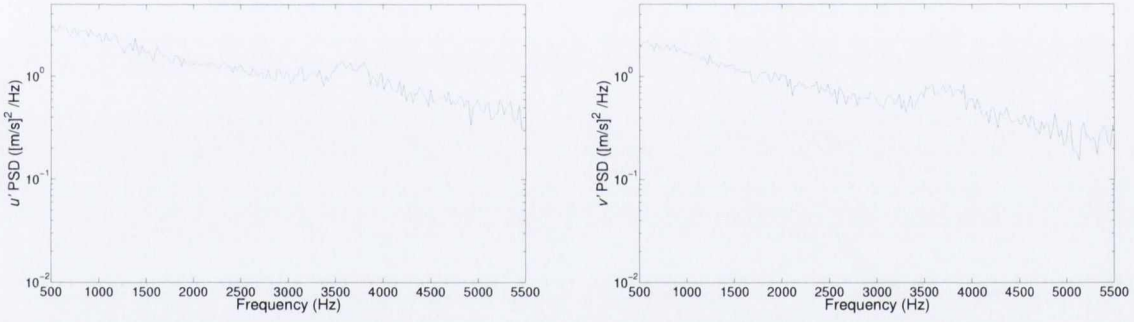

(a) Velocity autospectrum $G_{u'u'}$ (b) Velocity autospectrum $G_{v'v'}$

Figure 6.13: LDV's u' & v' auto-spectrums measured at the downstream location

The low pass filtered corrected cross-spectrum between the LDV measured fluctuations u' and v' and the output of a single microphone placed at the center of the array is presented in figures 6.14(a) and 6.14(b). As expected, both estimated cross-spectra peak at approximately 3.8kHz. These results again confirm the correlation between the flow perturbations measured at the downstream location and the pressure fluctuations at the microphone array location.

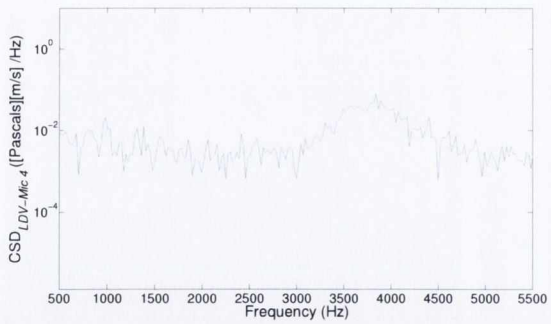

(a) Cross-spectrum between the LDV (u) signal and Mic No.4

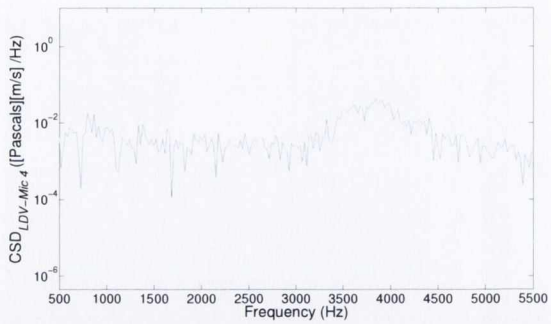

(b) Cross-spectrum between the LDV (v) signal and Mic No.4

Figure 6.14: Cross-spectrum between microphone No.4 and u' and v' velocity fluctuation components measured at the downstream location.

The outputs of the "reference" based beamforming algorithms for the downstream location are presented in figures 6.15 and 6.16. In this instance the LDV signal u' and v' acquired in the wake of the downstream set of rods was used as "reference". It is clear how in this occasion the upstream source is suppressed whilst the dominant source is localized at the center of the set of rods downstream. As in the upstream case, even though the LDV signal is acquired at a short distance downstream of the set of cylinders, both algorithms identify the rods location as the dominant radiating correlated region.

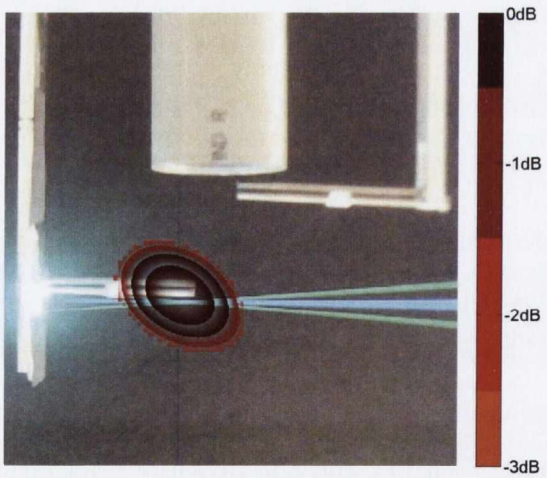

(a) u' velocity component used as "reference"

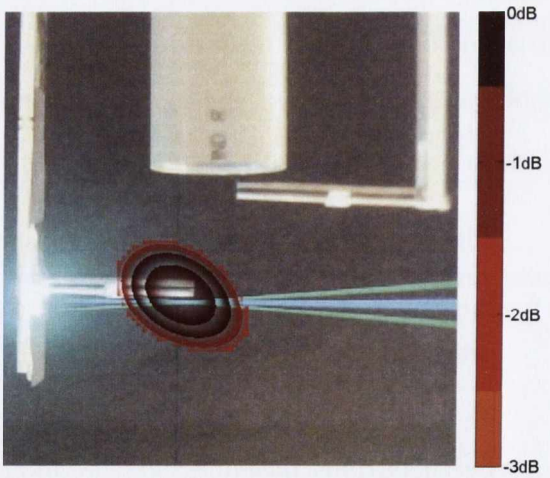

(b) v' velocity component used as "reference"

Figure 6.15: Output of Guidati's reference based beamforming focused at 3.8kHz.

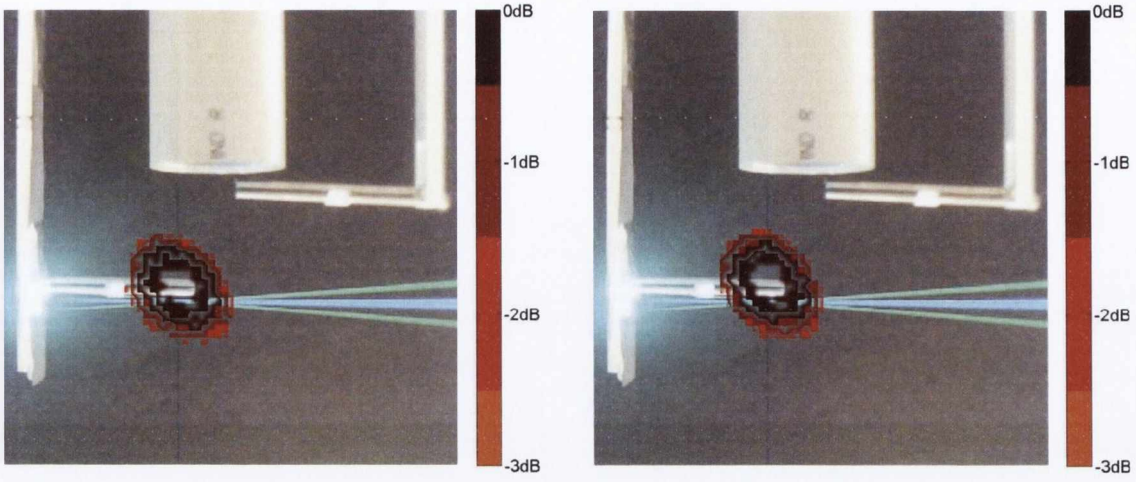

(a) u' velocity component used as "reference" (b) v' velocity component used as "reference"

Figure 6.16: Output of the *Cross-spectral Reference Beamforming* focused at 3.8kHz.

It is clear from these results that both of the aforementioned "reference" based beamforming algorithms (i.e. *Guidati's & Cross-spectral Reference Beamforming*) can be used in conjunction with an LDV flow measurement to identify radiating source regions that are correlated with the measured flow fluctuations. However, it is clear that maximum correlation between the beamformed signals and the in-flow measurement do not coincide with the exact location of the LDV's measurement volume. The following section presents a separate set of tests designed to further investigate this discrepancy.

6.2 Single Source & Correlated Vortex Street

6.2.1 Experimental Layout

As it has been shown in previous sections, "reference" based beamforming algorithms can be used to construct a "map" of the source/s that are coherent to the signal used as "reference". However, as seen in the previous examples where an LDV signal was used as "reference", maximum correlation did not coincide with the exact location of the LDV's measurement volume. This discrepancy can be due to a number of factors. In the first place, the measured flow perturbation may not be responsible for sound radiation. On the other hand, this measured non-radiating perturbation may be well correlated to a noise generating mechanism at a separate location (e.g. source upstream). Similarly, in the case where the measured perturbation is a radiating source, its localization by the

"reference" based beamforming algorithm is conditioned by 1- the dynamic range of the beamforming array, 2- the presence of correlated sources of higher amplitude 3- the source directivity.

An experimental approach was designed to exemplify these scenarii. A single set of threaded 4mm diameter rods spanning the entire width of the jet flow were located above the center of the microphone array in a cross flow configuration as shown in figures 6.17 & 6.18. The set up was chosen so as to generate an extended correlated vortex street with a clearly dominant radiating region at the rods location. For all measurements, the exit velocity of the jet was fixed at ≈ 87m/s. The in-flow "reference" measurements were acquired at three separate locations in the vortex wake created by the rods in cross flow as detailed in figures 6.17 and 6.18.

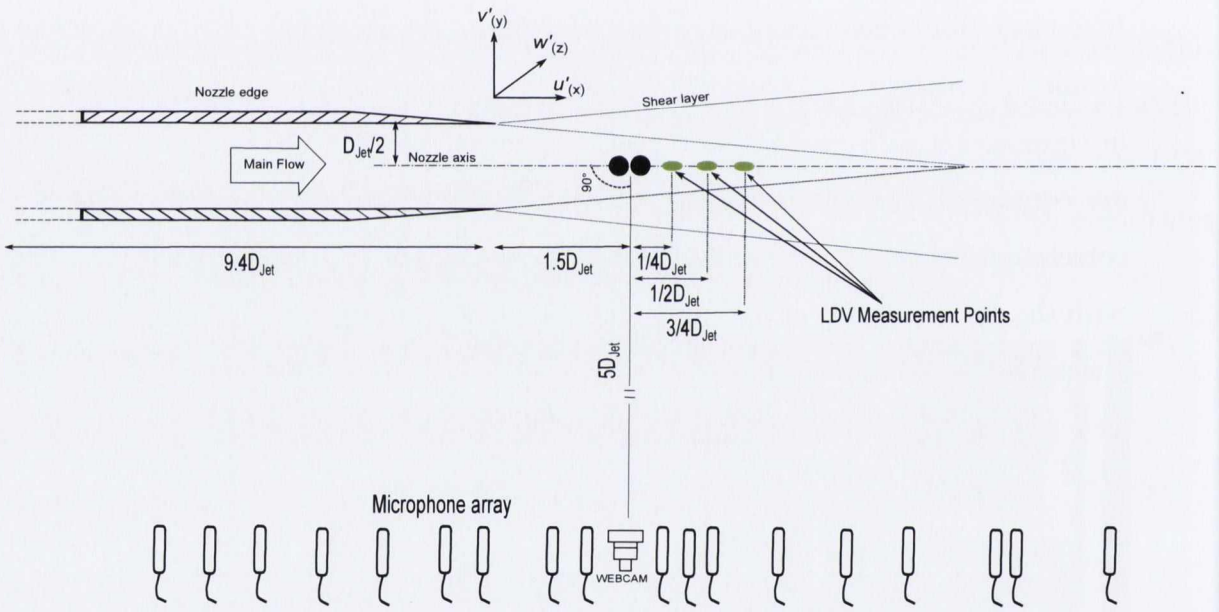

Figure 6.17: Experimental layout (Side view). The black dots represent the location of the 4mm diameter threaded rods in cross flow. The green dots represent the location of the LDV measurements

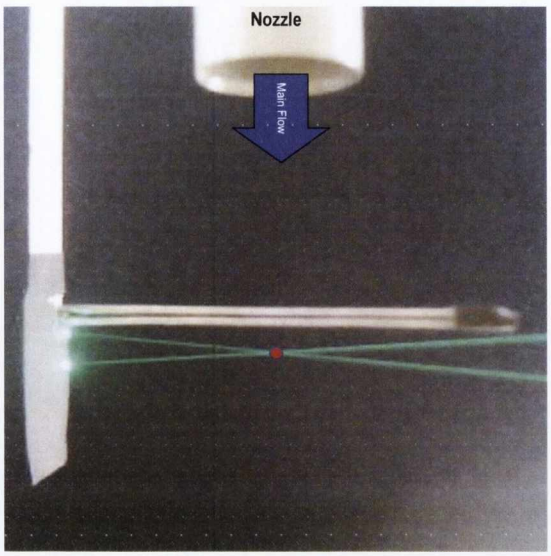

(a) LDV's measurement volume at location No.1

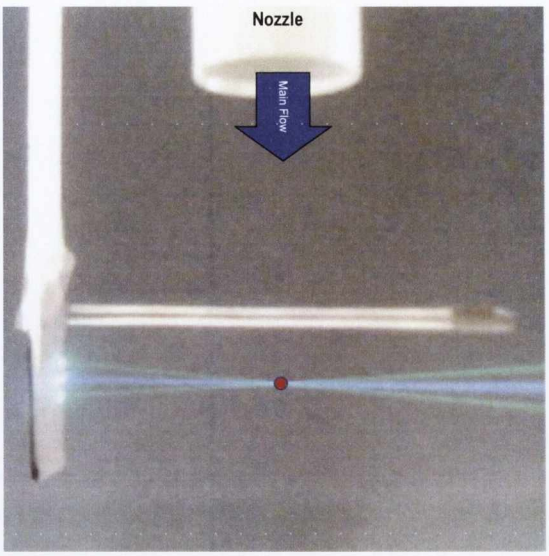

(b) LDV's measurement volume at location No.2

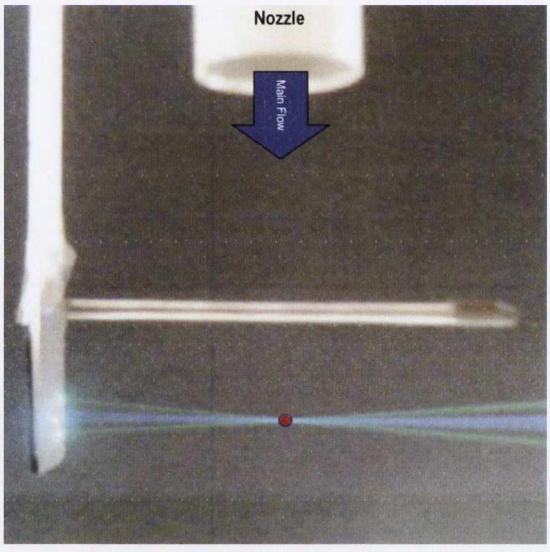

(c) LDV's measurement volume at location No.3

Figure 6.18: Camera view of the test setups. The red dot indicates the locations of the LDV's measurement volume at each separate test.

Synchronized measurements between the LDV and the microphone array were acquired at each of the three locations depicted in 6.18. As in the previous example, 10 seconds of audio data were acquired at a frequency of 12kHz whilst the LDV mean sample rates varied from approximately 20kHz to 40kHz. As the audio data was automatically low pass filtered, linear interpolation was used to up-sample the array data previous to the application of the *Cross-spectral Reference Beamforming* algorithm. The array data was up-sampled at 48kHz whilst the LDV sample-and-hold re-sampling frequency was fixed

at 480kHz. The frequency resolution was fixed at $\approx$ 23Hz by using window blocks of 2048 (audio) and 20480 (LDV) data points for the Fourier transforms in each case. In this occasion, only results attained via the *Cross-spectral Reference Beamforming* algorithm in combination with the LDV velocity fluctuations measured along the axial direction u' will be shown for brevity.

6.2.2 Experimental Results

6.2.2.1 Source characteristics

The step noise and filter corrected auto-spectra calculated at each of the LDV measurement locations are presented in figure 6.19(a). At each of the three locations a clear narrowband energy peak is observed at approximately 4.4kHz. The frequency characteristics of the fluctuations measured at the wake created by the 4mm rods spanning the full section of the jet flow can be contrasted to those measured in the previous section where sets of rods of equal characteristics (i.e. diameter) spanned only a section of the jet flow. A higher and narrower frequency band concentrates most of the fluctuating energy in the present case in contrast to the lower frequency broader peak seen in the u' auto-spectra shown in figures 6.8(a) & 6.13(a). Whilst the reasons for this behavior were not sought, it was noticed that the frequency characteristics of the source created by a set of rods spanning the full length of the jet flow where clearly tonal and of higher frequency than those created by the rods spanning only a section of the flow. This is also evident in the cross-spectrum results calculated between the measured u' flow perturbations and the acoustic pressure measured by a single microphone at the center of the array (see figure 6.19(b)). A clear narrowband of energy peaks at the same frequency of $\approx$ 4.4kHz confirming the relation between the in-flow and acoustic measurements. Interesting to notice that the auto-spectrum of the fluctuating component u' value peaks at measurement location No.2. Even though not demonstrated here, it is possible that small variations in the alignment of the LDV measurement volume with respect to the rods horizontal plane had more influence over the magnitude of the spectrum peak than its relative downstream location along the axial direction. The "shade" effect created by the rods directly upstream of the LDV measurement volume at position 1 (see 6.18(a)) could be the reason behind the smaller u' auto-spectrum peak measured at this location.

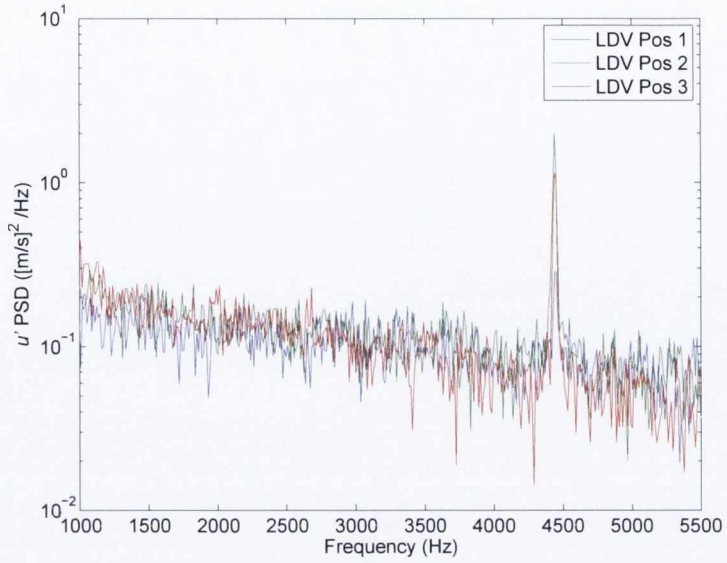

(a) u' auto-spectrum at positions 1,2 & 3

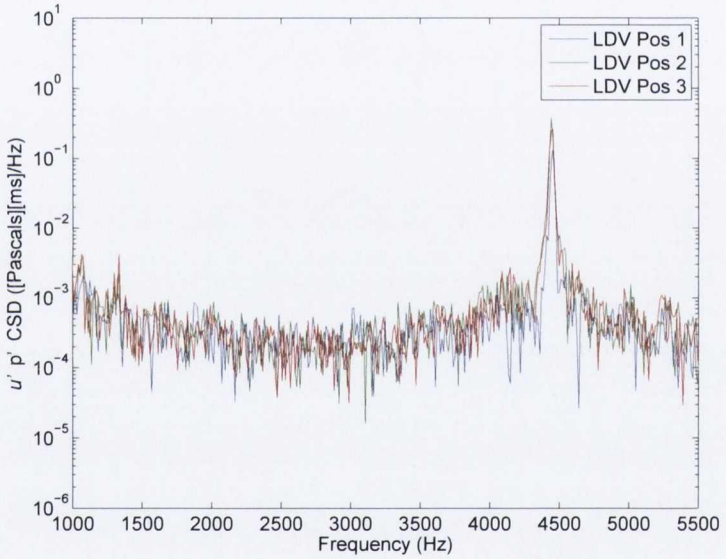

(b) Cross-spectrum between u' at positions 1,2 & 3 and p' recorded by a single microphone at the array's center (Mic 4)

Figure 6.19: LDV u' auto-spectra and cross-spectra between the LDV axial component u' and the output of a single array microphone p' calculated at each of the three flow measurement locations.

The microphone array data recorded for each test was first analysed using the standard delay-and-sum beamforming algorithm. As in the previous section, each microphone channel was band passed between 2.5-5.5kHz using phaseless 4th order Butterworth filters prior to the application of the delay-and-sum algorithm. The beamforming outputs for each test location are shown in figure 6.20.

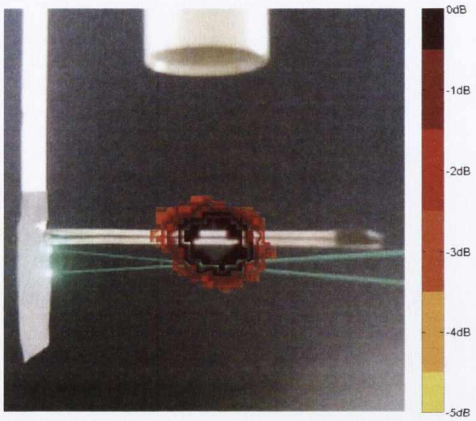

(a) Delay-and-sum beamforming output for the 2.5-5.5kHz frequency band, Measurement 1

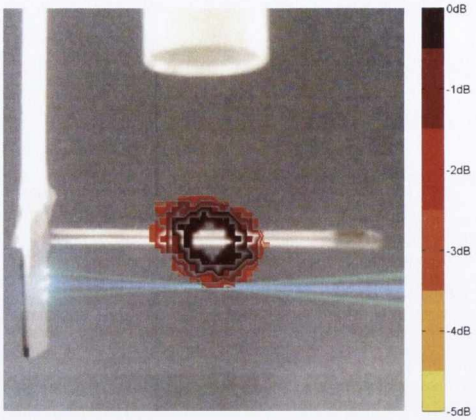

(b) Delay-and-sum beamforming output for the 2.5-5.5kHz frequency band, Measurement 2

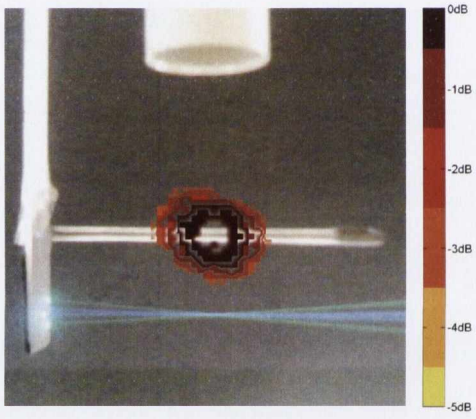

(c) Delay-and-sum beamforming output for the 2.5-5.5kHz frequency band, Measurement 3

Figure 6.20: Figure (a),(b) and (c), correspond solely to the output of the delay-and-sum beamforming array data acquired at each of the three separate tests carried out. Even though the LDV measurement volume can be observed at separate locations in each figure, its output was not used in the beamforming calculation presented here.

As expected, in all three measurements, the output of the delay-and-sum algorithm identifies the rods location as the dominant source within the scanned region.

6.2.2.2 Output of the *Cross-spectral Reference Beamforming* Algorithm.

The steered array data was then combined with the axial velocity component u' measured by the LDV at each of the three measurement locations via the *Cross-spectral Reference Beamforming* technique described in section 3.2.2. In each test the array response was steered over a grid of 4900 focal locations equally spaced over the 2 dimensional field of

view shown in figure 6.18. The output of equation 3.17 as a function of focal location focused at the 4.4kHz narrowband is presented superimposed over the pictures of the test area in figure 6.21

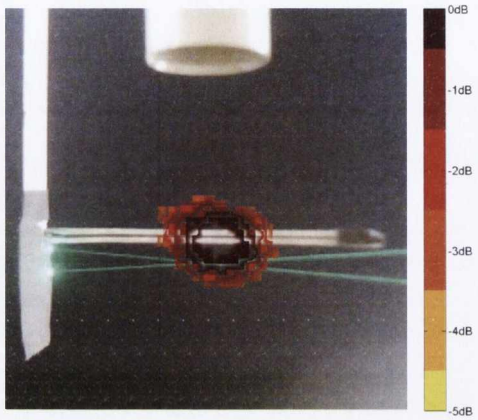

(a) Output of the *Cross-spectral Reference Beamforming* at 4.4kHz, LDV at **position 1**

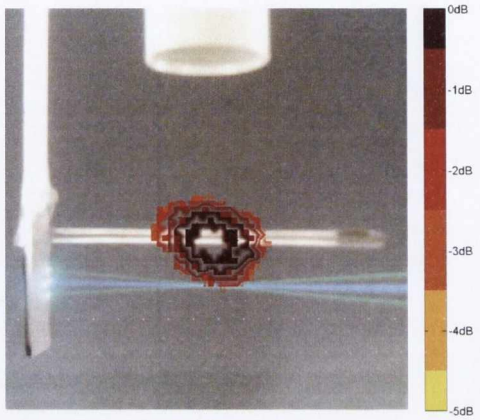

(b) Output of the *Cross-spectral Reference Beamforming* at 4.4kHz, LDV at **position 2**

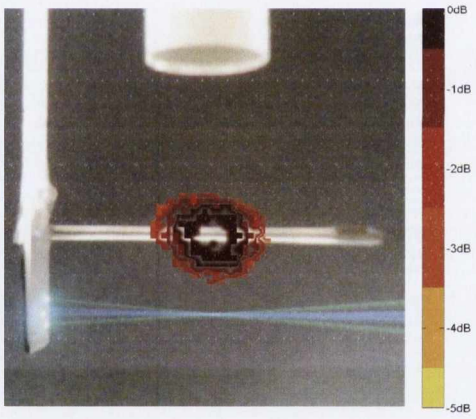

(c) Output of the *Cross-spectral Reference Beamforming* at 4.4kHz, LDV at **position 3**

Figure 6.21: Outputs of the *Cross-spectral Reference Beamforming* at 4.4kHz calculated for each test.

It is clear that, independently of the positioning of the LDV measurement volume used as "reference", the maximum output of the *Cross-spectral Reference Beamforming* identifies the rods location as the dominant source within the scanned region. This is a good example of how "reference" based beamforming techniques can be used in combination with an LDV signal in order to identify the origin of radiating regions that are correlated to that of the "reference" value.

A similar analysis was carried out by applying the *Cross-Correlation Reference Beamforming* technique described in equation 3.7. The delay-and-summed array signal focused at a number of pre-determined focal locations was cross-correlated with the raw, sample-and-hold reconstructed LDV output measured at each of the downstream locations shown in figure 6.22. In this occasion the array response was focused over 300 separate focal locations along the axial direction as detailed in figures 6.22(a),6.22(b) and 6.22(c).

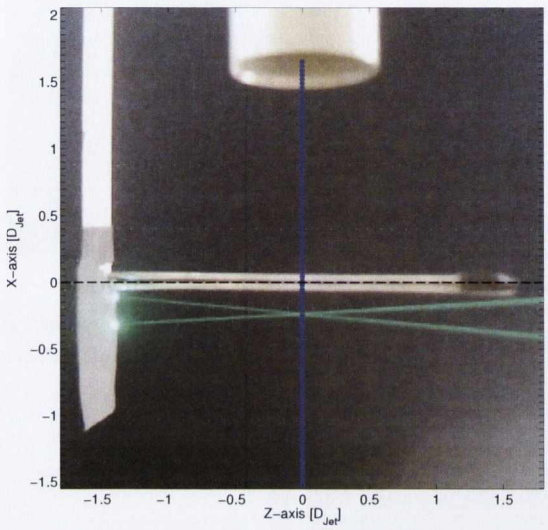

(a) Detail of LDV measurement volume at **position 1** and array focal locations in blue (*).

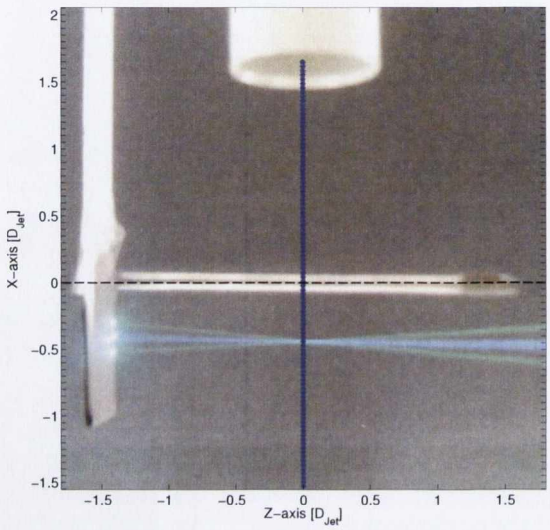

(b) Detail of LDV measurement volume at **position 2** and array focal locations in blue (*).

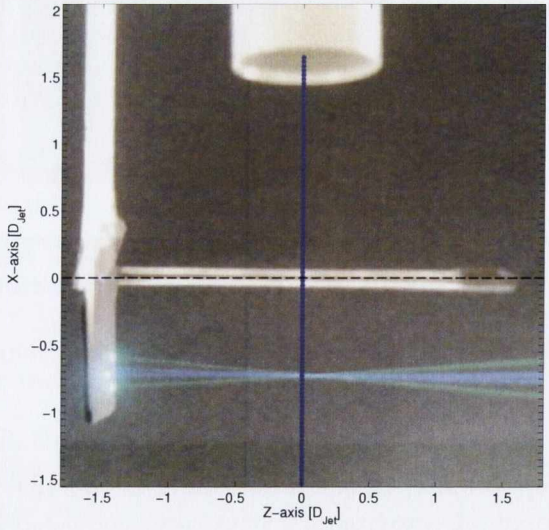

(c) Detail of LDV measurement volume at **position 3** and array focal locations in blue (*).

Figure 6.22: View from the center of the array of the three test setups. The origin of the x-axis represented by the bold dashed line(−)was assigned to the approximate location of the center of the set of tandem rods.

Figure 6.23 presents the time domain cross-correlations peak values attained between the "reference" LDV signal at position 1 and the output of the array "steered" at each of the focal locations depicted along the axial direction in figure 6.22(a). The black and green dotted vertical lines represent the position of the center of the rods and the LDV measurement volume along the x-axis respectively. The noise floor level was calculated by extracting the peak cross-correlation values between two independently random generated data series with the same number of points, mean and standard deviation as that of the LDV and beamformed array signals at each focal location.

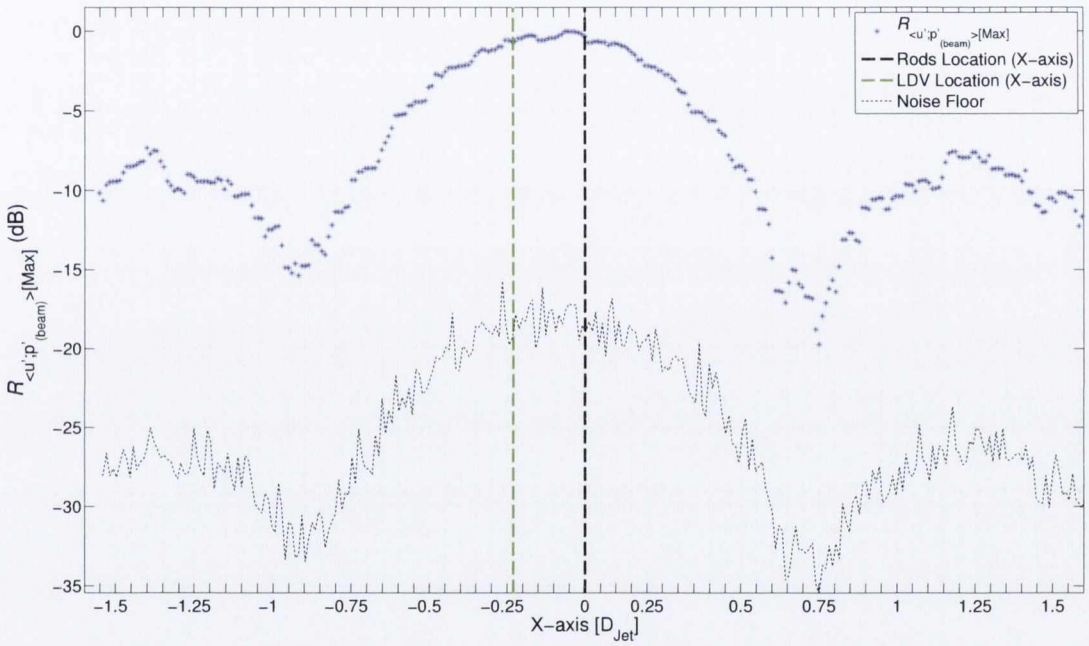

Figure 6.23: Maximum values of the time domain cross-correlation between the steered array signal at each focal point depicted by * (blue) and the velocity fluctuating component u' measured at the LDV position 1. The red and blue dotted vertical lines represent the position of the center of the rods and the LDV measurement volume along the x-axis respectively.

The maximum correlation value is obtained further upstream from the LDV measurement volume in close proximity to the location of the rods center represented by the red dotted line. Two secondary peaks at ≈7dB below that of the maximum value can be observed at 1.25 and -1.4D_{Jet} along x-axis. Recalling the sidelobe level rejection values presented in figure 4.3 of ≈7dB it is reasonable to assume that these secondary peaks are the produce

of cross-correlation between the "reference" signal and sidelobes of the dominant source [4]. In other words, correlation peaks below these level can not be attributed to the presence of secondary sources correlated to the "reference" signal.

A similar result is observed when the LDV signal is attained further downstream at positions 2 & 3. Figures 6.24 and 6.25 show how the cross-correlation maxima is again identified at the location of the set of rods even though the LDV measurement is attained even further downstream. As before, second maxima can not be attributed to the presence of secondary coherent sources as they appear below the sidelobe level rejection threshold of $\approx$ -7dB.

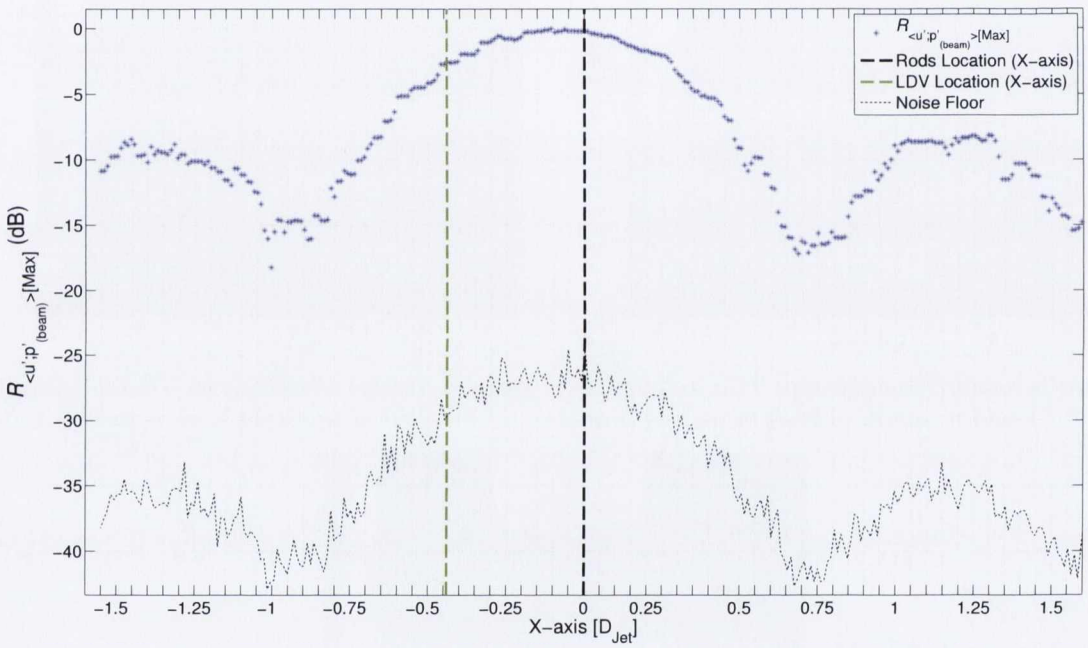

Figure 6.24: Maximum values of the time domain cross-correlation between the steered array signal at each focal point depicted by * (blue) and the velocity fluctuating component u' measured at the LDV position 2. The red and blue dotted vertical lines represent the position of the center of the rods and the LDV measurement volume along the x-axis respectively.

[4]This refers to "steered" array focal locations where sources arriving from a third location are summed somewhat constructively but still to a lesser extent than those arriving from the main focal location.

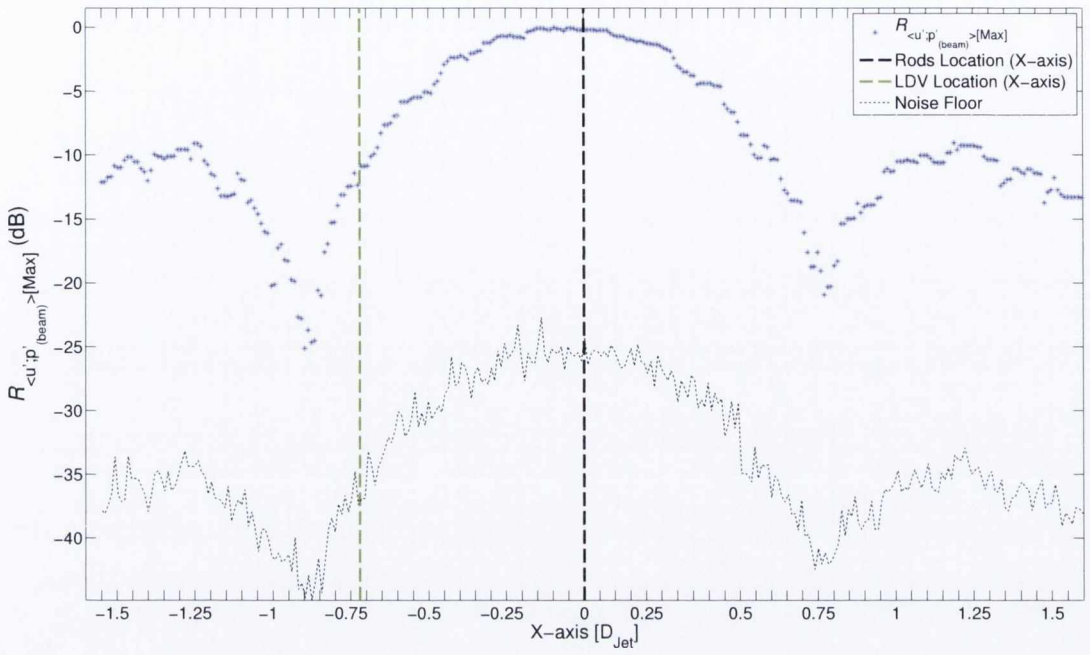

Figure 6.25: Maximum values of the time domain cross-correlation between the steered array signal at each focal point depicted by * (blue) and the velocity fluctuating component u' measured at the LDV position 3. The red and blue dotted vertical lines represent the position of the center of the rods and the LDV measurement volume along the x-axis respectively.

The cross-spectra shown in figure 6.19(b), identified a clear correlation between the u' velocity fluctuations measured in the wake generated by the set of rods and the acoustic pressure measured at the array location. However, the "reference" based beamformed results proved that high correlation levels between flow and acoustic signals do not constitute proof of noise emission by the measured perturbation. Whilst the measured flow perturbations were clearly correlated to the noise producing mechanisms, the output of the "reference" based beamforming algorithms identified the source at a separate location. In other words, "reference" based beamforming methods show the spatial location/s of the causal effects if these are directly correlated to the signal used as "reference". This explains why, even though the LDV measurements were obtained at a distance downstream of the set of rods, the main source location is still identified towards the center of the set of rods.

Chapter 7

Case 2: Free Flow Configuration

This chapter presents an experimental setup where the broad angle sound radiation from a Mach 0.25 jet is sampled by an array of receivers while simultaneously, TR-PIV is used to measure the axial and vertical velocity fluctuations, u' & v', along the lip and centerline of the jet axis (see also ref. [92]). The different variations of the delay-and-sum based "reference" beamforming algorithm presented in section 3.1.1 were the chosen signal processing techniques used to analyse the data throughout this chapter. Based on the type of source under study, a number of factors made these the preferred techniques for the task in hand. The first, was the inherent broadband capabilities of the time domain based beamforming algorithms. The second was the readily available format of the beamformed signal which allows the direct application of frequency and time domain standard signal processing techniques to the beamformed output.

The remaining parts of this chapter are organised as follows. Section 1 presents detailed information about the experimental rig and test layout. Sections 2 and 3 introduce independently, 1- the flow turbulence characteristics as measured by the TR-PIV system and 2- the jet acoustic signature as measured by the microphone array. Section 4 compares the results obtained by cross-correlating the flow velocity fluctuations measured by TR-PIV to the far field acoustic pressure measured by 1 - the array output focused at the TR-PIV measurement volume 2 - a single array microphone. The final section present a summary of the findings and conclusions drawn from the experimental results.

7.1 Test Design

7.1.1 Rig and Experimental Layout

The experimental setup is shown in figures 7.1 and 7.2. Planar sections of the flow were illuminated by the TR-PIV laser sheet oriented vertically along the center of the jet exit as detailed in figure 7.1. The light scattered by the seeding particles was captured by a high speed camera system located opposite the laser sheet. Figures 7.1 and 7.2 also show the location of the randomized microphone array with respect to the jet exit.

Each of the TR-PIV measurements allowed to record 1.2 seconds of 2 dimensional velocity data (u' & v') at a sample rate of 9kHz over an area of 1.2×0.28 jet diameters [1]. The microphone array data was acquired synchronously at three times that of the TR-PIV sample rate (i.e. 27kHz). The 25 channels were synchronized with the TR-PIV acquisition system via an external trigger. A multi-pass correlation routine as that described in section 4.3.2 was used to analyze the TR-PIV data. The final window size was 32×32 pixels with a 50% overlap. This allowed for a total of 64×16 velocity vectors fields per image with a spacing of 1.1mm. Each microphone signal was pre-amplified and stored ready for post-processing via the National Instruments DAQ system detailed in section 4.3.4. The seeding particles in the flow were generated using the Phantom PS31 smoke machine introduced in section 4.4.

[1] The jet diameter (D_{Jet}) was 0.05m for all measurements.

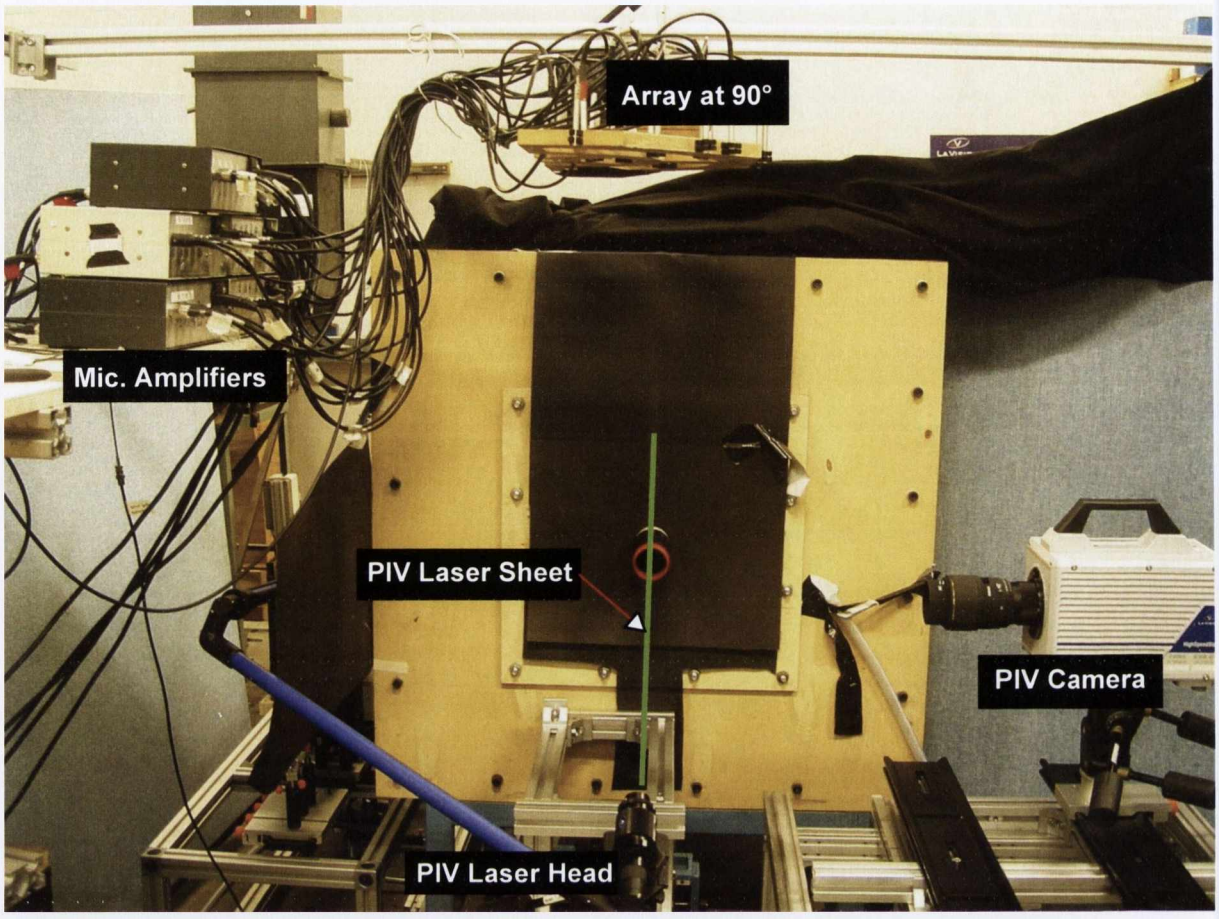

Figure 7.1: TR-PIV test setup (front view).

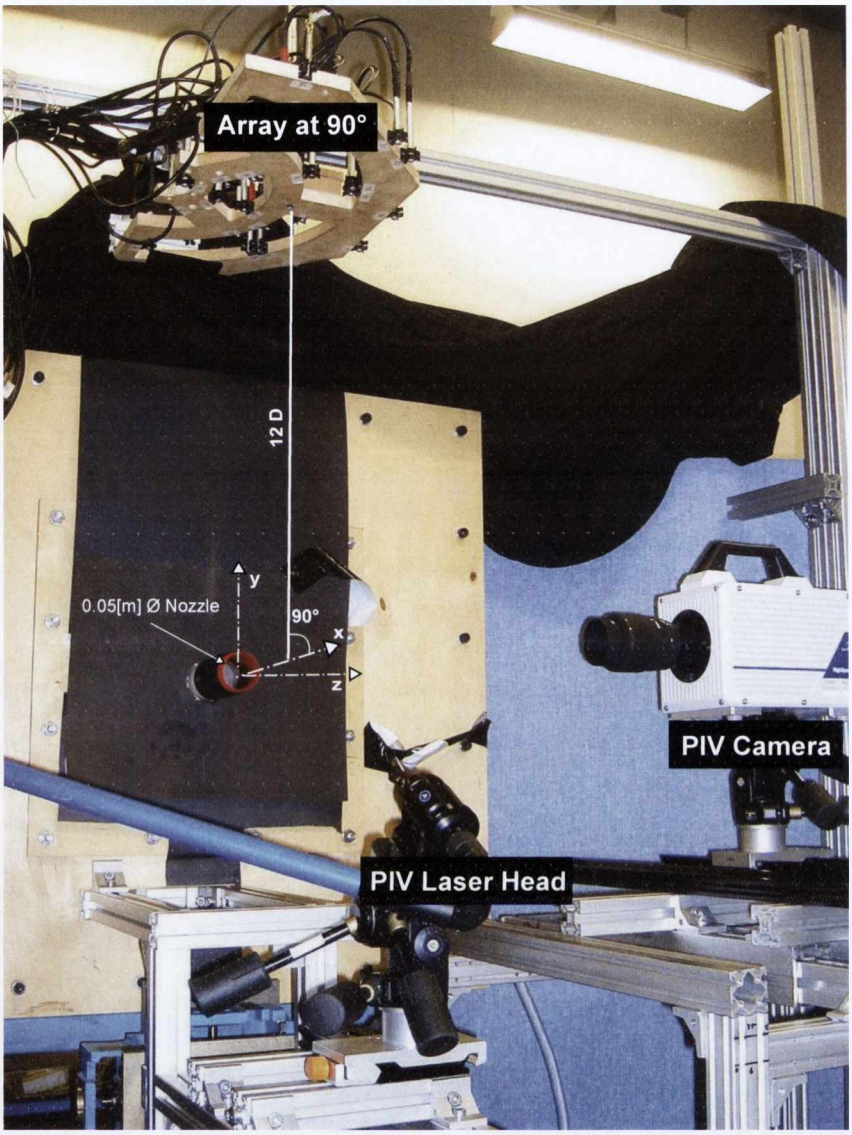

Figure 7.2: TR-PIV test setup (close up).

7.1.2 Centerline Test layout

The first of the two test setups, directed the TR-PIV measurement plane along the jet's centerline. To do this, a window size of area 1.2×0.28 jet diameters was focused at 5 contiguous locations along the jet's centerline as detailed in figure 7.3 covering an axial extent of approximately 6 jet diameters. A gap of 0.16 jet diameters was left between the nozzle exit and the edge of the TR-PIV located furthest upstream. This was done so as to avoid laser reflections from the nozzle impinging in the TR-PIV camera aperture. Additionally, each of the contiguous TR-PIV frames was overlapped by a length of 0.1

jet diameters to compensate for the lesser quality data obtained at these locations (see section 4.3.2). The array center was located at 5 diameters downstream of the jet exit and perpendicular to the jet axis at a distance of 12 jet diameters as detailed in the same figure.

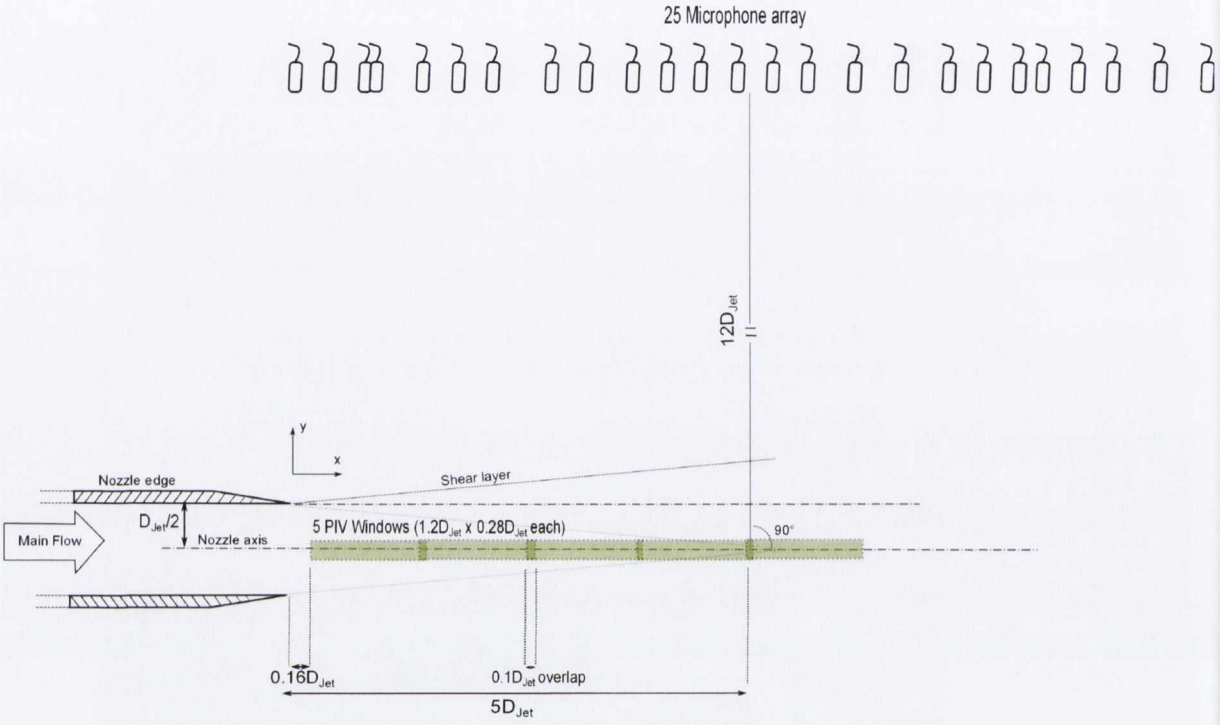

Figure 7.3: Centerline experimental layout (Side view).

7.1.3 Lipline Test layout

The second experimental setup directed the TR-PIV measurement plane along the jet's lipline. As in the centerline case, 5 TR-PIV windows of 1.2×0.28 jet diameters, with an overlap of approximately 0.1, were focused at 5 contiguous locations as detailed in figure 7.4 covering an axial extent of approximately 6 jet diameters downstream of the jet exit. As in the centerline case, a gap of 0.16 jet diameters was left between the nozzle exit and the edge of the TR-PIV located furthest upstream to avoid reflections from the jet's nozzle impinging in the TR-PIV camera aperture. The array center was located at 5 jet diameters downstream of the jet exit and perpendicular to the jet axis at a distance of 12 jet diameters.

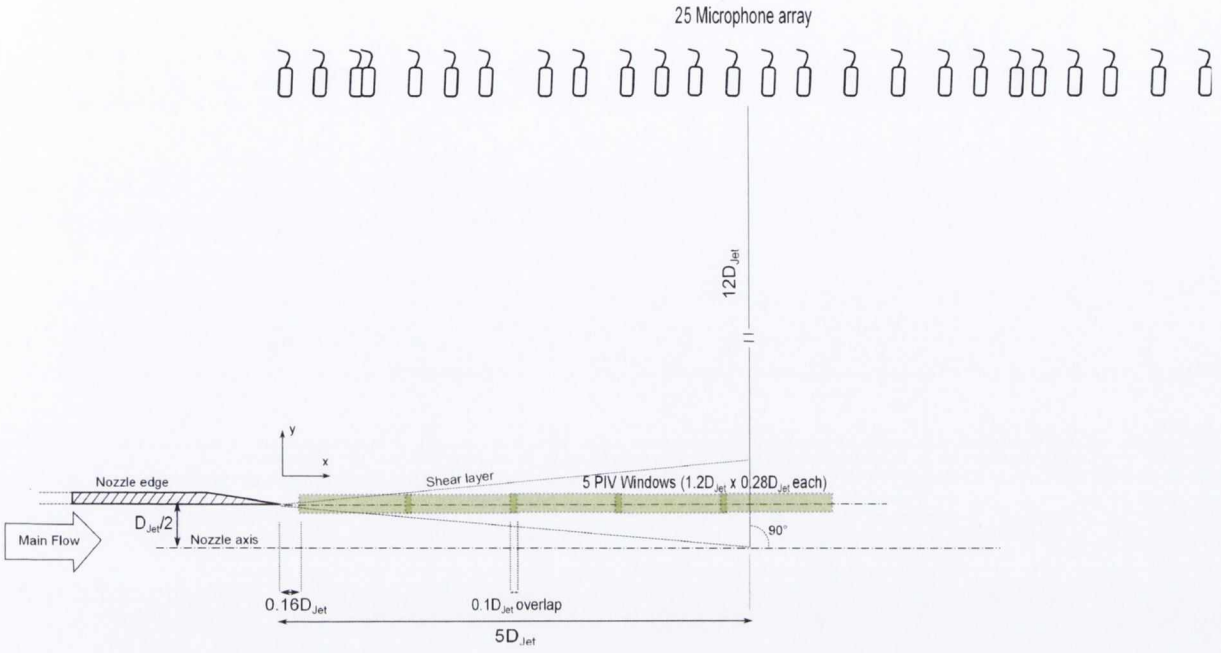

Figure 7.4: Lipline experimental layout (Side view).

7.2 Flow characteristics

7.2.1 Centerline TR-PIV Measurement Analysis

Figure 7.5 presents the RMS turbulence intensities normalised by the jet exit velocity u_j ≈87m/s at the location of each TR-PIV velocity vector measured along the jet centerline. The amplitude of these in both, u' and v' components, are at a minimum up to a distance of approximately 4 jet diameters downstream. The location of the end of the potential core, defined by $u = 0.95u_j$, was measured at approximately 5 diameters downstream of the jet exit. In this region, the effects of the entrainment of slower fluid into the jet's core results in an increase in turbulence intensities with maximum values measured by the u' component.

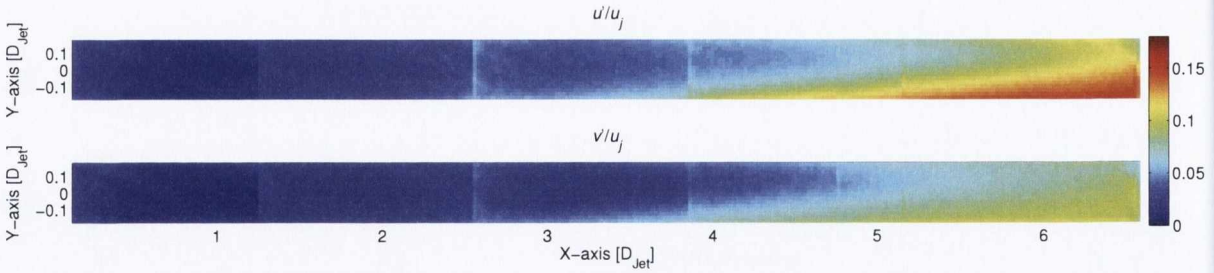

Figure 7.5: RMS turbulence intensities u'/u_j and v'/u_j measured along the jet's centerline region.

The Power Spectrum Density (PSD) of the fluctuating components u' and v' measured at 6 separate downstream locations along the jet's centerline are presented in figures 7.6 and 7.7. The PSD results show the presence of a dominant oscillating flow instability between the Strouhal number [2] values of $\approx 0.3 - 0.8$. This is clearly seen in the PSD calculated from both, u' and v' measured components between 1-4 jet diameters downstream with the exception of the PSD of the v' fluctuating data measured at 1 jet diameter downstream. At this location, little or no fluctuating energy was resolved from the TR-PIV data acquired. It is in the region between 5-6 jet diameters downstream where maximum fluctuating energy values are attained along with a peak energy shift towards lower Strouhal number values.

[2] All the Strouhal number values presented hereafter are based on a jet diameter of 0.05m and a jet exit velocity of 87 m/s

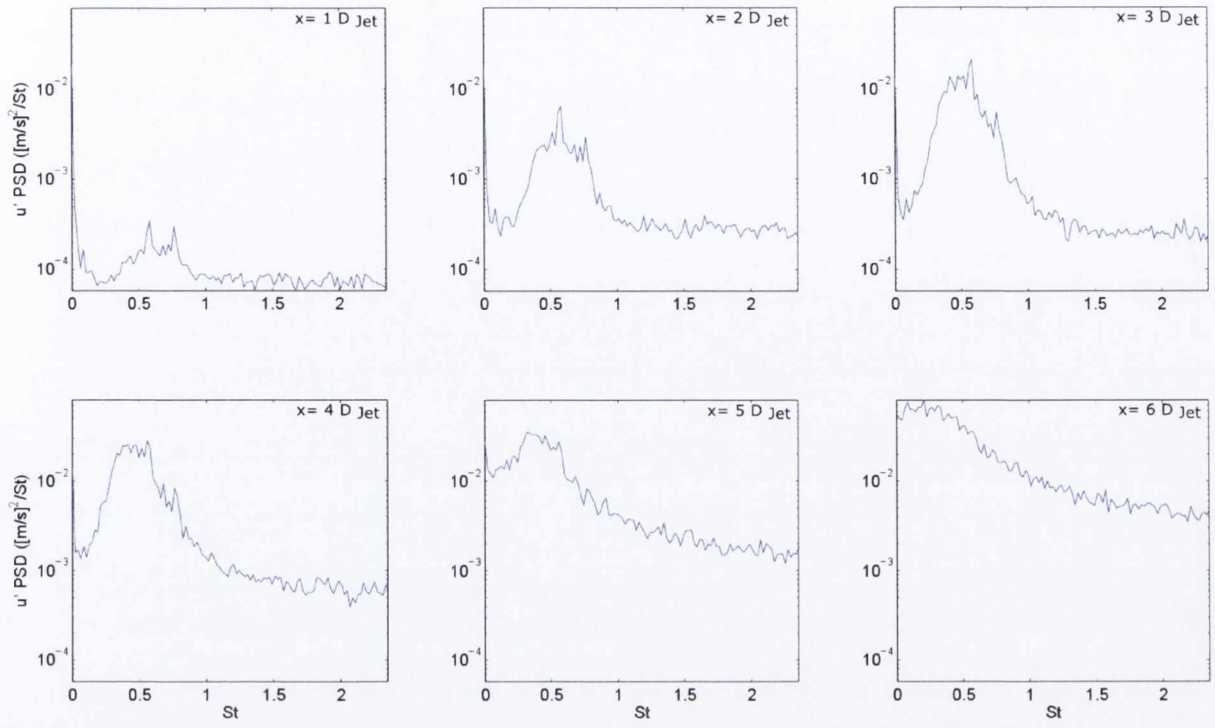

Figure 7.6: u' PSD as a function of Strouhal number (St) at 6 separate downstream locations along the jet's centerline

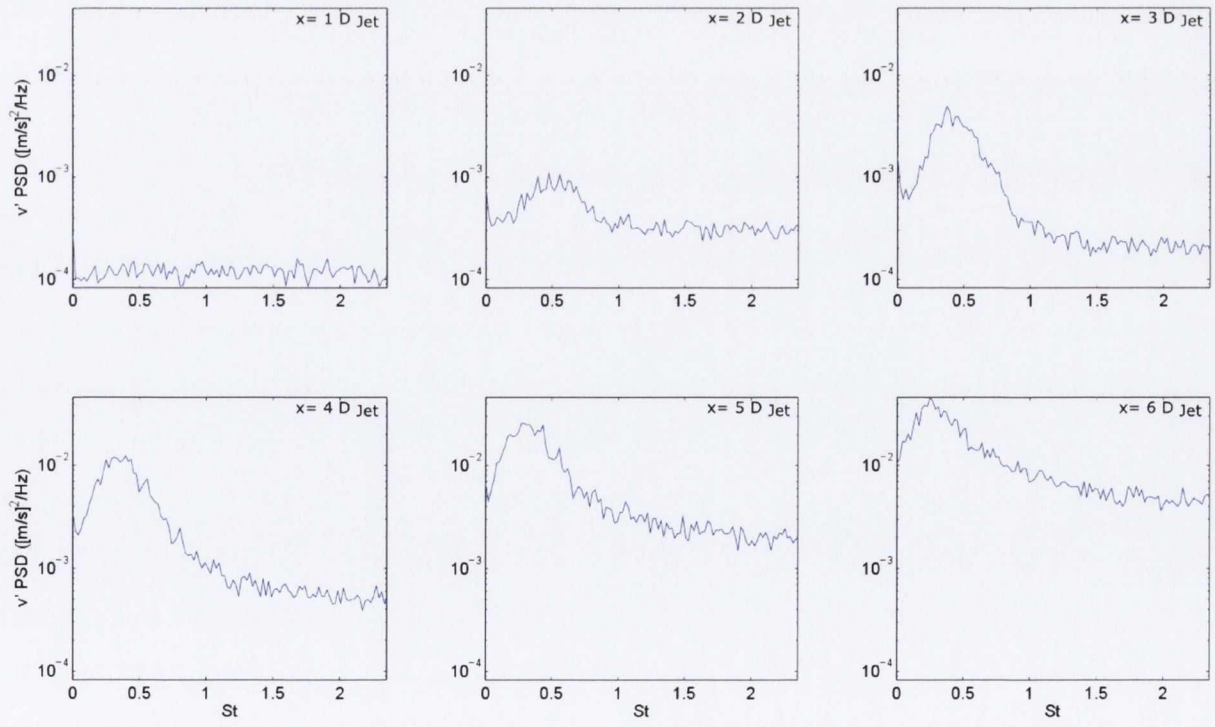

Figure 7.7: v' PSD as a function of Strouhal number (St) at 6 separate downstream locations along the jet's centerline

7.2.2 Lipline TR-PIV Measurement Analysis

The normalized RMS turbulence intensities measured along the lipline of the jet are presented in figure 7.8. The shear layer growth and the decreasing section of the potential core are evident in both, u' and v' measured fluctuations. However, the intensity of the fluctuations measured by the u' component are strongest at the transition region along the nozzle lipline. The level of the turbulent intensities measured here, agree well with those reported by Bradshaw [8] in a jet of similar characteristics. For instance, in his investigation Bradshaw reported u' RMS intensity levels of ≈ 0.15 along the lipline of the jet at 2 and 4 jet diameters downstream. Similarly, RMS turbulent intensities along the v' were found to be consistently weaker $\approx 0.13 - 0.1$ along the jet mixing region. Again, these results agree with the v' RMS turbulent intensities levels shown in figure 7.8.

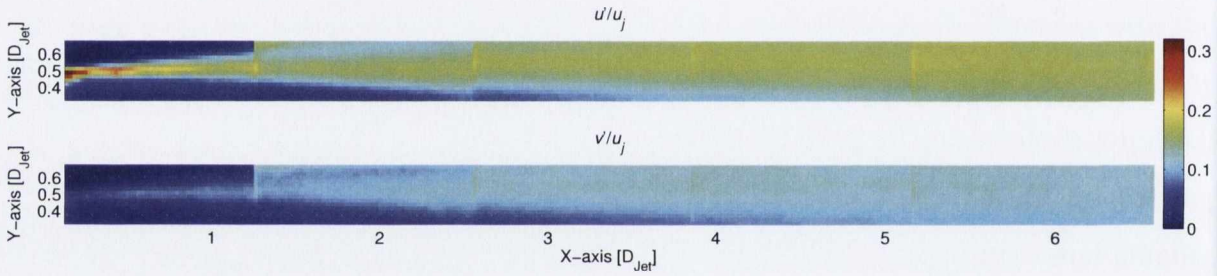

Figure 7.8: u'/u_j and v'/u_j along the jet's lipline.

The PSD of the fluctuating components u' and v' measured at 6 separate downstream locations along the lipline of the jet are presented in figures 7.9 and 7.10. The PSD estimated from the u' component, presents a broad energy spectrum peaking at ≈ 0.4 Strouhal number between 1-3 jet diameters downstream. Maximum fluctuating energy values are attained further downstream between 4-6 jet diameters along with a clear peak shift towards lower Strouhal number values. The PSD values obtained from the v' fluctuations measured between 1-4 jet diameters downstream resemble those obtained along the jet's centerline. A narrow band of energy is again identified between the Strouhal number values of $\approx 0.3 - 0.8$. This is especially the case at the measured points between 2-3 jet diameters downstream. Further downstream there is again a shift in the peak energy value towards lower Strouhal number values.

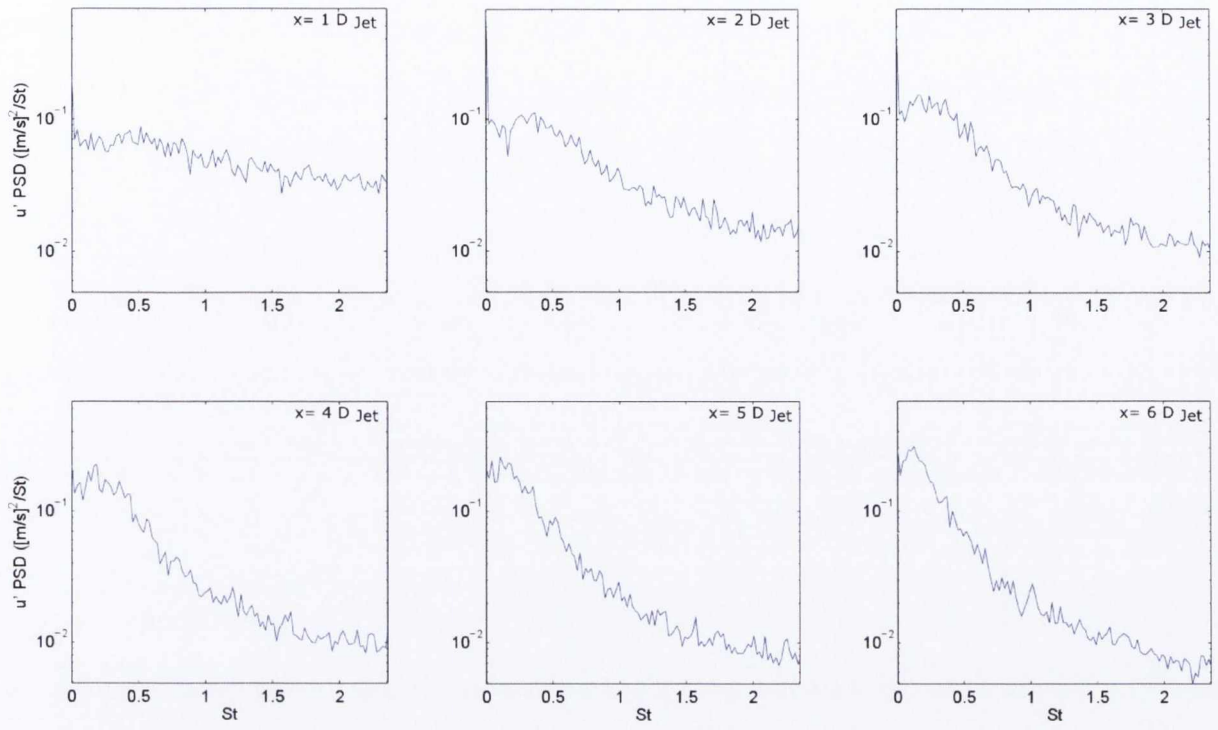

Figure 7.9: u' PSD as a function of Strouhal number (St) at 6 separate downstream locations along the jet's lipline

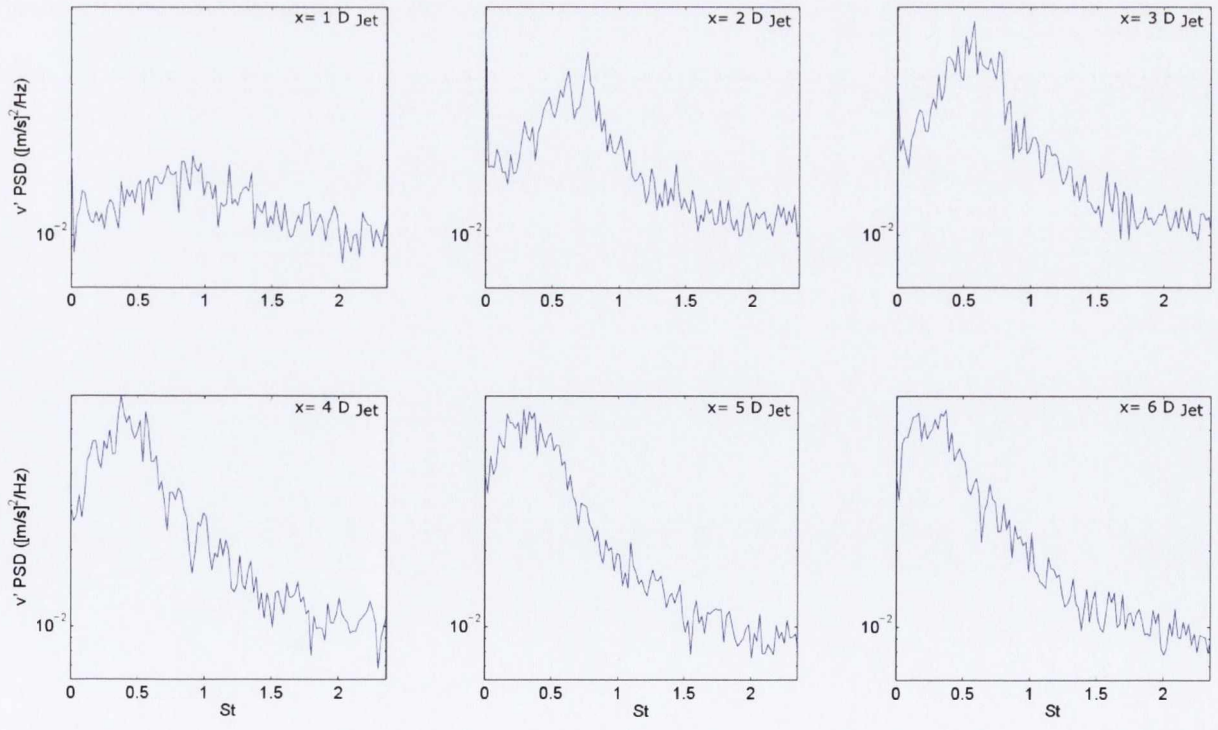

Figure 7.10: v' PSD as a function of Strouhal number (St) at 6 separate downstream locations along the jet's lipline

The lip and centerline PSD results showed the presence of a dominant oscillating flow instability at $\approx 0.3 - 0.8$ Strouhal number distributed between 2-4 jet diameters downstream. Whilst along the centerline this instability is clearly seen in the PSD of both fluctuating components, u' and v', along the jet's lipline this one is only noticeable in the PSD calculated from the vertical component v'. Further downstream, between 5-6 jet diameters, maximum energy values are recorded in both lip and centerline measurements along u' and v' with a common peak energy shift towards lower Strouhal numbers.

7.3 Array Data Analysis

As shown in the experimental layouts presented in figures 7.3 and 7.4, a total number of 10 synchronized TR-PIV and array measurements were carried out for which jet flow parameters and array location were unchanged. It is for this reason that there were no significant differences between the output of the beamformed results calculated for each individual test. This section presents the microphone array beamformed results obtained from one of these 10 measurements.

The first step was to define a focal region in the flow. For this purpose, a mesh of 10000 equally spaced focal points was created in the area delimited by the green dotted line in figure 7.11.

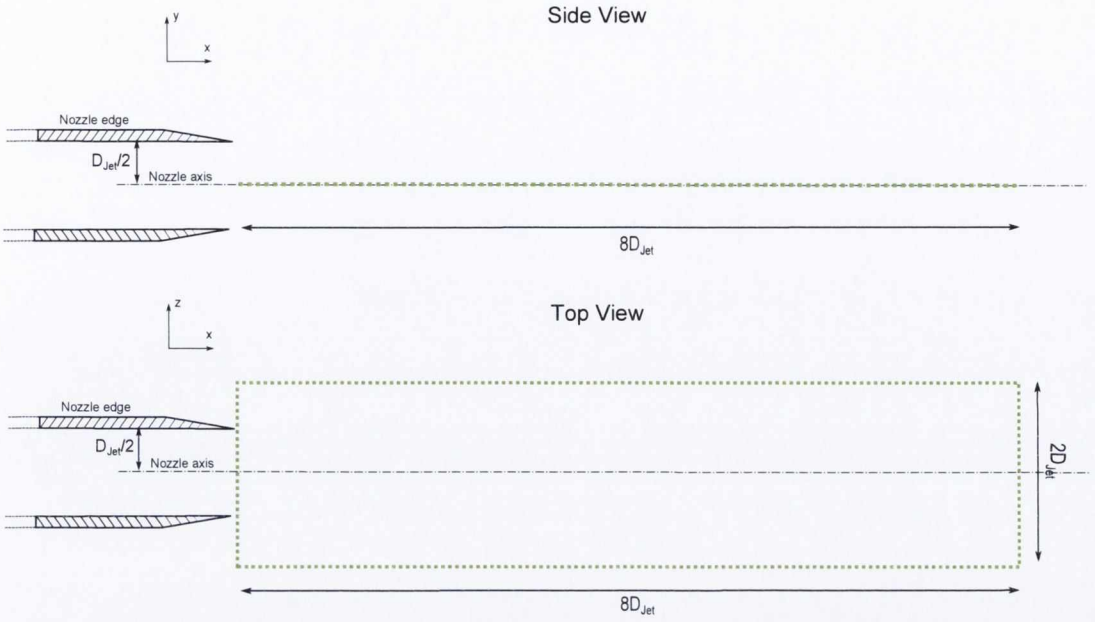

Figure 7.11: Detail of the nozzle location and the area scanned by the microphone array (Green dotted line).

Each microphone channel acquired 5 seconds of pressure data at a rate of 27kHz. Prior to the application of the delay-and-sum algorithm the array data was band pass filtered using three different, octave band, phaseless, 4th order Butterworth filters. The beamformed output calculated at each frequency band is presented in figure 7.12. The beamformed output for the first octave band, corresponding to the Strouhal numbers between 0.58 - 1.17 (1-2kHz), clearly identifies the nozzle exit as the main source within the scanned area. Highest dB levels are also attained within this lower frequency range. Similarly, in the frequency band corresponding to Strouhal number values between 1.17-2.35 (2-4kHz) the nozzle region is again identified as the dominant radiating region within the scanned area. The most noticeable difference in this frequency band is observed in the downstream spreading of the noise distribution along the jet axis. This is somewhat unexpected as most results reported in experimental investigations of these type show how the main noise contribution measured by the steered array moves further upstream with increasing Strouhal number. A good review of this type of experimental data is presented by Lee and Bridges [67]. The beamformer output at the frequency band corresponding to Strouhal number values of 2.35-4.37 (4-8kHz) clearly identifies the main source location upstream at the nozzle exit region. This result is comparable to the experimental studies presented

as for example by Lee and Bridges [67] and Dougherty and Podboy [76].

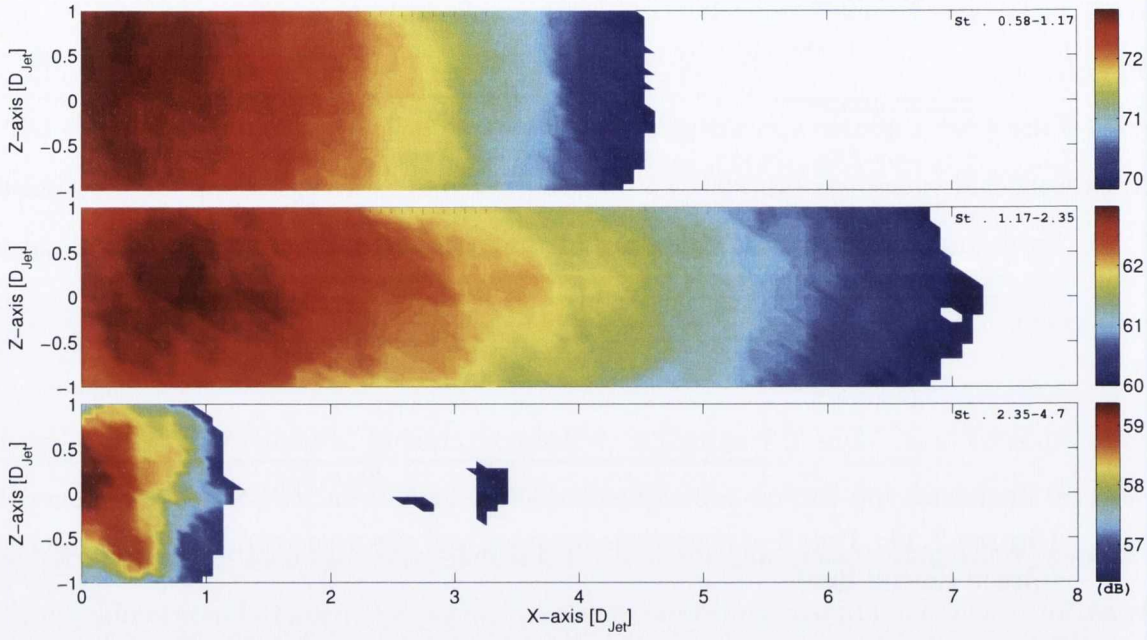

Figure 7.12: Output of the delay-and-sum beamforming algorithm calculated at three separate octave bands.

7.3.1 Peak Cross-Correlation Coefficients Between Array Microphones

The microphone to microphone peak correlation levels for one of the 10 sets of array data were calculated with reference to microphone No.1 in the array. This microphone was chosen as reference as its location lies directly above the centerline of the jet axis at $\approx [3.4, 12, 0]D_{Jet}$ in line with the TR-PIV frames. The relative location and indexing of each array microphone is presented in figure 7.13.

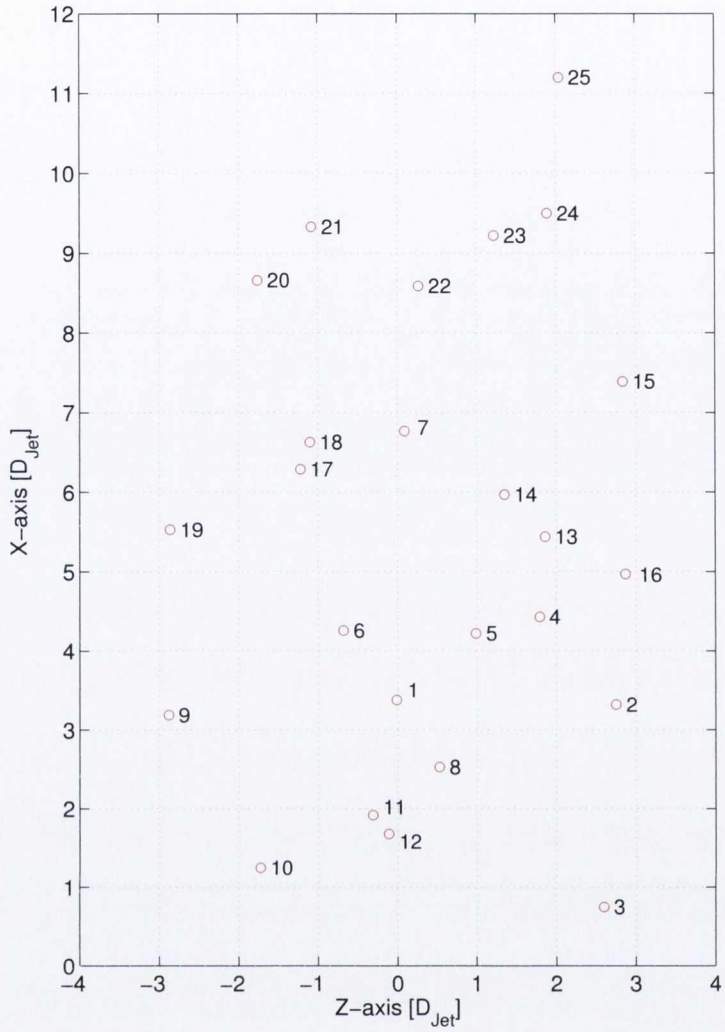

Figure 7.13: Layout and microphone index of the 25 microphone array used in the free flow configuration.

Prior to the cross-correlation calculation between receivers, all the microphone signals were band passed using the octave band pass filters used in the beamforming calculations shown in the previous section. This was done to evaluate the level of correlation between the microphone measured signals for each of the frequency bands used in the beamforming calculations shown in figure 7.12. The microphone to microphone cross-correlation coefficient results for the lowest of these frequency bands is presented in figure 7.14.

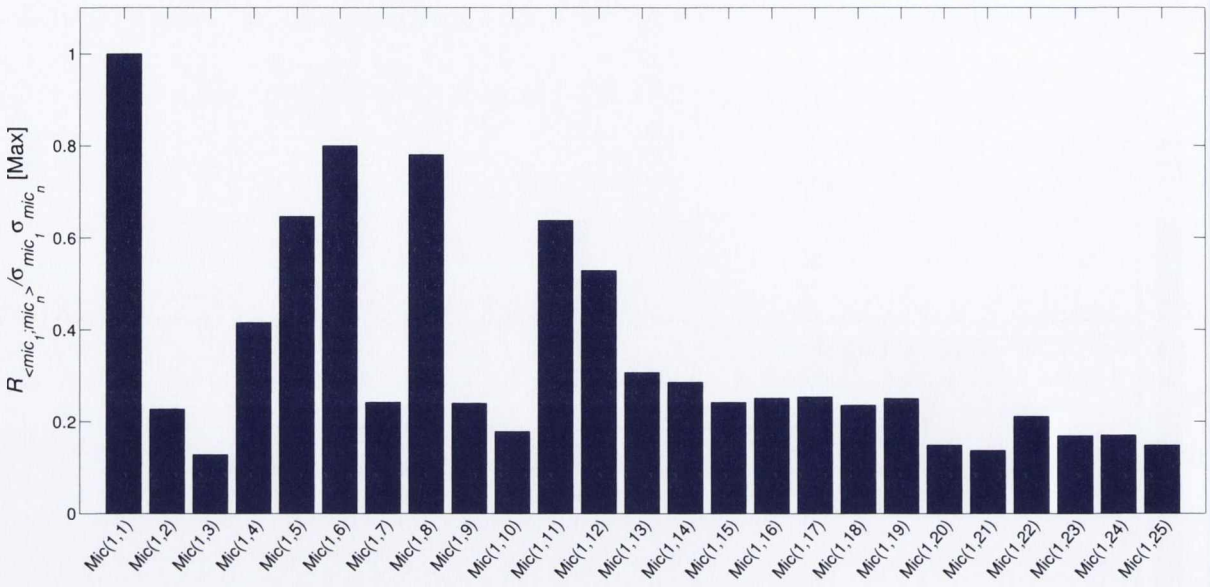

Figure 7.14: Microphone to microphone cross-correlation coefficients for the octave frequency band corresponding to Strouhal numbers 0.58-1.17 (1-2kHz).

As it could be expected, correlation coefficients are highest between microphones located in the vicinity of the reference microphone (e.g Mics 5,6,8,11). These are followed by a number of the microphones that are located further along the x-axis (e.g. Mics 16,14,19,18), whilst lowest correlation levels are measured with those microphones located upstream and furthest from the jet axis (e.g. Mics 3,10) and those placed further downstream along the x-axis (e.g. Mics 20-25).

At higher frequencies, the general drop in correlation levels across the array microphones presented in figure 7.15 is evident. Most noticeable is the drop in peak correlation coefficients with those array receivers at locations further downstream (e.g. Mics 13 - 25). A similar trend can be observed in the results attained at the highest frequency band corresponding to Strouhal numbers 2.35-4.7. However, in this occasion peak correlation levels of approximately 0.4 are measured between the reference and microphones No.2 and 9.

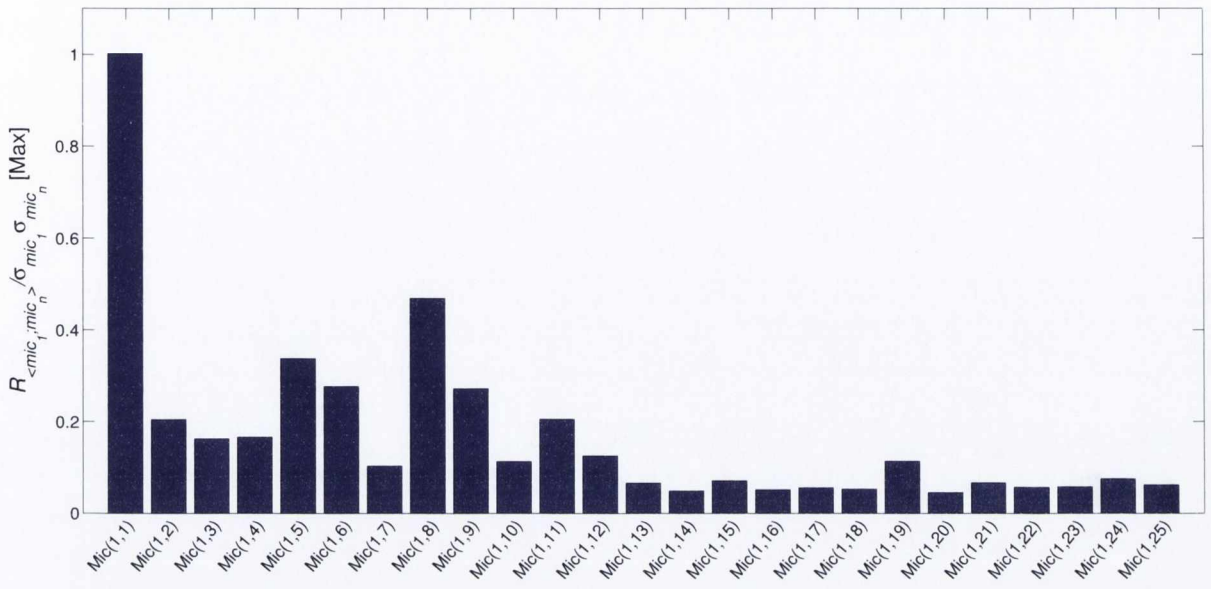

Figure 7.15: Microphone to microphone cross-correlation coefficients for the octave frequency band corresponding to Strouhal numbers 1.17-2.35 (2-4kHz).

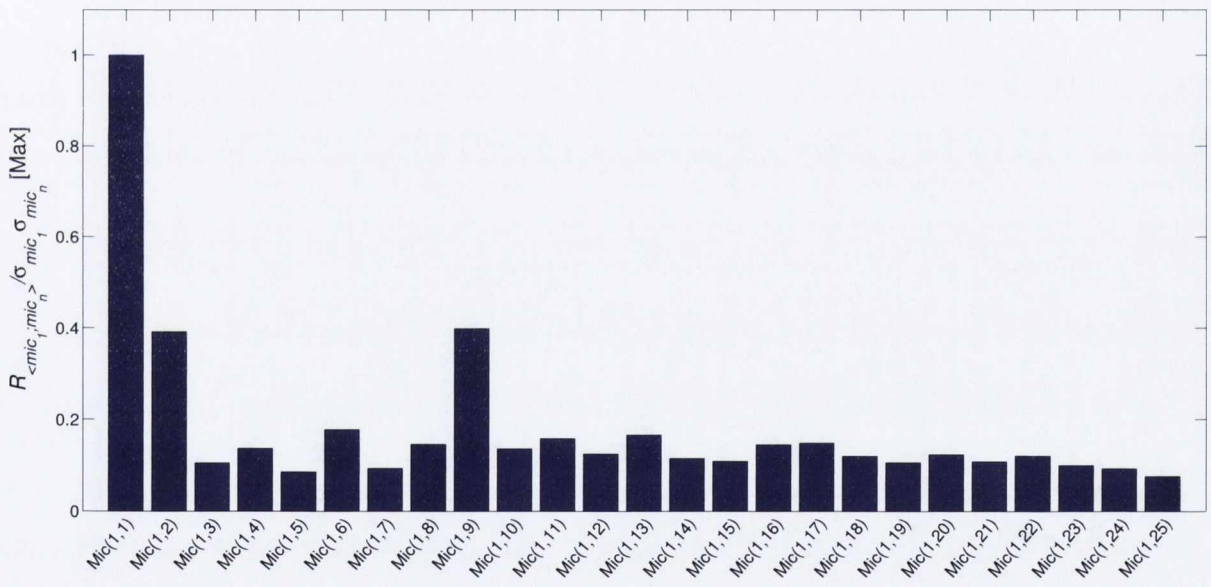

Figure 7.16: Microphone to microphone cross-correlation coefficients for the octave frequency band corresponding to Strouhal numbers 2.35-4.7 (4-8kHz).

Whilst these values are only an indication of the type of source impinging on the array aperture, it is clear that highest correlation coefficients are measured at the lowest frequency band corresponding to 0.58-1.17 Strouhal numbers. In other words, it is at this frequency band where the array aperture is exposed to a more uniform source directivity. The lower correlation coefficients measured at higher frequencies can indicate, among

other things, the presence of a complex sound field with varying directivity across the array aperture.

7.4 Flow-Acoustic Correlation Measurements

The previous two sections presented the analysis of 1- the flow field characteristics as measured by the TR-PIV 2- the sound field characteristics as measured at the location of the microphone array. What follows in this section are the results obtained by correlating both, the acoustic pressure at the array location and the flow data measured via TR-PIV.

7.4.1 Correlation Results Along the Centerline

The velocity fluctuating components u' and v' measured by the TR-PIV along the jet's centerline were correlated to the output of 1- a single array microphone 2 - the delay-and-summed beamformed array output focused at the location of each of the PIV vector fields. The TR-PIV vector fields corresponding to the jet's centerline across each of the 5 TR-PIV windows depicted in figure 7.3 were chosen as the flow fluctuating variables. 54 out of a total of 64 vectors along the length of each TR-PIV window were used for calculations. The first and last 5 vectors from each window were discarded as the data in these regions was found to be of lesser quality.

7.4.1.1 Normalized Cross-Spectrum (Coherence)

Figures 7.17 and 7.18 present an example of one of the 270 normalized cross-spectrum calculations carried out between the flow variables u' & v' measured at contiguous points along the jet's centerline and the output of a single microphone in the array (Mic No.1, see figure 7.13). The auto-spectrum of the centerline flow fluctuations u' and v' measured $\approx 1.3D_{Jet}$ downstream of the jet exit are presented in figure 7.17(a). In both, u' and v', the PSD is dominated by a band of energy between 0.3-0.9 Strouhal numbers. On the other hand, most of the acoustic energy in the auto-spectrum of the microphone signal (see figure 7.17(b)) is concentrated in the lower Strouhal number region. However, secondary peaks are also observed in the frequency region corresponding to 0.3-0.9 Strouhal numbers.

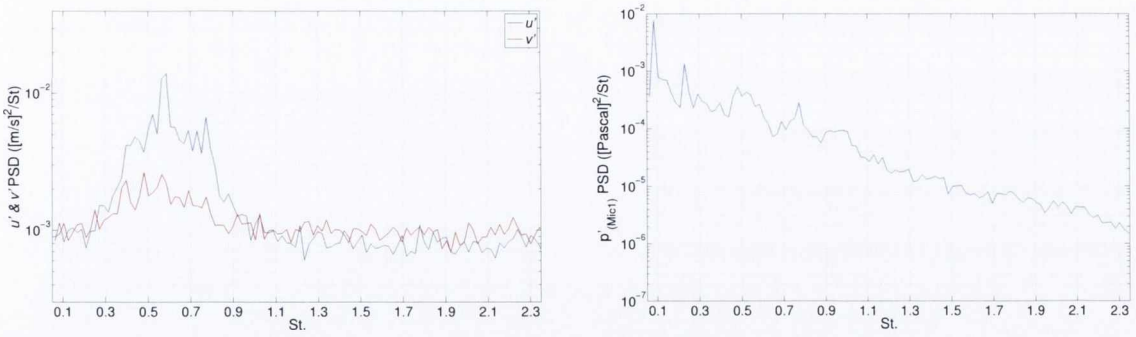

(a) PSD of the u' and v' flow components measured along the jet's centerline at $\approx$ 1.3 D_{Jet} downstream of the jet exit

(b) PSD of a single array receiver (Mic No.1)

Figure 7.17: PSD of the TR-PIV measured variables u' and v' and PSD of the acoustic pressure measured by a single microphone within the array (Mic No.1).

The normalized cross-spectrum (coherence) estimated between both u' & v' and the microphone signal is presented in figure 7.18.

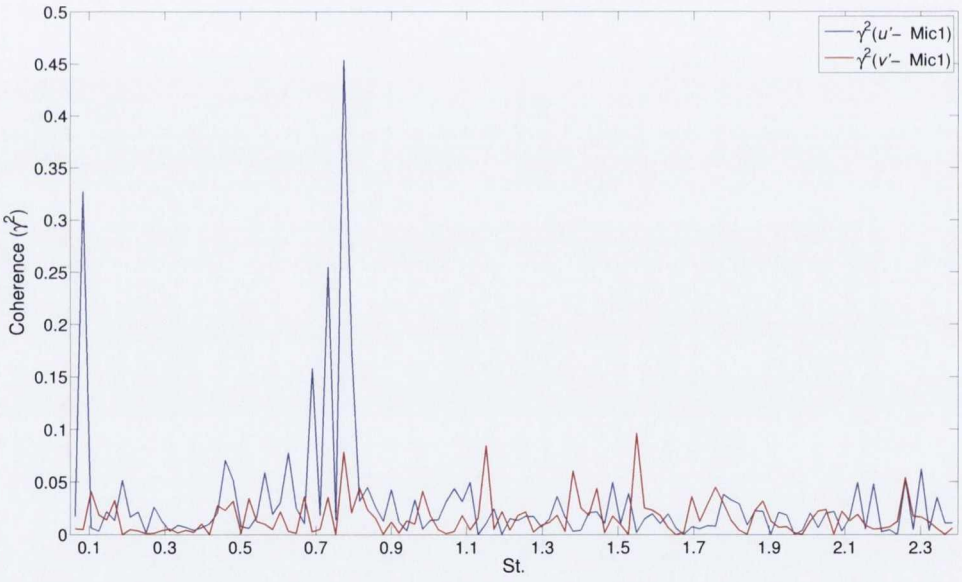

Figure 7.18: Calculated coherence between the flow variables u' & v' measured at $\approx$ 1.3 D_{Jet} downstream of the jet exit and the acoustic pressure measured by a single array microphone (Mic No.1).

The calculated coherence between flow and acoustic perturbations is clearly dominated by a set of narrow peaks in the 0.7-0.8 Strouhal number region an a secondary peak at a Strouhal number of $\approx$ 0.1. The same process was then followed to calculate the coherence between the acoustic pressure measured between the single microphone output and the

remaining 270 TR-PIV velocity vectors acquired at contiguous locations along the jet's centerline. The calculated coherence between each TR-PIV vector measured along the x-axis and the microphone signal is presented in figure 7.19.

Coherence values peaking at ≈ 0.5 are measured between the microphone signal and the u' component over extended regions of the flow. A clear flow-acoustic interaction is observed in the narrow frequency band corresponding to a Strouhal number of ≈ 0.77 (≈ 1.3kHz) between an extended region 1-5 jet diameters downstream. Additionally, high coherence levels are observed over an extended region of the flow between 0.2-3.5 jet diameters downstream at the narrowband frequency band corresponding to a 0.1 Strouhal number value (≈ 0.17kHz). Flow-acoustic interaction between the microphone pressure signal and the v' flow component is also dominated by a narrowband extended region centered at a Strouhal number of ≈ 0.77 between 2.5-4 jet diameters downstream. However, coherence levels peak at ≈ 0.23 in contrast with the maximum of ≈ 0.5 attained by the u' component.

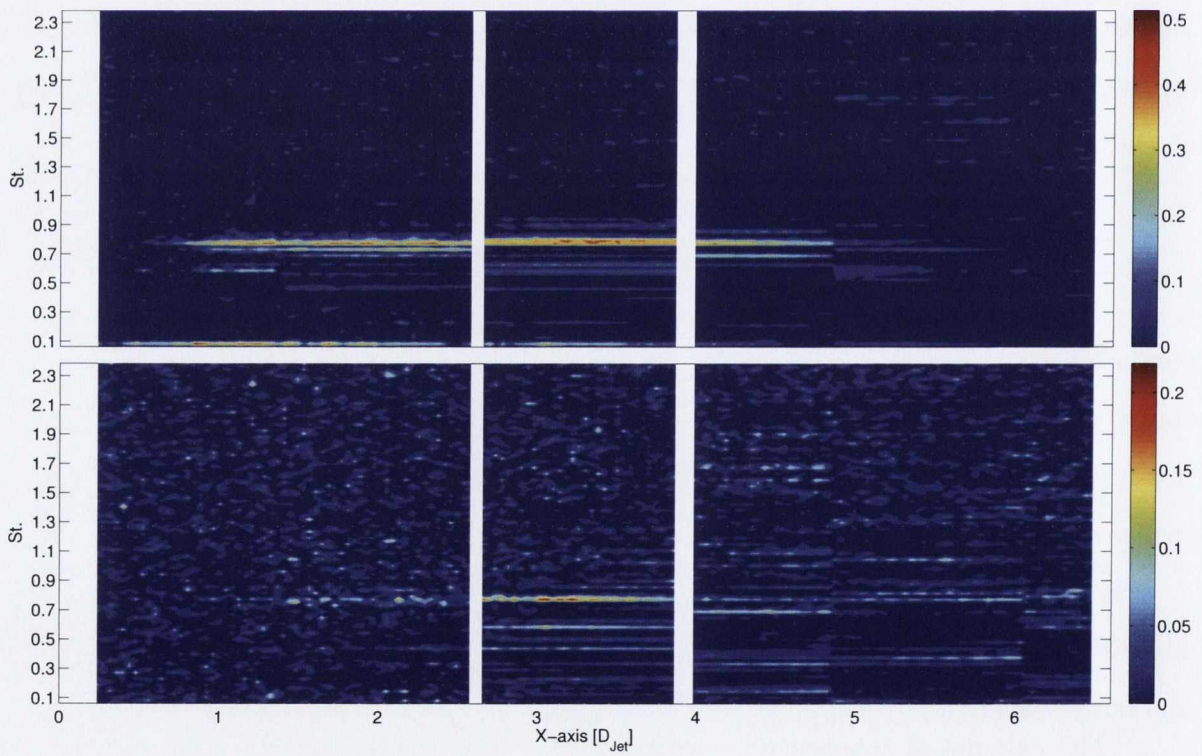

Figure 7.19: Top - Coherence output between u' and the acoustic pressure measured by a single array microphone (Mic No.1). Bottom - Coherence output between v' and the acoustic pressure measured by a single array microphone (Mic No.1).

The same process was applied to estimate the coherence between flow variables u' and v' measured along the jet's centerline and the output of the microphone array. For each separate calculation the array response was steered towards the location of the corresponding TR-PIV velocity vector as described in section 3.1.1.

Figure 7.20 presents the auto-spectrums of both, the steered array signal and the flow fluctuation components u' and v' measured at the $1.3D_{Jet}$ downstream location.

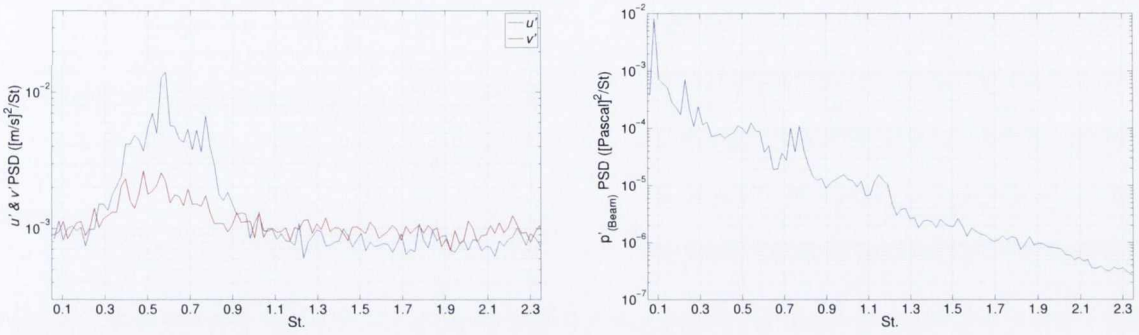

(a) PSD of the u' and v' flow components measured along the jet's centerline at $\approx$ 1.3 D_{Jet} downstream of the jet exit.

(b) PSD of a the steered array signal focused at the location of the TR-PIV in-flow measurement.

Figure 7.20: PSD of the TR-PIV measured variables u' and v' and PSD of the acoustic pressure measured by the array steered at the location of the in-flow measurements.

As in the previous example, the flow energy measured by the TR-PIV is concentrated in the 0.3-0.9 Strouhal number region. The main difference in this instance, is the reduction in the acoustic energy above frequencies corresponding to a 0.4 Strouhal number present in the PSD of the array signal (see figure 7.17(b)). Figure 7.21 presents the coherence levels, calculated as detailed in section 3.1.1 (see equation 3.3), between the TR-PIV velocity vector fields u' and v' and the steered array signal.

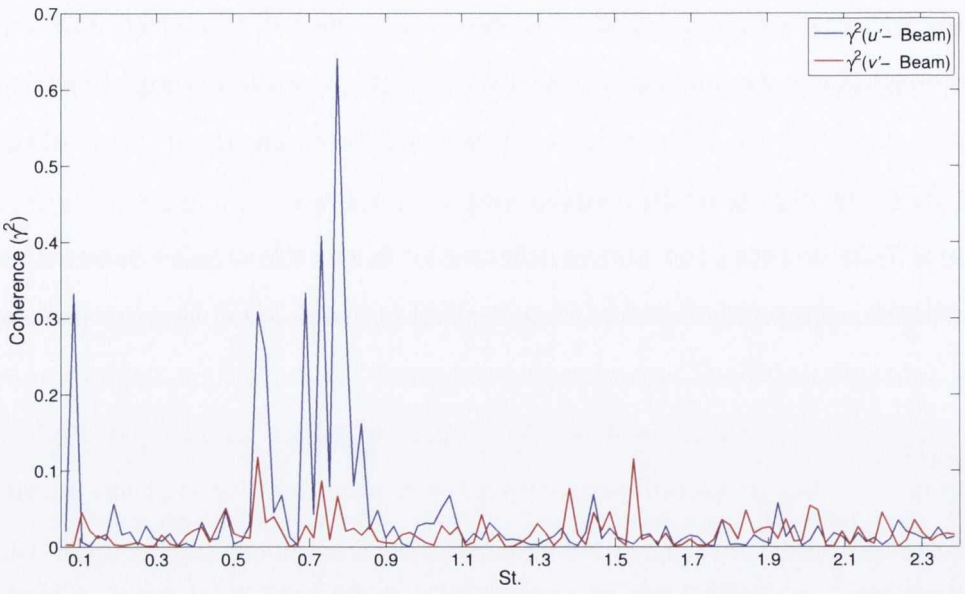

Figure 7.21: Calculated coherence between the flow variables u' & v' measured at ≈ 1.3 D_{Jet} downstream of the jet exit and the acoustic pressure measured by the microphone array steered towards the location of the in-flow measurements.

The coherence output calculated with the steered array signal is similar to that attained with a single array microphone (see figure 7.18). However, coherence levels, specially those measured with the u' component between Strouhal numbers of $\approx$ 0.7-0.8 are clearly improved.

The normalized cross-spectrum (coherence) was then estimated between each of the contiguous 270 measurements along the jet's centerline and the steered array signal. The calculated coherence between each TR-PIV vector measured along the x-axis and the steered array signal is presented in figure 7.22. In the u' case, coherence levels are increased $\approx$ 30% when compared to those attained by the use of a single receiver. Even though the main fluctuating flow instability is again measured over an extended region of $\approx$ 4 jet diameters at a 0.77 Strouhal number, secondary narrowband extended correlated regions appear at frequencies corresponding to a 0.55 Strouhal number.

In the v' case, a flow instability is again identified between 2.5-4 jet diameters at $\approx$ 0.77 Strouhal number. A second flow instability is also identified at a Strouhal number of $\approx$ 0.55 between 1.5-4 jet diameters along the x-axis. However, the coherence levels estimated between the steered array signal and the v' fluctuating component do not show a significant increase when compared to those calculated with a single microphone (see

figure 7.19). Whilst this result is somewhat unexpected, a reasonable explanation is that, meanwhile the v' flow measured perturbation may be well correlated with the acoustic pressure measured at the location of the single receiver (i.e. Mic No.1), this may not be the case across other microphones within the array. In the cases where there is a loss of coherence between the array receivers, the calculated correlation levels could even be reduced when compared to those attained by a single receiver. In this instances it could be beneficial to only include the output of those microphones within the array that have a high cross-correlation coefficient between them (see figure 7.14). However, this would also affect the array's spatial resolution as it will most likely imply a reduction of the spatial extent of the array aperture.

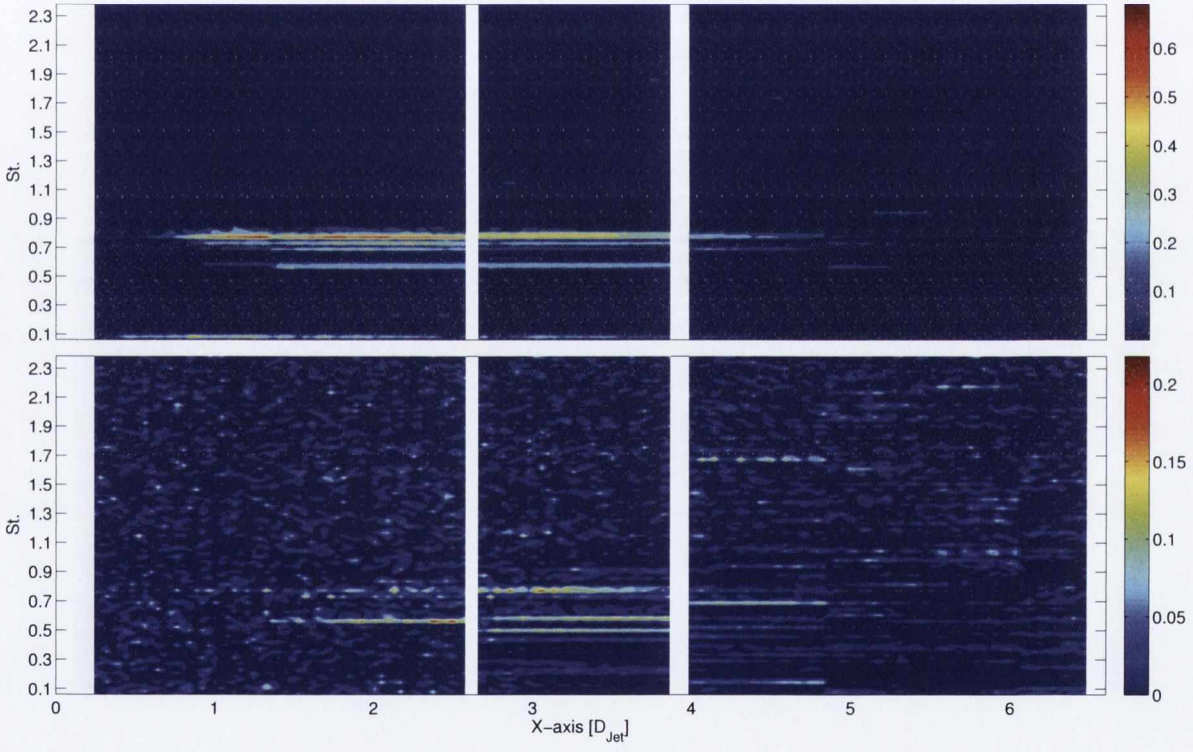

Figure 7.22: Top - Coherence output between u' and the steered array signal. Bottom - Coherence output between v' and the steered array signal.

Most noticeably is the fact that all the coherence based measurements results shown above, identify the interrelation between "non-compact" flow structures and the acoustic pressure measured at a broad angle from the jet axis. Interesting to note that, in an earlier investigation carried out in this same experimental facility, Breakey and Fitzpatrick [53]

also reported the existence of these extended coherent structures between flow perturbations measured via TR-PIV and a single microphone located at a shallow angle (30°) from the jet axis.

7.4.1.2 Time Domain Cross-Correlation Coefficients

Whilst high coherence levels were measured between the acoustic field and a number of narrowband, "non-compact" flow instabilities, these results are not conclusive evidence of sound radiation being originated by the flow measured perturbations. This is demonstrated by the time domain correlation signatures between the flow and acoustic pressure fluctuations measured at the array location presented in figures 7.23 & 7.25. Prior to the calculation of the cross-correlation coefficients, all microphone signals were bandpass filtered by a 4th order Butterworth phaseless filter between the frequencies of 1.15-3.5kHz corresponding to Strouhal numbers $0.65 - 2$. This was done to evaluate the time domain correlation signature of the dominant flow-acoustic interaction identified at a 0.77 Strouhal number ($\approx$ 1.3kHz). Additionally, the array spatial resolution capabilities are determined by the lowest frequency used in the band pass filter. Whilst a much higher lower frequency bound in the band pass filter would have been desirable to increase the array resolution, it is clear from the coherence based results that little or no correlation exist between the flow and acoustic pressure above a frequency corresponding to a 0.77 Strouhal number. This fact limited the array resolution in the axial direction to $\approx$ 6.5 jet diameters for all measurements (see figure 4.8).

Figure 7.23 presents the time domain cross-correlation signature calculated between u' & v' and the band passed signal of a single array microphone (Mic No.1). The thin dashed line along the position $\tau u_j / D_{Jet} = 0$ [3], represents the expected peak correlation time lag between the in-flow measurement and microphone locations. These expected peak correlation delays were estimated under the assumption of compact, uncorrelated source mechanism, radiating at the location of each individual TR-PIV velocity vector along the x-axis[4].

[3]Here, τ represents the retarded time relative to the time domain cross-correlation calculation, u_j in the jet exit velocity of $\approx$ 87 m/s and D_{Jet} is the jet diameter (0.05 m)

[4]In all cases, the microphone signal used for the cross-correlation calculation was evaluated at the retarded time $p'(t + r/c_0)$ where r is the distance between in-flow TR-PIV measurement and c_0 is the speed of acoustic wave propagation in air (344m/s).

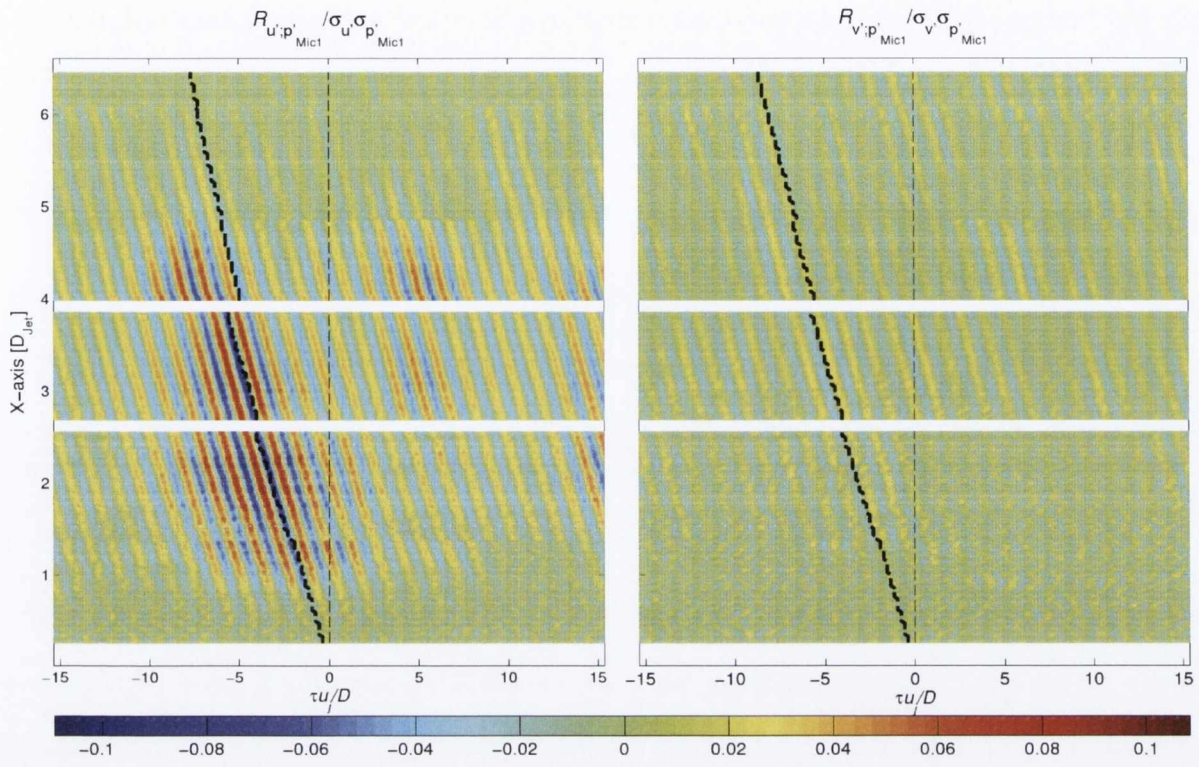

Figure 7.23: Normalised time domain correlations between a single array microphone (Mic. No1) and the flow velocity fluctuations measured along the jet's centerline. $[R_{<u';p'_{mic}>}/\sigma_{u'}\sigma_{p'_{mic}}]$(left), $[R_{<v';p'_{mic}>}/\sigma_{v'}\sigma_{p'_{mic}}]$(right). Dashed thin line −− represents expected peak correlation delay times based on straight wave propagation between each in-flow measurement and microphone location. Dashed bold line - - represents estimated peak correlation times based on a radiating convected source originating at the jet exit.

As with the coherence based correlation measurements presented in figure 7.19, the time domain cross-correlation signature is also dominated by the interaction between acoustic pressure and the longitudinal component u'. However, peak correlation values do not coincide with the estimated straight propagation delay times represented by the thin dashed line. Instead, peak correlation values follow a negative slope. In other words, acoustic pressure fluctuations measured at the microphone location lead those acquired by the TR-PIV within the flow. Bogey and Bailly [55], Henning et al. [49], Dougherty *et al.* and more recently by Breakey and Fitzpatrick [53] reported analogous results in simulation and experimental studies of this same type. In most of the aforementioned cases, this effect was related to the presence of convected turbulences at the location of the in-flow measurement that are well correlated to a source mechanism at a third location radiating directly towards the microphone location. This scenario was exemplified by

Breakey and Fitzpatrick [53] in a similar schematic representation to that presented in figure 7.24.

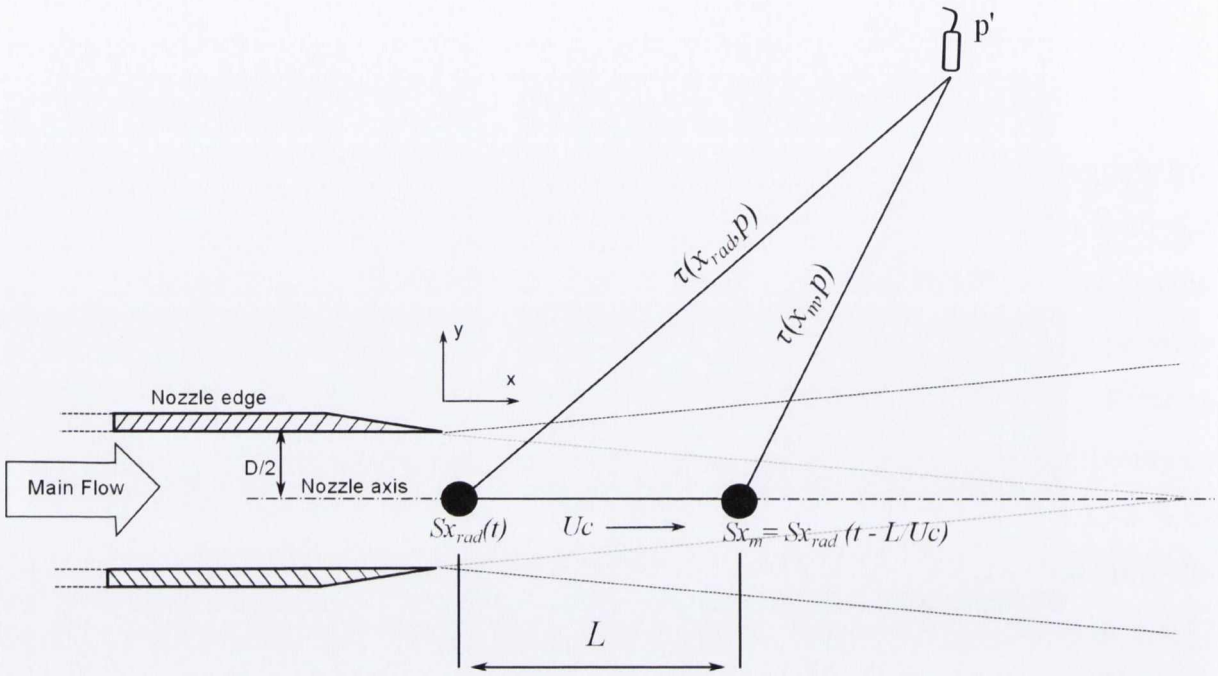

Figure 7.24: Schematic representation of the model used to estimate the time domain peak correlation delays between the in-flow and microphone signals in the presence of a correlated radiating source at a third location.

A flow disturbance responsible for sound radiation represented by Sx_{rad} at a localized upstream region is convected downstream at the convection velocity U_c over a distance L towards the location of the in-flow measurement volume at Sx_m. Assuming that the flow disturbance at the upstream location Sx_{rad} is solely responsible for radiation towards the observers location (i.e. microphone position), the associated peak correlation time lag between the flow perturbation at Sx_m and the acoustic pressure at the observers location can be estimated using equation 7.1[5].

$$\tau(x_m) = \tau_{(x_{rad},p)} - \tau_{(x_m,p)} + \int_{x_m}^{x_{rad}} \frac{dx}{U_c} \tag{7.1}$$

where $\tau(x_m)$ is the new estimated peak correlation lag between the observer and the in-flow measurement volume at position x_m, $\tau_{(x_{rad},p)}$ is the straight path acoustic propagation

[5]Equation 7.1 is based on the formulations of the same type presented by Bogey and Bailly [55] and Breakey and Fitzpatrick [53]

delay time between the radiating source presumed location and the observer, $\tau_{(x_m,p)}$ corresponds to the straight path acoustic propagation delay time between the observers and the in-flow measurement location and U_c is the flow convection velocity at each measured location between the in-flow measurement volume and the presumed source location along the jet axis.

The expected peak delay times calculated using equation 7.1, assuming the presence of a convected flow instability responsible for sound emission solely at the nozzle exit ($x_{rad} = [0, 0, 0]$), are represented by the bold dashed line in figure 7.23. The negative slope of the peak cross-correlation coefficients follow closely those estimated using equation 7.1. However, Breakey and Fitzpatrick [53] argued that this agreement between the actual peaks and expected correlation peaks did not constitute definite proof for the assumed source location (x_{rad}) to be the solely or even dominant radiating source present within the flow measured region. They concluded this by simulating an extended, narrowband, convected source radiating at two separate localized regions along the jet axis ($x_1 = [0, 0, 0]$, $x_2 = [6\mathrm{D_{Jet}}, 0, 0]$). In their simulation, the amplitude of the radiating region downstream was 10 times higher than that at the jet exit. Under these conditions, the time domain correlation signature peaks presented again a negative slope that coincided with the assumption of a single radiating region at the nozzle exit. In other words, the calculated time domain correlation signature failed to identify the contribution of a second radiating region within the flow even when this one was clearly of higher amplitude [6]. Based on these results, they concluded that the output of the time domain correlation signature between in-flow and acoustic pressure signals is at best ambiguous when trying to identify the location of source radiation.

The time domain cross-correlation signature between u' & v' and the band passed, delay-and-summed array signal steered at the location of each TR-PIV velocity vector is presented in figure 7.25. In this occasion, peak beamformed cross-correlation coefficients, again dominated by the u' measured fluctuations, are increased by $\approx 50\%$ in comparison to those obtained by the use of a single array microphone (see figure 7.23).

However, even though the steered array signal is used to estimate the cross-correlation

[6] However, the effects of extended source directivity towards the observer position from each source location were not discussed.

between in-flow and acoustic fluctuations, the negative slope followed by the correlation peaks between 0.5-4.5 jet diameters, closely match those estimated by equation 7.1 under the assumption of a single source mechanism at the nozzle exit. In other words, the time domain correlation signature shows that the beamformed signal does not suppress the contribution from the radiating mechanism at the nozzle exit when the array is steered at locations further downstream.

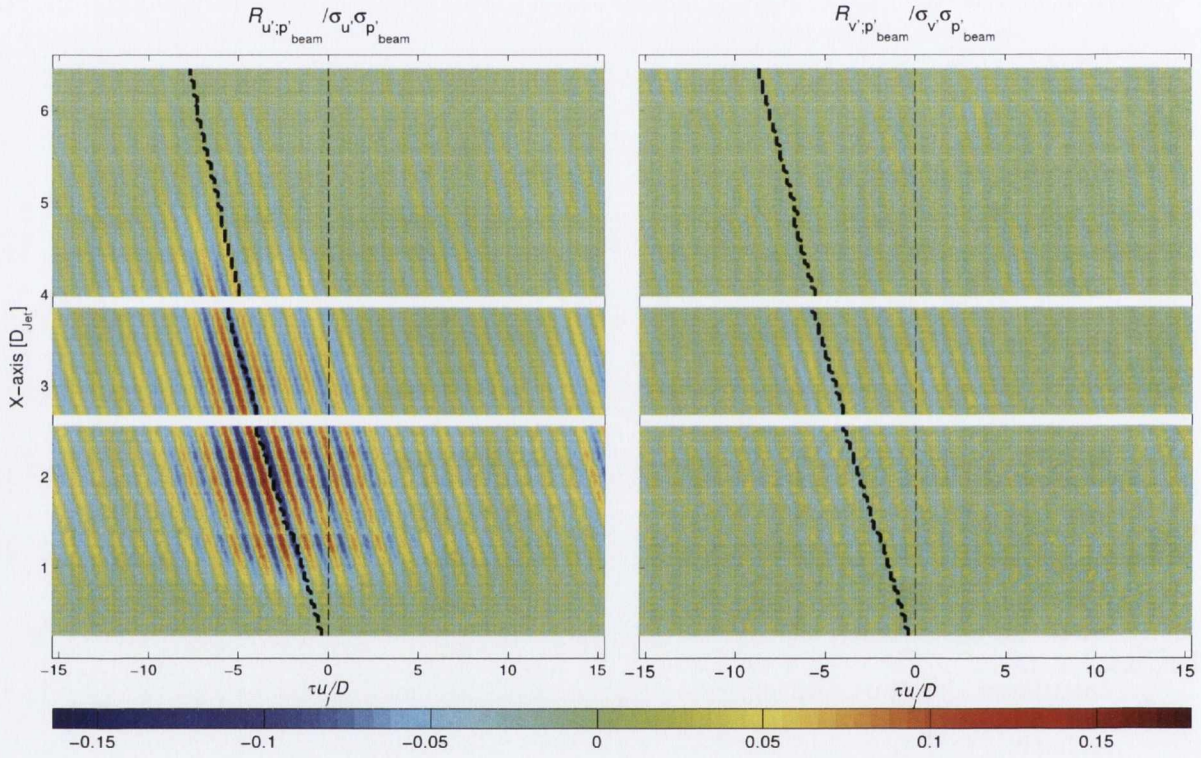

Figure 7.25: Normalised time domain correlations between the beamformed array output and the flow velocity fluctuations measured along the jet's centerline. $[R_{<u';p'_{beam}>}/\sigma_{u'}\sigma_{p'_{beam}}]$(left), $[R_{<v';p'_{beam}>}/\sigma_{v'}\sigma_{p'_{beam}}]$(right). Dashed thin line −− represents expected peak correlation delay times based on straight wave propagation between each in-flow measurement and microphone location. Dashed bold line - - represents estimated peak correlation times based on a radiating convected source originating at the jet exit.

The deviation from the expected peak correlation values ($\tau u_j/D = 0$), clearly state that strong correlations between flow and acoustic fields do not necessarily indicate significant noise emission. This is also applicable to the coherence plots shown in 7.22 and 7.19. Therefore, caution should be exerted when associating high correlation values to the presence of a radiating mechanism at the location of the in-flow measurement.

7.4.1.3 Peak Cross-Correlation Coefficients Using a Fixed In-flow Measurement

The cross-correlation measurements between the acoustic pressure and the in-flow fluctuating quantities measured along the jet's centerline, specially those measured by the u' component, identified a clear relation between a flow instability spanning across ≈ 4 jet diameters and the acoustic pressure measured at the array location.

In an effort to identify the radiating region/s associated to the dominant oscillation corresponding to an ≈ 0.77 Strouhal number, the output of the microphone array steered along the jet axis was cross-correlated to the flow fluctuating quantities u' and v' measured 2 jet diameters downstream of the nozzle exit. Data points at this flow location were selected as high correlation levels were recorded between the in-flow and acoustic pressure signals. The peak cross-correlation values between the steered array signal and the flow variables u' and v' measured at $[2D_{Jet},0,0]$ are presented in figure 7.26. In the same figure, the thin dashed line represents an estimate of the noise floor. This value represents the peak cross-correlation coefficients calculated between two randomly generated signals with the same number of points, mean and standard deviation as that of the time series of the in-flow and the beamformed signals.

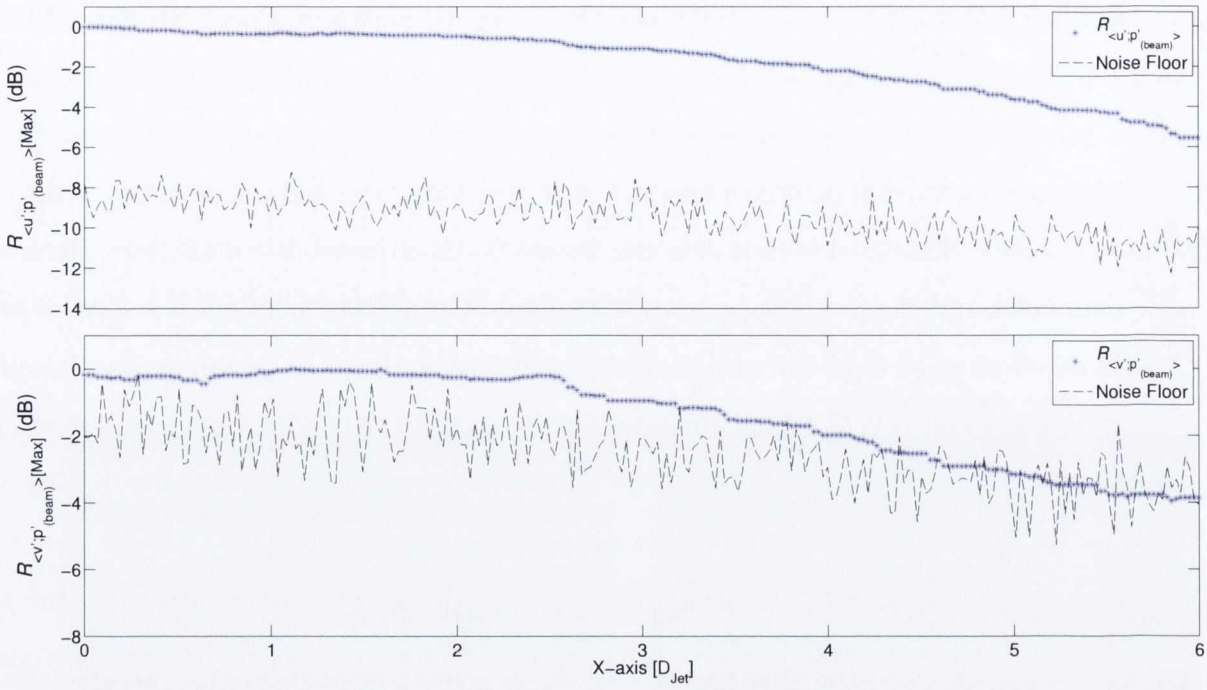

Figure 7.26: Peak correlation values in dB (dB ref.Max $R_{<u';p'_{beam}>}$ and $R_{<v';p'_{beam}>}$ respectively) between the TR-PIV vector field measured at [$2D_{Jet}$,0,0] and the steered array signal. The beamform array was focused along the jet centerline in steps of 0.02 D_{Jet} from its origin [0,0,0] up to the location [$6D_{Jet}$,0,0] downstream. The thin dashed line - - represents the noise floor levels calculated from two randomly generated signals with the same length and σ as that of the TR-PIV vectors and beamformed signals.

Maximum correlation levels between the steered array signal and the u' component measured at [$2D_{Jet}$,0,0] are obtained when the array is focused upstream of the measurement volume at the jet exit. The maximum correlation levels drop to $\approx$ -6dB at a $6D_{Jet}$ downstream. This result presents the nozzle exit as the main radiating region associated to the dominant flow instability. However, as it could be expected from the estimated array resolution of $\approx 6.5D_{Jet}$, the curve does not produce a clear peak that could be associated to a single compact radiating region at the jet exit.

The results obtained by cross-correlating the v' component measured at [$2D_{Jet}$,0,0] with the steered array signal, identify a region around 1.2 jet diameter as the main radiation location. However, main source region identification is questionable as maximum correlation levels approximate those of the estimated noise floor.

7.4.2 Correlation Results Along the Lipline.

The analysis of the data acquired in the experimental setup depicted in figure 7.4 is presented next. In this occasion, the TR-PIV velocity fluctuating components u' and v' measured along the lipline of the jet were cross-correlated with the output of 1- a single array microphone (Mic No.1) 2 - the beamformed phased array focused at the location of each of the TR-PIV vector fields.

The vector fields running along the centerline of each of the 5 TR-PIV windows depicted in figure 7.4 were chosen as the flow fluctuating variables. These were selected as they correspond to the jet's lipline. 54 out of the total of 64 vectors along the length of each TR-PIV window were used for calculations. As done previously with the TR-PIV data acquired along the jet's centerline, the first and last 5 vectors from each window were discarded as the data in these regions was found to be of lesser quality.

7.4.2.1 Normalized Cross-Spectrum (Coherence)

The calculated coherence between the in-flow variables u', v' and the signals from 1- a single array receiver 2- the steered array signal are presented in figures 7.27 and 7.28.

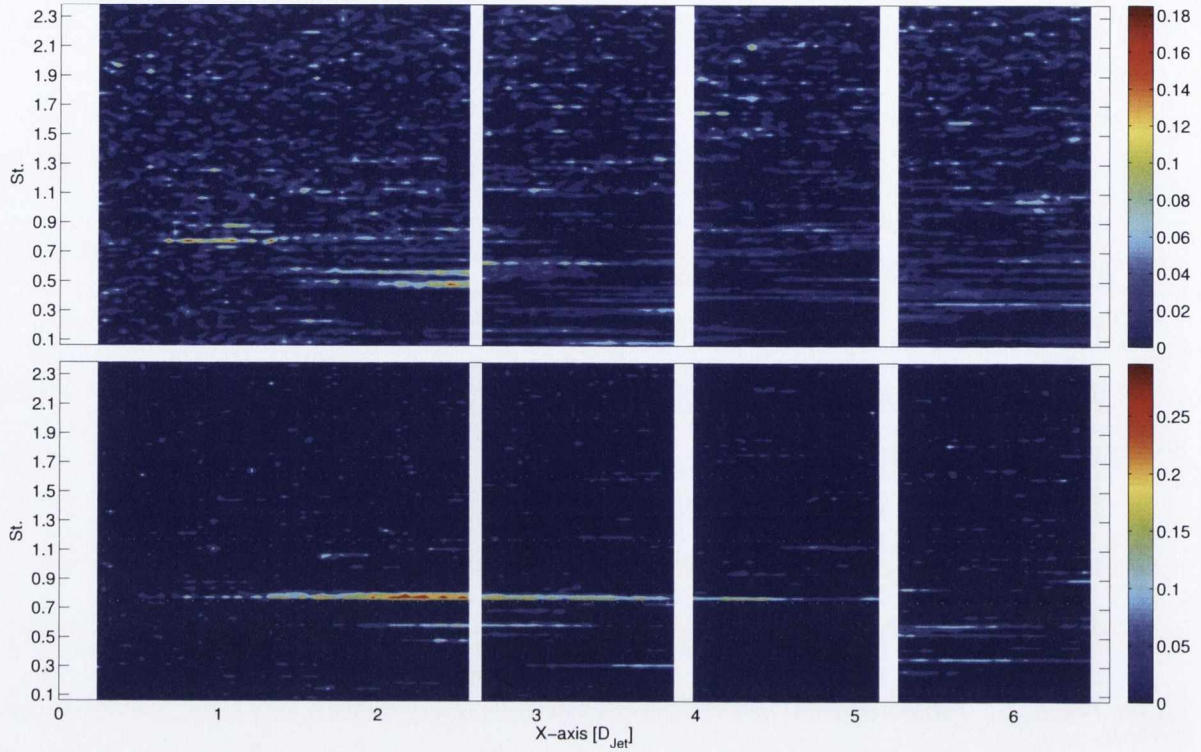

Figure 7.27: Top - Coherence output between u' and the acoustic pressure measured by a single array microphone (Mic No.1). Bottom - Coherence output between v' and the acoustic pressure measured by a single array microphone (Mic No.1).

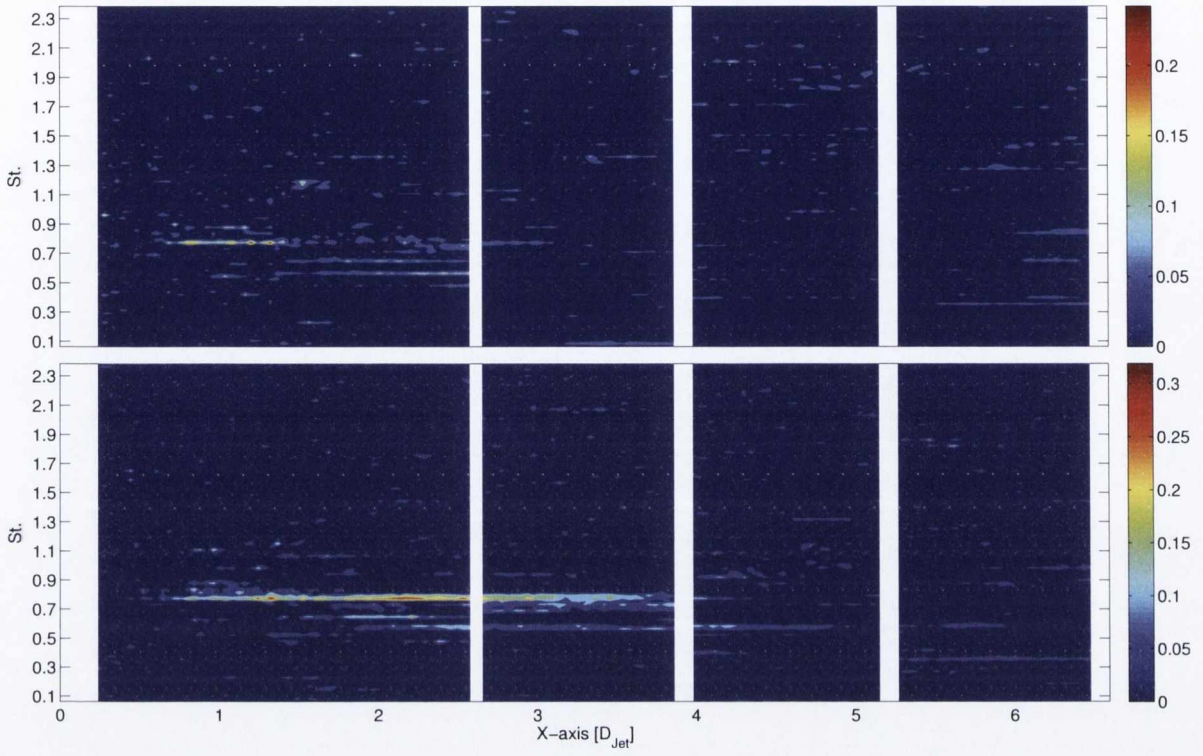

Figure 7.28: Top - Coherence output between u' and the steered array signal. Bottom - Coherence output between v' and the steered array signal.

As in the centerline case, improved coherence levels and a reduction in background levels, specially noticeable along the u' coherence output, are obtained by the coherence calculated between the flow variables and the beamformed signal (Figure 7.28 Top). Similarly, the calculated coherence is again dominated by a flow instability found at ≈ 0.77 Strouhal number that spans between 0.5-4 jet diameters downstream of the nozzle exit. The most noticeable difference with the centerline results shown in figures 7.19 and 7.22 is that, higher correlation coefficients between pressure and flow perturbations are now dominated by the v' component. These results suggest the presence of an organized narrowband flow instability that spans across the shear layer and the core of the jet flow. Equally, these results confirm that a linear relationship exists between the dominant extended narrowband instability measured at a 0.77 Strouhal number and the acoustic pressure measured at a broad angle from the jet axis.

The presence of a flow instability of these characteristics on low speed jets, coincides with those described in earlier studies by Fuchs [93], Crow and Champagne [11] and

Bradshaw [8].

Fuchs [93] and Crow and Champagne [11] reported, independently and making use of different flow measurement techniques, the existence of an orderly flow structure within the jet flow. By applying flow visualization techniques Crow and Champagne [11] found that the air flow within the first four jet diameters was dominated by an organized axisymmetric structure. They concluded that this was caused by an instability of the thin laminar boundary layer originated at the nozzle lip. In the case of Fuchs [93], significant correlation coefficients were reported between a fixed probe in the jet centerline and a moving probe placed at different locations along the, entrainment, lipline and centerline jet regions. The extent of these correlations spanned over $\approx$ 4 jet diameters in cases and were found to be dominated by a narrowband flow instability at a frequency corresponding to a 0.5 Strouhal number. The periodicity of these spacial correlations along the axial direction of the flow suggested the presence of a wave-like structure or "wave-packet" as referred to in modern literature. Even though no reference was made to the relation between the acoustic and hydrodynamic fields, the span and dominant flow characteristics of the dominant flow instabilities reported are similar to those presented here.

Similarly, Bradshaw [8] reported the presence of a narrowband fluctuation along the lipline of a jet of similar characteristics (D_{Jet}=0.05 & $u_j = 85m/s$) as the one used in this investigation. The PSD of the u' and more noticeably the v' component measured 2 jet diameters downstream along the jet lipline, was clearly dominated by a narrowband of energy at approximately 0.72 Strouhal number. This narrowband flow instability reported by Bradshaw, with a clearer peak in the PSD of the v' component, agrees well with the v' PSD results presented earlier in figure 7.10 and the coherence based cross-correlated measurements presented in figures 7.27 and 7.28.

7.4.2.2 Time Domain Cross-Correlation Coefficients

As shown by the centerline results, significant coherence levels between in-flow and acoustic signals are not conclusive evidence of sound radiation being originated by the flow measured perturbations. This is again demonstrated by the time domain correlation signatures presented in figures 7.29 and 7.30. As in the previous example, all the microphone signals were band passed between the frequencies corresponding to Strouhal numbers 0.52

- 2.

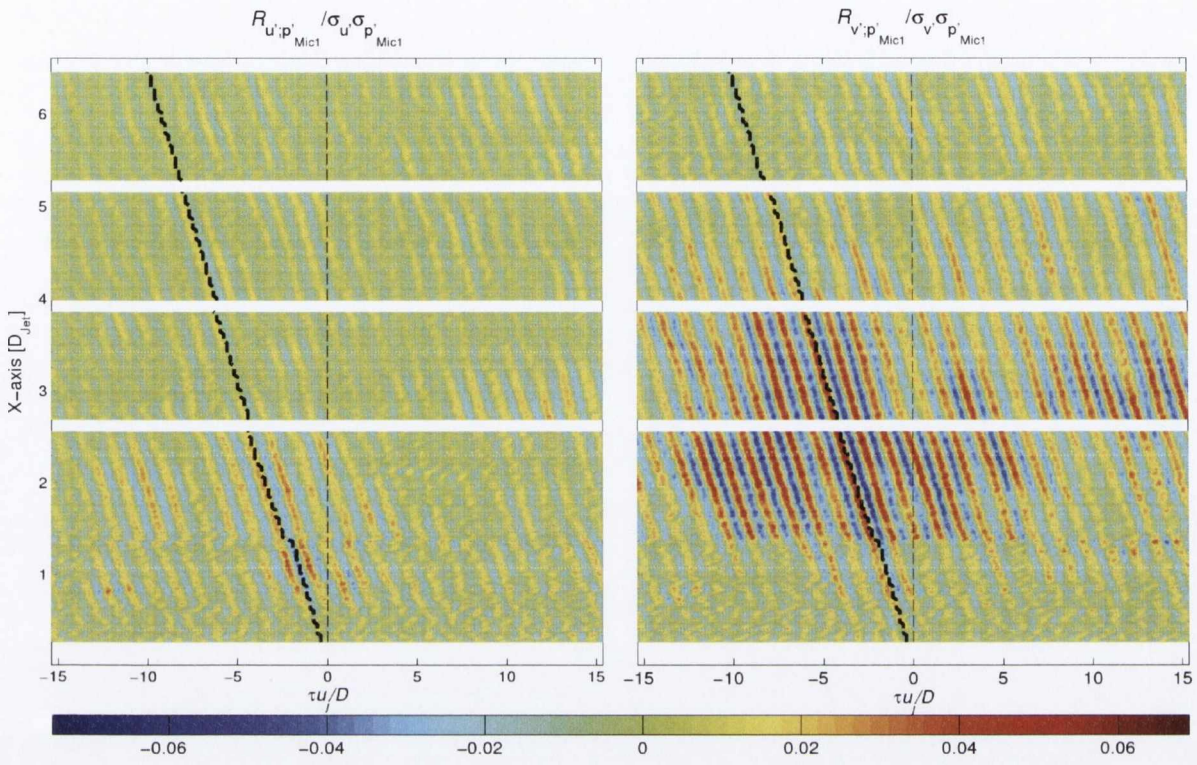

Figure 7.29: Normalised time domain correlations between a single array microphone (Mic No.1) and the flow velocity fluctuations measured along the jet's lipline. $[R_{<u';p'_{mic}>}/\sigma_{u'}\sigma_{p'_{mic}}]$(left), $[R_{<v';p'_{mic}>}/\sigma_{v'}\sigma_{p'_{mic}}]$(right). Dashed thin line −− represents expected peak correlation delay times based on straight wave propagation between each in-flow measurement and microphone location. Dashed bold line - - represents estimated peak correlation times based on a radiating convected source originating at the jet exit.

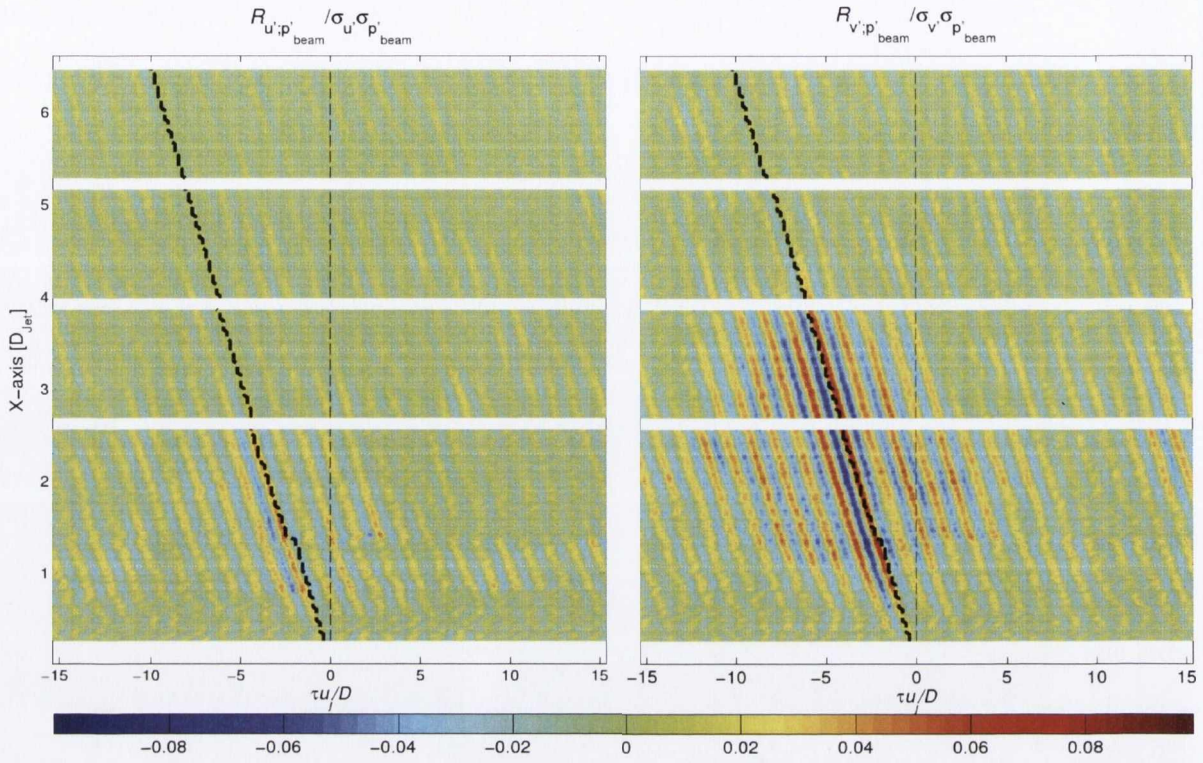

Figure 7.30: Normalised time domain correlations between the beamformed array output and the flow velocity fluctuations measured along the jet's lipline. $[R_{<u';p'_{beam}>}/\sigma_{u'}\sigma_{p'_{beam}}]$(left), $[R_{<v';p'_{beam}>}/\sigma_{v'}\sigma_{p'_{beam}}]$(right). Dashed thin line −− represents expected peak correlation delay times based on straight wave propagation between each in-flow measurement and microphone location. Dashed bold line - - represents estimated peak correlation times based on a radiating convected source originating at the jet exit.

As it could have been expected, based on the coherence based results, the time domain correlation signatures calculated between the acoustic pressure and the in-flow perturbations along the lipline are clearly dominated by the contribution of the v' component. Once again, correlation coefficient levels calculated with the steered array signal show a slight increase over those attained using the output of a single array receiver (Mic No.1). A noticeable difference between both results, is the reduction of the correlation extent along the temporal axis between the v' measured fluctuations and the steered array signal. Even though an answer for this was not sought, seems plausible to assume that this effect could be due to a broader frequency content in the signal recorded by the array aperture. However, the key piece of information to extract from these results, is that, as in the centerline case, the peak correlation values do not coincide with the expected straight propagation peak correlation delay times described by the thin dashed line along

$\tau u_j/\mathrm{D_{Jet}} = 0$. This is the case even in the time domain correlation signature calculated with the output of the array signal. Once again, peak correlation values follow closely the negative slope calculated using equation 7.1 under the assumption of a single compact radiating mechanism at the nozzle exit and the presence of correlated convected flow fluctuations at locations downstream along the lipline of the jet. In other words, the steered array signal does not suppress the contribution from a radiating mechanism at the nozzle exit when the array is steered at locations further downstream. As before, these results demonstrate that caution should be exerted when associating high correlation values to the presence of a radiating mechanism at the flow measured location. This is case even when a "reference" based beamforming algorithm is used to suppress/reduce the contribution from coherent sources arriving from third locations.

7.4.2.3 Max Cross-Correlation Coefficients Using a Fixed In-flow Measurement

In an attempt to identify the radiating region/s associated to the dominant extended flow instability measured at a 0.77 Strouhal number, the array signal steered along the jet axis was cross-correlated to the flow fluctuating quantities u' and v' measured 1.3 jet diameters downstream of the nozzle exit. The fluctuating quantities measured at this downstream location were selected as significant coherence levels were measured between the steered array signal and both fluctuating components u', v' (See figure 7.28).

The peak cross-correlation values between the steered array signal and the flow variables u' and v' measured at [$1.3D_{Jet}$,0,0] are presented in figure 7.31. In the same figure, the thin dashed line represents an estimate of the noise floor. This value represents the peak cross-correlation coefficient calculated between two randomly generated signals with the same number of points, mean and standard deviation as that of the time series of the in-flow and the beamformed signals.

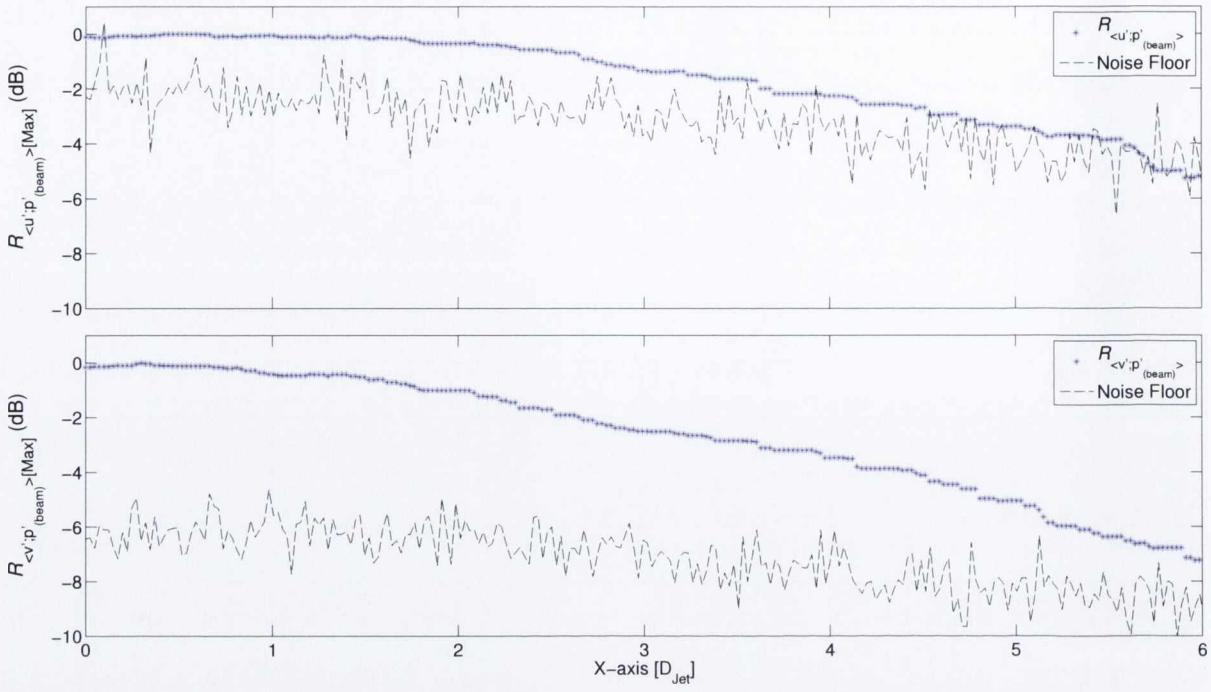

Figure 7.31: Peak correlation values in dB (dB ref.Max $R_{<u';p'_{beam}>}$ and $R_{<v';p'_{beam}>}$ respectively) between the TR-PIV vector field measured at [1.3D_{Jet},0,0] and the steered array signal. The beamform array was focused along the jet centerline in steps of 0.02 D_{Jet} from its origin [0,0,0] up to the location [6D_{Jet},0,0] downstream. The thin dashed line - - represents the noise floor levels calculated from two randomly generated signals with the same length and σ as that of the TR-PIV vectors and beamformed signals.

Maximum correlation levels between the array signal and the v' component measured at [1.3D_{Jet},0,0] are obtained when the array is steered upstream along the region between the nozzle exit and $\approx$ 0.5 jet diameters downstream. The maximum correlation levels drop to $\approx$ -7dB at a distance of 6 jet diameters downstream. This result suggest again that the main noise radiation associated to the dominant flow instability measured at a 0.77 Strouhal number is located in the vicinity of the nozzle exit. However, the curve does not produce a clear single peak that could be associated to the radiation of a compact source. A much higher array resolution would have been desirable for this to be the case. The results obtained by cross correlating the u' component with the steered array signal, obtain highest correlation levels in the region between the jet exit and $\approx$ 1.2 jet diameters downstream. However, associating these correlation peak values to the existence of a linear relationship between u' and the steered array signal is questionable as correlation levels approximate those of the estimated noise floor between two uncorrelated randomly

generated signals.

7.5 Further Analysis

The data presented in previous sections identified a clear narrowband correlation centered a 0.77 Strouhal number between extended flow regions and the acoustic pressure measured at a broad angle from the jet exit. In the literature however, the characteristic spectra associated to broad angle radiation from unbounded free flows is defined by a rather broad spectra peaking at approximately 0.4-0.5 Strouhal numbers (see Tam et al. [13]). It is for this reason that the origin of this dominant flow-acoustic interaction is though to be generated by mechanisms other than those associated with undisturbed free turbulent flows. Further investigation was carried out in an attempt to determine if any of the components of the experimental rig was responsible for the presence of the measured narrowband flow disturbance. In the first instance, the blade passing frequency (BPF) of the motor in the experimental rig was estimated. The BPF was found to correspond to a 0.2 Strouhal number and therefore its contribution to the dominant flow-acoustic interaction measured at a 0.7 Strouhal number was dismissed. A second approach tried to identify direct correlation between solid surfaces along the nozzle exit and the acoustic pressure measured in the acoustic field. To do this, a laser vibrometer was focused at separate locations along the nozzle and nozzle port whilst a single microphone was located at an angle of 45 degrees from the jet axis as shown in figure 7.32. [7]

[7]The location of the microphone was chosen as a compromise between broad and shallow angle radiation (i.e 90° & 30°) as further flow-acoustic array measurements, not considered in this investigation, were acquired at a shallow angle from the jet axis. The author agrees that direct comparison measurements should have been carried out by location the microphone at the broad angle location corresponding to the array location, however these results can be used to determine if any of the solid surfaces under consideration is well correlated to the acoustic pressure in the acoustic field.

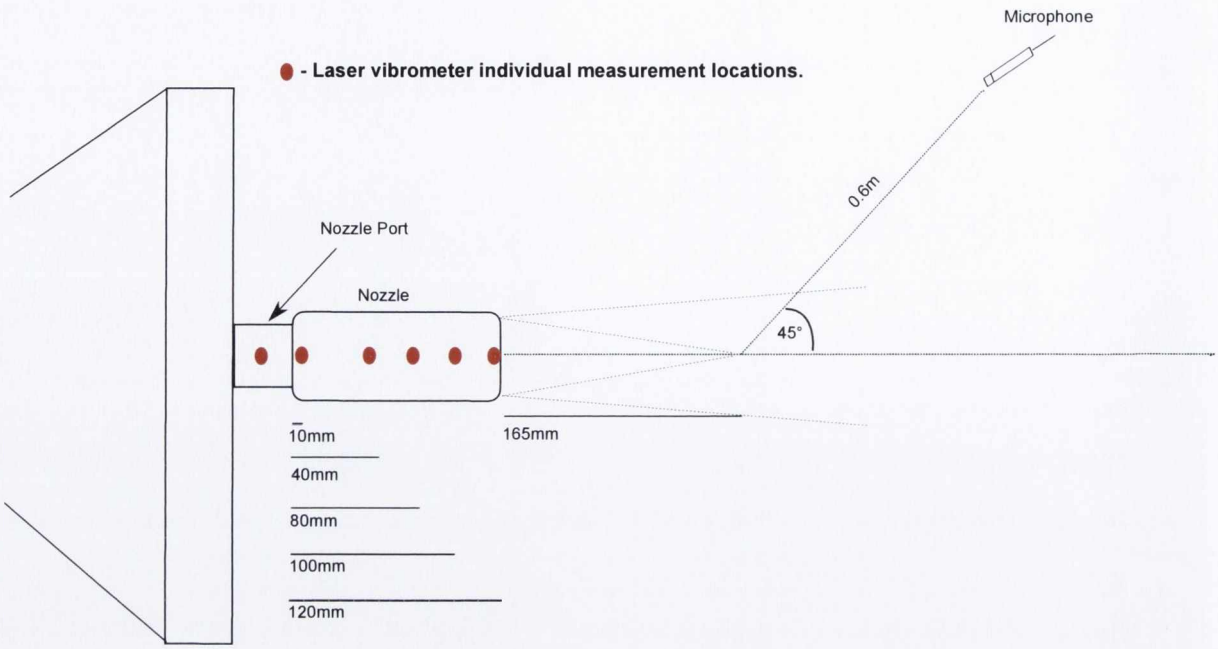

Figure 7.32: Vibro-acoustic test set up. Red circles represent the individual location where the vibrometer was focused along the solid surfaces surrounding the jet exit region.

The calculated coherence between the vibrometer signal at each of the measured locations and the acoustic pressure at the microphone location is shown in figure 7.33.

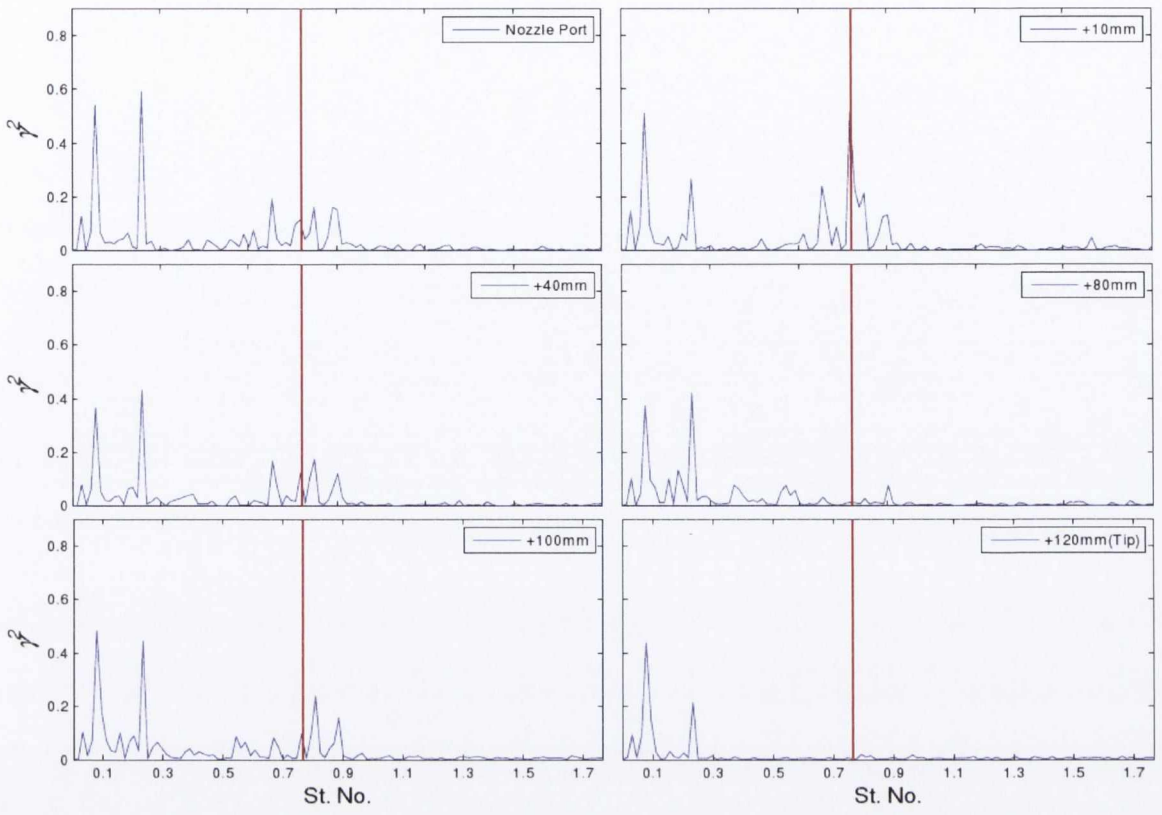

Figure 7.33: Calculated coherence between the laser vibrometer signal and a single microphone in the acoustic field. Red bold vertical line depicts the location of the 0.77 Strouhal No. along the x-axis.

Little correlation is measured between the microphone and vibrometer signal when this one is located along the nozzle's tip and mid section (i.e. 40, 80, 100 & 120mm from the nozzle base). However, when the vibrometer is placed in the aft section of the nozzle, a clear 0.5 amplitude peak is observed at the approximate 0.77 Strouhal number (see red vertical bold line). This result coincides with the dominant flow-acoustic interaction measured between the jet flow and acoustic pressure shown in previous sections. An interaction between flow and solid surfaces at this location could well be associated to the narrowband source mechanism identified in previous sections. In other words, based on these results and the characteristics of the source in question, it is save to assume that the dominant flow-acoustic interaction measured at a 0.77 Strouhal number is the produce of a mechanism other than those expected from free flow turbulence. Despite of this particularity, the application of a steered array signal in combination with that of a TR-PIV is still justified as the output did identify a clear correlation between in-flow and

acoustic signals and the presumed location of a dominant radiating mechanism.

7.6 Concluding Remarks

The results presented in this chapter showed a clear interaction between an extended region of the flow and the acoustic pressure measurements acquired at a broad angle from the jet exit. A narrowband flow instability at a frequency corresponding to a 0.77 Strouhal number, that spanned not only axially but radially across the jet, was found to dominate the acoustic-flow measured correlations. However, as shown by the time domain correlation signatures, caution should be exerted when associating the measured acoustic pressure to the presence of a radiating source at the in-flow measurement location.

The negative slope followed by the peak coefficients of the time dome cross-correlation signatures, agreed well with the peak correlation delays estimated under the assumption of a localized radiating mechanism at the nozzle exit and the presence of associated flow instabilities convected along the jet's flow. Whilst increased correlation levels were consistently reported by the use of a steered array signal, the cross-correlation signatures calculated with the steered array signal did not provide new information about the specific source/s location when compared to those attained by the use of a single receiver.

It was only when the array signal, steered along the jet axis, was correlated with that of a single "reference" in-flow measurement that maximum correlation levels were reported upstream at the nozzle exit. These results again suggested the presence of a dominant source mechanism at the nozzle exit. However, the array resolution was insufficient to define a clear curve that could be associated to the presence of a single compact source at this location.

These findings can be contrasted to those presented in section 6.2, in which the source location was well defined thanks to the increased array resolution available. In that occasion however, in addition to the aforementioned increased resolution, the source type impinging on the array aperture approximated that assumed by the array algorithms' ansatz. That is a, compact, uncorrelated source type with homogeneous directivity across the array aperture. In the free flow case presented in this chapter however, the specific source characteristics are not so clear. Whilst the flow-acoustic observations assumed the

presence of uncorrelated eddies as those described by Lighthill's source theory, the flow-acoustic measured interactions suggested the presence of narrowband flow instabilities correlated over distances far exceeding the integral scales of turbulence. The signature of this measured flow-acoustic interaction lead to the conclusion that the source under study was not representative of free flow turbulence sound propagation. In other words, the measured flow-acoustic interactions were affected by a inherent characteristic of the experimental rig.

In the cases where the proposed flow-beamformed correlation technique is directed to the study of free flow turbulence where the presence of extended coherence sources has been well documented (see Jordan and Colonius [17]), the sound emitted from different parts of an extended coherent source region is bound to mutually interfere in the acoustic field (see Fuchs [93]). This interference would produce a clearly defined source directivity and possible coherence loss across an extended aperture in the acoustic field. Based on these findings, a question can be raised about the suitability of a "reference" based beamforming algorithm that uses a simplistic omnidirectional compact source ansatz when trying to determine the source/s location in the presence of what clearly could be an extended correlated source with complex directivity. The work presented in the following chapter tries to answer this question by varying the parameters on a simplified extended source model and an optimized linear array aperture.

Chapter 8

Case 3: Modeled Convected Correlated Source

The output of the "reference" based beamforming algorithm presented in the previous chapter, identified the jet exit as the main radiating region associated to an extended, narrowband flow instability measured across the jet's flow. However, it was argued that the characteristics of the source generated by such flow structure may well depart from those assumed by the array algorithm. Based on this, a question was raised about the suitability of a "reference" beamforming algorithm under such conditions. The work presented next, attempts to answer this question by simulating a case scenario where a known narrowband, extended convected source mechanism is cross-correlated with the output of an array aperture via the delay-and-sum based "reference" beamforming algorithms introduced in section 3.1.1.

8.1 Simulated Source and Microphone Signals

A similar approach to that presented by Breakey and Fitzpatrick [53] was used to simulate this setup. A monochromatic, convected, wave-packet type source, as that described by Cavalieri et al. [94], was generated by a line of correlated monopoles localised in time by a gaussian envelope using

$$q(x,t) = A\cos[2\pi f_s(t - \frac{x}{U_c})]exp[-|t - \frac{x}{U_c}|/t_c] \tag{8.1}$$

where A is the source amplitude, f_s is the source frequency, x is the source position along the axial direction, U_c is the convection velocity and t_c describes the temporal wave-packet

amplitude modulation. The extent of the generated source was determined by a separate gaussian function of the form

$$Env(x) = B\ exp[-(x - x_{sc})^2/h^2] \tag{8.2}$$

where B is the maximum amplitude of the envelope, x_{sc} is the centroid of the radiating region and h describes the spatial wave-packet amplitude modulation. The contribution to each of the array receivers from each of the source locations q was estimated using

$$Mic_n(t) = \frac{1}{4\pi r_n} \int_0^\infty q(x, t - r_n/c_0) Env(x) dx \tag{8.3}$$

where r_n is the distance between the source location and the n^{th} array receiver described by $Mic_{(n)}$ and c_0 represents the acoustic propagation speed.

All the correlated monopole signals $q(x,t)$ were generated in the time domain at the sampling frequency f_{samp} (see table 8.1). The corresponding delayed microphone signals were generated by evaluating each source q at the retarded time $q(t - r_n/c_0)$ and multiplied by the corresponding amplitude of the $Env(x)$ function and the spacing between source locations dx. The parameters chosen for the two separate simulations carried out are presented in tables 8.1 and 8.2.

8.2 Test Layout

The simulation layout is presented in figure 8.1. All distances were normalized by the diameter of the nozzle ($D_{Jet} = 0.05m$) used in the previous chapter. A linear 25 equispaced receivers array was located at an angle of 90 degrees parallel to the axis of the convected line of monopole sources created along the x-axis between $[0 - 10D_{Jet}, 0]$. The frequency of the simulated source f_s was chosen so as to obtain an array resolution (-3dB) of approximately 2 jet diameters. An example of the generated source and the estimated Point Spread Function (PSF) of the equispaced linear array to a point source at the location $[5D_{Jet}, 0]$ is shown in figures 8.2 & 8.3.

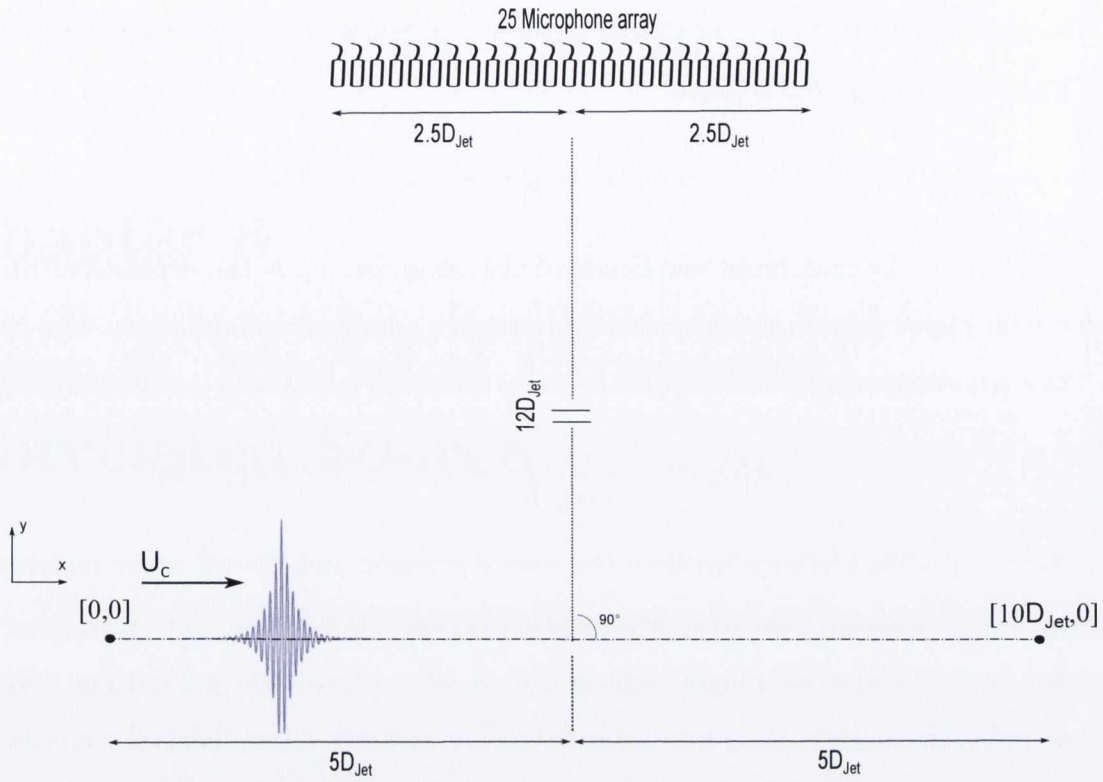

Figure 8.1: Layout of the simulation setup and example of the simulated convected source along the x-axis.

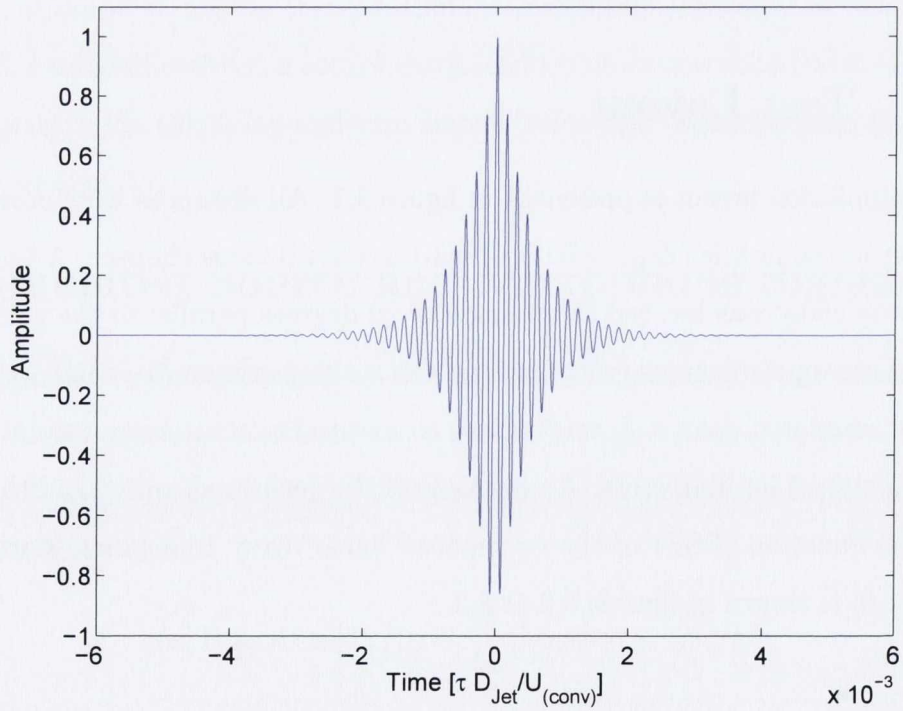

Figure 8.2: Simulated source example.

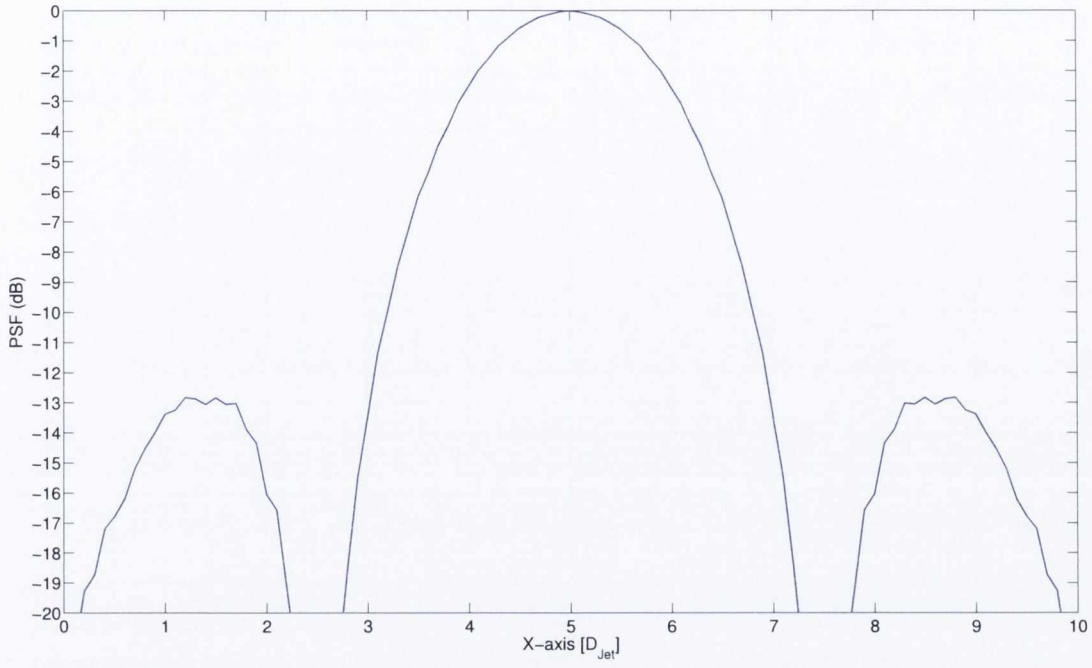

Figure 8.3: Array's Point Spread Function (PSF) for a 6.5kHz monopole source located at $[5D_{Jet}, 0]$.

8.3 Simulation Results

Figure 8.4 presents the location of the coherent monopole source grid generated along the x-axis and the spatial characteristics of the gaussian function $Env(x)$ that was used to determine the radiation extent and amplitude at each monopole location along the x-axis. The parameters chosen for this simulation are presented in table 8.1.

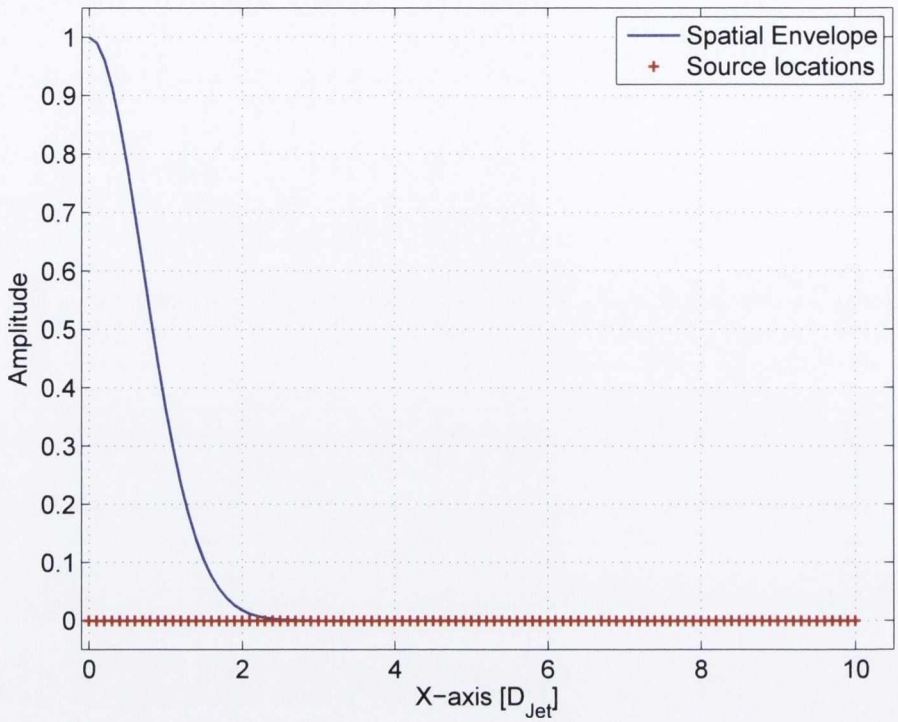

Figure 8.4: Grid of locations generated for the convected instability and amplitude and spatial extent of the gaussian function $Env(x)$.

$A = 1$	$f_{samp} = 250\text{kHz}$	$U_c = 100m/s$	$x_{sc} = 0$	$h = 0.05$
$t_c = D_{Jet}/U_c$	$-20D_{Jet}/U_c < t < 20D_{Jet}/U_c$	$B = 1$	$f_s = 6.5\text{kHz}$	$dx = D_{Jet}/1$

Table 8.1: Case 1 simulation parameters.

Figure 8.5 shows the calculated directivity across the array microphones for the source generated with the simulation parameters presented in table 8.1. To account for the difference in propagation decay between receivers, the source amplitude was normalised to that observed at the array center. This was done by multiplying each microphone signal by the ratio r_n/r_c where r_c is the distance between the array focal location and the center of the array. A small variation in source intensity of approximately 1dB is observed between the array receivers. In other words, the radiation of the simulated convected extended source is homogeneous over the array aperture. As pointed out by Kinns [59] and Billingsley & Kinns [22], the array output can only reproduce the source region when 1- the array resolution is larger than that of the extent of source correlated components, 2- the directionality of the source region does not lead to large changes in signal intensity

across the microphone array. Both of these conditions are met by the source generated using the parameters shown in table 8.1. This is clearly seen in the output of the delay-and-sum beamforming algorithm shown in figure 8.6. The array output clearly reproduces the source region generated in figure 8.4 convolved with the PSF of the array aperture shown in figure 8.3. The main source location is identified at $[0, 0]$ whilst secondary lobes corresponding to the main source appear at $\approx$ -13dB further downstream of the x-axis.

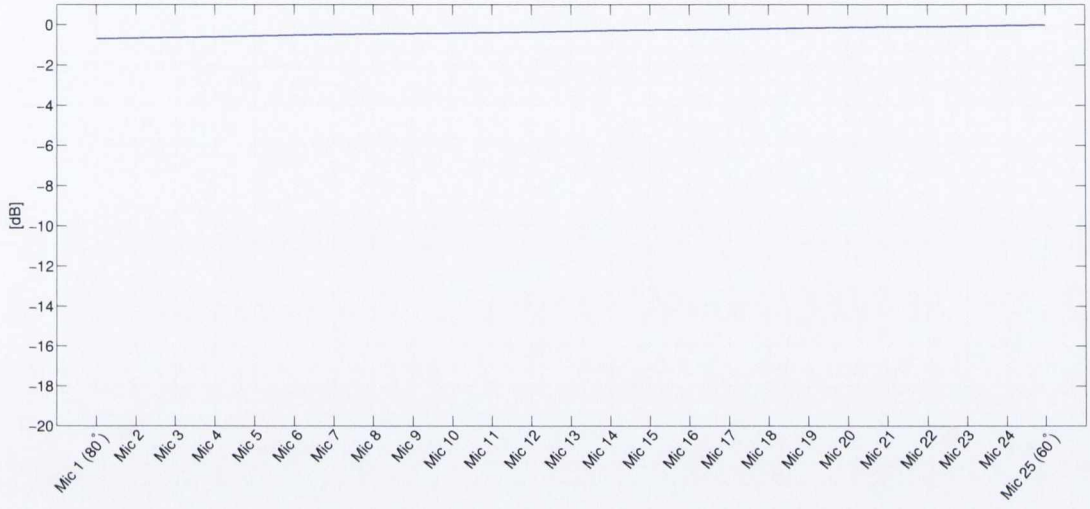

Figure 8.5: Source intensity variation across the array receivers. The polar angle sustained by the first and last array microphones with respect to the axis origin [0,0] is detailed in the abscissa label.

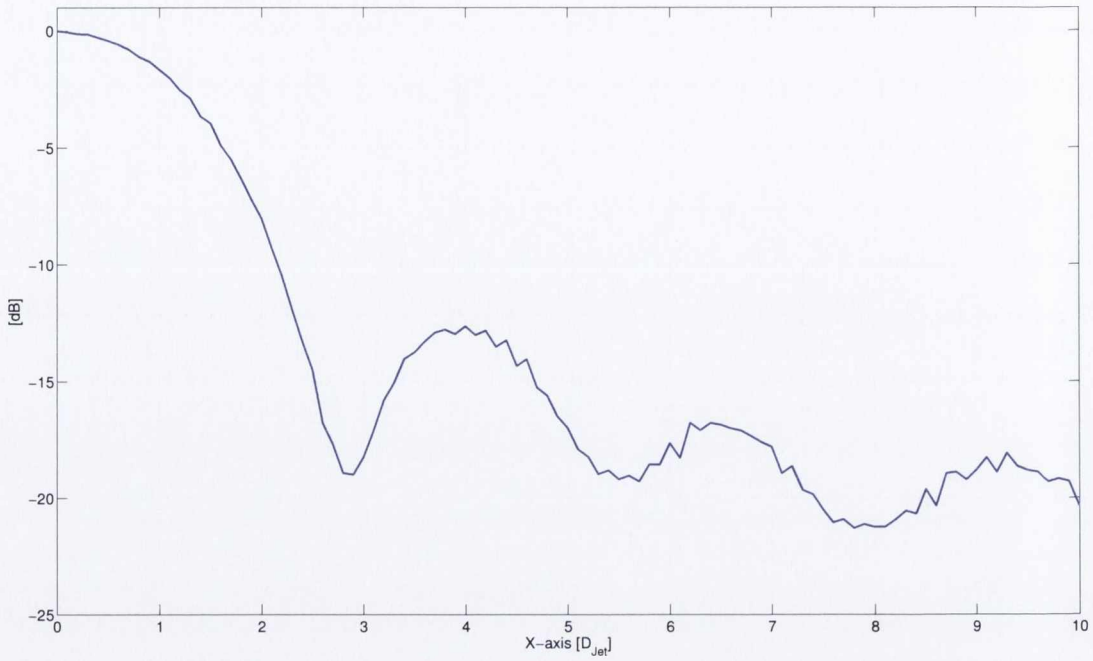

Figure 8.6: Output of the delay-and-sum beamforming algorithm (microphone data only).

The un-normalized peak cross-correlation values measured between the delay-and-sum array signal focused at each grid location along the x-axis and its corresponding simulated source are presented in figure 8.7. The thin dashed line represents an estimate of the noise floor. This value was calculated by cross-correlating two randomly generated signals with the same number of points, mean and standard deviation as that of the time series of the steered array signal and the simulated source at each position along the x-axis.

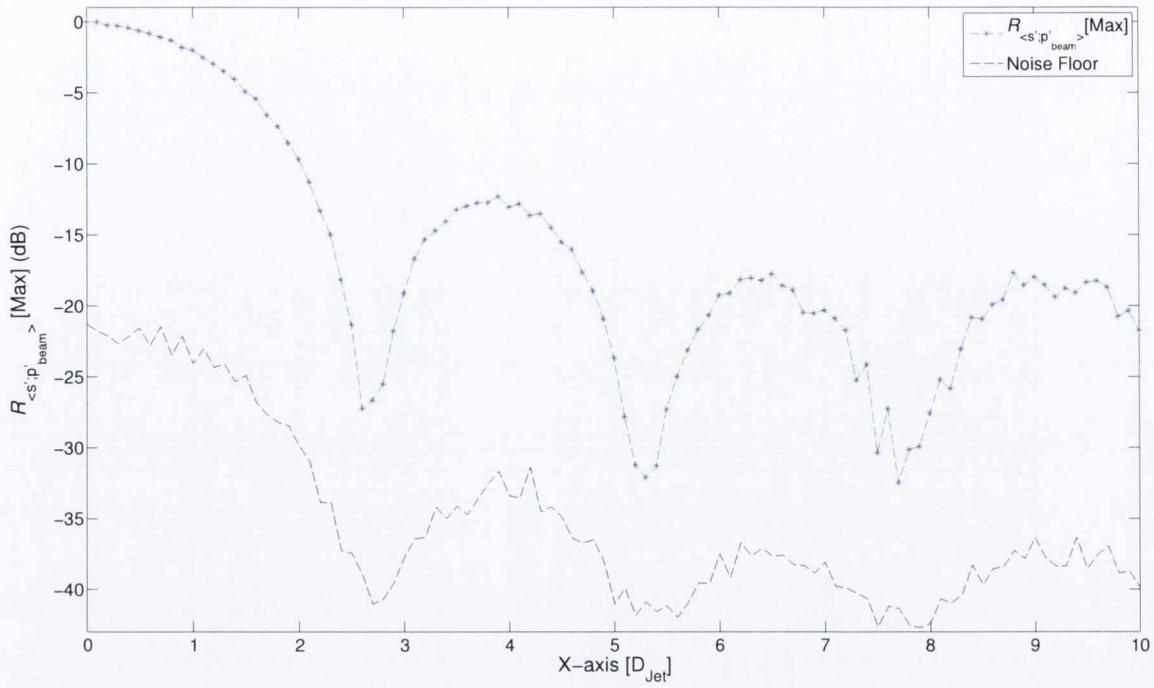

Figure 8.7: Peak cross-correlation values calculated between the generated signal at each grid location and the output of the steered array signal.

Peak cross-correlation levels between the steered array signal and the convected source are measured at the location of the source centroid x_{sc}. In this occasion, a well defined main lobe between $\approx 0 - 2.5D_{Jet}$ determines the location of the source along the x-axis. Secondary lobes appear at $\approx$ 13dB below that of the peak value. These can not be attributed to the presence of secondary sources as they appear below the sidelobe levels measured in the array PSF shown in figure 8.3. Similarly, the spatial filtering effects introduced by the steered array signal can be observed in the un-normalized time domain cross-correlation signature shown in figure 8.8.

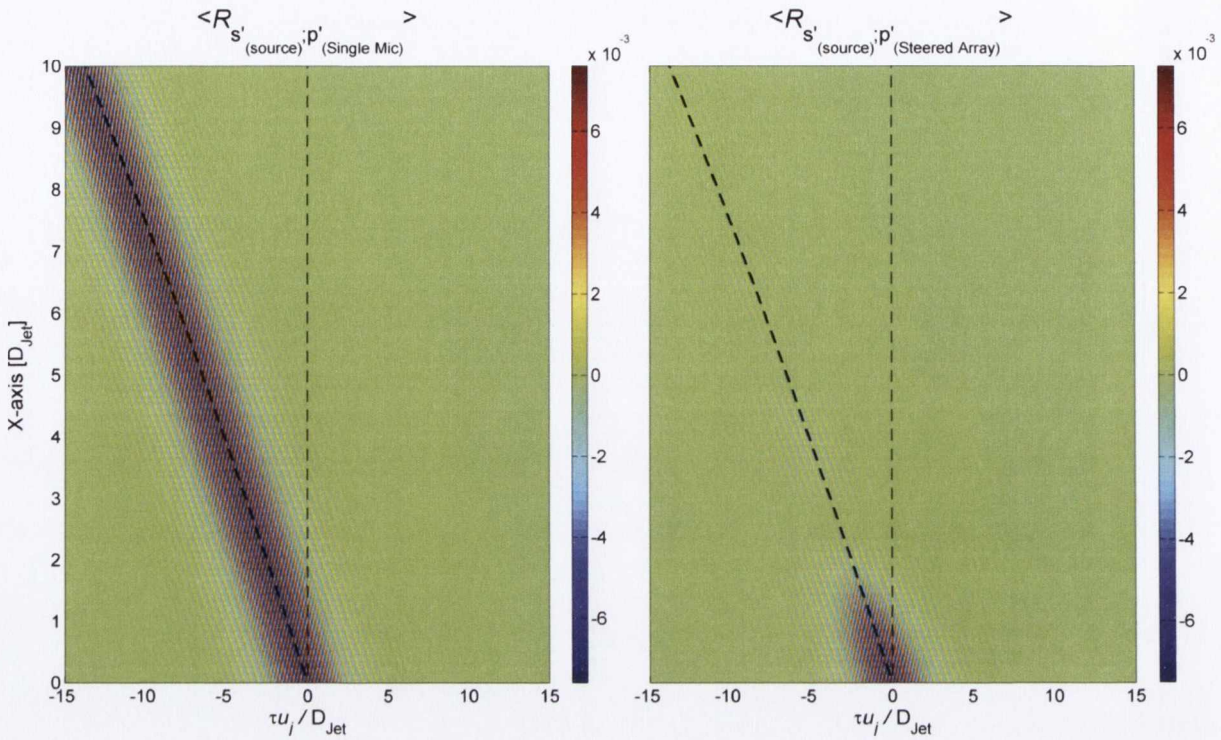

Figure 8.8: Time domain correlations between the convected wave-packet type source along the x-axis and 1- a single microphone at the array center (left) 2- steered array signal (right). The dashed thin line −− represents expected peak correlation delay times based on straight wave propagation between each grid location along the x-axis and the array center and/or single microphone location. The dashed bold line - - represents the estimated peak correlation times based on a radiating convected source present at the axis origin [0,0].

The peak correlation coefficients calculated between the signal generated at each grid location and the output of a single microphone at the center of the array (Mic No.12), follow the negative slope described by the thick dashed line estimated using equation 7.1 under the assumption of a radiating source mechanism at the axis origin ($x_{sc} = [0, 0]$). As the microphone response is omnidirectional, high correlation levels are measured over the full extent of the x-axis. In contrast, the time domain correlation signature calculated using the steered array signal, shows the spatial filtering effects of the array aperture when its maximum response is focused away from the source location. Peak correlation levels follow the same negative slope for the first 2 jet diameters along the x-axis. However, the amplitude of these is clearly suppressed at locations further downstream. In other words, the contribution of the source at the upstream location [0,0] is minimized by the spatial filtering characteristics of the array. It is for this reason that

the un-normalized cross-correlation coefficients rapidly decay when these are estimated between non-radiating grid locations along the x-axis and the beamformed array signal.

A second simulation was carried out to demonstrate the limitations of an experimental arrangement as that shown in figure 8.1 when the radiating pattern of the source under study departs from the assumed homogeneous radiation across the aperture of the array. The parameters used in this second scenario are presented in table 8.2.

$A = 1$	$f_{samp} = 250\text{kHz}$	$U_c = 100m/s$	$x_{sc} = 5D_{Jet}$	$h = 0.025$
$t_c = D_{Jet}/U_c$	$-20D_{Jet}/U_c < t < 20D_{Jet}/U_c$	$B = 1$	$f_s = 6.5\text{kHz}$	$dx = D_{Jet}/10$

Table 8.2: Case 2 simulation parameters.

The grid of coherent convected source locations and the shape of the gaussian function $Env(x)$ that defines the radiating region are presented in figure 8.9. The calculated variation in source intensity across the array microphones is shown in figure 8.10. In this occasion, the effects of destructive interference across the array microphones is evident. The effects of this difference in source intensity across the array aperture are clearly observed in the output of the delay-and-sum beamforming algorithm shown in figure 8.11. As noted by Billingsley & Kinns [22] in this instance the array algorithm, which assumes a point source with omnidirectional radiation, is unable to approximate the source region presented in figure 8.9.

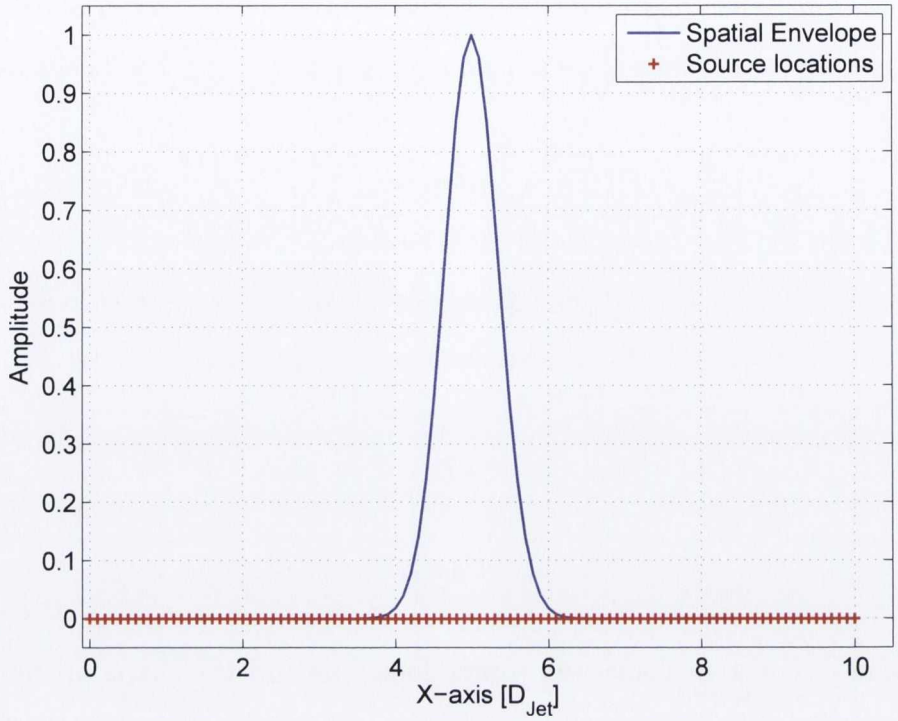

Figure 8.9: Grid of locations generated for the convected instability wave and amplitude and spatial extent of the gaussian function $Env(x)$.

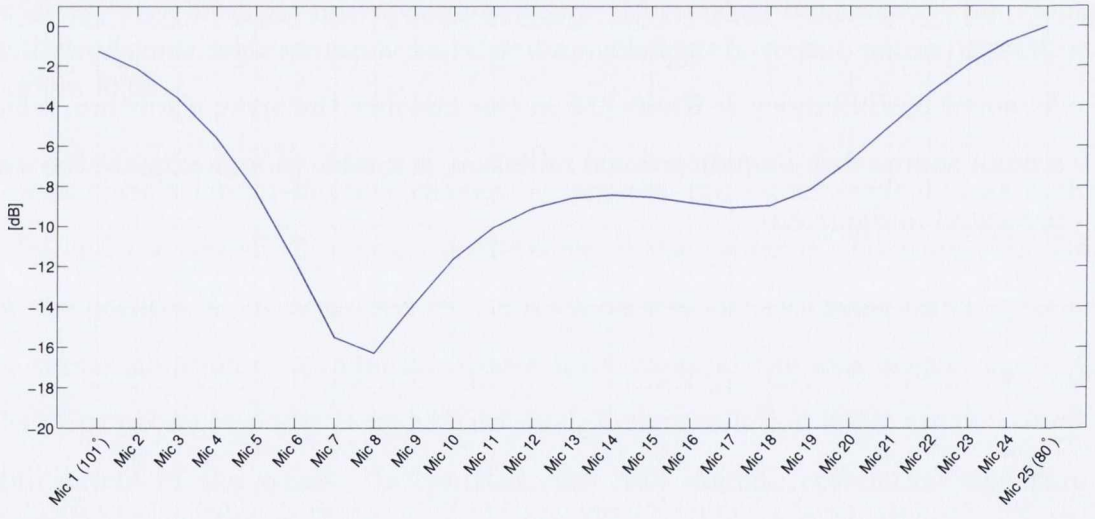

Figure 8.10: Source intensity variation across the array receivers. The polar angle sustained by the first and last array microphones with respect to the axis origin [0,0] is detailed in the abscissa label.

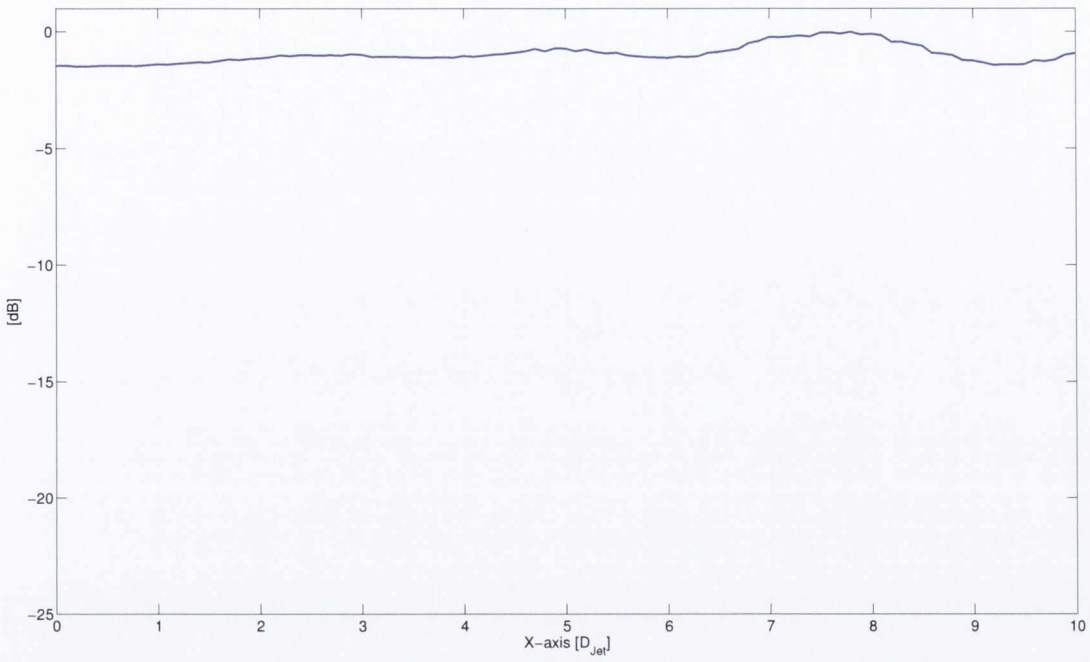

Figure 8.11: Output of the "delay-and-sum" beamforming algorithm (microphone data only).

These effects are in turn translated to the cross-correlation calculated between the steered array signal and the modeled convected source (see figure 8.12). Peak correlation levels are attained 8 diameters downstream along the x-axis. This result clearly misinterprets the characteristics of the source field presented in figure 8.9.

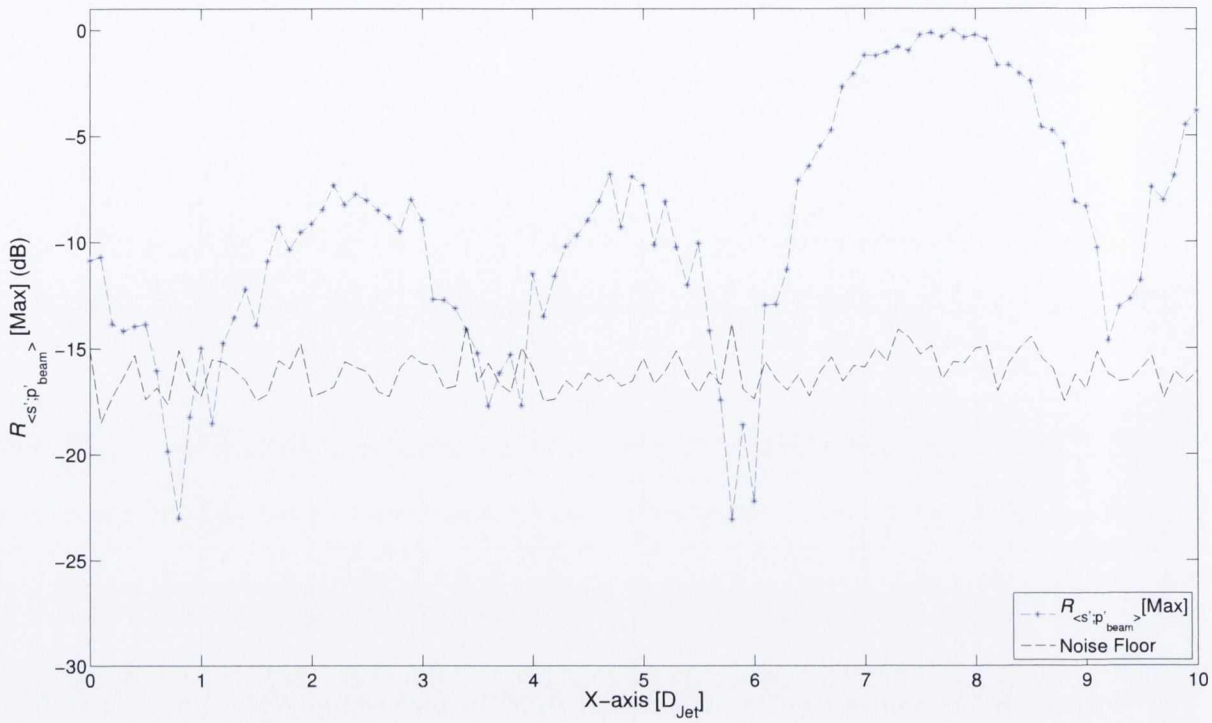

Figure 8.12: Peak cross-correlation values calculated between the generated signal at each grid location and the output of the steered array signal.

The time domain cross-correlation signature presented in figure 8.13 further proves this. The delay of the peak correlation coefficient measured at ≈ 8 diameters along the x-axis, clearly does not correspond to the direct propagation delay expected for a radiating source present at this location represented by the thin dashed line along $\tau u_j / D_{Jet} = 0$. Instead, peak correlation levels still follow the negative slope calculated under the assumption of a compact radiating mechanism present at $[5D_{Jet}, 0]$ represented by the thick dashed line. However, maximum cross-correlation coefficients are measured when the array is focused at third locations away from the radiating mechanism. This in turn can lead to misinterpretations when trying localize the source generating mechanism.

The peak levels of the correlation signature calculated with the output of the single array microphone (Mic No.12), also follow the estimated delay under the assumption of a source mechanism present at $[5D_{Jet}, 0]$. Surprisingly, in this occasion, a slight shift of $\approx 1 \cdot \tau u_j / D_{Jet}$ can be observed in the delay between the estimated and measured correlation peaks. An explanation for this slight shift could be that, even though the source centroid x_{sc} is located at $5D_{Jet}$, a region further upstream ($\approx 4.5D_{Jet}$) is responsible

for maximum radiation towards the single microphone location.

Another interesting point that can be drawn from these results is shown by the difference in the correlation levels measured between the generated source and the output of the single microphone and steered array signals. The loss of coherence across the array aperture, causes the absolute levels of the cross-correlation coefficients to drop below those attained by the use of a single receiver. Recalling that one of the main aims behind the use of an aperture array in this type of studies was to improve correlation levels between flow and acoustic observations, this result shows how its use can be detrimental under certain conditions.

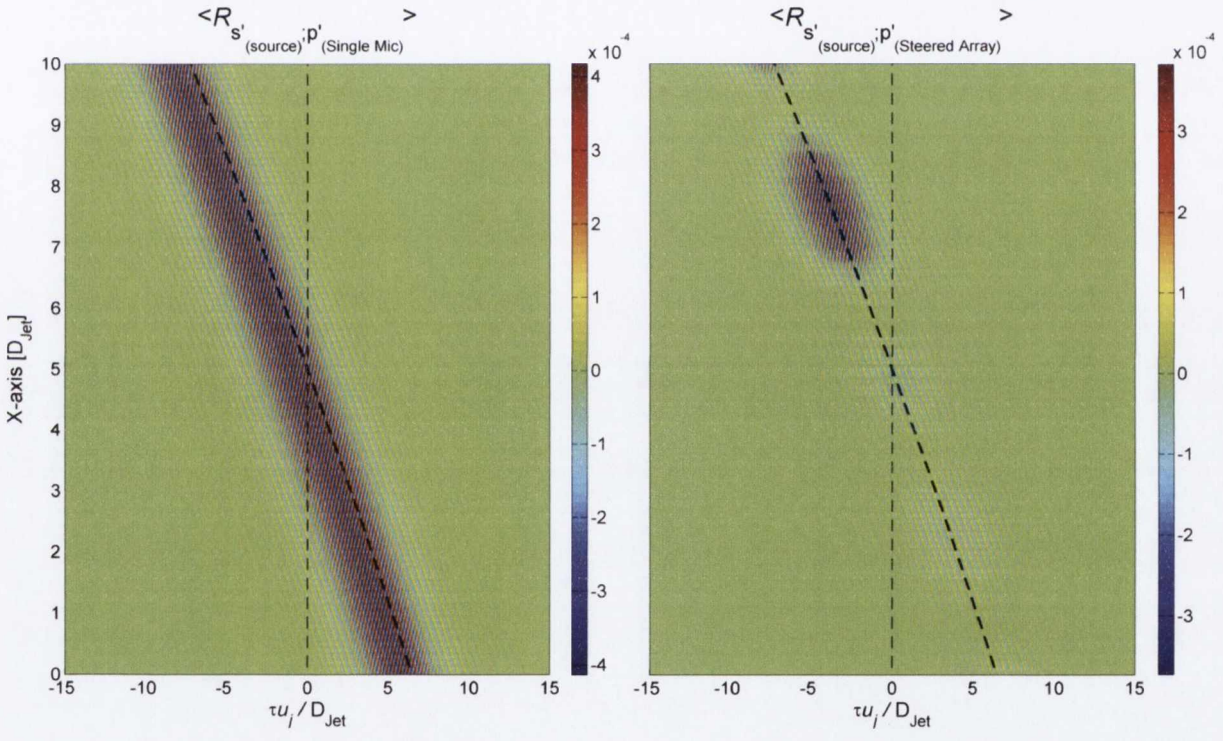

Figure 8.13: Time domain correlation signatures calculated between the convected wave-packet type source along the x-axis and 1- a single microphone at the array center (left) 2- steered array signal (right). The dashed thin line −− represents expected peak correlation delay times based on straight wave propagation between each grid location along the x-axis and the array center and/or single microphone location. The dashed bold line - - represents the estimated peak correlation times based on a radiating convected source present at location $[5D_{Jet},0]$.

These results highlight the limitations of the application of an array algorithm that assumes a field of omnidirectional, uncorrelated, compact source/s in the presence of a sound field generated by a non-compact source with complex directivity across the aper-

ture of the array. These limitations are also obvious when trying to characterize the sound field by cross-correlating the output of the steered array with that of the convected source mechanism at each location along the x-axis. However, as it was shown, there are potential benefits when using a steered array signal in these type of cross-correlation studies between the cause (source) and the effect (acoustic pressure) when the actual source mechanism/s characteristics approximate those assumed by the beamforming algorithm.

Chapter 9

Conclusion and Future Work

This chapter presents a summary of the conclusions from the previous chapters followed by suggestions for possible future work.

The work presented in this thesis was aimed at the characterization of the sound generated by flow instabilities by estimating the direct correlation between simultaneous flow-acoustic observations. To do this the output of two non-intrusive flow measurement techniques (i.e. LDV & TR-PIV) was combined with the acoustic pressure measured by an array of receivers. The two separate types of "reference" based beamforming algorithms used for this purpose where introduced in detail in chapter 3.

The source identification capabilities of the proposed beamforming techniques were experimentally validated in chapter 5. It was shown how both approaches were able to identify the location of the source/s of interest even when uncorrelated sources of much higher amplitude and overlapping frequency content were present within the test region. The same results also highlighted the need for a higher sample rate when applying the "reference" based algorithm which performed the spatial filtering process via the delay-and-sum algorithm. This particularity was found to be consistent with the experimental comparison of standard time and frequency domain beamforming techniques presented earlier in the chapter.

The first experimental campaign that made use of the "reference" based beamforming algorithms in conjunction with an in-flow measurement was presented in chapter 6. The first test setup, was designed to demonstrate the source identification capabilities of both types of "reference" based beamforming algorithms when an irregularly sampled LDV signal was used as "reference". In all cases, the origin of the radiating mechanism of interest

was successfully discriminated even when radiating mechanisms of similar amplitude and frequency content were present within the test region. However, a small discrepancy was observed between the location of the LDV in-flow measurement volume and the maximum output of the "reference" based array algorithms. Peak radiation was associated to a third location other than that of the LDV measurement volume. A separate test setup demonstrated how peak correlation levels between the "reference" and the steered array signal are independent of the location of the in-flow measurement. In other words, the "reference" based algorithms identify the peak radiating region associated to the perturbation measured by the in-flow device (LDV). These results were used to demonstrate how high correlation levels between in-flow and acoustic pressure signals do not constitute proof of noise emission by the in-flow measured fluctuations.

In the free flow study case presented in chapter 7, TR-PIV was used to sample the lip- and centerline of a Mach 0.25 jet whilst simultaneously, an array of receivers measured the acoustic pressure fluctuations at a broad angle from the jet exit. The measured flow-acoustic interaction was found to be dominated by an extended, narrowband flow instability at a frequency corresponding to a 0.77 Strouhal number. Further analysis directed to the characterization of this dominant flow-acoustic interaction, confirmed that correlation levels measured downstream of the jet exit where not the produce of direct radiation by the in-flow measured perturbations. Even though correlation levels were consistently improved by the addition of a steered array signal, the negative delays followed by the peak values in the estimated cross-correlation signatures agreed well with the assumed presence of a radiating mechanism at the nozzle exit. A similar conclusion was attained when the array signal, steered along the jet axis, was cross-correlated with the output of a fixed TR-PIV in-flow measurement location. Peak cross-correlation levels were attained when the steered array signal was focused at the jet exit location. However, due to limited array resolution at the corresponding frequency of the source of interest, the output of the "reference" based beamforming algorithm did not generate a clear lobe that could be associated to the presence of a single radiating mechanism. Improved array resolution would have been desirable for this to be the case.

All the results discussed above highlighted the capabilities of the different "reference" based beamforming algorithms applied in this investigation. Guidati's approach was

deemed superior for the study cases where a compact narrowband was present. Satisfactory results were achievable in this way whilst applying a much lower sampling frequency when compared to the "reference" based beamforming method that perform the spatial filtering in the time domain. In the cases where the characteristics of the source under study were more complex (i.e. free flow case), the time domain "reference" based algorithm was the preferred option due to its inherent broadband characteristics and the readily available spatial filtered time domain information. In addition, as shown in chapter 7, time domain based "reference" beamforming techniques are not limited by the sampling frequency achievable by the in-flow measurement device as the spatial filtering is performed prior to the cross-spectrum calculations with the in-flow measurement device. The experimental results attained in chapter 7 raised a question about the limitations of the "reference" based beamforming algorithms presented in chapter 3 in the presence of what could clearly be a non-compact, coherent, radiating mechanism. It was determined that the characteristics of such radiating mechanism could well depart from those assumed by the source ansatz in "reference" based beamforming algorithms. The simulation test presented in chapter 8 was designed to exemplify this scenario. The simulation results demonstrated how when the source characteristics (e.g. directivity) depart from those assumed by the array algorithm, this can lead to misinterpretations of the source field under study. These results highlighted the need for careful consideration when applying "reference" based algorithms in the presence of a source/s of unknown characteristics.

9.1 Future Work

The results presented in the free flow (jet) case study, identified the presence of extended flow coherent structures that were correlated with the acoustic pressure measured by an array of receivers located at a broad angle from the jet exit. Whilst the sound generation mechanisms behind free flow turbulence are out of the scope of this investigation, it is probable that the radiation of such flow structures may well depart from the assumed simplistic radiation assumed by standard array signal processing techniques. This being specially the case in those instances where the array aperture extends over large polar sections of the jet exit. It is in these occasions where the application of beamforming

algorithms that include a more representative source ansatz could shed new information about the source characteristics present in complex flows. A clear step in this direction has been presented recently by Koenig *et al.* [95]. In their study, a beamforming approach previously applied by Papamoschou [96] for the identification of compact uncorrelated source mechanisms, was adapted for the study of extended coherent "wave-packet" type sources. This source imaging method applies a minimization technique between a CSM calculated between the signal at the array receivers and a modeled CSM formed using an educated guess of the source mechanism. In their investigation similar results between the modeled and experimental CSM's where attained when a wave-packet type source was used to form the modeled CSM. Future research efforts in which array apertures in combination with in-flow statistics are directed to the study of complex sound fields, particularly as in the case of free flows, should allow to include a more representative source ansatz in the array algorithm. As global, non-intrusive, flow measurement techniques such as TR-PIV develop, these will allow to resolve flow characteristics over larger sections of the flow. This information, along with modal decomposition techniques, could potentially allow to identify the contribution of these measured flow characteristics by including their signature in the source ansatz of array signal processing approaches as that introduced by Koenig *et al.* [95].

Bibliography

[1] ACARE (Advisory Council for Aeronautical Research in Europe). European aeronautics: Vision for 2020, 2001. http://www.acare4europe.org/docs/Vision

[2] European Commission. Flightpath 2050 europes vision for aviation. *Report of the High Level Group on Aviation Research, DOI*, 10:50266, 2011.

[3] M. J. Lighthill. On sound generated aerodynamically. i. general theory. *Proceedings of the Royal Society of London. Series A, Mathematical and Physical Sciences*, 211(1107):564–587, 1952.

[4] Lawrence E Kinsler, Austin R Frey, Alan B Coppens, and James V Sanders. *Fundamentals of acoustics*, volume 1. Wiley-VCH, 4th edition edition, 1999.

[5] L. J. Ziomek. *Fundamentals of acoustic field theory and space-time signal processing.* CRC Press, 1995.

[6] P. Jordan and Y. Gervais. Modelling self- and shear-noise mechanisms in inhomogeneous, anisotropic turbulence. *Journal of Sound and Vibration*, 279(3-5):529–555, 2005.

[7] B.S. Massey and J. Ward-Smith. *Mechanics of fluids.* Taylor and Francis, 8th edition, 1998.

[8] P. Bradshaw, D. H. Ferriss, and R.F. Johnson. Turbulence in the noise producing region of a circular jet. *Journal of fluid Mechanics*, 19:591–625, 1963.

[9] W. K George. The self-preservation of turbulent flows and its relation to initial conditions and coherent structures. *Advances in Turbulence*, pages 39–73, 1989.

[10] E. Mollo-Christensen. Jet noise and shear flow instability seen from an experimenter's viewpoint. *Journal of Applied Mechanics*, 34:1–7, 1967.

[11] S.C. Crow and F.H. Champagne. Orderly structure in jet turbulence. *Journal of Fluid Mechanics*, 48(3):547–591, 1971.

[12] G.L. Brown and A. Roshko. On density effects and large structure in turbulent mixing layers. *Journal of Fluid Mechanics*, 64(04):775–816, 1974.

[13] C. Tam, M. Golebiowski, and J. Seiner. On the two components of turbulent mixing noise from supersonic jets. In *2nd AIAA/CEAS Aeroacoustics Conference*, State College, PA., 1996. American Institute of Aeronautics and Astronautics. doi:10.2514/6.1996-1716.

[14] C.K.W. Tam and P. Chen. Turbulent mixing noise from supersonic jets. *AIAA Journal*, 32(9):1774–1780, 1994.

[15] J.M. Seiner and E.A. Krejsa. Supersonic jet noise and the high speed civil transport. In *AIAA, ASME, SAE, and ASEE, 25th Joint Propulsion Conference*, volume 1, 1989.

[16] C.K.W. Tam, K. Viswanathan, K.K. Ahuja, and J. Panda. The sources of jet noise: experimental evidence. *Journal of Fluid Mechanics*, 615(1):253–292, 2008.

[17] P. Jordan and T. Colonius. Wave packets and turbulent jet noise. *Annual Review of Fluid Mechanics*, 45(1):173–195, 2013.

[18] D. Papamoschou. Wavepacket modeling of the jet noise source. In *17th AIAA/CEAS Aeroacoustics Conference*, volume 2835, Portland, Oregon, 2011.

[19] D.H. Johnson and D.E. Dudgeon. *Array signal processing: concepts and techniques.* P T R Prentice Hall, 1993.

[20] D.E. Dudgeon. Fundamentals of digital array processing. *Proceedings of the IEEE*, 65(6):898–904, 1977.

[21] B.D. Van Veen and K.M. Buckley. Beamforming: A versatile approach to spatial filtering. *ASSP Magazine, IEEE*, 5(2):4–24, 1988.

[22] J. Billingsley and R. Kinns. The acoustic telescope. *Journal of Sound and Vibration*, 48(4):485–510, 1976.

[23] L. J. Ziomek. *Fundamentals of acoustic field theory and space-time signal processing.* CRC Press, 1995.

[24] T.J. Mueller. *Aeroacoustic measurements.* Springer Verlag, 2002.

[25] P.Sijtsma. Experimental techniques for identification and characterisation of noise sources, 2004. Advances in Aeroacoustics and Applications, VKI Lecture Series 5 (2004): 15-19.

[26] R.P. Dougherty. Advanced time-domain beamforming techniques. In *Proceedings of the AIAA 10th AIAA/CEAS Aeroacoustics Conference and Exhibit.*, Reston, VA., 2004.

[27] M. W. Raffel, C.E. Wereley, and J. Kompenhans. *Particle Image Velocimetry A Practical Guide.* Springer, 2nd edition, 2007.

[28] L. Simon and J. Fitzpatrick. An improved sample-and-hold reconstruction procedure for estimation of power spectra from lda data. *Experiments in Fluids*, 37(2):272–280, 2004.

[29] R.J. Adrian and C.S. Yao. Power spectra of fluid velocities measured by laser doppler velocimetry. *Experiments in Fluids*, 5(1):17–28, 1986.

[30] L. Boyer and G. Searby. Random sampling: distortion and reconstruction of velocity spectra from fast fourier-transform analysis of the analog signal of a laser doppler processor. *Journal of Applied Physics*, 60:2699–707, 1986.

[31] J. Fitzpatrick and L. Simon. Estimation of cross-power spectra using sample-and-hold reconstruction of laser doppler anemometry data. *Experiments in Fluids*, 39(6):954–965, 2005.

[32] J.S. Bendat and A.G. Piersol. *Random data: analysis and measurement procedures.* John Wiley and Sons, Inc. New York, NY, USA, 1990.

[33] LaVision. Product manual for davis 7.2, (accessed on 04-2013 on http://www.lavision.de/en/techniques/piv.php) 2007.

[34] P. Jordan and Y. Gervais. Subsonic jet aeroacoustics: associating experiment, modelling and simulation. *Experiments in Fluids*, 44(1):1–21, 2008.

[35] H.K. Lee and H.S. Ribner. Direct correlation of noise and flow of a jet. *The Journal of the Acoustical Society of America*, 52:1280, 1972.

[36] T. E. Siddon. New correlation method for study of flow noise. In *Proceedings of the 7th International Congress of Acoustics*, pages pp. 533–536, Budapest, 1971.

[37] I. Proudman. The generation of noise by isotropic turbulence. *Proceedings of the Royal Society of London. Series A, Mathematical and Physical Sciences*, 214(1116):119–132, 1952.

[38] H.S. Ribner. Quadrupole correlations governing the pattern of jet noise. *Journal of Fluid Mechanics*, 38(01):1–24, 1969.

[39] J.M. Seiner and G. Retthof. On the distribution of source coherency in subsonic jets. In *12th Aerospace Sciences Meeting.*, Washington, D.C, 1974. AIAA-1974-4 14 p. NASA-supported research.

[40] P. H. White and T. D. Scharton. Simple pressure source model of jet noise. *The Journal of the Acoustical Society of America*, 51(1A):95–95, 1972.

[41] P. M. Hurdle, W. C. Meecham, and B. K. Hodder. Investigation of the aerodynamic noise generating region of a jet engine by means of the simple source fluid dilatation model. *The Journal of the Acoustical Society of America*, 56(6):1708–1721, 1974.

[42] T. E. Siddon. On noise mechanisms. noise sources diagnostics using causality correlations. In *AGARD CP 13 1*, 1973.

[43] M. Schaffar. Direct measurements of the correlation between axial in-jet velocity fluctuations and far field noise near the axis of a cold jet. *Journal of Sound and Vibration*, 64(1):73–83, 1979.

[44] D. Juve, M. Sunyach, and G. Comte-Bellot. Intermittency of the noise emission in subsonic cold jets. *Journal of Sound and Vibration*, 71(3):319–332, 1980.

[45] M. Schaffar and J. P. Hancy. Investigation of the noise emitting zones of a cold jet via causality correlations. *Journal of Sound and Vibration*, 81(3):377–391, 1982.

[46] J. Panda and R. G. Seasholtz. Experimental investigation of density fluctuations in high-speed jets and correlation with generated noise. *Journal of Fluid Mechanics*, 450(-1):97–130, 2002.

[47] J. Panda, R. G. Seasholtz, and K. A. Elam. Investigation of noise sources in high-speed jets via correlation measurements. *Journal of Fluid Mechanics*, 537(-1):349–385, 2005.

[48] A. Henning, K. Kaepernick, Kl. Ehrenfried, L. Koop, and A. Dillmann. Investigation of aeroacoustic noise generation by simultaneous particle image velocimetry and microphone measurements. *Experiments in Fluids*, 45(6):1073–1085, 2008.

[49] A. Henning, A. Schrder, I. Krebs, and J. Agocs. Aeroacoustic investigations on a cold jet by means of simultaneous piv and microphone measurements. In *15th Int Symp on Applications of Laser Techniques to Fluid Mechanics*, Lisbon, 2010.

[50] A. Henning, A. Schroder, and L. Koop. Causality correlation analysis on a cold jet by means of simultaneous piv and microphone measurements. In *16th AIAA/CEAS Aeroacoustics Conference 2010. 31st AIAA Aeroacoustics Conference*, pages 803–13, Reston, VA, USA, 2010.

[51] J. Veltin, B. J. Day, and D. K. McLaughlin. Correlation of flow and acoustic field measurements in high speed jets. In *15th AIAA/CEAS Aeroacoustics Conference (30th AIAA Aeroacoustics Conference)*, Miami, FL, United states, 2009.

[52] M. J. Doty and D. K. McLaughlin. Spacetime correlation measurements of high-speed axisymmetric jets using optical deflectometry. *Experiments in Fluids*, 38(4):415–425, 2005.

[53] D. Breakey and J. Fitzpatrick. Time-resolved piv for aeroacoustic source analysis. In *16th International Symposium on the Application of Laser Techniques to Fluid Mechanics*, Lisbon, Portugal, 2012.

[54] C. Bogey and C. Bailly. Investigation of downstream and sideline subsonic jet noise using large eddy simulation. *Theoretical and Computational Fluid Dynamics*, 20(1):23–40, 2006.

[55] C. Bogey and C. Bailly. An analysis of the correlations between the turbulent flow and the sound pressure fields of subsonic jets. *Journal of Fluid Mechanics*, 583(-1):71–97, 2007.

[56] J. Panda, R.G. Seasholtz, and K.A. Elam. Measurement of correlation between flow density, velocity, and density*velocity2 with far field noise in high speed jets. *AIAA-2002-2485 - NASA / TM–2002-211791*, 2002.

[57] J. I. Hileman, B. S. Thurow, E. J. Caraballo, and M. Samimy. Large-scale structure evolution and sound emission in high-speed jets: real-time visualization with simultaneous acoustic measurements. *Journal of Fluid Mechanics*, 544:277–307, 2005.

[58] D.Arthurs, J.Fitzpatrick, C.Bogey, and C. Bailly. Spectral estimation of the sound sources in jet flows. In *EURONOISE*, Edinburgh, Scotland., 2009.

[59] R. Kinns. Binaural source location. *Journal of Sound and Vibration*, 44(2):275–289, 1976.

[60] P.T. Soderman and S.C. Noble. A four-element end-fire microphone array for acoustic measurements in wind tunnels. In *8th AIAA/AT Conference*, volume AIAA paper 74-640, Bethesda, MD., 1974.

[61] T. F. Brooks, M. A. Marcolini, and D. S. Pope. A directional array approach for the measurement of rotor noise source distributions with controlled spatial resolution. *Journal of Sound and Vibration*, 112(1):192–197, 1987.

[62] W.M. Humphreys, T.F. Brooks, W.W. Hunter, and K.R. Meadows. Design and use of microphone directional arrays for aeroacoustic measurements. In *36 st Aerospace Sciences Meeting and Exhibit*, pages 98–0471, Reno NV, 1998. AIAA.

[63] R. K. Amiet. Refraction of sound by a shear layer. *Journal of Sound and Vibration*, 58(4):467–482, 1978.

[64] R.H. Schlinker and R.K. Amiet. Refraction and scattering of sound by a shear layer. *Final Report United Technologies Research Center, East Hartford, CT.*, 1, 1980.

[65] T.F. Brooks and W.M. Humphreys. Effect of directional array size on the measurement of airframe noise components. *AIAA paper*, 1958:10–12, 1999.

[66] S. Oerlemans, L. Broersma, and P. Sijtsma. Quantification of airframe noise using microphone arrays in open and closed wind tunnels. *International Journal of Aeroacoustics*, 6(4):309–333, 2007.

[67] S.S. Lee and J. Bridges. Phased-array measurements of single flow hot jets. In *11th AIAA/CEAS Aeroacoustic Conference*, Monterey, California, 2005.

[68] W.T. Chu, J. Laufer, and K. Kao. Noise source distribution in subsonic jets. *Internoise 72*, pages 472–476, 1972.

[69] F.R. Grosche. Distributions of sound source intensities in subsonic and supersonic jets. In *AGARD Conference Proceedings, CP-131*, 1973.

[70] S.R. Venkatesh, D.R. Polak, and S. Narayanan. Beamforming algorithm for distributed source localization and its application to jet noise. *AIAA Journal*, 41(7):1238–1246, 2003.

[71] D. Papamoschou and A. Dadvar. Localization of multiple types of jet noise sources. *AIAA paper*, 2644:21, 2006.

[72] C. K. W. Tam. Jet noise: Since 1952. *Theoretical and Computational Fluid Dynamics*, 10(1):393–405, 1998.

[73] C. K. W. Tam, N. N. Pastouchenko, and R. H. Schlinker. Noise source distribution in supersonic jets. *Journal of Sound and Vibration*, 291(1-2):192–201, 2006.

[74] T.F. Brooks and W.M. Humphreys. A deconvolution approach for the mapping of acoustic sources (damas) determined from phased microphone arrays. *Journal of Sound and Vibration*, 294(4-5):856–879, 2006.

[75] R. P. Dougherty. Extensions of damas and benefits and limitations of deconvolution in beamforming. In *Collection of Technical Papers - 11th AIAA/CEAS Aeroacoustics Conference*, volume 3, pages 2036–2048, Monterey, CA, United states, 2005. American Institute of Aeronautics and Astronautics Inc.

[76] R.P. Dougherty and G. Podboy. Improved phased array imaging of a model jet. In *15th AIAA/CEAS*, Aeroacoustics Conferences, Miami, Florida., 2009. American Institute of Aeronautics and Astronautics. doi:10.2514/6.2009-3186.

[77] P. Sijtsma. Clean based on spatial source coherence. *International Journal of Aeroacoustics*, 6(4):357–374, 2007.

[78] U. Michel. Influence of source interference on the directivity of jet mixing noise. In *13th AIAA/CEAS Aeroacoustics Conf., Rome, Italy, 2123 May 2007*, 2007.

[79] K. Viswanathan, M.L. Shur, P.R. Spalart, and M.K. Strelets. Computation of the flow and noise of round and beveled nozzles. In *12th AIAA/CEAS Aeroacoustics Conference*, pages 628–657, Cambridge, MA, United states, 2006. American Institute of Aeronautics and Astronautics.

[80] C.E. Tinney and P. Jordan. The near pressure field of co-axial subsonic jets. *Journal of Fluid Mechanics*, 611:175–204, 2008.

[81] R.P. Dougherty, J. Panda, and S.S. Lee. Non-intrusive jet noise study combining rayleigh scattering and phased array measurement techniques. In *11th AIAA/CEAS*

Aeroacoustics Conference, Aeroacoustics Conferences, Monterey, California, 2005. American Institute of Aeronautics and Astronautics. doi:10.2514/6.2005-2843.

[82] H.A. Siller, F. Arnold, and U. Michel. Investigation of aero-engine core-noise using a phased microphone array. In *7th AIAA/CEAS Aeroacoustics Conference and Exhibit, Maastricht, Netherlands*. American Institute of Aeronautics and Astronautics, 2001.

[83] A. Henning, L. Koop, and K. Ehrenfried. Causality correlation in aeroacoustic experiments by means of simultaneous piv and microphone-array. In *BeBeC*, Berlin, 2010.

[84] D. Papamoschou, P.J. Morris, and D.K. McLaughlin. Beamformed flow-acoustic correlations in a supersonic jet. *AIAA Journal*, 48(10), 2010.

[85] S. Guidati. Advanced beamforming techniques in vehicle acoustics. In *BeBeC*, Berlin, 2010.

[86] K. Shin and J.K. Hammond. *Fundamentals of signal processing for sound and vibration engineers*. Wiley, 2008.

[87] F. V. Hutcheson and T. F. Brooks. Noise radiation from single and multiple rod configurations. *International Journal of Aeroacoustics*, 11(3):291–334, 2012.

[88] L. Chatellier and J. Fitzpatrick. Spatio-temporal correlation analysis of turbulent flows using global and single-point measurements. *Experiments in Fluids*, 38(5):563–575, 2005.

[89] P. Jordan, J. A. Fitzpatrick, and JC. Valiere. Measurement of an aeroacoustic dipole using a linear microphone array. *The Journal of the Acoustical Society of America*, 111(3):1267–1273, 2002.

[90] O. Jaeckel. Strengths and weaknesses of calculating beamforming in the time domain. In *BeBeC*, Berlin, 2006.

[91] M. Garcia-Pedroche and G. J. Bennett. Aeroacoustic noise source identification using irregularly sampled ldv measurements coupled with beamforming. In *17th*

AIAA/CEAS Aeroacoustics Conference, Portland, Oregon, USA, 2011. American Institute of Aeronautics and Astronautics.

[92] M. Garcia-Pedroche and G. J. Bennett. Aeroacoustic source identification measurements coupling time-resolved piv and array signal processing. In *19th AIAA/CEAS Aeroacoustics Conference*, Berlin, Germany, 2013. American Institute of Aeronautics and Astronautics.

[93] H. V. Fuchs. Space correlations of the fluctuating pressure in subsonic turbulent jets. *Journal of Sound and Vibration*, 23(1):77–99, 1972.

[94] A. V. G. Cavalieri, P. Jordan, A. Agarwal, and Y. Gervais. Jittering wave-packet models for subsonic jet noise. *Journal of Sound and Vibration*, 330(1819):4474–4492, 2011.

[95] M. Koenig, A.V. G. Cavalieri, P. Jordan, J. Delville, Y. Gervais, and D. Papamoschou. Farfield filtering and source imaging of subsonic jet noise. *Journal of Sound and Vibration*, Article In Press, 2013. http://dx.doi.org/10.1016/j.jsv.2013.02.040.

[96] Dimitri Papamoschou. Imaging of directional distributed noise sources. *Journal of Sound and Vibration*, 330(10):2265–2280, 2011.